Université du Québec
Institut National de la Recherche Scientifique (INRS),
Department of Energy, Materials and Telecommunications (EMT)

Integrated Photonic Devices for Optical Pulse Shaping, Processing and Measurement

By
Hamed Pishvai Bazargani

Dissertation submitted in partial fulfillment of the requirements for the degree of
Doctor of Philosophy in Telecommunications

Assessment of jury:

External referee	Prof. John (Xiupu) Zhang Concordia University
External referee	Prof. Pavel Cheben, National Research Council of Canada
Internal referee	Prof. Tarek Djerafi, INRS-EMT
Director of research	Prof. José Azaña, INRS-EMT

Université du Québec
Institut National de la Recherche Scientifique (INRS),
Énergie Matériaux Télécommunications (EMT)

Dispositifs photoniques intégrés pour la mise en forme, traitement et la mesure des impulsions optiques

Par
Hamed Pishvai Bazargani

Thèse présentée pour l'obtention du grade de
Doctorat en Télécommunication, Ph.D.

Jury d'évaluation

Examinateur externe	Prof. John (Xiupu) Zhang Concordia University
Examinateur externe	Prof. Pavel Cheben, National Research Council of Canada
Examinateur interne	Prof. Tarek Djerafi, INRS-EMT
Directeur de recherche	Prof. José Azaña, INRS-EMT

Dedication

To: My wonderful wife, love of my life, for her love, support and encouragements

My mom, my angel, for making me who I am

My dad, my best friend, for his unconditional love and self-sacrifices

My sister, my mentor, for helping me through difficulties

Acknowledgements

I would like to thank Yalda, my wonderful wife, from depth of my heart for her love, support, encouragements and patience. Yalda, I remember you making our home such a warm place where I used to totally forget all the challenges that I had throughout the day. I cannot thank you enough for all your self-sacrifices during these years. I also thank my parents, Madam Sakineh Mozaffari Bazargani and Mr. Hassan Pishvai Bazargani, and my sister, Mrs. Sahar Pishvai Bazargani for believing in me, giving me positive energy and staying by my side for all the decision that I made in my life.

I thank my supervisor, Prof. José Azaña, for his trust, allowing me to follow my dreams. During years, José has supported me, not only in my research, but also in my personal life. I am always very grateful to him.

I would like to express my gratitude to Prof. Lukas Chrotowski for organizing Silicon Electronic-Photonic Integrated Circuits (SiEPIC) workshops and teaching me how to design, simulate and test integrated photonics devices.

I would like to acknowledge Canadian Microelectronics Corporation (CMC) for providing access to different fabrications runs and CAD tools.

My specials thanks goes to government of Quebec for supporting my PhD studies through scholarship “Bourse de doctorat en recherche pour étudiants étrangers – FRQNT”.

I thank Sylvain Fauvel, our IT expert at INRS, for helping me setting up the CAD tools and Rob Helsten, our lab technician, for his extensive help with the development of characterization setups.

I shall not forget my dear colleagues. I thank Rosario, Reza Maram, Reza Ashrafi, Maurizio, Luis, Jeonhyun, Bo, Hossein, and Ming for their help with simulations and experiments, fruitful discussions and most importantly for their friendship.

Finally, I gratefully acknowledge the Natural Sciences and Engineering Research Council of Canada (NSERC), le Fonds Québécois de la Recherche sur la Nature et les Technologies (FQRNT), and Institut National de la Recherche Scientifique – Énergie, Matériaux et Télécommunications (INRS-EMT), for providing the financial support which allowed me to undertake this PhD research.

Abstract

Over the last decade significant increase in internet access, high speed communication, high definition media streaming and high volume cloud storage have affected our daily lives. This has resulted in an unprecedented demand in the speed and volume of data transfer. To overcome the severe speed limitations of present electronic circuits, which are practically limited to processing and switching speeds below a few tens of GHz, all-optical or alternatively electro-optical solutions have attracted considerable attention, offering generation/processing speeds from 10s of GHz to several THz. Over the years engineers have moved light ever closer to the heart of computing systems, the microprocessor, in order to keep up with the switching and processing speeds required to manipulate the gigantic amount of data being passed to telecommunication networks. This topic is particularly important for applications in data centers[1], due to the limitations of electronics circuits and copper wires in handling and processing high data rates.

In particular, silicon photonics is seen as a great foundation for optics and electronics to meet. Leveraging from mature complementary metal oxide semiconductor (CMOS) fabrication process, silicon photonics offers wafer scale testing, low cost packaging, scaling to high levels of integration, solves electrical interconnect limitation in data centers, supercomputers and integrated circuits.

Despite all the advantages offered by silicon photonics, it has been mostly implemented in interconnects and/or switching applications in industry. Significant effort has been put into development of signal processing building blocks, which already exist in electronics, alternatively in optical domain with unprecedented operation bandwidths (processing speeds). These signal processors generally fall into two categories: (1) linear optics and (2) nonlinear optics-based devices. Linear optics signal processors are of higher interest in telecommunications, because they usually work with lower levels of power (few to tens of milliwatts). These processors offer 100 to 1000 times improvement in processing speed as compared with their electronic counterparts.

[1] Data centers consist of a large group of networked computer servers typically used by organizations for the remote storage, processing, or distribution of large amounts of data.

The main objective of this Thesis is to develop integrated photonics devices for on-chip optical pulse shaping, processing and measurement. The Thesis includes proposals and developments of novel theories, designs, numerical analysis, layout preparations and experimental demonstrations. Specific accomplishements of this Thesis include:

a) Proposal and development of a novel theoretical frame work, namely discrete space-to-time mapping in cascaded co-directional couplers, enabling practical on-chip arbitrary optical pulse shaping with time resolutions ranging from a few femtoseconds up to the sub-nanosecond regime.

b) Modelling, layout design and experimental demonstration of on-chip optical pulse shaping devices based on discrete space-to-time mapping theory. Demonstrated functionalities include: (1) high quality sub-picosecond/picosecond flat-top pulse generation; (2) Tsymbol/s optical phase coded bit-packet generation; (3) Tsymbol/s optical phase and amplitude coded bit-packet generation.

c) Proposal and development of a nondispersive, tunable band-pass/band-reject filtering scheme using photonics Hilbert transformers (PHTs) incorporated in a Michelson interferometer. By controlling the central frequency of PHTs with respect to each other, both the central frequency and the spectral width of the rejection/pass bands of the filter are proved to be tunable. In this project bandwidth tuning from 260 MHz to 60 GHz is numerically demonstrated using two readily feasible fiber Bragg grating-based PHTs. The designed filter offers a high extinction ratio between the pass band and rejection band (>20dB in the narrow-band filtering case) with a very sharp transition with a slope of 170-dB/GHz from rejection to pass band.

d) Proposal, modelling, layout design and experimental demonstration of on-chip fractional and integer-order PHTs on silicon-on-insulator (SOI) wafer, based on laterally apodized integrated waveguide Bragg gratings. In this work high-performance photonic integer and fractional-order Hilbert transformers, with processing bandwidths above 750 GHz, have been experimentally realized.

e) Experimental demonstration of on-chip, single-shot and real-time phase characterization of GHz-rate optical telecommunication signals. In particular, phase reconstruction based on optical ultrafast differentiation (PROUD) is implemented using an integrated-waveguide Mach-Zehnder Interferometer (MZI) to demonstrate self-referenced phase characterization of GHz-rate complex modulated signals (e.g. Quadrature Phase Shift Keying(QPSK), and Amplitude Phase Shift Keying (APSK) modulation formats), through a single-shot and real-time technique.

Finally, I strongly believe that the ideas, techniques and devices demonstrated throughout this Thesis can contribute to the development of novel integrated-waveguide all-optical/electro-optical processors.

Student	Director of research

Résumé

A. Motivation

Au cours de la dernière décennie, l'augmentation significative de l'accès à Internet, la communication à haute vitesse, la diffusion des médias à haute définition, et les grands volumes de stockage en nuage ont affecté nos vies quotidiennes. Cela a abouti à une demande sans précédent de vitesse et de volume de transfert de données. Malgré les progrès révolutionnaires accomplis dans la transmission des données et la capacité de traitement au cours des 30 dernières années, le trafic de données continue à croître à un rythme beaucoup plus rapide. Selon des études réalisées par CISCO, le trafic global annuel du protocole internet (IP) dépassera le seuil des zettabits (ZB) (octets) en 2016 et atteindra 2,3 ZB d'ici 2020 [1]. Afin de répondre à cette demande croissante, les télécommunications optiques ont été mises en œuvre comme une solution puissante, offrant de hauts débits de transmission et de vitesse de traitement. En particulier, les liens de fibre optique qui ont supplanté les fils de cuivre pour la transmission de données sur de longues distances (télécommunications longue distance i.e. quelques centaines/milliers de kilomètres [2]). La raison derrière cela est leur plus grande bande passante disponible, leur plus faible perte, un poids plus léger, une sécurité de données plus élevée, un moindre coût et une énergie plus faible requise pour transférer les données. Malgré les avantages des communications optiques, le traitement des signaux d'information au niveau de l'émetteur et du récepteur, dans une liaison de réseau de communication optique, se fait encore principalement dans le domaine électronique. Par conséquent, le traitement du signal tout-optique et les systèmes de commutation/ conversion optoélectronique à grande vitesse ont attiré une attention considérable.

Historiquement, les circuits photoniques intégrés (CPIs) à base de silice sur silicium, Niobate de lithium ($LiNbO_3$), et les CPIs III-V, tels que InP et GaAs, représentaient les principaux choix pour le traitement/commutation du signal optique sur puce [3]. Cependant, en raison du succès du silicium dans l’industrie de la microélectronique, plusieurs groupes de recherches ont commencé des projets dans les années 80 sur l'adoption de silicium comme matériau de base pour la fabrication des circuits photoniques [4]. La photonique sur silicium offre une compatibilité avec la plate-forme métal-oxyde semi-conducteur complémentaire (CMOS), le test en plaquettes, l'emballage à faible coût, des niveaux élevés d'intégration, résout la limitation d'interconnexion électrique dans les centres de données, les superordinateurs et les circuits intégrés.

En dépit de tous les avantages offerts par la photonique sur silicium, elle a été principalement mise en œuvre pour des applications d’interconnexions et /ou commutation dans l’industrie. Des efforts considérables ont été mis dans le développement de circuits optiques équivalents aux blocs électroniques de traitement du signal, en ciblant des améliorations considérables en termes de bande passante de fonctionnement (vitesse de traitement). Ces processeurs de signal tombent généralement dans deux catégories : des dispositifs basés sur (1) l’optique non linéaire et (2) L’optique linéaire. Dans cette thèse nous nous concentrons sur les techniques basées sur l’optique linéaire pour trois fonctionnalités principales : 1) la mise en forme d’impulsions optiques, 2) le traitement/ filtrage du signal optique, et 3) la caractérisation du signal optique. Dans ce qui suit, nous passons en revue brièvement les techniques qui ont été proposées/mises en œuvre précédemment pour les applications de traitement du signal, mentionnés ci-dessus, que nous visons.

A.1. Mise en forme d’impulsion optiques (MIO)

Le terme (MIO) désigne la synthèse des variations d’amplitude et/ou de phase d’une onde électromagnétique dans le domaine temporel, spatial ou fréquentiel dans le but de réaliser une forme d’onde optique visée [5]. Cette thèse porte principalement sur la synthèse précise et le contrôle de la forme temporelle des impulsions optiques avec des résolutions dans les régimes des picosecondes et sous-picosecondes, avec des porteuses ayant des longueurs d’ondes dans la gamme 1460 nm à 1625 nm (bandes S, C et L des fenêtres de transmission standard des télécommunications par fibre optiques). En pratique les impulsions optiques de type Gaussien, générées typiquement à partir d’un laser à verrouillage de mode, sont refaçonnées en une forme d’onde d’impulsion cible en utilisant différentes méthodes de MIO.

La MIO avec des bandes passantes en fréquence dans la gamme de GHz jusqu’au THz, est devenue de plus en plus importante pour une large gamme d’applications. Notamment, les impulsions optiques avec des formes temporelles définies par l’utilisateur qui sont utilisées pour les télécommunications par fibre optique à ultra-haut débit [6, 7], le traitement ultrarapide du signal optique [8, 9], etc.

Actuellement, les dispositifs de mise en forme d'impulsions optiques basés sur l'approche bien établie du traitement dans le domaine spatial sont disponibles dans le commerce, et ils permettent une synthèse programmable de formes d'ondes arbitraires avec une résolution meilleure que 100 fs [10]. Cependant, l'inconvénient majeur de cette méthode est sa relative complexité, nécessitant l'utilisation des composants optiques de haute qualité encombrants, ce qui affecte également les pertes d'insertion de l'appareil dans les systèmes à fibres optiques. Pour pallier à certaines de ces difficultés, des appareils basés sur des principes de mise en forme d'impulsions similaires ont été mis en œuvre en utilisant des réseaux de guide-d'onde intégrés sur puce [11]. Malgré leurs avantages importants, notamment en termes de compacité, ces dispositifs souffrent encore de la résolution spectrale limitée et la sensibilité aux erreurs de fabrication. Dans la quête de dispositifs de mise en forme / codage d'impulsion plus compacts, à plus faible perte et relativement simples, les structures tout-fibre et guides d'onde à réseaux intégrés ont attirés beaucoup d'attention [12]. Une approche de conception, particulièrement intéressante pour les réseaux à fibres optiques ou à guides d'ondes utilise l'approximation appelée approximation de Born du premier ordre, selon laquelle la réponse impulsionnelle du dispositif est une version directe, remise à l'échelle du profil d'apodisation du réseau [12, 13]. Cette propriété de projection espace-temps (STM for Space to Time Mapping en anglais) simplifie considérablement la conception des dispositifs de mise en forme d'impulsions temporelles. Cependant, les dispositifs basés sur des réseaux de Bragg (RB) à courte ou à longue période se sont avérés difficiles à fabriquer dans des configurations guide-d'ondes intégrés, en particulier s'ils sont destinés à synthétiser des formes d'onde complexes, par exemple, avec de hautes résolutions, au-dessous du régime sous-picoseconde sur de longues durées au-dessus de quelques picosecondes. En outre, les dispositifs à RB doivent être utilisés en réflexion, et il serait également difficile d'ajouter une reconfigurabilité dans ces structures, par exemple, à travers l'intégration de contrôleurs thermo/électro-optiques, et ce à cause des dimensions nanométriques des éléments des réseaux.

A.2. Traitement/ filtrage du signal optique

Les filtres optiques sont des dispositifs qui transmettent sélectivement la lumière à différentes fréquences. Les filtres optiques accordables de type passe/coupe-bande sont très demandés pour une large gamme d'applications importantes dans les systèmes de télécommunications WDM[2], traitement tout-optique du signal, la photonique micro-onde etc. [14, 10, 15]. Ces filtres optiques doivent répondre à certaines exigences, notamment : (1) La capacité de réglage de la fréquence centrale et la bande passante du filtre de façon indépendante, (2) Un passage abrupt de la bande passante à la bande rejetée, (3) Un fort taux d'extinction, (4) Un fonctionnement non dispersif, et (5) La compacité.

Différentes architectures ont déjà été proposées pour réaliser des filtres optiques accordables. Dans cette thèse, nous nous concentrons sur les filtres à base de réseaux qui sont particulièrement intéressants pour les applications de télécommunications [16]. La sélectivité en longueur d'onde d'un réseau est utilisée pour concevoir les filtres qui tombent dans cette catégorie. Cela comprend les filtres à base de réseaux en espace libre, à fibre, ou à guide-d'ondes intégrés. Dans le premier cas (à base de réseaux en espace libre), le faisceau à filtrer illumine d'abord un réseau de diffraction (RD[3]). Lorsqu'un faisceau de lumière polychromatique illumine un RD, toutes les longueurs d'onde qui le composent sont diffractées selon des angles différents. Dans cette configuration, une lentille est utilisée pour collimater la lumière diffractée du RD. Ensuite, un filtre accordable peut être réalisé par l'application d'un miroir mobile ou simplement une ouverture à cette lumière collimatée. Les avantages des filtres à base de RD en espace libre sont les faibles pertes d'insertion, la faible diaphonie, et le potentiel pour un fonctionnement stable sur une large plage de températures. Leurs principales limitations en revanche, sont l'encombrement et sensibilité des optiques à l'humidité et la contamination. En outre, la résolution spectrale ou la bande passante minimale offerte par ces filtres est généralement limitée à quelques dizaines de GHz [17].

Un principe de fonctionnement similaire au RD a été utilisé pour des applications de filtrage sur-puce en utilisant des réseaux de guide-d'ondes (AWG pour Arrayed waveguide gratings) [18]. Un AWG se compose de deux coupleurs en étoile à base de guides à ruban, reliés par un réseau de guides d'ondes dispersifs. Ces coupleurs en étoile sont utilisés dans des applications qui nécessitent plusieurs ports (entrée et / ou sortie). Ces coupleurs effectuent une répartition égale de la puissance optique d'un ou de plusieurs ports d'entrée sur deux ou plusieurs ports de sortie. Malgré leurs avantages importants, notamment en termes de compacité, les AWGs souffrent encore de la résolution spectrale limitée, par exemple, 25 GHz pour AWG réalisée sur SOI [18] (Silicium sur

---

2 Wavelength division multiplexing (WDM) en anglais : multiplexage par division en longueur d'onde, démontré la première fois par AT & T 1978 [14], est technologie qui multiplexe un certain nombre de porteuses optiques sur une seule fibre optique en utilisant différentes longueurs d'onde (couleurs) de lumière laser.

3 Un RD est composant optique qui exploite le phénomène de diffraction de la lumière. La lumière incidente sur ce dispositif est réfléchie dans une direction qui dépend de son angle d'incidence, sa longueur d'onde, et la période du réseau [5, 91].

isolant, en anglais Silicon On Insulator) et la sensibilité aux erreurs de fabrication et de phase qui sont dues aux variations de la largeur du guide-d'onde et de la hauteur des plaquettes.

Des RBs à base de guides-d'onde intégrés fabriqués sur la plate-forme technologique SOI ont également été mises en œuvre pour des applications de filtrage optique accordable. À titre d'exemple, Un filtre à guide-d'onde intégré basé sur RB constitué d'une paire de coupleurs contra-directionnels (DCs) en cascade, chacun fonctionnant comme un filtre d'extraction (les coupleur-CD sont des filtres à insertion-extraction assistés par réseau), a été précédemment démontré [19]. De façon similaire aux guide-d'ondes à RB, la sélectivité en longueur d'onde dans les coupleurs-CD est basée sur des perturbations périodique du matériau diélectrique. Cependant, au lieu d'une rétroflexion dans le même guide-d'onde, la longueur d'onde sélectionnée est extraite vers un autre guide-d'onde par couplage contra-directionnel. Cela, permet le fonctionnement insertion-extraction sans l'ajout d'un circulateur [19]. En dépit de la large plage d'accordabilité offerte par ce dispositif, sa bande passante minimale est encore limitée à quelques dizaines de GHz. En général, cela est une limitation fondamentale, car les RBs avec une bande-passante sous-GHz, nécessitent de longs/faible réseaux qui sont difficiles à fabriquer sur SOI, à cause de l'effet nuisible du bruit de phase [20]. Les RBs de fibre/guide-d'onde à période uniforme ont également été utilisés pour le filtrage optique. Mais la bande passante de ces filtres n'est pas accordable et leur résolution spectrale minimale est comprise dans l'intervalle d'au moins quelques gigahertz (compte tenu des limitations de fabrication standards) [21]. Par ailleurs, des filtres optiques à réseaux de Bragg de fibre (RBF) à phase décalée fonctionnant en transmission ont été conçus pour atteindre une bande passante ultra-étroite (<1 GHz) [22]. Cependant, dans ces systèmes, la largeur spectrale du signal à filtrer doit être inférieure à la largeur de bande de réflexion du réseau, qui est généralement limitée à quelques dizaines de GHz.

A.3. Caractérisation du signal optique

La mesure précise et la caractérisation des signaux optiques ultrarapides avec des résolutions de temps de l'ordre de la femtoseconde, a un large champ d'applications en physique, chimie, micro-ondes, et les télécommunications [10, 23, 24]. De nombreuses techniques de caractérisation d'impulsions optiques ont été développées au fil des ans, offrant différents ensembles de spécifications de performances. Cette thèse porte sur des techniques adaptées au problème de la caractérisation complète des signaux de données optiques généralement trouvés dans télécommunications par fibres optiques et / ou les systèmes de traitement d'information, à savoir, les impulsions optiques ultra-courtes ou les flux de données dans lesquels l'information est encodée sur porteuse optique provenant d'une source laser. Idéalement, dans les systèmes de télécommunication par fibres optiques et de traitement de l'information il faut avoir la capacité de caractériser des signaux optiques rapides (gamme de GHz) et de faible intensité (puissance moyenne en dessous du milliwatt), en utilisant de préférence des plateformes de mesure à fibres optiques ou à guide-d'ondes intégrés. Étant donné que les signaux de données sont généralement aléatoires (non répétitifs), les mesures en temps réel et en une seule fois sont également nécessaires. Enfin, les techniques auto-référencées sont d'un grand intérêt, car ils contournent la nécessité d'avoir une impulsion de référence bien caractérisée ou oscillateur local [25, 26, 27]. En outre, la capacité à mesurer l'information de la phase optique dans le domaine temporel devient de plus en plus importante dans les télécommunications optiques. La raison de cela est la tendance à l'augmentation des taux de transmission des données dans les systèmes de télécommunication par fibre optiques en utilisant des formats de modulation complexes, par exemple, par déplacement de phase [28]. Dans la pratique, les photodétecteurs quadratiques conventionnels ne peuvent être utilisés que pour caractériser l'intensité des signaux optiques avec une largeur de bande spectrale généralement inférieure à ~ 50 GHz. Par conséquent, plusieurs techniques ont été mises au point au cours des années pour caractériser complètement l'intensité et la phase du flux de données optiques ou les impulsions optiques ultra-courtes dans les domaines temporel et fréquentiel. Ces techniques peuvent être classées en deux groupes principaux, 1) techniques basées sur des méthodes d'optique non-linéaire, 2) basées sur des méthodes d'optique linéaire

A.3.1 Techniques de caractérisation basées sur l'optique non-linéaire

Parmi les méthodes répandues de caractérisation d'impulsions optiques on trouve le FROG (pour Frequency-Resolved Optical Gating) [23, 29], et SPIDER (pour Spectral Phase Interferometry for Direct Electric-Field Reconstruction) [30], ainsi que leurs multiples variantes. Ces techniques ont été traditionnellement mis en œuvre par l'utilisation des non-linéarités optiques dans une variété de matériaux et /ou de technologies guide-d'ondes [31]. Au fil des ans, ces méthodes ont été adaptées pour fonctionner sur une large gamme de durées d'impulsions, bandes de fréquences et des énergies. Néanmoins, en raison de la forte puissance nécessaire dans les méthodes non linéaires, souvent elles ne peuvent pas être appliquées dans les télécommunications optiques [32, 33].

A.3.2 Techniques de caractérisation basées sur l'optique linéaire

Un effort considérable a été mis dans le développement des techniques basées sur les effets linéaires. Comparées aux techniques classiques de l'optique non-linéaire, les méthodes d'optique linéaire offrent une sensibilité accrue. En outre, ils peuvent être mis en œuvre en utilisant des plateformes simples et pratiques (par exemple, à base de fibre ou à base de guide-d'ondes intégrés). Parmi les démonstrations récentes on trouve l'implémentation linéaire de concepts déjà prouvé avec les processus non linéaires (i.e., spectrographie [34] et l'auto-interférométrie spectrale [35]) ainsi que de nouveaux systèmes de mesures d'optique linéaire [36, 37, 38, 39]. La détection cohérente est l'une des techniques linéaires les plus utilisées pour extraire l'information de phase d'un signal optique. En principe, un récepteur cohérent est une structure à base d'interféromètre combinée avec une photo-détection équilibrée [40]. Dans cette technique, un oscillateur local (OL) doit être mélangé avec le signal sous test afin de démoduler ce dernier. La détection cohérente nécessite que le récepteur ait connaissance de la phase de la porteuse, car le signal reçu est démodulé par un OL qui sert de référence de phase absolue. Un des principaux inconvénients liés à cette technique est qu'une configuration donnée ne fonctionne que pour un format de modulation spécifique et à un débit binaire prédéterminé. Malgré les nombreux avantages offerts par les méthodes de caractérisation cohérentes, les techniques auto-référencées de caractérisation impulsions basées sur l'optique linéaire ont été également développées pour contourner la nécessité d'un OL stable avec une synchronisation très précise [41, 42]. À titre d'exemple, la méthode PROUD (pour Phase Reconstruction Using Ultrafast Optical Differentiation) est une méthode linaire auto-référencée pour la reconstruction de la phase et basée uniquement sur la mesure de l'intensité [43, 44, 45, 46, 47, 48]. PROUD est particulièrement adaptée à la caractérisation du signal dans le contexte des télécommunications optiques. Cette technique peut être utilisée pour la caractérisation complète des signaux optiques, sur une très large gamme de durées d'impulsion, de l'ordre de 100 fs et jusqu'au régime de la nanoseconde [43, 44, 45]. Les précédentes implémentations de PROUD sont basées sur les fibres-optiques, par conséquent, ces implémentations souffrent d'instabilités du système qui affectent, au final les performances de mesure. Par exemple, pour une mesure unique et à temps réel, les précédentes implémentations de PROUD nécessitent l'utilisation d'un système complexe basé sur deux filtres optiques linéaires parfaitement complémentaires, une photo-détection équilibrée, et un système de refroidissement à eau pour stabiliser l'interféromètre à fibre optique [48]. En conséquence, la mesure en une seule fois et à temps réel n'a pu être démontrée que sur des variations relativement simples de forme d'onde optique, en particulier un signal sinusoïdal à 1 GHz modulé en intensité et avec une fréquence modulée linéairement (chirped) ainsi qu'un signal PRBS (pseudo-random binary sequence) à 3-Gbps modulé en phase, avec deux niveaux de modulation seulement (0 et π) [48].

B. contributions originales

- Développement d'une nouvelle solution basée sur un guide d'onde intégré pour répondre aux problèmes des méthodes existantes de mise en forme d'impulsion optique (MIO), à savoir, 1) limitations de bande-passante de fonctionnement associée à l'utilisation des dispositifs électroniques classiques de mise en forme d'impulsion [49], 2) complexités associées à l'utilisation de composants d'optiques encombrants, par exemple, réseaux de diffraction en espace-libre, modulateurs spatiaux de lumière, etc. [10], 3) les défis de conception associés à l'utilisation des méthodes indirectes de mise en forme d'impulsion dans le domaine fréquentiel [10, 9], et 4) la limitation de la bande passante associée aux façonneurs d'impulsion basés sur des réseaux de Bragg, limité par a résolution spatiale réalisable avec les technologies de fabrication existantes [12, 21]. Parmi nos contributions les plus pertinentes nous mentionnons les suivantes :

    - Proposition et développement théorique d'une méthode MIO basée sur la projection espace-temps discrète dans les coupleurs co-directionnels en cascade. La modélisation précise du système proposé a été réalisée pour sa mise en œuvre sur puce [50, 51].

    - Démonstration expérimentale de la MIO sous-picoseconde en technologie SOI, basé sur la projection espace-temps discrète. Dans ce projet nous avons réalisé une mise en forme d'intensité et de phase d'impulsion en régime sous-picoseconde. En particulier, des impulsions à sommet plat d'une durée allant de 440 fs à 3 ps, et des séquences d'impulsions à phase codée de 8-bits à 0.6-Tbit/s avec 4 niveaux de phase différents ont été générées avec succès dans une puce SOI compact [52, 53].

    - De plus, nous avons synthétisé expérimentalement des signaux de longue durée avec modulation d'intensité et avec modulation complexe (modulation simultanée de phase et d'intensité). En particulier, des impulsions à sommet plat avec des durées de l'ordre de 70 ps, et des séquences de données de durée de 40 ps et avec une modulation d'amplitude à 16 quadratures à 200-Gbaud ont été générées avec succès en utilisant notre système proposé, ce qui démontre son unique capacité de synthèse des impulsions optiques avec des durées allant de la femtoseconde jusqu'à plusieurs dizaines de picosecondes [54, 55].

- Développement d'un nouveau dispositif de filtrage à base de guide-d'onde intégrés pour surmonter les limites de performance des méthodes de filtrage proposées précédemment basées sur des réseaux, ce qui permet, 1) La réalisation des filtres accordables à bande étroite (sous-GHz), 2) La capacité d'accorder la bande passante et la fréquence centrale de manière indépendante. 3) un fonctionnement non dispersif, et 4) la compacité. Parmi nos contributions les plus pertinentes nous mentionnons les suivantes :

    - Proposition et conception d'un filtre optique accordable, non-dispersif utilisant la transformation de Hilbert photonique (THP). Dans ce travail nous avons proposé et démontré numériquement un nouveau principe de conception pour la mise en œuvre des filtres optiques accordables non-dispersifs et complémentaires (passe-bande/ coupe-bande) avec une accordabilité sur une large gamme de fréquences et de bande passantes. Le dispositif est constitué de deux transformateurs de Hilbert photoniques intégrés dans un interféromètre de Michelson. En contrôlant la fréquence centrale des transformateurs de Hilbert l'un par rapport à l'autre, la fréquence centrale et la largeur spectrale de la bande passante et la bande rejetée du filtre s'avèrent accordables. En particulier, une accordabilité de 260 MHz jusqu'à 60 GHz a été démontrée numériquement en utilisant deux configurations THPs basées sur des réseaux de Bragg et facilement réalisables. Le filtre conçu offre un taux d'extinction élevé entre la bande passante et la bande de rejet (> 20 dB dans le cas de filtrage à bande étroite) et une transition abrupte entre les deux bandes avec une pente de 170 dB/GHz [56, 57, 58].

    - Pour assurer une haute qualité des transformateurs de Hilbert, afin de réaliser les filtres proposé plus haut, nous avons proposé et démontré expérimentalement des conceptions de THP à base de réseaux de Bragg à guide-d'onde sur SOI avec une apodisation latérale. Dans ce travail, des transformateurs d'Hilbert photoniques de haute performance à ordre entier et fractionnaire, avec des bandes passantes de traitement supérieures à 750 GHz, ont été réalisés expérimentalement [59].

- Développement d'un système d'optique linéaire à base de guide-d'onde intégré pour surmonter les limites des méthodes de caractérisation du signal optique proposées précédemment, à savoir, 1) le besoin de haute intensité des signaux dans les techniques d'optique non-linéaire [23], 2) la nécessité d'un oscillateur local (OL) dans les méthodes de détection cohérente [60], 3) la nécessité d'une photo-détection équilibrée dans la méthode PROUD (Phase Reconstruction using Optical Ultrafast Differentiation) pour réaliser un fonctionnement temps réel et à mesure unique [47], nos contributions sont :

- Démonstration expérimentale de la caractérisation temps réel et à mesure unique sur puce des signaux optiques complexe à des vitesses de l'ordre du GHz. Dans ce travail la reconstruction de la phase à l'aide de la différentiation optique ultra-rapide (PROUD) a été mise en œuvre, en utilisant interféromètre Mach-Zehnder à base de guide-d'onde intégré, pour démontrer l'auto-référencement de phase.

- La caractérisation des signaux rapides (régime du GHz) à modulation complexe (par exemple, décalage de phase à quadrature, et modulation d'amplitude et de phase), en utilisant une technique temps réel et à mesure unique. Cette méthode est indépendante du format de modulation et du débit binaire, limitée seulement par les capacités en bande passante des instruments de mesure de l'intensité temporelle, tout en évitant la nécessité d'un signal de référence (par exemple, OL) [60].

Les dispositifs d'optique intégrée proposés et démontrés dans cette thèse ouvrent de nouvelles voies potentielles pour d'autres développements de dispositifs ultrarapides de télécommunication optique, des unités de calcul tout-optique, des sous-systèmes tout-optique de mesure et de traitement d'information, intégrés sur puce de silicium et compatible avec les plateformes de fabrication CMOS.

C. Résumé des projets

L'objectif principal de cette thèse est de développer des dispositifs photoniques intégrés pour la mise en forme d'impulsions optiques, le traitement et la mesure sur puce. Cette thèse comprend des propositions et des développements de nouvelles théories, conceptions, analyse numérique, et des démonstrations expérimentales. Les objectifs spécifiques visés dans cette thèse sont : (1) Développement d'un façonneur d'impulsion optique sur puce, capable de remodeler une impulsion Gaussienne limitée par transformée, en une forme d'onde arbitraire ou un code à profil complexe avec une résolution temporelle allant de quelques femtosecondes à la sous-nanoseconde ; (2) Développement d'un filtre sur puce passe/coupe-bande accordable (fréquence centrale et bande passante) avec une plage d'accordabilité allant du sous-GHz à quelques dizaines de GHz ; (3) Développement d'un transformateur d'Hilbert photonique à ordre entier/ fractionnaire intégré sur-puce ; (4) Caractérisation sur puce en temps réel et en une seule mesure des signaux optiques complexes et rapide (régime du GHz).

D. Mise en forme d’impulsion sur puce

Dans cette thèse nous introduisons une nouvelle structure discrète de coupleur co-directionnel et son approche de conception générale de la MIO dans le domaine temporel. La conception proposée est basée sur le couplage direct entre un guide d’onde principal et un guide d’onde bus, où le couplage est contrôlé de façon discrète (point par point) à travers des coupleurs co-directionnel standard, voir schéma de la Figure 1 (a).

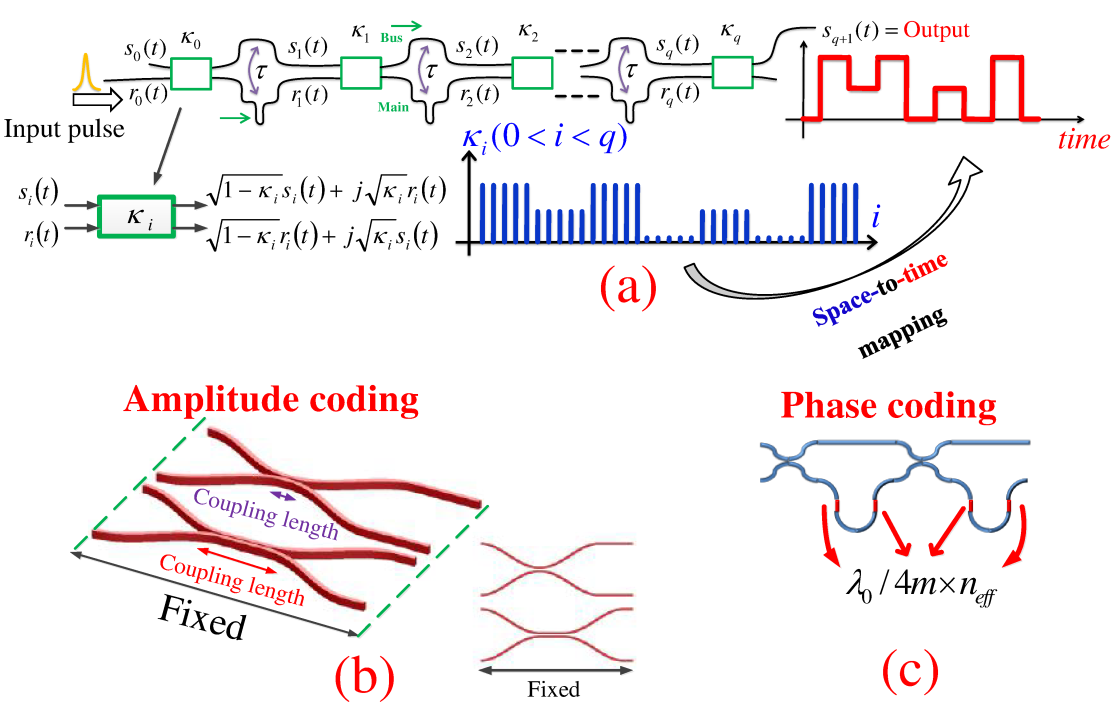

Figure 1 (a) Schéma du dispositif de mise en forme d'impulsions proposé et son principe de fonctionnement (projection espace-temps discrète); (b) Codage d'amplitude en réglant la longueur de couplage (la longueur totale du coupleur directionnel doit être fixée afin d'éviter les changements de phase indésirables dans les différents étages du dispositif); (c) Codage de phase en réglant la longueur du guide d'ondes dans les lignes à retard différentiel.

En particulier, nous montrons que le dispositif peut être conçu de telle sorte que les profils d’apodisation discrète de phase et d’amplitude le long des coupleurs concaténés, à savoir la force de couplage et le retard temporel relatif entre les coupleurs, peut être directement transférée dans la réponse temporelle de sortie. Cette approche peut être interprétée comme une version discrète du processus STM dans les réseaux de guide d'ondes [12]. De même, cette approche facilite considérablement la conception des structures basées sur des coupleurs co-directionnel concaténés pour les opérations de mise en forme d'impulsion temporelle, par rapport aux méthodes de conception classique basées sur la synthèse de la réponse dans le domaine spectral, par exemple, les filtres dits en treillis [61]. En outre, les dispositifs résultants sont sensiblement plus simples à fabriquer que leurs homologues à base de réseaux de guide d'ondes, tout en permettant reconfigurabilité grâce à des mécanismes bien établis. Par exemple, un contrôle précis de la réponse temporelle en amplitude ou en phase peut être obtenu en réglant la longueur de couplage, Figure 1 (b), ou le retard différentiel entre les coupleurs, Figure 1 (c). En mettant en œuvre notre idée nouvellement proposée, nous avons pu générer des impulsions à sommet plat avec des durées sous-picoseconde jusqu'à quelques dizaines de picosecondes, des séquences d'impulsions de 8-bit à 0.6-Tbit/s à phase codée avec 4 niveaux de phase différents, ainsi que des séquences de données de durée de 40 ps avec une modulation 16-QAM à 200-Gbaud, le tout à partir de dispositifs complètement passifs (aucun processus de réglage post-fabrication n'a été utilisé).

D.1. Génération d'impulsion à sommet plat sur puce

Dans ce projet, nos principales formes d'ondes ciblées expérimentalement sont des impulsions à sommet plat de durée de 1.25-ps et 3-ps (FWHM) synthétisées à partir d'une impulsion optique Gaussienne d'une durée 540-fs à l'entrée, qui est directement générée à partir d'un laser à fibre à verrouillage de mode passif (Pritel) avec un taux de répétition de 16.8 MHz [52]. 10 ou 20 coupleurs (pour des impulsions de 1.25 ps ou 3 ps, respectivement) avec des coefficients de couplage identiques de ~0.001 sont connectés en série à travers des lignes à retard de 11.5 µm de long, correspondant à un temps d'échantillonnage de 174 fs. La lumière a été couplée au dispositif de la partie supérieure de la puce en utilisant une matrice de fibre. Le mécanisme de couplage se produit entre une fibre, polie avec un angle spécifique (en fonction de la conception du réseau de couplage, 28° pour ce cas) et le réseau-coupleur de surface [62]. Les fibres d'entrée / sortie ont été placées dans une matrice qui doit être soigneusement alignée sur les coupleurs de réseau appropriés de manière à optimiser le couplage de puissance optique. L'espacement entre les fibres dans la matrice est fixé à 127 nm. Cela a déjà été pris en compte dans la configuration conçue et les trois coupleurs à réseau, à savoir l'entrée, la sortie du guide d'onde-bus et la sortie du guide d'ondes principal, ont un espacement similaire pour correspondre au pas de la matrice.

Ces ensembles de façonneurs d'impulsions ont été fabriquées à l'université de Washington à l'aide de la lithographie à faisceau d'électron (E-beam) en utilisant une seule gravure sur une plaquette SOI. La caractérisation directe de la sortie dans le domaine temporel, les formes d'ondes synthétisées ont été réalisées en utilisant interférométrie spectrale à base de transformée de Fourier (FTSI) avec l'impulsions d'entrée comme référence [25]. Le dispositif expérimental utilisé est représenté sur la Figure 2.

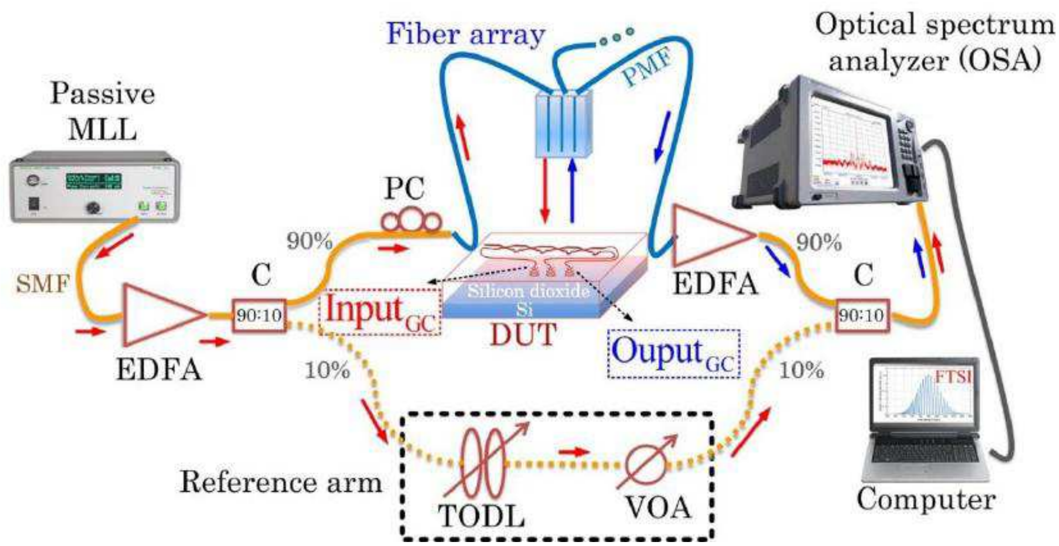

Figure 2 Schéma de la configuration FTSI, mise en œuvre pour la caractérisation du façonneur d'impulsions dans le domaine temporel. MLL, le laser à verrouillage de mode; C, coupleur; PC, contrôleur de polarisation; SMF (lignes oranges), fibre monomode; PMF (lignes bleues), fibre à maintien de polarisation; GC, réseau coupleur.

En outre, afin de caractériser les dispositifs en fréquence, leurs réponses spectrales de puissance (RSPs) ont été mesurées en utilisant un analyseur optique vectoriel (AOV), Luna Innovations, avec une résolution spectrale de 1,6 pm. Figure 3(b-e) montre les formes d'ondes et les RSPs mesurés expérimentalement à la sortie pour les deux conceptions décrites, montrant un assez bon accord avec les résultats attendus des simulations numériques.

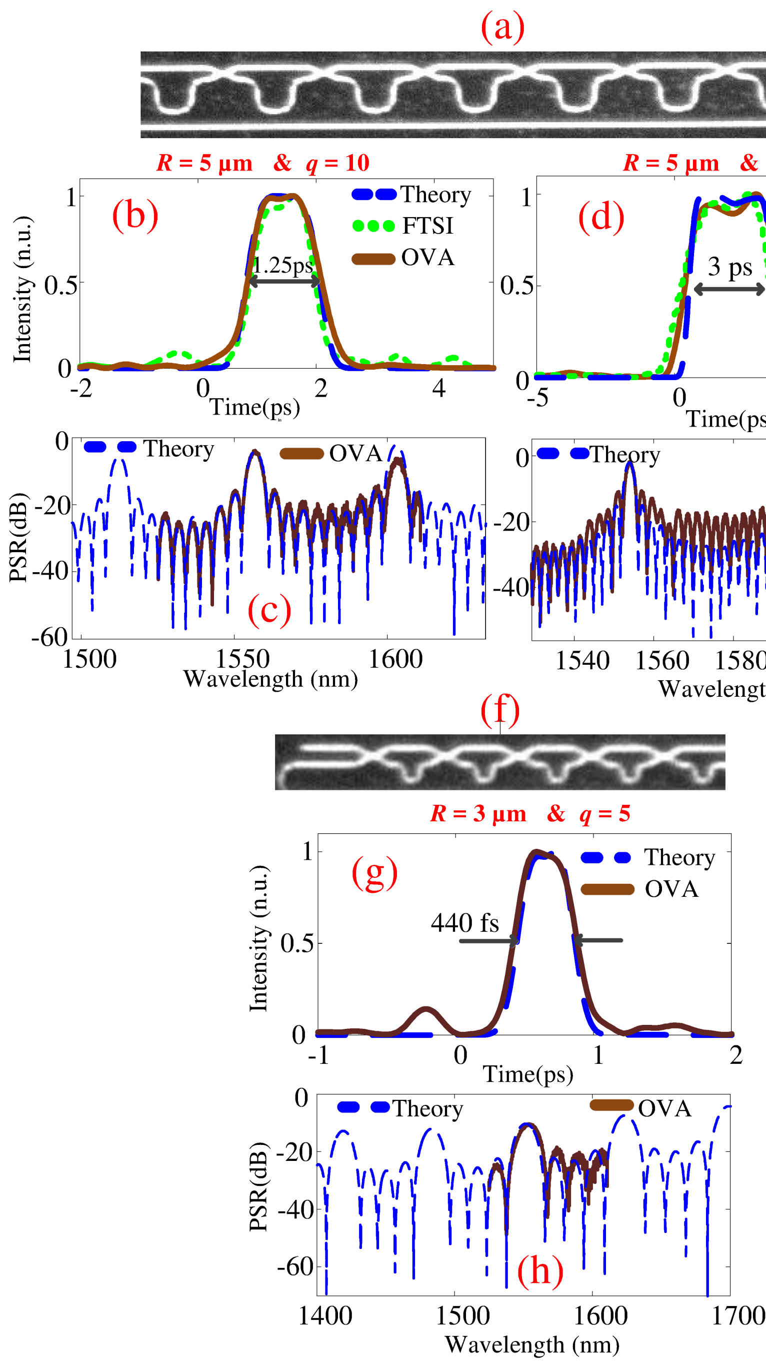

Figure 3 Micrographies, prises en utilisant une caméra montée sur un microscope, d'une partie des dispositifs fabriqués avec R = 5 µm et 3 µm (a et f, respectivement); La réponse temporelle d'amplitude et la réponse spectrale de puissance (RSP) simulées et mesurées d'un dispositif constitué de q = 10 coupleurs identiques en cascade (b et c, respectivement); q = 20 coupleurs identiques en cascade (d et e, respectivement); et q = 5 coupleurs identiques en cascade avec une différence de retard plus courte (g et h, respectivement). Pour les formes d'ondes temporelles, les résultats sont présentés à partir de mesures FTSI directes et par la transformation de Fourier du produit de spectre gaussien considéré en entrée avec les réponses spectrales complexes mesurées par un AOV et, comme obtenues par des simulations numériques. (AOV a une plage de mesure spectrale de 1520 nm à 1610 nm).

Une autre expérience de synthèse d’impulsions à sommet plat dans le régime femtoseconde est montrée dans la Figure 3. Dans ce cas, cinq coupleurs identiques ont été mis en cascade avec une différence de longueur relative de 6.8 µm (rayon de courbure de 3 µm), ce qui correspond à un temps de retard $\tau \approx 100$ fs. En raison de l'absence d’impulsions optiques suffisamment courtes (<100 fs) dans notre laboratoire, la réponse temporelle représentée dans la Figure 3(g) a été obtenue par simulation, en utilisant une impulsion Gaussienne de 100 fs (FWHM) à l'entrée et la vraie fonction de transfert du dispositif (amplitude et phase mesurés par l'AOV, voir Figure 3(h)). Les résultats montrés confirme la synthèse avec succès d’une impulsion à sommet plat de 440-fs limitée par transformée. Afin de montrer la large gamme de bande passante de fonctionnement offerte par notre méthode proposée, nous ciblons la synthèse d’impulsions à sommet plat avec des durées dans la gamme de dizaines de picosecondes. En particulier, notre deuxième expérience vise des impulsions de durées de ~70 ps synthétisées à partir d’impulsions Gaussiennes de 3 ps, 5 ps et 6 ps à l’entrée, qui sont générées directement d’un laser à fibre à verrouillage de mode passif (Pritel) avec un taux de répétition de 16.8 MHz. En raison des valeurs relativement élevées de perte dans guides d’ondes monomodes en silicium, l’augmentation de la longueur des lignes à retard conduit habituellement à une réponse temporelle évanescente (en forme de pente) au lieu de la réponse d’amplitude plate visée à la sortie du dispositif. De plus, pour des longues lignes à retard, les variations dans la largeur du guide d’onde, appelées rugosités des murs latéraux, introduites par les processus de lithographie et de gravure, ainsi que les variations dans la hauteur du guide d’onde causée principalement par les non-uniformités de la plaquette SOI, détériorent sévèrement les performances du dispositif [63].

Sur la base des simulations effectuées en utilisant le logiciel Lumerical solution, pour étudier l’effet des variations de la largeur et de la hauteur sur l’indice effectif (n_{eff}) du mode fondamental quasi-TE à la longueur d’onde 1550 nm, n_{eff} est bien moins sensible pour des rubans plus larges que ~1000 nm (voir Figure 4(a)). En particulier, le paramètre défini pour étudier la sensibilité de l’indice de réfraction effectif aux variations de la largeur du guide d’ondes ($\mathrm{d}n_{eff}/\mathrm{dW}$) est presque constante pour ces ensembles de guides d’ondes. Par conséquent, l’utilisation des guides d’ondes larges peut être considérée comme une solution pour atténuer l'effet de bruit de phase dans les lignes à retard longues. En outre, selon les résultats de simulation illustrés sur la Figure 4 (b) la sensibilité du n_{eff} aux variations de la hauteur du guide-d’onde ($\mathrm{d}n_{\mathrm{eff}} / \mathrm{d}h$) est plus faible dans les guides plus épais. Cependant, dans la fabrication en fonderie la hauteur du guide d’onde est prédéfinie (par exemple la norme 220 nm) et elle ne peut pas être considérée comme un paramètre de conception. Afin de réduire la sensibilité aux non-uniformités de la plaquette, une technique consiste à concevoir lignes à retard longues sous une forme très compacte, par exemple en serpentine ou en spirale [20]. Comme indiqué plus haut, les pertes de propagation dans les guides d'ondes en forme de ruban peuvent être réduites en augmentant la largeur du ruban. Cependant, les guides d'onde plus larges que 500 nm (en supposant que la hauteur est de 220 nm) commencent à supporter des modes d'ordre supérieur. La présence de ces derniers est indésirable, car elle peut conduire à la dispersion et le comportement imprévisible des dispositifs basés sur l'interférence entre les différents modes optiques [64]. Une solution pour cela consiste à utiliser des guides d'ondes hybrides dans lesquels un guide d'ondes monomode (SMW pour Single Mode waveguide en anglais) est relié par un rétrécissement (cône) à un guide d'onde multimode (MMW pour Multi Mode Waveguide en anglais), et vice versa. Un cône adiabatique entre les deux régions de guide d'ondes assure l'excitation du mode fondamental dans la région multimode. Bien que la région multimode peut supporter des modes d'ordre supérieur, aussi longtemps que le guide d'onde est rectiligne et sans défauts, le mode fondamental se propage sans exciter les modes d'ordre supérieur. En dépit du fait que les défauts de rugosité excitent les modes d'ordre supérieur dans MMW, ces modes ne peuvent pas se propager dans les sections SMW et donc provoquent simplement une perte de puissance. Grâce à la mise en œuvre de cette technique une amélioration des performances (presque multipliées par 30) en termes de pertes optiques a été rapportée [65].

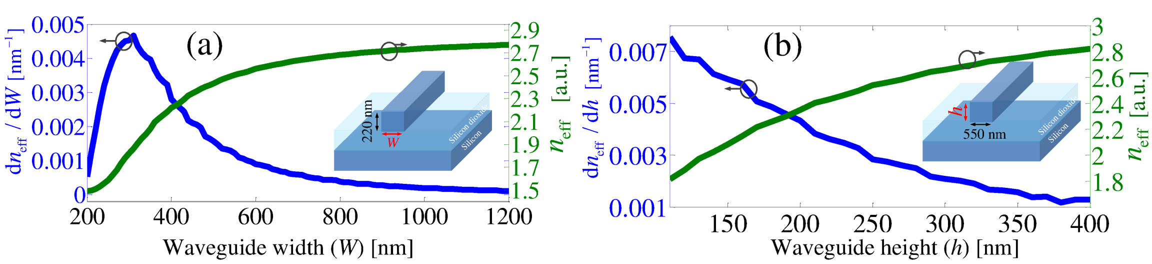

Figure 4 L'indice de réfraction effectif du mode fondamental quasi-TE et sa sensibilité à (a) la largeur (b) des variations de hauteur du guide d'ondes à la longueur d'onde de 1550 nm.

Dans ce travail, des MMWs avec une largeur de ruban de 1 µm, et une hauteur de 220 nm ont été mis en œuvre [66]. Cependant, SMWs avec des dimensions de 500 nm (largeur) x 220 nm (hauteur) sont encore utilisés dans les régions de couplage et de courbure, afin d'assurer un fonctionnement monomode du dispositif. Pour exciter seulement le mode fondamental du MMW, des cônes linéaires de 52 µm de longueur sont utilisés pour la conversion entre les SMWs et MMWs, voir Figure 5 (a-b). Les coupleurs concaténés, dans les trois dispositifs étudiés ici, ont un écart de couplage de 200 nm et une longueur de couplage nulle. En utilisant la simulation 3D des différences finies dans le domaine temporel (FDTD) un taux de couplage de puissance de ~0.001 a été estimé pour chaque coupleur. Un couplage efficace supérieur à zéro pourrait être atteint grâce à l'effet des régions de courbure du coupleur. Ces ensembles de dispositifs ont été fabriqués à l'IMEC en utilisant un procédé compatible-CMOS avec une lithographie à ultraviolet (UV) profonde à 193 nm sur plaquette SOI. La RSP a été mesurée en utilisant un AOV, voir la Figure 5(c-e) en répétant le processus expliqué ci-dessus. La caractérisation directe de la sortie dans le domaine temporel, des formes d'ondes synthétisées a été réalisée en utilisant interférométrie spectrale à base de transformée de Fourier (FTSI pour Fourier Transform Spectral Interferometry) [25]. Comme montré dans la Figure 5(f-h), des impulsions à sommet plat pratiquement identiques sont refaçonnées à partir d'une forme d'onde Gaussienne avec des durées temporelles plus courtes, de façon correspondante à l'augmentation de la bande passante en fréquence et le Produit Temps-Bande passante (PTB) des dispositifs. Enfin, en effectuant un filtrage passe-bande des spectres des signaux de sortie, on peut réaliser les formes d'onde à sommet plat visées.

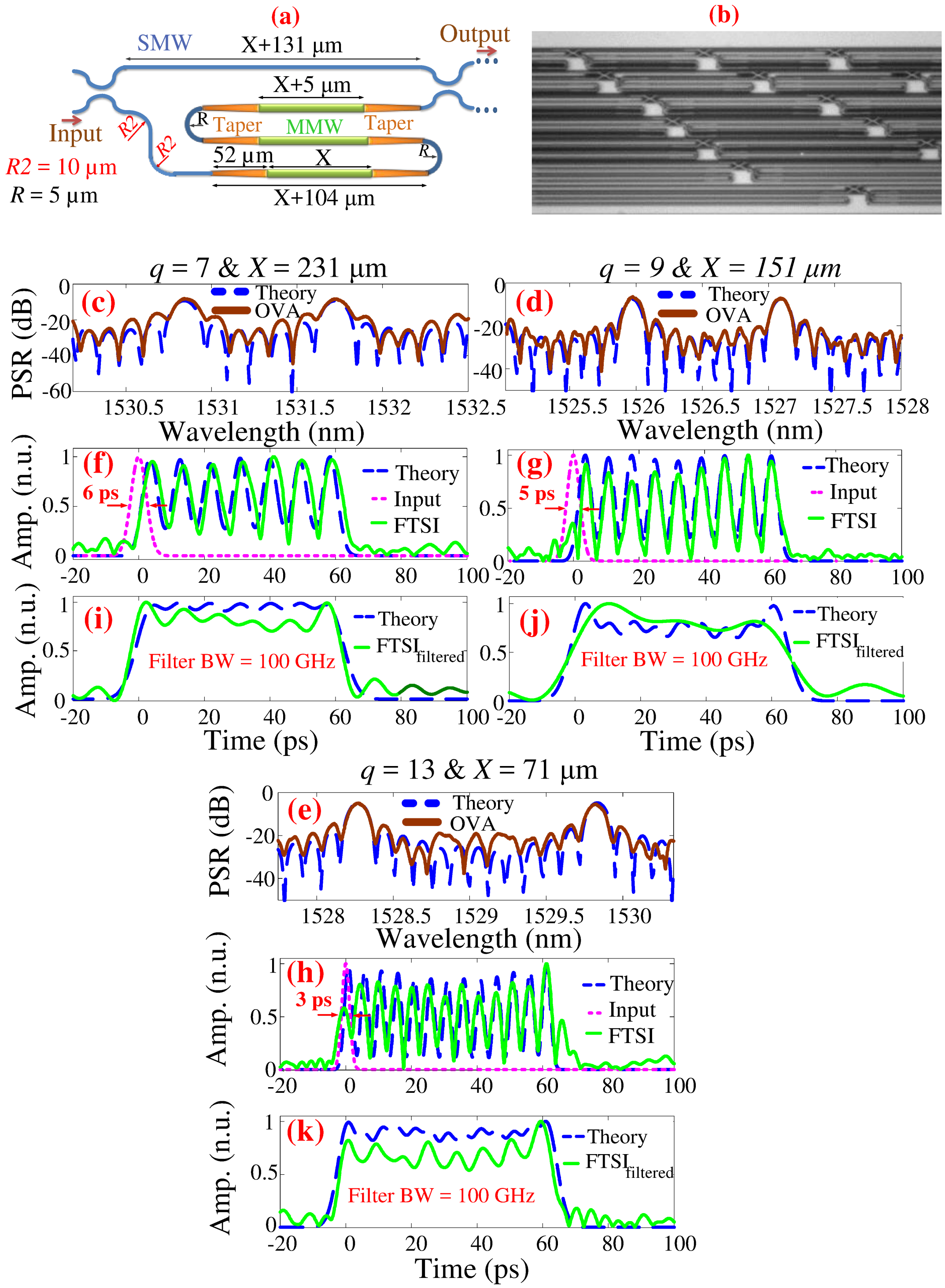

Figure 5 (a): Schéma d'un des étages des générateurs d'impulsions à sommet plat (X: la longueur du guide d'ondes et n: nombre de coupleurs en cascade); (b): Microscopie des parties du façonneur d'impulsions conçus; (C-e): RSPs simulées et mesurées en utilisant AOV; (F-h): les réponses temporelles des appareils, prévues théoriquement et mesurées expérimentalement en utilisant la méthode FTSI; (I-k): Formes d'ondes temporelles filtrées afin de réaliser les formes des impulsions à sommet plat.

D.2. Séquence de bit codé en phase

Dans ce projet, nous ciblons la synthèse d'une séquence d'impulsions de huit bits à phase codée avec un taux symbole de 0.3 Tbaud (vitesse de 0.6 Tbit/s) à partir d'une impulsion Gaussienne de 3.2 ps (FWHM) à l'entrée [52]. Les déphasages successifs sont les suivants: $0, \pi, \pi/2, 0, 3\pi/2, \pi, 0, 3\pi/2$. Huit coupleurs directionnels identiques avec des coefficients de couplage de ~ 0.001 sont connectées en série avec des lignes à retard de 588 µm de long. Une approche de conception similaire, comme expliqué plus haut, est mise en œuvre pour réduire les pertes de diffusion et la sensibilité au bruit de phase dans les lignes à retard longues (voir Figure 6 (a-b)). La fabrication de cet ensemble de dispositifs a été réalisée à l'aide de la lithographie E-beam en utilisant une seule gravure, à l'université de Washington. Les résultats des mesures temporelles et spectrales correspondantes sont représentés sur la Figure 6 (c-f).

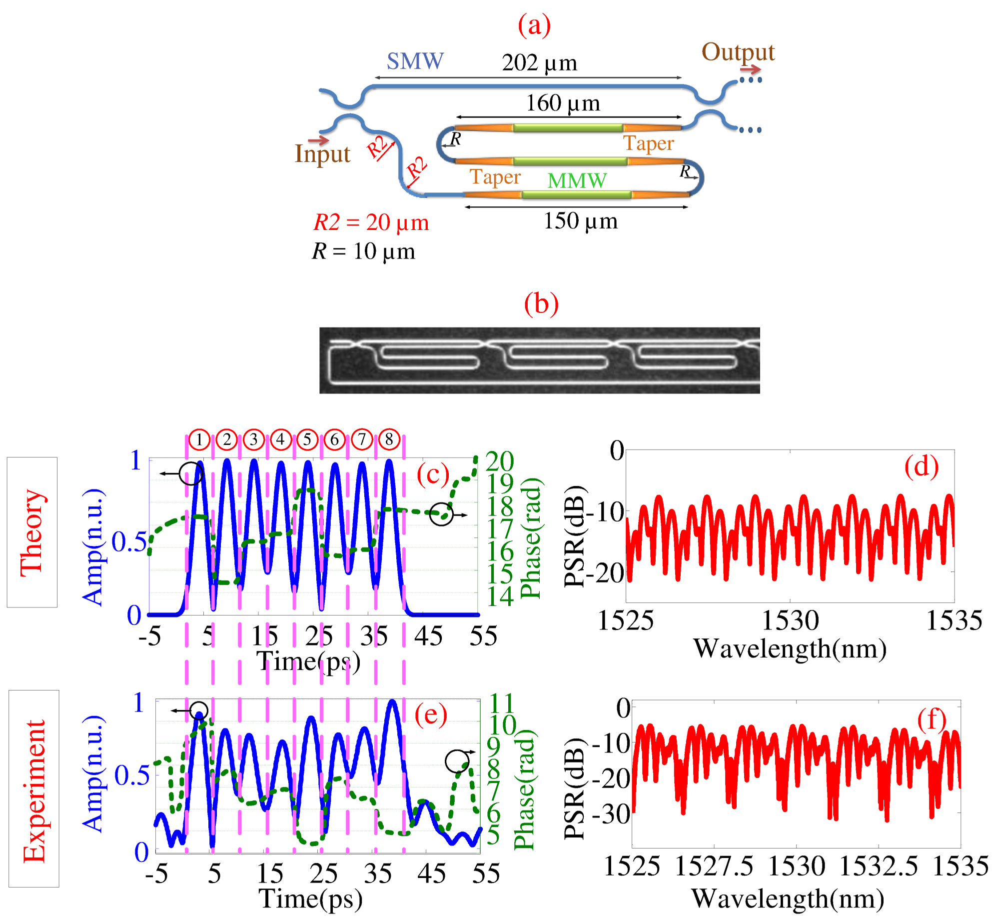

Figure 6 (a) Représentation schématique d'un étage du dispositif et (b) micrographie d'une coupe du dispositif fabriqué. (c) Les réponses temporelle (d) et spectrale (E) prévues théoriquement. Forme d'onde de sortie mesurée expérimentalement dans le domaine temporel en utilisant la caractérisation FTSI, (f) mesures de la RSP en utilisant l'AOV.

En outre, les valeurs précises des sauts de phase mesurées expérimentalement ont été comparées avec les prévisions théoriques figurant dans le Tableau 1.

Tableau 1 Les valeurs précises de sauts de phase pour la séquence de phase codée.

No.	1	2	3	4	5	6	7
Idéal (rad)	3.14	1.57	0	1.57	3.14	0	1.57
Théorie (rad)	2.93	1.84	0.33	1.96	2.9	0.3	1.7
Exp. (rad)	2.89	1.55	0.52	2.3	2.97	0.7	1.6

D.3. Séquence de bit avec modulation complexe 16-QAM

Dans notre dernière expérience nous ciblons la génération d'une séquence binaire modulée en phase et en amplitude avec une modulation complexe à 8 bits, synthétisée à partir d'une impulsion Gaussienne de 2.5 ps de durée [55]. 24 coupleurs directionnels sont connectés en série par l'intermédiaire des lignes à retard relatif de 114 μm de long ($\tau = 1.66$ ps) pour générer une séquence binaire avec une modulation complexe 16-QAM à 0.2-Tbaud (0.8-Tbit/s). Le procédé de fabrication a été effectué à l'université de Washington à l'aide de la lithographie à faisceau d'électron (E-beam) en utilisant une seule gravure. Des coupleurs directionnels, chacun avec un intervalle de couplage nominal de 300 nm et des longueurs de couplage de 6,2 μm, 4,4 μm, 1,5 μm ou 0 μm, ont été mis en cascade, réalisant quatre niveaux d'amplitude différents. En dépit de la différence entre les longueurs de couplage, destinées à contrôler l'amplitude d'impulsion dans l'intervalle de temps correspondant, la longueur totale de tous les coupleurs directionnels est fixée pour assurer la superposition en phase des différentes copies de l'impulsion d'entrée à chaque étage du dispositif, voir la Figure 1 (c). La caractérisation dans le domaine temporel a été effectuée en utilisant un procédé similaire à celui du FTSI dans l'exemple précédent, la Figure 7 (d-e) montre les résultats de la simulation et les profils d'amplitude et de phase mesurés expérimentalement en utilisant de la conception décrite.

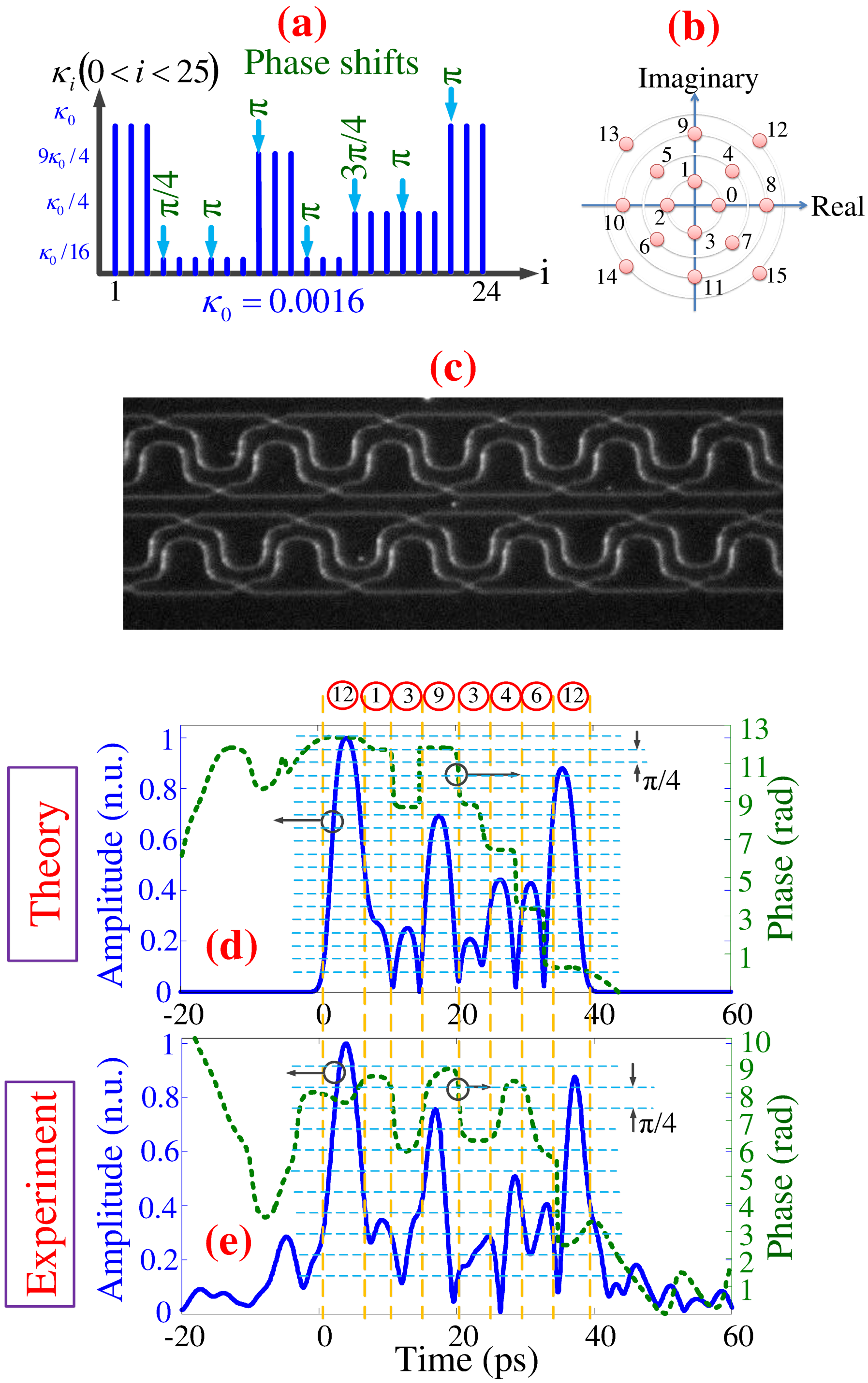

Figure 7 (a) rapport de couplage de puissance correspondant à chaque étage du dispositif et les niveaux de phase introduits; (b) Diagramme de constellation de type 16-QAM circulaire, (c) Micrographie d'une partie des dispositifs fabriqués; (d) Réponse temporelle du dispositif prévue théoriquement et (e) mesurées expérimentalement. Les décalages de phase consécutifs visés sont $0, \pi/4, \pi, \pi, \pi, 3\pi/4, \pi, \pi$, et les niveaux d'amplitude sont 1, 1/4, 1/4, 3/4, 1/4, 2/4, 2/4, 1.

Par ailleurs, les niveaux d'amplitude et de phase obtenus expérimentalement sont comparés dans le Tableau 2 à ceux obtenus à partir de la simulation.

Tableau 2 Comparaison entre les valeurs précises de phase (en rad) et les niveaux d'amplitude (théorie par rapport à l'expérience)

Bit no.	1	2	3	4	5	6	7	8
Idéal (Ph./Am)	0 / 1	0.63/0.25	2.93/0.23	3.05/0.69	2.84/0.2	2.29/0.44	3/0.42	3.09/0.87
Théorie (Ph./Am)	0 /1	0.63/0.25	2.93/0.23	3.05/0.69	2.84/0.2	2.29/0.44	3/0.42	3.09/0.87
Exp. (Ph./Am)	0 / 1	0.9/0.34	2.73/0.34	2.99/0.76	2.62/0.24	2.16/0.5	2.67/0.4	3.39/0.87

En matière de limites de la méthode proposée, nous prévoyons que la technique de projection espace-temps discrète peut être utilisée pour la mise en forme d'impulsions optiques avec une résolution temporelle dans le régime sous-femtoseconde, compte tenu d'une résolution de fabrication meilleure que ~ 5 nm. Cependant, pour des résolutions temporelles aussi élevées le bruit de phase devient un paramètre important. De plus, en utilisant des guides d'ondes de forme spirale pour réaliser des lignes à retard avec une longueur de l'ordre du millimètre, des impulsions optiques avec des durées temporelles dans le régime sous-nanoseconde peuvent être réalisées en utilisant la méthode proposée. Bien que le facteur limitant dans ce cas soit la perte de propagation du guide d'ondes.

E. Traitement du signal optique sur puce (filtrage)

Dans la structure que nous proposons, deux transformateurs de Hilbert photoniques (THPs) sont incorporés dans les deux bras d'un Interféromètre de Michelson (IM) symétrique, mettant en œuvre un filtre optique passe/coupe-bande non-dispersif et avec une large plage d'accordabilité. Un THP est essentiellement un filtre optique passe-tout linéaire produisant un seul décalage de phase à la fréquence centrale [67]. La réponse spectrale d'un THP est définie comme suit :

$$H_{PHT}(f) = \begin{cases} \exp\left(iP\frac{\pi}{2}\right) & f < f_0 \\ 0 & f = f_0 \\ \exp\left(-iP\frac{\pi}{2}\right) & f > f_0 \end{cases} \tag{1}$$

Où f est la fréquence optique, i est l'unité imaginaire, P définit l'ordre du THP et f_0 est la fréquence optique centrale. Pour P=1 la transformation est dite entière, sinon elle est dite d'ordre fractionnaire [68]. Il est à noter qu'en pratique la réponse spectrale d'un THP est à bande limitée et la transition de phase nécessaire se produit d'une manière lisse dans une région spectrale finie. La Figure 8(a) montre les réponses en amplitude et en phase idéales (ligne pointillée) et pratiques (ligne continue) d'un THP.

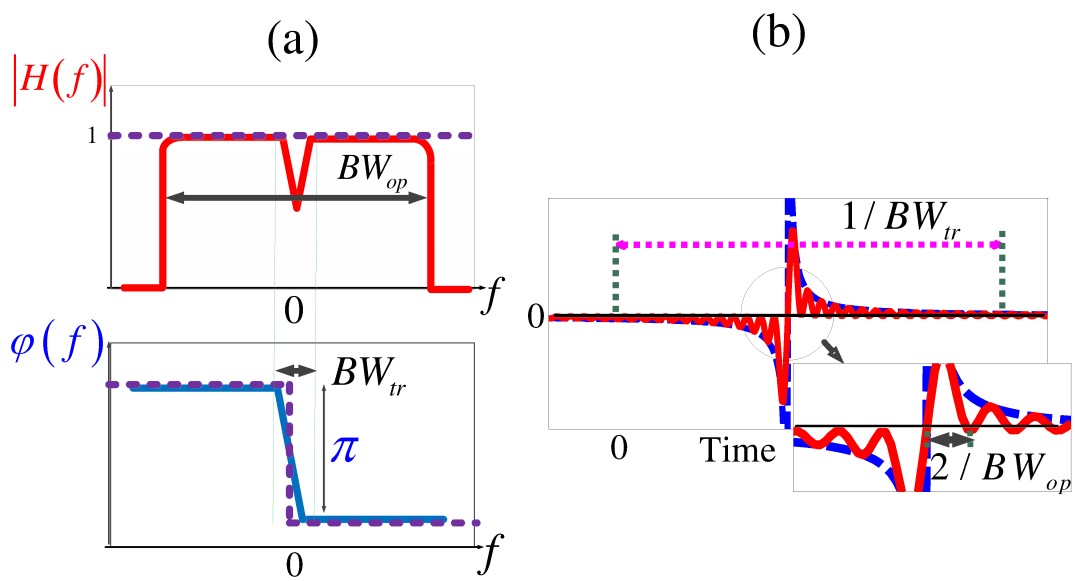

Figure 8 (a) Réponses spectrales d'amplitude et de phase de d'un THP d'ordre entier idéal (en pointillés), et pratique (line continue). (b) Enveloppe de la réponse impulsionnelle temporelle d'un THP idéal (en pointillés), et physiquement réalisable (line continue).

Plusieurs méthodes ont été démontrées pour réaliser des THPs, par exemple, en utilisant des réseaux de Bragg apodisés à base de fibre (RBFs) à phase décalée [67, 68], et des réseaux de Bragg (RBs) apodisé intégrés [69, 70].

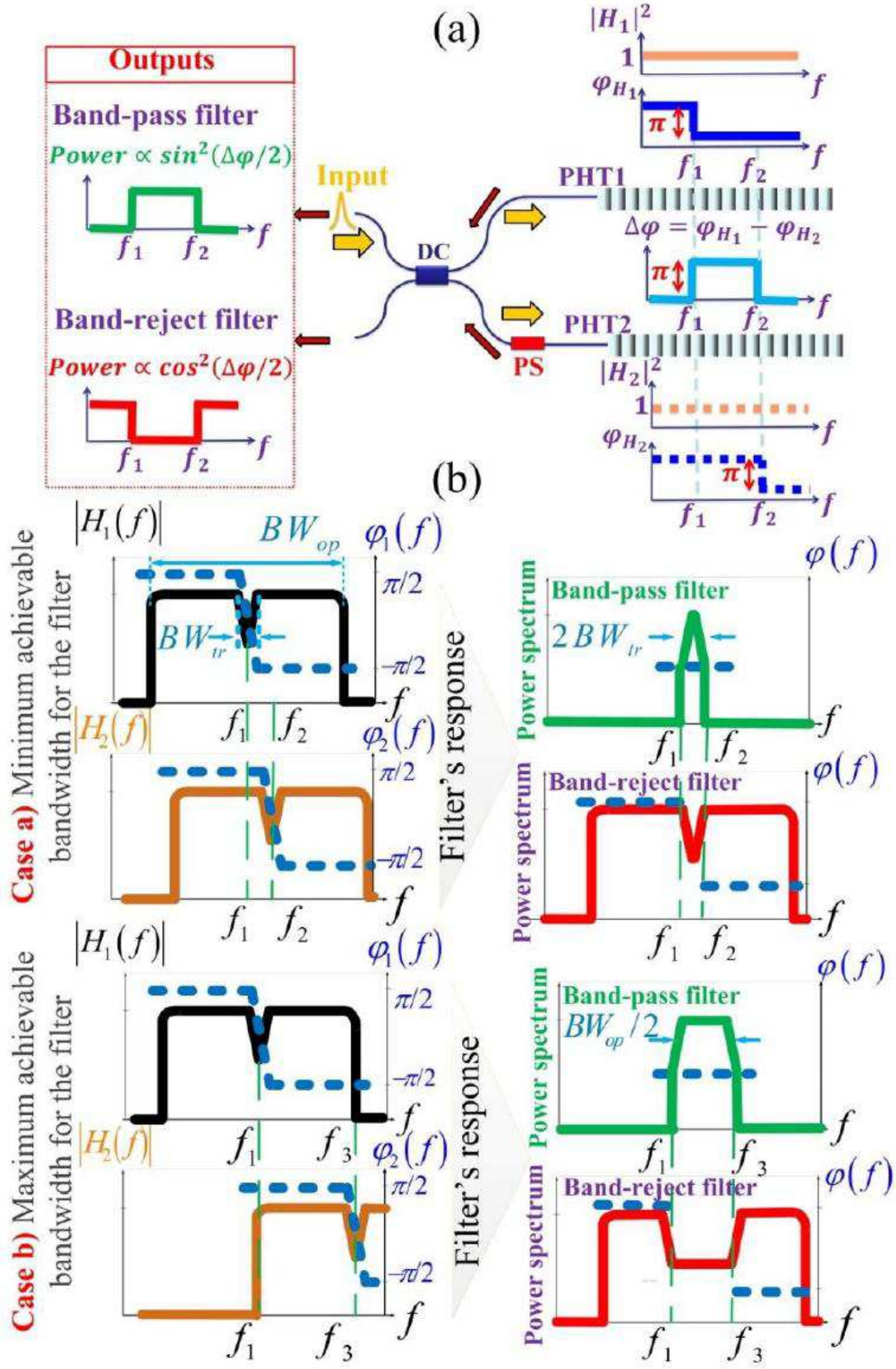

Figure 9 (a): La configuration de la structure du filtre optique proposée. (B): Réalisation du FPB / FCB aux deux ports de sortie de l'IM. DC: coupleur directionnel, et PS: (pour phase shifter) déphaseur.

Comme illustré dans la Figure 9, l'incorporation des THPs à base de RB apodisés dans un IM permet de contrôler à la fois la bande passante et la fréquence centrale du filtre proposé, et ce, simplement en modifiant la fréquence Bragg de l'un des réseaux par rapport à l'autre, cela peut être effectué à l'aide des méthodes largement accessible de contrôle de contrainte axiale ou de température [66].

Pour valider le principe, une conception facilement réalisable de THPs à base de RBF est simulée numériquement, ce qui démontre la capacité du filtre pour le réglage de la bande passante de 260 MHz à 60 GHz. Le filtre conçu offre un taux d'extinction élevé (> 20 dB pour le cas de filtrage à bande étroite) avec une transition bande-rejeté /bande passante très abrupte. Il convient de noter qu'une configuration similaire peut être réalisée avec un guide d'onde planaire en utilisant la technologie silice ou SOI. En outre, un Filtre Passe-Bande (FPB) et un Filtre Coupe-Bande (FCB) peuvent être réalisés simultanément aux deux ports de sortie de l'IM.

Afin de concevoir des THPs à base de RB, les profils d'apodisation requis sont obtenus au moyen d'un algorithme de diffusion inverse basée sur la théorie des modes couplés (TMC) combinée avec la méthode de matrice de transfert (MMT) [71]. Les caractéristiques cibles sont celles des RBF-THPs démontrés expérimentalement dans [68], en considérant f_0 =193 THz (fréquence centrale du THP), un bande passante d'opération à 3 dB $BW_{op} = 120$ GHz, et une réflectivité maximale de 99%. Les RBFs résultants ont une longueur de 14.5 cm et une période constante de 534.89 nm. La modulation d'indice de réfraction a une valeur maximale de 8×10^{-4}, et plusieurs oscillations sont nécessaires dans le profil d'apodisation du réseau, comme illustré sur la Figure 10(a). Ces oscillations imposent la nécessité de trois sauts de phase dont les positions sont marquées en rouge dans la Figure 10(a).

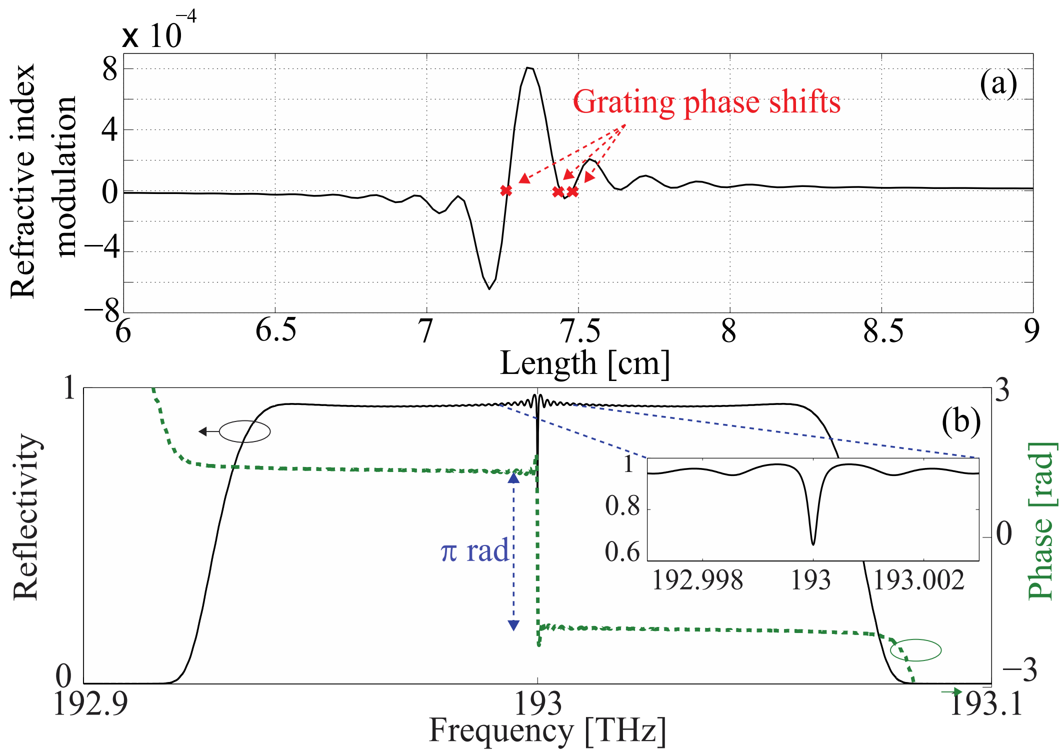

Figure 10 (a) le profil apodisation des réseaux conçus. (B) Réflectivité et phase de la réponse spectrale des réseaux.

En supposant que l'un des deux réseaux a une période fixe tel que défini ci-dessus tandis que l'autre RBF est étiré axialement, la bande passante spectrale à 3 dB du filtre peut être accordée de 260-MHz (bande passante à 20 dB de 560 MHz) à plus de 60 GHz. Cet accord pourrait être réalisé pratiquement en étirant axialement les fibres de ~30 nm à ~ 45 µm (augmentation de la période de réseau correspondant d'environ 0.17 nm). Dans le cas où on utilise la thermique pour accorder le filtre, la température doit être réglée à partir ~0.194 ° C à ~44.883 ° C (variation de la température ambiante). Les réponses spectrales simulées numériquement des filtres au niveau des deux ports de sortie de l'IM sont représentées sur la Figure 11 (a-c). Pour obtenir la réponse spectrale du filtre, on considère une fonction delta de Dirac au port d'entrée, i.e. un spectre uniforme, puis nous montrons la réponse spectrale obtenue à la sortie.

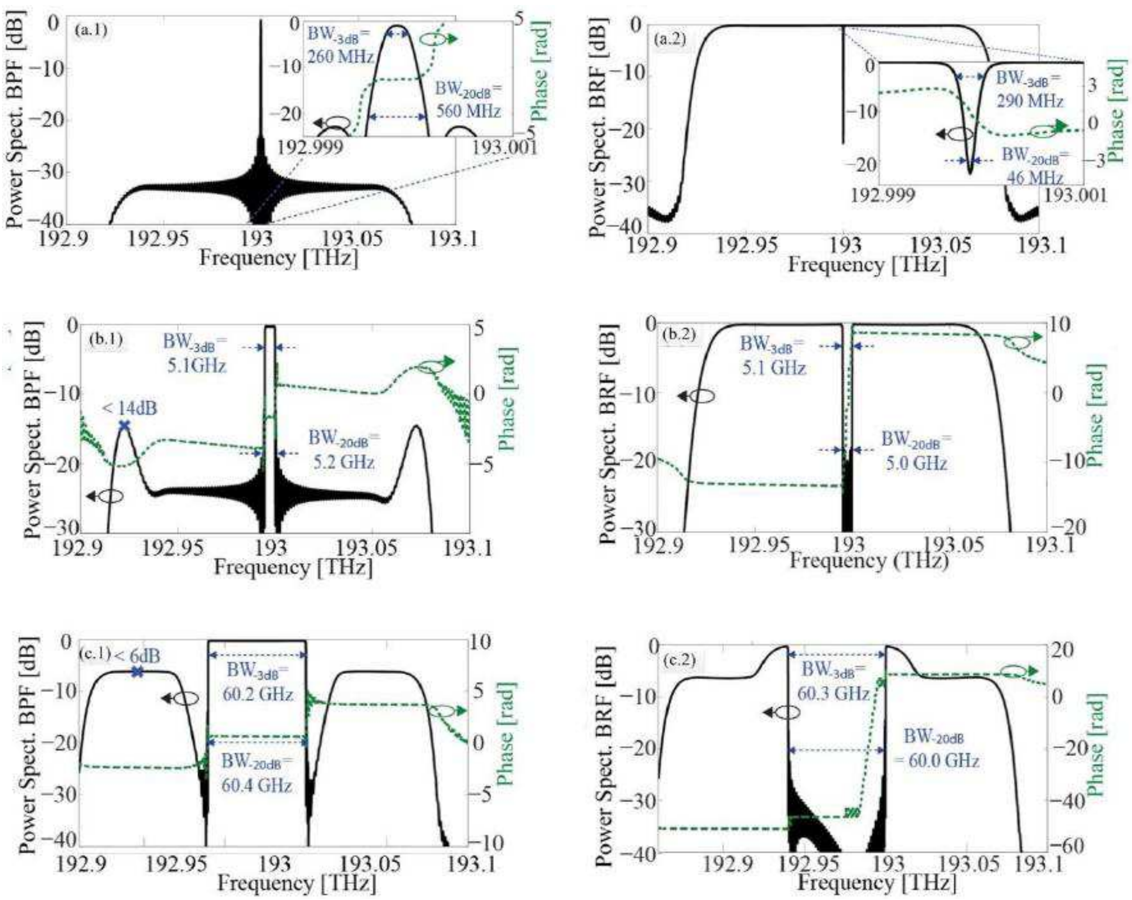

Figure 11 Réponse spectrale du filtre optique avec une bande passante minimale èa 3 dB de 260 MHz; ((a.1) FPB et (a.2) FCB), 5.1 GHz ((b.1) FPB et (b.2) FCB) et 60.2 GHz ((c.1) FPB et (c.2) FCB).

En conclusion, nous avons proposé une nouvelle architecture pour la mise en œuvre de filtres optiques, passe-bande et coupe-bande largement accordables, non dispersifs et à transition abrupte, à l'aide d'un système de fibre optique ou guide d'onde intégrée basée sur deux THPs incorporés dans un IM. Une accordabilité de la bande passante de 260 MHz jusqu'à > 60 GHz a été démontrée numériquement en utilisant des dispositifs THP à base de RBF facilement réalisables. Il importe de noter qu'il a été démontré que l'accordabilité de la bande passante dans le régime sous-GHz est très difficile à réaliser en utilisant les technologies disponibles.

E.1. Réalisation d’un transformateur de Hilbert photonique (THP) sur SOI

Dans la quête de THPs de haute qualité pour la réalisation de la conception du filtre proposée (ci-dessus), nous avons proposé et démontré expérimentalement des conceptions de THPs basées sur des réseaux de Bragg à guides d’ondes latéralement apodisés, en technologie SOI. Dans ce travail, des transformateurs de Hilbert de haute performance d’ordre entier et d’ordre fractionnaire, avec des bandes passantes de traitement approchant la gamme THz ont été expérimentalement réalisés [59].

Cette conception utilise deux réseaux superposés dans lesquels un décalage approprié entre leurs périodes respectives est imposé le long du guide d’onde afin d’atteindre le profil d’apodisation de force de couplage visé. Cette approche offre une tolérance accrue aux erreurs de fabrication, en comparaison aux réseaux de Bragg conventionnels à parois latérales ondulées, de sorte qu’elle nous permet de contrôler l’apodisation du réseau avec une très grande précision et sur une grande plage dynamique, ce qui permet par exemple la réalisation de THPs d’ordre entier avec une bande passante de traitement aussi large que ~ 750 GHz et un PTB au-dessus de 20. Comme cela est illustré sur la Figure 12, notre système utilise deux réseaux superposés, avec une profondeur d’ondulation de la paroi latérale (ΔW) fixe, où le profil d'apodisation visé est traduit en un décalage entre les périodes correspondantes de ces deux réseaux.

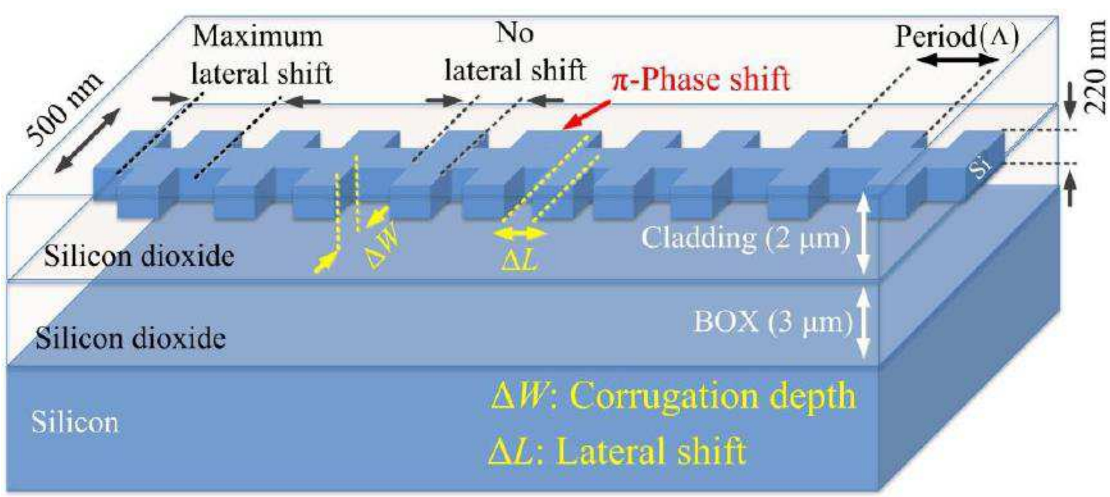

Figure 12 Schéma du THP conçu à base d'un RB apodisé latéralement.

Cette approche de conception permet un contrôle de haute précision de la force de couplage du réseau, de 0 -réalisée avec un désalignement maximum d'une demi-période de réseau, $\Lambda / 2$ entre les réseaux superposés- jusqu'à la modulation maximale réalisable d'indice de réfraction (Δn) pour un ΔW définit, qui est atteint quand il n'y a pas de désalignement entre les réseaux superposés.

Un défi majeur dans la conception de RBs sur puce est la complexité associée à la recherche du profil d'apodisation de la force du réseau (couplage) nécessaire à l'implémentation d'une réponse temporelle/ spectrale linéaire spécifique, par exemple, comme celle requise pour la réalisation d'une fonctionnalité de traitement de signal (HT). Cela est le résultat des effets non négligeables de la dispersion du guide d'ondes, des pertes et des variations de dimensions dues aux incertitudes de fabrication, etc [63]. L'approximation de Born du premier ordre est considérée comme une solution très puissante pour la conception de réseaux à faible couplage. Dans cette approximation, le profil d'apodisation de la modulation d'index de réfraction nécessaire pour obtenir une réponse linéaire visée, est simplement une version de la réponse impulsionnelle projetée de manière appropriée le long du dispositif [13]. Le profil d'apodisation de la modulation d'indice de réfraction requis pour réaliser un HT d'ordre entier, une version mise à l'échelle de l'enveloppe de la réponse impulsionnelle temporelle du dispositif représenté sur la Figure 8 (b), est définie mathématiquement comme [67] :

$$\Delta n(z) \propto \frac{\sin^2\left(\pi n_{av} \Delta f \left(z - z_c\right) / c\right)}{z - z_c}, \tag{2}$$

où n_{av} est l'indice de réfraction moyen du réseau, c est la vitesse de la lumière dans le vide, z_c est le centre du réseau, et $\Delta f = c / n_{av} \Delta z$ est la bande passante du dispositif, Δz étant la largeur de zéro à zéro des lobes principaux du profil d'apodisation du réseau de diffraction. Par conséquent, la bande passante du dispositif peut être contrôlée, en changeant Δz.

Comme le montre la Figure 12, notre conception utilise deux réseaux superposés avec une profondeur d'ondulation de la paroi latérale fixe, où le profil cible d'apodisation est projetée dans les décalages latéraux (ΔL) entre les périodes correspondantes de ces deux réseaux. En supposant une profondeur d'ondulation fixe, l'apodisation du réseau de diffraction a été transférée au décalage latéral entre les périodes du dispositif selon l'équation suivante [72]:

$$\Delta n = n_0 \cos\left(\pi \Delta L / \Lambda\right) \tag{3}$$

où n_0 est la modulation de l'indice effectif pour le dispositif RB sans désalignement ($\Delta L = 0$). La période du réseau (Λ) est considérée égale à 318 nm, avec un rapport cyclique de 50%, pour obtenir un fonctionnement autour de la longueur d'onde de télécommunication (~ 1555 nm). Le désalignement (ΔL) est varié de 0 à 159 nm ($\Lambda / 2$).

La méthodologie de conception proposée a été validée expérimentalement par la réalisation des HTs d'ordre entier et fractionnaire fonctionnant à des longueurs d'onde typiques de télécommunication optiques. Les premiers exemples sont des HTs d'ordre entier, conçu en utilisant des RBs apodisés latéralement avec 500 et 1000 périodes, respectivement, et une profondeur d'ondulation de 5 nm. Les résultats obtenus avec des profondeurs d'ondulations plus petites n'ont pas été satisfaisants à cause de l'impact des erreurs de fabrication.

Les réponses spectrales en amplitude et en phase du dispositif ont été mesurées en utilisant un analyseur optique vectoriel (AOV), Luna Innovations, avec une résolution spectrale de 1,6 pm ; Les résultats expérimentaux et de simulation sont présentés sur la Figure 13 (a-b, d-e). En général, il y a une différence entre les profondeurs d'ondulation des guides d'ondes fabriqués et celles considérées dans les simulations. Cela pourrait être attribué principalement aux variations (réductions) dans la profondeur des réseaux fabriqués induites par les effets de lissage des parois latérales dus à la lithographie et au processus de gravure [72]. Par conséquent, tout au long du processus de conception, la modulation d'indice de réfraction effectif a été réduite d'environ ~41% pour correspondre aux résultats expérimentaux

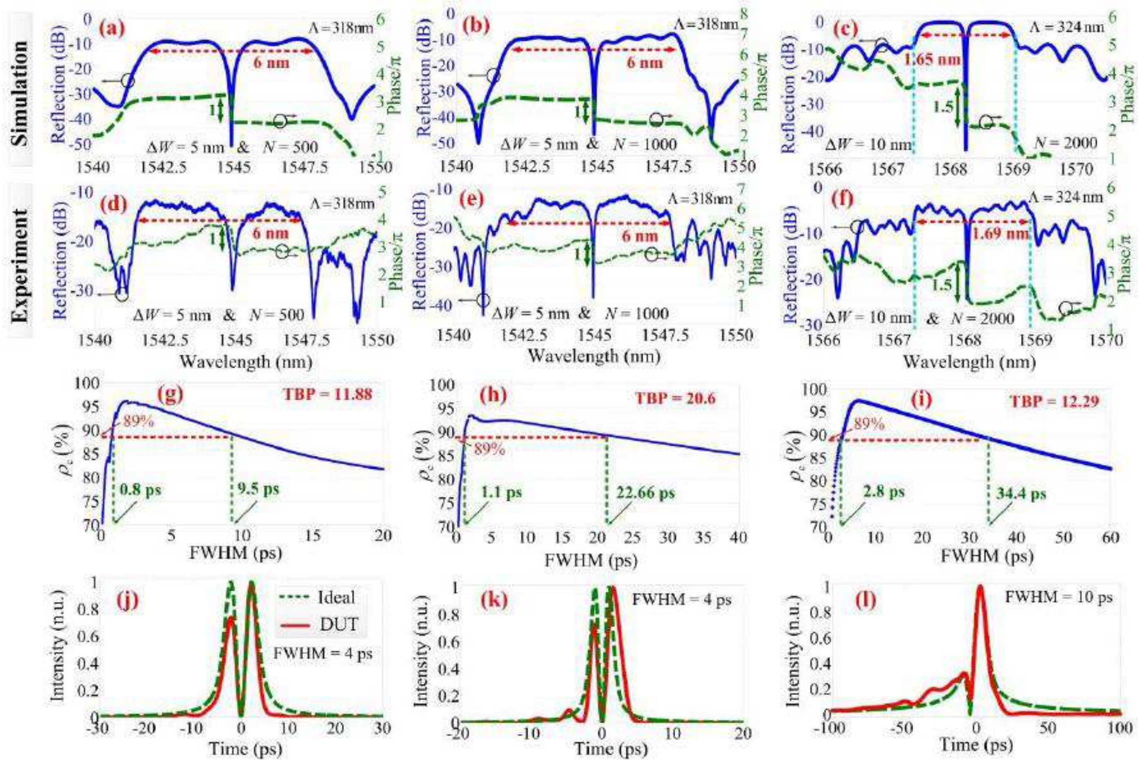

Figure 13 Réponses spectrales d'amplitude et de phase simulées (a-c) et mesurées (d-f), (g-i) les coefficients de corrélation croisée (j-l) comparaison entre les réponses temporelles de THPs idéals avec la réponse des DSTs à différentes impulsions Gaussiennes, pour les THPs d'ordre entier et fractionnaire.

Afin de fournir une estimation de la PTB du dispositif, nous avons simulé numériquement la réponse dans le domaine temporel d'un filtre optique linéaire d'une impulsion optique Gaussienne idéale, en utilisant la fonction de transfert spectrale (amplitude et phase spectrales) mesurée à l'aide de l'AOV, puis nous avons calculé le coefficient de corrélation croisée (ρ_c) en fonction de la largeur temporelle de l'impulsion à mi-hauteur. ρ_c fournit une estimation précise de la similitude entre les deux champs complexes dans le domaine temporel, provenant 1) d'un THP idéal, et 2) du Dispositif Sous Test (DST). Le PTB de chaque dispositif étudié est estimé en prenant le rapport entre la plus grande largeur temporelle d'impulsion à l'entrée et la plus courte largeur temporelle d'impulsion donnant un coefficient de corrélation croisé minimum (89% dans l'évaluation présentée ici). Selon la Figure 13 (g-h), en doublant le nombre de périodes du réseau, le PTB est amélioré de presque deux fois, de près de 12 à plus de 20. La Figure 13 (j-k) représente des exemples mesurés de la réponse temporelle du DST à une impulsion Gaussienne échantillon de 4-ps de largeur à mi-hauteur (FWHM), comparée avec une réponse d'un THP idéal.

Le deuxième exemple de dispositif testé, est un THP d'ordre fractionnaire avec *P=1.5,* conçu en utilisant une structure de réseau similaire mais avec 2000 périodes de 324 nm, et une plus grande profondeur d'ondulation de parois de 10 nm. À nouveau, les réponses spectrales en amplitude et en phase du dispositif ont été mesurées en utilisant un AOV; la simulation et les résultats expérimentaux sont présentés sur la Figure 13 (c, f). La largeur de bande passante de fonctionnement mesurée est d'environ 212 GHz, et des calculs similaires de la réponse temporelle du dispositif (Figure 13(f,i)), fournissent une estimation du PTB légèrement supérieure à 12. Enfin, la réponse temporelle mesurée du DST à une impulsion Gaussienne échantillon de 10-ps (FWHM) est comparée avec une réponse d'un THP idéal dans la Figure 13(l).

Sur la base des résultats présentés, nous concluons que l'approche de conception de RB à guide d'ondes apodisés latéralement offre des améliorations significatives en termes de plage dynamique d'indice effectif, qui à son tour permet la réalisation des fonctionnalités de traitement du signal nécessitant des profils complexes d'apodisation, par exemple, les dispositifs THPs de haute performance (haut PTB) démontrés sur plate-forme SOI dans ce travail. Nous prévoyons q'une telle approche devrait se révéler utile pour la mise en œuvre d'autres fonctionnalités de filtrage optique et de traitement de signaux complexes, au-delà des capacités des systèmes classique de RB à guide d'ondes. Il importe de noter que le THP d'ordre entier conçu peut être utilisé pour réaliser notre système de filtrage proposé sur la plate-forme technologique SOI.

Il importe de noter que les THPs conçus dans ce projet ont été fabriqués en utilisant la lithographie par faisceau d'électrons. Ce processus de fabrication offre une très haute résolution (jusqu'à ~ 2 nm). Cependant, dans ce cas la rugosité des parois latérales est plus importante que dans un dispositif similaire fabriqué à l'aide de la lithographie par ultra-violet. Comme expliqué précédemment, l'utilisation des réseaux plus longs permet la réalisation de THPs de meilleure qualité (produit temps-bande passante plus élevé). Dans une puce fabriquée par lithographie par faisceau d'électrons, la réalisation de réseaux de Bragg plus longs devient difficile car le bruit de phase induit par la rugosité des parois latérales s'accumule lorsque la lumière se propage le long des dispositifs. Par conséquent, nous prévoyons que la fabrication des dispositifs proposés à l'aide de la lithographie à ultra-violet tout en utilisant des réseaux de Bragg plus courts se traduira par l'obtention de THPs de meilleure qualité et un filtrage avec une plus grande plage d'accordabilité.

F. Caractérisation du signal optique sur puce

Un exemple pertinent de méthodes de caractérisation appropriées pour les ensembles, cités plus haut, de signaux qu'on trouve dans les systèmes de télécommunications (expliqué dans la section A.3), est PROUD (Phase Reconstruction using Optical Ultrafast Differentiation en anglais), qui est une méthode linéaire, auto-référencée et basée sur la mesure d'intensité temporelle seulement. PROUD est particulièrement bien adaptée au problème de caractérisation du signal dans le contexte des télécommunications optiques. Le principe de fonctionnement de PROUD est basé sur un algorithme numérique non-itératif de récupération de phase qui permet la caractérisation du signal en temps réel et en une seule mesure. Dans sa mise en œuvre de base, la méthode PROUD dans le domaine temporel [43, 44, 45], permet de récupéré le profil temporel de phase d'un signal optique à partir de deux mesures de l'intensité, à savoir le profil d'intensité du signal sous test et celui du signal résultant de la différenciation photonique temporelle réalisée à l'aide d'un algorithme non itératif (voir Figure 14).

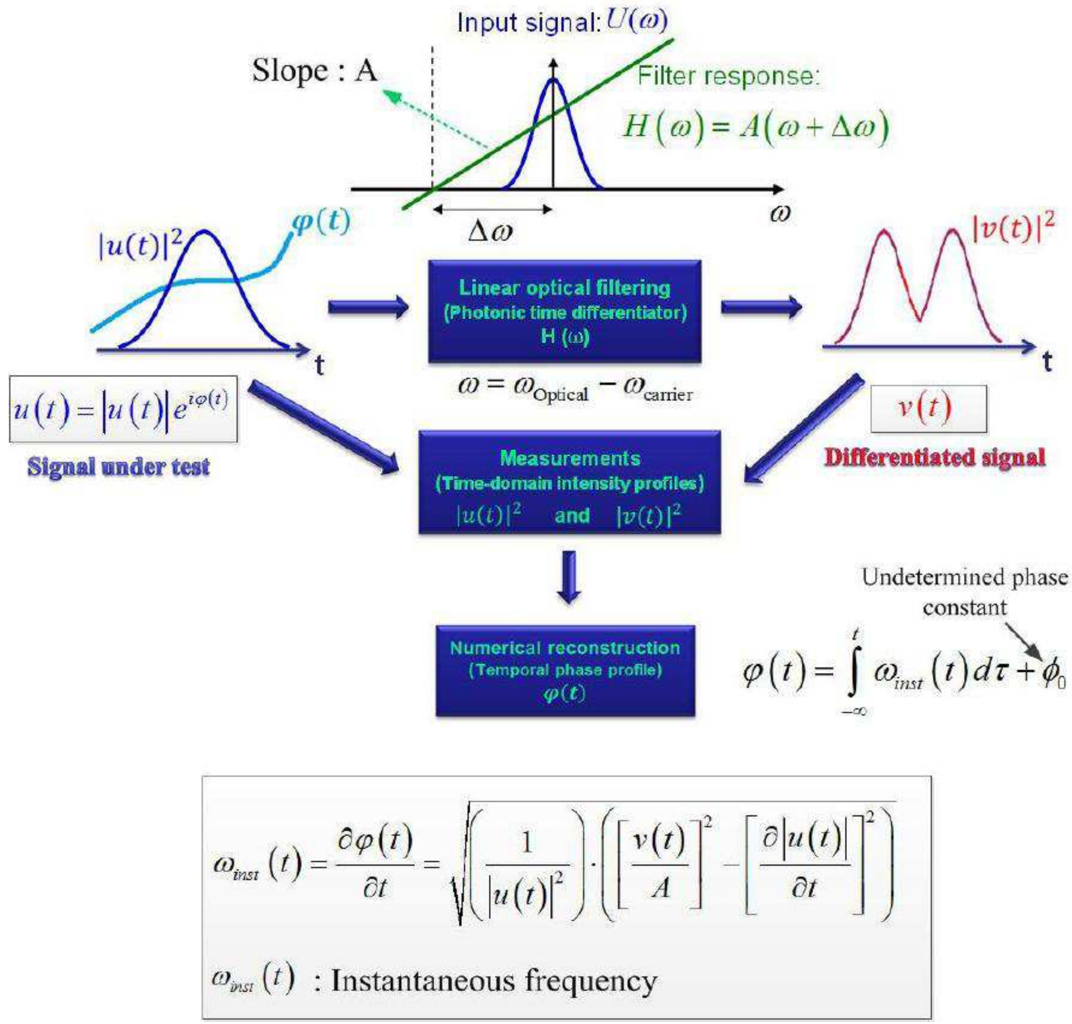

Figure 14 Schéma du concept de reconstruction de la phase dans le domaine temporel basé sur la différenciation optique ultrarapide (PROUD) [73].

Un différenciateur photonique dans une configuration PROUD, également appelé, discriminateur de fréquence photonique, est un filtre optique linéaire capable de fournir la dérivée temporelle de l'enveloppe complexe d'un signal optique [74, 75]. Cette fonctionnalité peut être réalisée en utilisant un réseau de fibre/guide d'ondes intégré à longue période [76], un RB décalé en phase [77], ou un interféromètre de Mach-Zehnder (IMZ) [78]. PROUD en domaine temporel permet, essentiellement la caractérisation complète du profil temporel de phase d'un signal en utilisant une photo-détection classique suivie d'une intégration temporelle cumulative. Dans ce projet, nous avons proposé et démontré expérimentalement, la mise en œuvre d'un système PROUD en une seule mesure dans le domaine temporel dans un guide d'onde intégré en utilisant un IMZ en silice sur silicium à contraste d'indice élevé (4%) comme un différenciateur optique ultra-rapide. Cela nous permet de réaliser la caractérisation de la phase des signaux complexes et rapides (GHz) ayant différents format (arbitraire) de modulation complexe et différent taux binaires, en utilisant une configuration simple (étape de filtrage unique et simple photodétection) et sans avoir besoin d'un oscillateur de référence. En particulier, la méthode proposée est transparente au format de modulation et au débit binaire. Pour démontrer cela, différent débits binaires et de symboles ont été délibérément utilisés dans les deux expériences rapportées ici sur des signaux : 1) avec modulation de décalage de phase à quadrature, (QPSK) à 1 Gbaut ; 2) avec modulation d'amplitude et de phase (APSK) à 0.7-Gbaud. Nous notons qu'aucun mécanisme de stabilisation de la température n'a été utilisé dans l'expérience réalisée [60].

La lumière est couplée dans les deux bras de l'IMZ à travers un coupleur à interférence multimode (IMM). Le dispositif est basé sur des guides d'onde de silice sur silicium à contraste d'indice élevé (4%) avec $2\times2\ \mu m^2$ de section transverse, fabriqués en utilisant une combinaison de procédés : un dépôt chimique en phase vapeur assisté par plasma, la photolithographie et de gravure sèche [79]. L'Intervalle Spectral Libre (ISL) de l'IMZ mesuré est de 100 GHz (0.8 nm). La Figure 15 montre le schéma du dispositif expérimental utilisé dans notre nouvelle implémentation du système PROUD. La source laser à onde continue (CW) fonctionne à une longueur d'onde centrale de 1551.77 nm. En choisissant cette dernière comme la longueur d'onde porteuse du signal et en veillant à ce que la largeur spectrale du signal modulé soit plus étroite que ~ 25 GHz, le bon fonctionnement de la méthode est assuré.

Dans la première expérience, un générateur de forme d'onde arbitraire électronique (AWG) avec une fréquence d'échantillonnage allant jusqu'à 24 GS/s et une largeur de bande passante analogique de 9,6 GHz, relié à un modulateur de phase est utilisé pour moduler la phase du laser à ondes continues à quatre niveaux différents $(0, \pi/2, \pi, \text{ and } 3\pi/2)$, une durée temporelle de 82 ps et une période de 1 ns, créant ainsi le signal QPSK à 1 Gbaud (2 Gb/s) sous test. Nous avons défini une séquence de vingt sauts de phase différents à l'entrée de système, pour émuler un signal de télécommunication QPSK.

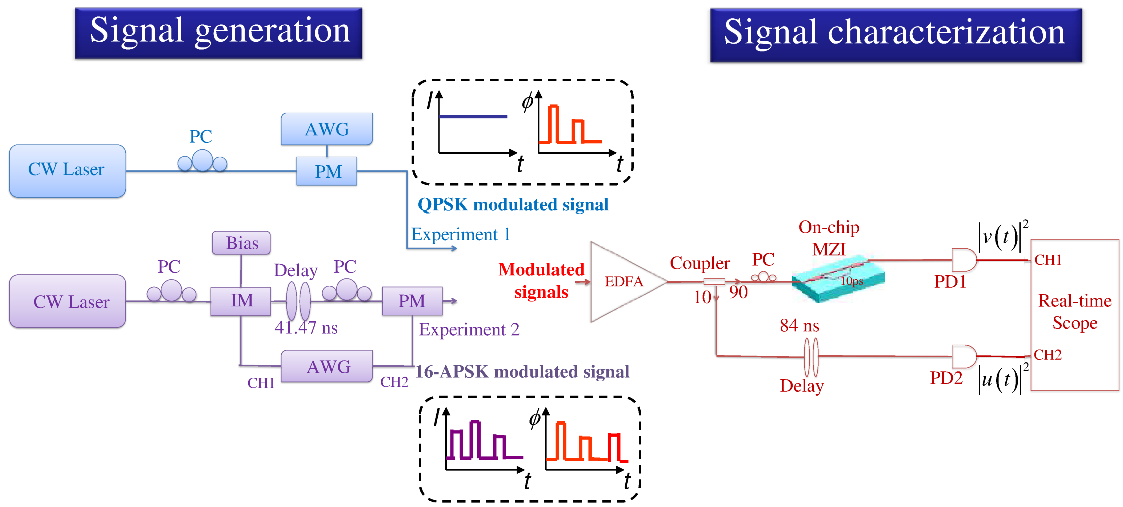

Figure 15 Le dispositif expérimental pour la génération et la caractérisation du signal (laser CW: laser continu, PC: contrôleur de polarisation, PM: modulateur de phase, IM: modulateur d'intensité, AWG: générateur de signaux arbitraires, EDFA: amplificateur à fibre dopée à l'erbium, et PD: photo-détecteur).

Les profils temporels d'intensité du signal sous test $|u(t)|^2$ et le signal après différentiation $|v(t)|^2$ ont été mesurés à l'aide de deux photo-détecteurs rapides, chacun ayant une bande passante à 3 dB de 45 GHz, relié à deux canaux différents d'un oscilloscope temps réel de 8 GHz. Pour synchroniser les signaux différentiés et de référence, un retard de 84 ns a été utilisé (le délai dépend de la longueur du dispositif et de la longueur de chemin optique entre le coupleur et le photodétecteur). Aucune moyenne n'a été utilisée dans ces mesures afin de prouver les capacités de mesure avec une seule acquisition de notre système. En utilisant ces mesures, le profil de phase QPSK est reconstruit avec succès en temps réel conformément à la méthodologie décrite ci-dessus. Les résultats correspondants sont présentés dans la Figure 16.

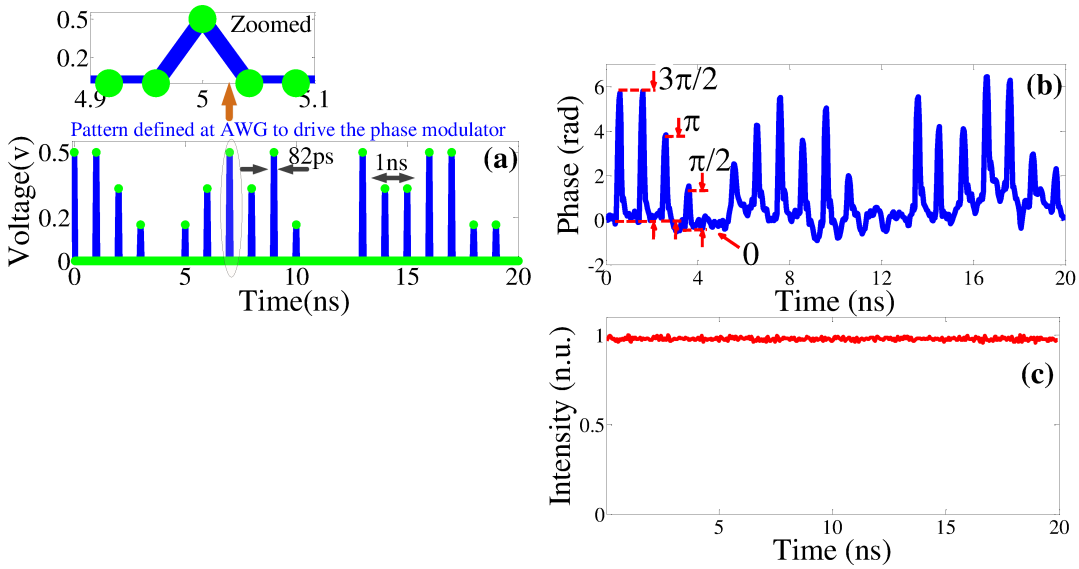

Figure 16 (a) Le profil de phase définie à l'AWG utilisé pour piloter le modulateur de phase. La région agrandie montre qu'un seul échantillon de l'AWG définit chaque symbole de la séquence de données. (B) la phase reconstruite et (c) les profils d'intensité du signal modulé QPSK.

Dans une deuxième expérience, la caractérisation d'un signal modulé APSK a été visée. Dans ce cas, un modulateur d'intensité en cascade avec un modulateur de phase ont été utilisés pour générer un signal spécifique de 0.7 Gbaud (2.8 Gb/s), la durée de chaque échantillon est de 82 ps et la période est de 1.4 ns. À nouveau, la récupération de la phase avec une seule mesure et en temps réel a été réalisée avec succès à partir de l'entrée mesurée et l'intensité temporelle différenciée en utilisant la même stratégie et la configuration que celle décrite ci-dessus pour le signal QPSK (résultats dans la Figure 17).

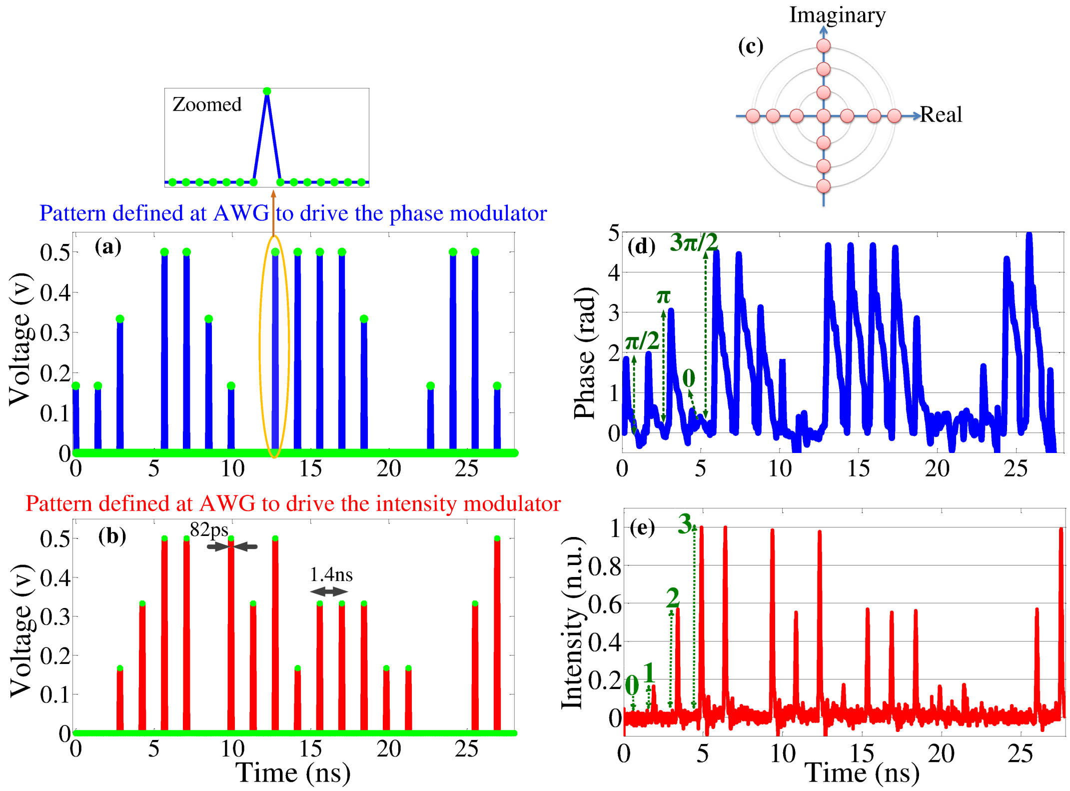

Figure 17 (a) les profils qui ont été définis à l'AWG pour piloter le modulateur de phase et (b) le modulateur d'intensité. (c) Le diagramme de constellation du signal à modulation APSK. (d) La phase reconstruit et (e) les profils d'intensité du signal à modulation APSK.

En conclusion, une simple mise en œuvre de PROUD à l'aide d'un guide-onde intégré a été démontrée pour la caractérisation complète (phase et amplitude) avec une seule mesure en temps réel des flux de données optiques ayant des modulations complexes et des taux de l'ordre du GHz, sans utiliser un oscillateur local de référence. Le système de caractérisation comprend un seul filtre et un seul photodétecteur classique. Les résultats présentés montrent clairement que la méthode est entièrement transparente pour le format de modulation ainsi que le débit de symbole, à condition que le spectre de données corresponde à la zone linéaire du filtre de différentiation. Par ailleurs, la ligne à retard accordable de référence et les deux photo-détecteurs peuvent être intégrés avec l'IMZ [80, 81]. De cette façon, la méthode proposée pourrait être utilisée pour créer un module entièrement intégré capable de caractériser des signaux de données rapides (GHz), avec une mesure unique en temps réel, et avec potentiellement une compacité, stabilité et sensibilité améliorées.

Références

[1] P. J. Winzer, "Challenges and evolution of optical transport networks," in *36th European Conference on Optical Communication (ECOC 2010)*, Torino, 2010.

[2] N. S. Bergano, "Wavelength division multiplexing in long-haul transoceanic transmission systems," *Journal of Lightwave Technology,* vol. 23, no. 12, pp. 4125-4139, 2005.

[3] C. R. Doerr, "Silicon photonic integration in telecommunications," *Frontiers in Physics,* vol. 3, no. 37, pp. 1-16, 2015.

[4] R. A. Soref and B. R. Bennett, "Electro-optical effects in silicon," *IEEE Journal of Quantum Electronics,* vol. QE, no. 23, pp. 123-129, 1987.

[5] M. C. Teich and B. Saleh, Fundamentals of photonics, New York: John Wiley & Sons, 1991.

[6] O. Wada, "Femtosecond all-optical devices for ultrafast communication and signal processing," *New Journal of Physics,* vol. 6, no. 1, pp. 183-218, 2004.

[7] J. Aracil, F. F. Callegati and V. Lopez, Enabling optical internet with advanced network technologies, J. Aracil and F. F. Callegati, Eds., Springer, 2009.

[8] J. Azaña, C. K. Madsen, K. Takiguchi and G. Cincontti, "Special issue on optical signal processing," *Journal of Lightwave Technology,* vol. 24, no. 7, pp. 2484-2767, 2006.

[9] A. M. Weiner, "Femtosecond optical pulse shaping and processing," *Progress in Quantum Electronics,* vol. 19, pp. 161-237, 1995.

[10] A. M. Weiner, Ultrafast Optics, G. Boreman, Ed., John Wiley & Sons, Inc., 2008.

[11] N. K. Fontaine, D. J. Geisler, R. P. Scott, H. J. P. T. He and S. J. B. Yoo, "Demonstration of high-fidelity dynamic optical arbitrary waveform generation," *Optics Express,* vol. 18, no. 22, pp. 22988-22995, 2010.

[12] L. M. Rivas, M. J. Strain, D. Duchesne, A. Carballar, M. M. R. Sorel and J. Azaña, "Picosecond linear optical pulse shapers based on integrated waveguide Bragg gratings," *Optics Letters,* vol. 33, no. 21, pp. 2425-2427, 2008.

[13] H. Kogelnik, "Filter response of nonuniform almost-periodic structures," *Bell System Technical Journal,* vol. 55, no. 1, pp. 109-126, 1976.

[14] G. P. Agrawal, Fiber-optic communications systems, 3rd, Ed., John Wiley & sons, Inc., 2005.

[15] J. Yao, "Arbitrary waveform generation," *Nature Photonics,* vol. 4, pp. 79-80, 2010.

[16] R. Kashyap, Fiber Bragg gratings, London: Academic Press, 1999.

[17] 2015. [Online]. Available: http://www.santec.com/en/products/instruments/manualproducts/otf-350.

[18] S. Cheung, T. Su, K. Okamoto and S. J. B. Yoo, "Ultra-compact silicon photonic 512 x 512 25 GHz arrayed waveguide grating router," *IEEE Journal of Selected Topics in Quantum Electronics,* vol. 20, no. 4, pp. 8202207-8202207, 2014.

[19] J. St-Yves, H. Bahrami, P. Jean, L. S. and W. Shi, "Widely bandwidth-tunable silicon filter with an unlimited free-spectral range," *Optics Letters,* vol. 40, no. 23, pp. 5471-5474, 2015.

[20] A. D. Simard, Y. Painchaud and S. LaRochelle, "Integrated Bragg gratings in spiral waveguides," *Optics Express,* vol. 21, no. 7, pp. 8953-8963, 2013.

[21] M. H. Asghari, Ultrafast optical signal processing: devices and techniques, LAMBERT Academic Publishing, 2012.

[22] X. M. Liu, "A novel ultra-narrow transmission-band fiber Bragg grating and its application in a single-longitudinal-mode fiber laser with improved efficiency," *Optics Communications,* vol. 280, no. 1, pp. 147-152, 2007.

[23] R. Trebino, frequency-resolved optical gatng: The measurement of ultrashort laser pulses, Springer Science & Business Media, 2002.

[24] C. Dorrer, "High-Speed Measurements for Optical Telecommunication Systems," *IEEE Journal of Selected Topics in Quantum Electronics,* vol. 12, no. 4, pp. 843-858, 2006.

[25] L. Lepetit, G. Chériaux and M. Joffre, "Linear techniques of phase measurement by femtosecond spectral interferometry for applications in spectroscopy," *Journal of the Optical Society of America B,* vol. 12, no. 12, pp. 2467-2474, 1995.

[26] V. R. Supradeepa, D. E. Leaird and A. M. Weiner, "Single shot amplitude and phase characterization of optical arbitrary waveforms," *Optics Express,* vol. 17, no. 16, pp. 14434-14443, 2009.

[27] N. K. Fontaine, R. P. Scott, J. P. Heritage and S. J. B. Yoo, "Near quantum-limited, single-shot coherent arbitrary optical waveform measurements," *Optics Express,* vol. 17, no. 15, pp. 12332-12344, 2009.

[28] A. H. Gnauck and P. J. Winzer, "Optical Phase-Shift-Keyed Transmission," *Journal of Lightwave Technology,* vol. 23, no. 1, pp. 115-129, 2005.

[29] D. J. Kane and R. Trebino, "Single-shot measurement of the intensity and phase of an arbitrary ultrashort pulse by using frequency-resolved optical gating," *Optics Letters,* vol. 18, no. 10, pp. 823-825, 1993.

[30] C. Laconis and l. A. Walmsley, "Spectral phase interferometry for direct electric-field reconstruction of ultrashort optical pulses," *Optics Letters,* vol. 23, no. 10, pp. 792-794, 1998.

[31] A. Pasquazi, M. Peccianti, Y. Park, B. E. Little, S. T. Chu, R. Morandotti, J. Azana and D. J. Moss, "Sub-picosecond phase-sensitive optical pulse characterization on a chip," *Nature Photonics,* vol. 5, p. 618–623, 2011.

[32] C. Dorrer and I. Kang, "Linear self-referencing techniques for short-optical-pulse characterization [Invited]," *Journal of the Optical Society of America B,* vol. 25, no. 6, pp. A1-A12, 2008.

[33] I. A. Walmsley and C. Dorrer, "Charaterization of ultrashort electromagnetic pulses," *Advances in Optics and Photonics,* vol. 1, no. 2, pp. 308-437, 2009.

[34] D. Reid and J. Harvey, "Linear spectrograms using electro-optic modulators," *IEEE Photonics Technology Letters,* vol. 19, no. 8, pp. 535 - 537, 2007.

[35] C. Dorrer and I. Kang, "Simultaneous temporal characterization of telecommunication optical pulses and modulators by use of spectrograms," *Optics Letters,* vol. 27, no. 15, pp. 1315-1317, 2002.

[36] P. Kockaert, J. Azaña, L. R. Chen and S. LaRochelle, "Full characterization of uniform ultrahigh-speed trains of optical pulses using fiber Bragg gratings and linear detectors," *IEEE Photonics Technology Letters,* vol. 16, no. 6, pp. 1540-1542, 2004.

[37] C. Dorrer, "Chromatic dispersion characterization by direct instantaneous frequency measurement," *Optics Letters,* vol. 29, no. 2, pp. 204-206, 2004.

[38] T. Ahn, Y. Park and J. Azaña, "Fast and accurate group delay ripple measurement technique for ultralong chirped fiber Bragg gratings," *Optics Letters,* vol. 32, no. 18, pp. 2674-2676, 2007.

[39] Y. Park, T. Ann and J. Azaña, "Real-time complex temporal response measurements of ultrahigh-speed optical modulators," *Optics Express,* vol. 17, no. 3, pp. 1734-1745, 2009.

[40] E. Ip, A. P. T. Lau, D. J. F. Barros and J. M. Kahn, "Coherent detection in optical fiber systems," *Optics Express,* vol. 16, no. 2, pp. 753-791, 2007.

[41] J. Bromage, C. Dorrer, I. A. Begishev, N. G. Usechak and J. D. Zuegel, "Highly sensitive, single-shot characterization for pulse widths from 0.4 to 85 ps using electro-optic shearing interferometry," *Optics Letters,* vol. 31, no. 23, pp. 3523-3525, 2006.

[42] V. R. Supradeepa, C. M. Long, D. E. Leaird and A. M. Weiner, "Self-referenced characterization of optical frequency combs and arbitrary waveforms using a simple, linear, zero-delay implementation of spectral shearing interferometry," *Optics Express,* vol. 18, no. 17, pp. 18171-18179, 2010.

[43] F. Li, Y. Park and J. Azaña, "Complete temporal pulse characterization based on phase reconstruction using optical ultrafast differentiation (PROUD)," *Optics Letters,* vol. 32, no. 22, pp. 3364-3366, 2007.

[44] J. Azaña, Y. Park, T. Ahn and F. Li, "Simple and highly sensitive optical pulse-characterization method based on electro-optic spectral signal differentiation," *Optics Letters,* vol. 33, no. 5, pp. 437-439, 2008.

[45] F. Li, Y. Park and J. Azaña, "Linear Characterization of Optical Pulses With Durations Ranging From the Picosecond to the Nanosecond Regime Using Ultrafast Photonic Differentiation," *Journal of Lightwave Technology,* vol. 27, no. 21, pp. 4623-4633, 2009.

[46] F. Li, Y. Park and J. Azaña, "Single-shot real-time frequency chirp characterization of telecommunication optical signals based on balanced temporal optical differentiation," *Optics Letters,* vol. 34, no. 18, pp. 2742-2744, 2009.

[47] Y. Park, M. Scaffardi, L. Potì and J. Azaña, "Simultaneous single-shot real-time measurement of the instantaneous frequency and phase profiles of wavelength-division-multiplexed signals," *Optics Express,* vol. 18, no. 6, pp. 6220-6229, 2010.

[48] Y. Park, M. Scaffardi, A. Malacarne, L. Potì and J. Azaña, "Linear, self-referenced technique for single-shot and real-time full characterization of (sub-)picosecond optical pulses," *Optics Letters,* vol. 35, no. 15, pp. 2502-2504, 2010.

[49] 2016. [Online]. Available: http://www.tek.com/signal-generator/awg7000-arbitrary-waveform-generator.

[50] H. P. Bazargani and J. Azaña, "Optical pulse shaping based on discrete space-to-time mapping in cascaded co-directional couplers," *Optics Express,* vol. 23, no. 18, pp. 5423-5426 , 2015.

[51] H. P. Bazargani, R. Ashrafi and J. Azaña, "Time-domain optical signal processing based on discrete space-to-time mapping in cascaded co-directional couplers," in *OSA Topical Meeting*

on Bragg Gratings, Photosensitivity and Poling in Glass Waveguides (BGPP 2014), Barcelona, 2014.

[52] H. P. Bazargani, M. Burla and J. Azaña, "Experimental demonstration of sub-picosecond optical pulse shaping in silicon based on discrete space-to-time mapping," *Optics Letters,* vol. 40, no. 23, pp. 5423-5426 , 2015.

[53] H. P. Bazargani, M. Burla and J. Azaña, "On-chip optical pulse shaping based on discrete space-to-time mapping in concatenated co-directional couplers," in *41st European Conference on Optical Communications (ECOC 2015)*, Valencia, 2015.

[54] H. P. Bazargani, M. Burla and J. Azaña, "Long-duration, picosecond optical pulse shaping on SOI using discrete space-to-time mapping," in *Conference on Lasers and Electro-optics (CLEO 2016)*, San Jose, CA, USA, 2016.

[55] H. P. Bazargani, M. Burla, Z. Chen, F. Zhang, L. Chrostowski and J. Azaña, "Long duration optical pulse shaping and complex coding on SOI," *IEEE Photonics Journal,* vol. 8, no. 4, pp. 1-7, 2016 .

[56] H. P. Bazargani, M. R. Fernández-Ruiz and J. Azaña, "Bandwidth-tunable optical filters based on photonic Hilbert transformation," in *IEEE Photonics Conference (IPC 2013)*, Bellevue, 2013.

[57] H. P. Bazargani, M. R. Fernández-Ruiz and J. Azaña, "Tunable optical filter using photonic Hilbert transformation," in *OSA Topical Meeting on Signal Processing in Photonics Communications (SPPCom 2013)*, Rio Grande, 2013.

[58] H. P. Bazargani, M. R. Fernández-Ruiz and J. Azaña, "Tunable, nondispersive optical filter using photonic Hilbert transformation," *Optics Letters,* vol. 39, no. 17, pp. 5232-5235 , 2014.

[59] H. P. Bazargani, M. Burla and J. Azaña, "Photonic Hilbert transformer based on laterally apodized waveguide Bragg gratings on a SOI wafer," in *Conference on Lasers and Electro-optics (CLEO 2016)*, San Jose, CA, USA, 2016.

[60] H. P. Bazargani, J. B. Quelene, P. Dumais, A. Malacarne, M. Clerici, R. Morandotti, C. L. Callender and J. Azaña, "On-Chip, Single-Shot Characterization of GHz-Rate Complex Optical Signals," *IEEE Photonics Technology Letters,* vol. 26, no. 23, pp. 2345-2348, 2014.

[61] K. Jinguji and M. Kawachi, "Synthesis of coherent two-port lattice-form optical delay-line circuit," *Journal of Lightwave Technology,* vol. 13, no. 1, pp. 73-82, 1995.

[62] L. Chrostowski and M. Hochberg, Silicon photonics design book-from devices to systems, Cambridge University press, 2011.

[63] A. D. Simard, G. Beaudin, V. Aimez, Y. Painchaud and S. LaRochelle, "Characterization and reduction of spectral distortions in Silicon-on-Insulator integrated Bragg gratings," *Optics Express,* vol. 21, no. 20, pp. 23145-23159, 2013.

[64] W. Bogaerts and S. K. Selvaraja, "Compact single-mode silicon hybrid rib/strip waveguide with adiabatic bends," *IEEE Photonics Journal,* vol. 3, no. 3, pp. 422-432, 2011.

[65] M. A. Guillén-Torres, K. Murray, H. Yun, M. Caverley, E. Cretu, L. Chrostowski and N. A. F. Jaeger, "Effects of backscattering in high-Q, large–area silicon-on-insulator ring resonators," *Optics Letters,* vol. 41, no. 7, pp. 1538-1541, 2016.

[66] C. R. Raum, R. N. Tait and R. C. Gauthier, "Fabrication and characterization of a thermo-mechanically tunable grating-assisted suspended waveguide filter," *Proceeding SPIE,* vol. 6898, pp. 1-9, 2008.

[67] M. H. Asghari and J. Azaña, "All-optical Hilbert transformer based on a single phase-shifted fiber Bragg grating: design and analysis," *Optics Letters,* vol. 34, no. 3, pp. 334-336, 2009.

[68] M. Li and Y. J., "All-fiber temporal photonic fractional Hilbert transformer based on a directly designed fiber Bragg grating," *Optics Letters,* vol. 35, no. 2, pp. 223-225, 2010.

[69] C. Sima, J. C. Gates, C. Holmes, P. L. Mennea, M. N. Zervas and P. G. R. Smith, "Terahertz bandwidth photonic Hilbert transformers based on synthesized planar Bragg grating fabrication," *Optics Letters,* vol. 38, no. 17, pp. 3448-3451, 2013.

[70] M. Burla, M. Li, L. R. Cortés, X. Wang, M. R. Fernández-Ruiz, L. Chrostowski and J. Azaña, "Terahertz-bandwidth photonic fractional Hilbert transformer based on a phase-shifted waveguide Bragg grating on silicon," *Optics Letters,* vol. 39, no. 21, pp. 6241-6244, 2014.

[71] T. Erdogan, "Fiber grating spectra," *Journal of Lightwave Technology,* vol. 15, no. 8, pp. 1277-1294, 1997.

[72] X. Wang, Y. Wang, J. Flueckiger, R. Bojko, A. Liu, A. Reid, J. Pond, N. A. F. Jaeger and L. Chrostowski, "Precise control of the coupling coefficient through destructive interference in silicon waveguide Bragg grating," *Optics Letters,* vol. 39, no. 19, pp. 5519-5522, 2014.

[73] J. Azaña, Y. Park and F. Li, "Linear self-referenced complex-field characterization of fast optical signals using photonic differentiation [invited]," *Optics Communications,* vol. 284, no. 15, pp. 3772-3784, 2011.

[74] J. Azaña, "Ultrafast analog all-optical signal processors based on fiber-grating devices," *IEEE Photonics Journal,* vol. 2, pp. 359-386, 2010.

[75] N. Q. Ngo, S. F. Yu, S. C. Tjin and C. H. Kam, "A new theoretical basis of higher-derivative optical differentiators," *Optics Communications,* vol. 230, pp. 115-129, 2004.

[76] R. Slavík, Y. Park, M. Kulishov, R. Morandotti and J. Azaña, "Ultrafast all-optical differentiators," *Optics Express,* vol. 14, no. 22, pp. 10699-10707, 2006.

[77] L.-M. Rivas, K. Singh, A. Carballar and J. Azaña., "Arbitrary-order ultra-broadband all-optical differentiators based on fiber Bragg gratings," *IEEE Photonic Technology Letters,* vol. 19, no. 16, pp. 1209-1211, 2007.

[78] Y. Park, T. Ahn and J. Azaña, "Stabilization of a fiber-optic two-arm interferometer for ultra-short pulse signal processing applications," *Applied Optics,* vol. 47, no. 3, pp. 417-421, 2008.

[79] C. L. Callender, P. Dumais, C. Blanchetiere, S. Jacob, C. Ledderhof, C. W. Smelser, K. Yadav and a. J. Albert, "Compact silica-on-silicon planar lightwave circuits for high speed optical signal processing," *Proceeding SPIE,* vol. 8357, pp. 82570.1-83570.10, 2012.

[80] H. Lee, T. Chen, J. Li, O. Painter and K. J. Vahala, "Ultra-low-loss optical delay line on a silicon chip," *Nature Communications,* vol. 3, no. 867, pp. 1-7, 2012.

[81] Y. Zhang, S. Yang, Y. Yang, M. Gould, N. Ophir, A. E. Lim, G. Lo, P. Magill, K. Bergman, T. Baehr-Jones and M. Hochberg., "A high-responsivity photodetector absent metal-germanium direct contact," *Optics Express,* vol. 22, no. 9, p. 11367–11375, 2014.

[82] G. Wilson, C.-J. Chen, P. Gooding and J. E. Ford, "Spectral passband filter with independently variable center wavelength and bandwidth," *IEEE Photonics Technology Letters,* vol. 18, no. 15, pp. 1660-1662, 2006.

Table of contents

List of figures

List of tables

Abbreviations

APSK	Amplitude Phase Shift Keying
AWG	Arbitrary waveform generator
BPF	Band-pass filter
BRF	Band-rejection filter
BG	Bragg grating
CW	Continuous wave
CMT	Coupled-mode theory
DWDM	Dense wavelength-division multiplexing
DUT	Device under test
DSP	Digital signal processing
DGW	Direct UV grating writing
EO	Electro-optic
EDFA	Erbium-doped fiber amplifier
ER	Extinction ratio
FBG	Fiber Bragg grating
FSR	Free spectral range
FROG	Frequency-Resolved Optical Gating
FTM	Frequency-to-time mapping
IM	Intensity modulator
IF	Intermediate frequency
ISI	Intersymbol interference
ITRS	International Technology Roadmap for Semiconductors
LIDAR	Laser detection and ranging
LCFBG	Linearly chirped fiber Bragg grating
LPG	Long-period grating

MZI	Mach-Zehnder interferometer
MI	Michelson interferometer
MWP	Microwave photonics
MLL	Mode-locked laser
MMI	Multi-mode interference
MMW	Multi-mode waveguide
NOLM	Nonlinear optical loop mirror
OCDMA	Optical code-division multiple access
OIC	Optical integrated circuit
OSA	Optical spectrum analyzer
OTDM	Optical time-division multiplexed
OVA	Optical variable attenuator
OFDM	Orthogonal frequency division multiplexing
PM	Phase modulator
PROUD	Phase Reconstruction using Ultrafast Optical Differentiation
PS	Phase shifter
PHT	Photonic Hilbert transformer
PIC	Photonics integrated circuit
PLC	Planar lightwave circuit
PC	Polarization controller
PSR	Power spectral response
PRBS	Pseudo-random binary sequence
QPSK	Quadrature Phase Shift Keying
SEM	Scanning electron microscope
SHG	Second harmonic generation
SPM	Self-phase modulation
SOI	Silicon-on-insulator
SMW	Single-mode waveguide
STM	Space-to-time mapping
SPIDER	Spectral Phase Interferometry for Direct Electric-Field Reconstruction
TBP	Time-bandwidth product
TMM	Transfer matrix method

TODL	Tunable optical delay line
TPA	Two-photon absorption
VOA	Variable optical attenuator
WDM	Wavelength division multiplexing
XPM	Cross-phase modulation

“Those who went in pursuit of knowledge
Soared up so high, stretched the edge
Were still encaged by the same dark hedge
Brought us some tales ere life to death pledge.”

-Omar Khayyam[1]

[1] Omar Khayyám (1048 – 1131) was a Persian polymath: philosopher, mathematician, astronomer and poet. He also wrote treatises on mechanics, geography, mineralogy, music, climatology and Islamic theology.

Born in Nishabur, at a young age he moved to Samarkand and obtained his education there, afterwards he moved to Bukhara and became established as one of the major mathematicians and astronomers of the medieval period. He is the author of one of the most important treatises on algebra written before modern times, the Treatise on Demonstration of Problems of Algebra, which includes a geometric method for solving cubic equations by intersecting a hyperbola with a circle. He also contributed to a calendar reform.

Chapter 1 Introduction

In this chapter, a brief introduction to optical signal processing, with a focus on its application for high-speed telecommunications is given. In this contest, the evolution of silicon photonics for interconnects and switching applications is reviewed, including a brief overview of previous implementations of silicon chips for optical signal processing applications. Finally, the objectives of this Thesis, original contributions by the author and the Thesis organization are presented.

1.1 Motivation

Over the last decade, significant increase in internet access, high speed communication, high definition media streaming and high volume cloud storage have affected our daily lives. This has resulted in an unprecedented demand in the speed and volume of data transfer. Despite the ground-breaking advances in data transmission and processing capacity during the past 30 years, the data traffic is still growing at a much faster rate. According to studies carried out by CISCO, annual global internet protocol (IP) traffic will surpass the zettabyte (ZB) (10^{21} bytes) threshold in 2016 and will reach 2.3 ZB by 2020 [1]. In order to meet this increasing demand, optical telecommunications has been implemented as a powerful solution, offering high transmission rate and processing speed. In particular, fiber optic links have shown to be more desirable than copper wires for transmitting data over long distances (long-haul telecommunications i.e. few hundreds/thousands of kilometers [2]). The reason is their higher available bandwidth, lower loss, lighter weight, higher data security, lower cost and lower required energy to transfer the data. Optical fibers show only 0.2 dB/km loss at telecommunication wavelength (e.g. 1550 nm) which is several orders of magnitude lower than the propagation loss measured for coax cable at 20 GHz, e.g., 1000 dB/km. Besides, fiber offers a bandwidth capacity of 300 THz compared to 20 GHz for Coax cable [3].

In communication systems, both lasers and light emitting diodes (LEDs) are used to transmit light through optical fiber. There are ranges of wavelengths at which the fiber operates best in terms of propagation loss and chromatic dispersion[2]. As illustrated in Figure 1-1, each range is known as an operating window and is centered on a typical operational wavelength, i.e., 850 nm, 1310 nm, and 1550 nm. These wavelengths were chosen because they best match the transmission properties of available light sources with the transmission qualities of optical fiber namely, the amount of propagation loss and chromatic dispesion.

[2] In fiber optic transmissions, **chromatic dispersion** is a term used to describe the spreading of a light pulse as it travels down a fiber. When light pulses are launched relatively close together (high data rates), each pulse may spread in time overlap with the adjacent pulse, resulting in errors and a loss of information.

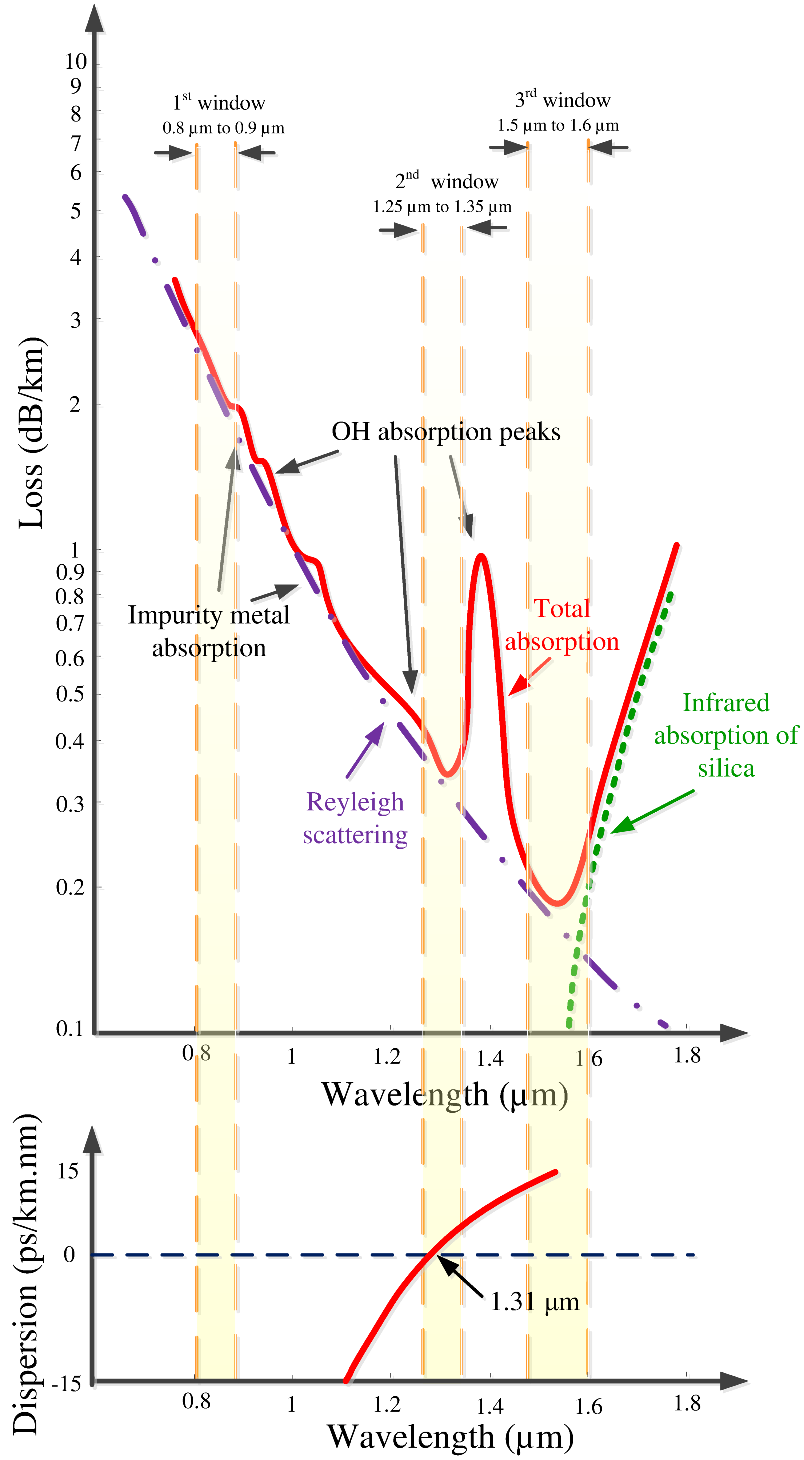

Figure 1-1 Measured loss spectrum and chromatic dispersion of a single-mode silica fiber.

Another unique feature of optical fiber telecommunication is the possibility of increasing data transmission capacity, without increasing the number of fibers, using wavelength division multiplexing (WDM). WDM, first demonstrated by AT&T in 1978 [3], is a technology which multiplexes a number of optical carrier signals onto a single optical fiber by using different wavelengths (colors) of laser light. The ever increasing demand for data transmission capacity has led to considering complex modulation formats as a solution to increase the spectral efficiency of WDM systems. While the spectral efficiency of conventional binary modulation formats, e.g., on-off keying (OOK), is limited to 1 bit/s/Hz/polarization, complex modulation formats, e.g., phase modulation in so-called coherent communication systems, enable *N* bits of information be coded on one symbol, resulting in an spectral efficiency up to *N* bit/s/Hz/polarization [4]. However, the processing of the information signals at the transmitter and receiver, in a communication network link, is still mainly done in the electronic domain. Particularly, in order to decode complex modulated signals at the receiver, complex, energy consuming and relatively slow electrical digital signal processing (DSP) is still required. Therefore, over the years, engineers have moved light ever closer to the heart of computing systems, the microprocessor, in order to keep up with the switching and processing speeds required to manipulate the gigantic amount of data being passed to telecommunication networks. This topic is particularly important for applications in data centers[3], due to the limitations of electronics circuits and copper wires in handling and processing high data rates. As a result, all-optical signal processing and high-speed opto-electronic conversion/switching systems have attracted considerable attention.

Historically, silica-on-silicon photonics integrated circuits (PICs), lithium niobate ($LiNbO_3$), and III–V PICs, such as InP and GaAs, were the primary choices for optical signal processing/switching on-chip [5]. However, due to the success of the microelectronic industry in using silicon, in the 1980s several research groups began projects on the adoption of silicon as the base material for the fabrication of photonic circuits, e.g., the work of Richard Soref at the Rome Air Development Center [6] and Graham Reed at the University of Surrey, UK [7]. The later was of particular importance for the future commercialization of silicon photonic technology because Reed's group showed that very low-loss propagation was possible in silicon-on-insulator (SOI) rib waveguides (see Figure 1-2), a structure in which light could be confined and manipulated.

[3] Data centers consist of a large group of networked computer servers typically used by organizations for the remote storage, processing, or distribution of large amounts of data.

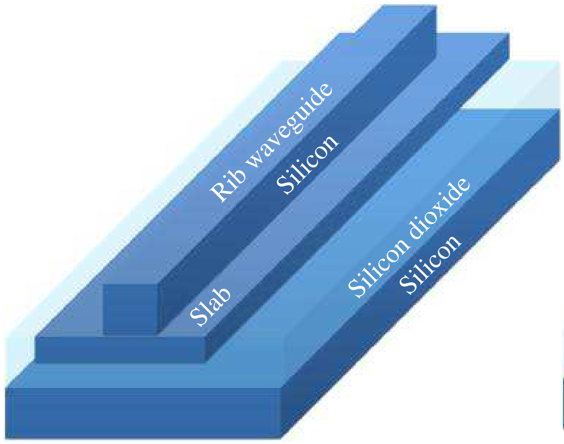

Figure 1-2 Schematic of silicon rib and strip waveguides on SOI.

Many of the optical properties of silicon would suggest it to be an ideal material for planar lightwave circuit (PLC) fabrication. Silicon is virtually transparent to wavelengths > 1100 nm. Besides, it has a relatively high refractive index, around 3.5 (compared to that for glass fiber which is around 1.5), which allows the fabrication of waveguides down to the nanometer scale. However, silicon's indirect bandgap prevents the straightforward implementation of efficient optical sources (maybe the greatest challenge to silicon photonics technology), and detectors compatible with sub-bandgap wavelengths [8].

Prior to year 2000, the so-called first-generation silicon photonics was dominated by the development of relatively large waveguides (cross sections of $\sim 10-100\ \mu m^2$), which were suitable for use in fiber-optic networks, performing roles such as wavelength division multiplexing and optical switching.

It is generally accepted that second-generation silicon photonics was introduced in 2004, when the group led by M. Paniccia at Intel Corporation announced the demonstration of an optical device, fabricated wholly in silicon with the same procedures and protocols as those used for transistor fabrication, which was able to modulate an embedded optical signal at speeds greater than 1 GHz [9]. The potential for integration of photonic and electronic functionalities, with a potential for reducing the excessive power dissipation in microelectronic circuits was thus demonstrated. In a relatively short period since 2004, waveguide dimensions are measured in square nanometers, rather than square microns, and modulation speeds in the order of tens of GHz have been demonstrated [10]. Nowadays, companies like IBM are investing over $3 billion, for the period of the next decade, in producing major breakthroughs in chip technologies [11].

Silicon photonics offers compatibility with complementary metal oxide semiconductor (CMOS) technology, wafer scale testing, low cost packaging, scaling to high levels of integration, solves electrical interconnect limitation in data centers, supercomputers and integrated circuits.

Despite all the advantages offered by silicon photonics, it has been mostly implemented for interconnects and/or switching applications in industry. Significant effort has been put into the development of optical counterparts of electrical signal-processing building blocks, targeting considerable improvements in terms of operation bandwidth (processing speed). These signal processors generally fall into two categories: (1) nonlinear-optics and (2) linear-optics based devices.

1.2 Nonlinear-optics based signal processing

Nonlinear optics describes the behavior of light when propagating in a nonlinear medium, i.e., a medium in which the polarization density ($\vec{P}$) responds nonlinearly to the applied electric field ($\vec{E}$).

In general, a linear dielectric medium is characterized by a linear relation between the polarization density and the electric field, $\vec{P} = \varepsilon_0 \chi \vec{E}$, where ε_0 is the permittivity of free space and χ is the electric susceptibility of the medium. A nonlinear dielectric medium, on the other hand, is characterized by a nonlinear relation between $\vec{P}$ and $\vec{E}$. Since externally applied optical electric fields are typically small in comparison with characteristic inter-atomic or crystalline fields, even when focused laser light is used, the nonlinearity is usually weak. Therefore, the relation between $\vec{P}$ and $\vec{E}$ is approximately linear for small $\vec{E}$, deviating only slightly from linearity as $\vec{E}$ increases. Under these circumstances, the function that relates $\vec{P}$ to $\vec{E}$ can be expanded in a Taylor series about $\vec{E} = 0$,

$$\vec{P} = \varepsilon_0 \left[\chi^{(1)} \vdots \vec{E} + \chi^{(2)} \vdots \vec{E}\vec{E} + \chi^{(3)} \vdots \vec{E}\vec{E}\vec{E} + \cdots \right] \tag{1.1}$$

where $\chi^{(m)}$ is the mth order susceptibility. The first term, which is linear, dominates at small $\vec{E}$. Clearly, where $\chi^{(1)}$ is the linear susceptibility, which is related to the dielectric constant and the refractive index of the material by $n^2 = 1 + \chi^{(1)}$. The second term represents a quadratic or second-order nonlinearity, the third term represents a third-order nonlinearity, and so on. In centrosymmetric media, e.g., silica and silicon, which have inversion symmetry [12], the $\vec{P} - \vec{E}$ function must have odd symmetry. As a result, the second-order nonlinear coefficient must then vanish, and the lowest order nonlinearity is of third order. Materials with third order nonlinearity are called ***Kerr medium***. Kerr media respond to optical fields by generating third harmonics and sums and differences of triplets of frequencies. The response of a third-order nonlinear medium to a monochromatic optical field $E(t) = \mathrm{Re}\{E(\omega)\exp(j\omega t)\}$ is a nonlinear polarization $P_{NL}(t)$ containing a component at frequency ω and another at frequency 3ω,

$$P_{NL}(\omega) = 3\chi^{(3)}\left|E(\omega)\right|^2 E(\omega) \tag{1.2a}$$

$$P_{NL}(3\omega) = \chi^{(3)} E^3(\omega) \tag{1.2b}$$

The polarization component at frequency ω in Eq. (1.2a) corresponds to an incremental change of the susceptibility $\Delta\chi$ at frequency ω. This is equivalent to an incremental refractive index $\Delta n = \Delta\chi / n = n_2 I$, where is called ***optical Kerr coefficient.*** Thus, the change in the refractive index is proportional to the optical intensity. The overall refractive index is therefore a linear function of the optical intensity *I*,

$$n(I) = n + n_2 I \tag{1.3}$$

This effect is known as the ***optical Kerr effect*** because of its similarity to the electro-optic Kerr effect, for which Δn is proportional to the square of the steady electric field. The optical Kerr effect is a self-induced effect in which the phase velocity of the wave depends on the wave's own intensity. In particular, in a Kerr medium third harmonics and sums/differences of triplets frequencies, as well as different modulation interactions among them can be generated, depending on the number of optical waves (i.e., at different carrier frequencies) propagating together through the medium. The most general case involves the effects induced by the propagation of three different input waves in which the nonlinear processes that concern the generation of new frequency components must satisfy the frequency matching condition (Eq. 1.4a) and the phase matching condition (Eq. 1.4b):

$$\omega_{out} = \pm\omega_1 \pm \omega_2 \pm \omega_3 \tag{1.4a}$$

$$\beta_{out} = \pm\beta_1 \pm \beta_2 \pm \beta_3 \tag{1.4b}$$

where ω_m and β_m ($m = 1,2,3$) are the carrier angular frequency and propagation constant of each optical wave. The dispersion characteristic of silicon waveguides makes the phase matching condition very challenging to satisfy. This in turn limits the efficiency of nonlinear processes such as ***third-harmonic generation*** ($\omega_1 = \omega_2 = \omega_3$, $\beta_1 = \beta_2 = \beta_3$) or ***four-wave mixing (FWM).*** Most of the nonlinear effects therefore originate from nonlinear refraction, a phenomenon referring to the dependence of the refractive index to the intensity of the light propagating through the medium. This dependence leads to other interesting nonlinear effects; the two most widely studied are ***self-phase modulation (SPM)*** and ***cross-phase modulation (XPM).*** In particular, when two monochromatic waves of angular frequencies ω_1 and ω_2 propagate through a Kerr medium, wave 1 travels with an effective refractive index controlled by its own intensity as well as that of wave 2. Wave 2 encounters a similar effect, so that the waves are coupled. Since the phase shift encountered by wave 1 is modulated by the intensity of wave 2, this phenomenon is known as XPM. On the other hand, the applied phase change due to the intensity of a wave on itself results in SPM.

In general, nonlinear refraction involves the spectral spreading of an optical signal due to a phase modulation process. Therefore, the newly generated frequency components do not need to satisfy the phase matching condition [19].

For all the above-mentioned nonlinear effects, there is no exchange of energy between the electromagnetic field and the dielectric medium. In another class of observed nonlinear effects, there is a transfer of energy between the optical field and the medium. The most important effects in this category are ***stimulated Raman scattering (SRS)*** and ***stimulated Brillouin scattering (SBS)*** [19].

Nonlinear-optics based techniques, mostly requiring high optical powers, have been used for a variety of on-chip optical signal processing applications [13, 14, 15]. Note that silicon suffers from an inherent problem at telecommunication wavelengths (1260 nm – 1675 nm). When a high-power optical signal is pumped into a silicon waveguide (as required to excite a nonlinear optics phenomenon) a mechanism called two-photon absorption (TPA) kicks in [16]. Based on TPA, two photons can cooperate to excite an electron out of the valence band into the conduction band. TPA creates a population of free carriers that can also absorb light through free-carrier absorption [17]. As mentioned before, silicon has an indirect electronic band structure; consequently its intrinsic recombination rate of free carriers is low (only $10^3 - 10^6$ per second, depending on its purity, compared with approximately 10^9 per second in direct-band structure semiconductors such as GaAs [18]). As a result of this property, the free-carrier population quickly builds up at high light intensities. This in turn increases the optical losses significantly. Note that TPA becomes quite insignificant when the wavelength of the incident light exceeds ~2200 nm [18]. This is a reason why silicon-based nonlinear optical signal processing is quite challenging in the wavelengths of interest for telecommunication applications (below 2200 nm).

In what follows we briefly overview a few relevant examples in which nonlinear-optics based effects have been successfully used for on-chip optical signal processing:

- Integrated optical auto-correlator based on third-harmonic generation in a silicon photonic crystal waveguide [13]. In this work, a CMOS-compatible device has been implemented for single-shot time-domain measurements of picosecond optical pulses. In particular, two counter-propagating replicas of the pulse under test (with their carrier wavelength at 1550-nm) interact in a photonic crytal waveguide to generate a stationary spatial profile at the third-harmonic frequency (visible wavelength) directly related to the pulse auto-correlation trace.
- All-optical wavelength conversion in a silicon ring resonator based on cavity enhanced FWM [19]. As an example, a ring resonator with a quality factor of ~10,000 and a free spectral range (FSR) of 100 GHz has been used for all-optical wavelength conversion of a 10 Gb/s (33% Return-to-Zero) differential phase-shift keying (DPSK) pseudorandom bit sequence (PRBS) data stream. A signal and pump beam are launched into a ring resonator from the bus waveguide, producing an idler wave at a frequency shifted from the pump by an amount equal to the signal-pump spacing – a condition resulting from energy conservation. If the signal and pump wavelengths are aligned to a cavity resonance, both beams will be trapped in the resonator and experience significant enhancement in intensity. In addition to enhancing the intra-cavity power, the resonance condition also enhances the effective interaction length with respect to the physical length of the resonator. Further, if the phase-matching condition [20] for the FWM process is met, this results in the idler wave also coinciding with a ring resonance, yielding a triply resonant condition which results in extremely efficient FWM at continuous wave (CW) power levels of only a few milliwatts.
- SPM-based optical regeneration in an 8-mm-long nano-waveguide followed by a ring resonator bandpass filter [21]. Optical regeneration can be used to reshape and "clean up"

deteriorated data signals. For example, the regeneration process based on nonlinear spectral broadening in a relatively long silicon waveguide and a subsequent spectral filtering through the ring resonator has been reported. This technique has been used for optical regeneration of 10 Gb/s return-to zero (RZ) data signals [21]. In principle, when a signal passes through a nonlinear medium, its spectrum will be broadened proportional to its power, as a result of SPM. However, noise experiences less spectral broadening because of its lower power, and remains around the center of the broadened spectrum. Therefore by proper spectral filtering, noise can be rejected and optical regeneration will be performed.

- All-optical logic gate based on FWM in silicon nanowire. In this work exclusive-OR (XOR) logic gate has been demonstrated via FWM in a 6 mm long silicon photonic waveguide achieving error-free operation for 40 Gb/s quadrature phase-shift keying (QPSK) signal [22].
- Silicon-based optical phase conjugator for dispersion compensation. Implementing an 8-cm long silicon waveguide, an efficient wavelength conversion with efficiency of -8.5 dB based on FWM process has been previously demonstrated [23]. In addition to being shifted in wavelength, the converted signal represents the optical phase conjugation of the original input signal. This phase conjugation process has enabled full compensation of accumulated dispersion on a 40 Gb/s optical data stream transmitted over 320 km of standard fiber [23].
- Optical time lens based on FWM on a silicon chip [24]. 20 times magnification of a signal consisting of two 3 ps pulses has been demonstrated using centimeter-long silicon waveguide. To realize a spatial imaging system in the time domain, a temporal equivalent of the spatial lens is required. Such a device, which is often referred to as a time lens, imparts a quadratic phase to the input waveform. Nonlinear optical processes can be used to impart a quadratic phase to the input signal. For example, XPM between a pump pulse with a quadratic temporal profile and the input signal results in adding a quadratic phase to the signal. Alternatively, in the FWM process with a properly chirped pulse, (ultrashort pulse that is dispersed through a dispersive medium) the converted wavelength is generated at nearby wavelengths, which makes it easier to detect or transmit the signal for telecommunication applications.
- Amplitude and phase characterization of optical pulses based on FWM. In this work a 45-cm long spiral waveguide made on high index doped silica glass has been used for both amplitude and phase characterization of ultrafast optical pulses with the aid of a

synchronized incoherently related clock pulse [25]. The method is based on a variation of spectral phase interferometry for direct electric-field reconstruction (SPIDER) that exploits degenerate FWM in a CMOS-compatible chip. Implementing this technique pulses with a peak power of <100 mW, a frequency bandwidth of >1 THz, and up to 100 ps pulse widths have been characterized, yielding a time–bandwidth product of >100.

1.3 Linear-optics based signal processing

Linear devices/filters have the property called superposition based of which the net response of the system at a given place and time caused by two or more stimuli is the sum of the responses which would have been caused by each stimulus individually [26]. Additionally, we call a system time-invariant if the system response does not depend explicitly on time [26]. The system satisfying both above conditions is called a linear time-invariant (LTI) system. An LTI system can be easily described using techniques of frequency analysis (or Fourier transform) [26]. Linear devices with time-invariant characteristics are fully characterized by their temporal impulse response, i.e., response of the filter to an input temporal impulse, or the corresponding frequency response (spectral transfer function), i.e. frequency-domain representation of the device's temporal impulse response. Note that LTI systems referred to as “filters” in this Thesis.

In linear optical devices light is deflected or delayed but its frequency is unchanged (superposition principle holds). However, in non-linear optical devices the superposition principle is not valid. In general, linear optical systems offer much higher power efficiencies as compared with their non-linear counterparts. As mentioned above, nonlinear optical devices, in contrast with linear optical signal processing devices, typically require high-power input optical signals. Moreover, a large number of important functionalities in information processing and telecommunication applications are linear and time invariant. Additionally, mostly low-power optical signals are transmitted, received and processed in these applications.

For the reasons stated above, in this Thesis, we focus on linear-optics based techniques for three main functionalities: 1) optical pulse shaping, 2) optical signal processing/filtering, and 3) optical signal characterization.

1.3.1 Optical pulse shaping (OPS)

The term OPS in general refers to synthesizing the amplitude and/or phase variations of an optical electromagnetic wave in time, space or frequency domains in order to realize a target optical waveform [12]. In this Thesis we focus on the reshaping of the optical waveforms in time-domain. In practice Gaussian-like optical pulses, typically generated from a mode-locked laser, are re-shaped into a target pulse waveform using different OPS methods.

OPS with frequency-bandwidths in the GHz up to the THz range, has become increasingly important for a wide range of applications. In particular, optical pulses with user-defined temporal shapes are used for ultrahigh-bitrate optical fiber communications [27, 28], ultrafast optical signal processing [29, 30], THz wireless communication systems [31], optical imaging for medical applications [32], laser detection and ranging (LIDAR) [33], optical techniques for materials/devices characterization [34], advanced optical sensors [35], fundamental studies of dynamic chemical and physical systems [36] etc.

In this Thesis, we focus on techniques mostly implemented for the precise synthesis and control of the temporal shape of optical pulses with resolutions in the picosecond and sub-picosecond regimes, with carrier wavelengths in the range of 1460 nm to 1625 nm (S, C and L band fiber optics communication standard transmission windows) [30]. This family of waveforms are of fundamental importance for applications in ultrahigh-bitrate optical communications, information processing and computing systems. In particular, optical pulses with THz frequency-bandwidth have been used in nonlinear optics-based data processing/switching to enhance the performance of high speed telecommunication sub-systems [37].

As a very relevant example, ***(sub) picosecond flat-top (rectangular-like) optical pulses*** are highly desired in applications requiring the use of a well-defined temporal gating window, for example, for time-domain gating of optical telecommunication data using nonlinear effects, e.g., Kerr effect [3]

Figure 1-3, illustrates the concept of nonlinear optical switching for temporal demultiplexing of serial optical time-division multiplexed (OTDM) data. An OTDM data signal consists of different optical pulse streams, called tributaries, originating from a same laser source (or located at similar central frequency). The tributaries are first separately encoded by electrically generated data signals. Then the modulated sequences are serially bit interleaved in order to form a high speed serial OTDM data signal. At the receiver side, an ultrafast data recovery system is needed to extract the individual time-domain tributaries, which are subsequently processed by conventional (opto)electronics. For optimum performance, the gating pulse at the receiver side has to be shorter than the one-bit time window and at the same time it should have a constant intensity over a time interval of interest. Both of these requirements can be fulfilled using flat-top pulses. As a very relevant example we consider a 640-to-10 Gb/s demultiplexing configuration [37]. In order to carry out the conversion, a flat-top gate pulse with temporal duration shorter than ~1.5-ps is required. Generation of such a short pulse is well beyond the bandwidth capabilities of optoelectronics-based switches (usually limited to tens of GHz). Briefly, direct laser light modulators, electro-optics and electro-absorption modulators can be considered as optoelectronics-based pulse shaping methods [38, 39]. Moreover, it is extremely challenging to generate arbitrary electronic waveforms with bandwidths larger than ~15 GHz based on purely electronic circuits [40]; therefore, the speed limitation of electronics typically restricts the minimum temporal features of an arbitrary user-defined optical waveform generated by optoelectronics-based pulse shaper to below ~15 GHz. In this regard, the required flat-top optical pulse to control the optical gate need to be generated using an OPS device. As illustrated in Figure 1-3**,** flat-top optical control pulses increase the tolerance to timing jitter in the system, thus improving the overall performance of the nonlinear switching scheme, for example, leading to a significantly improved receiver sensitivity [37, 41].

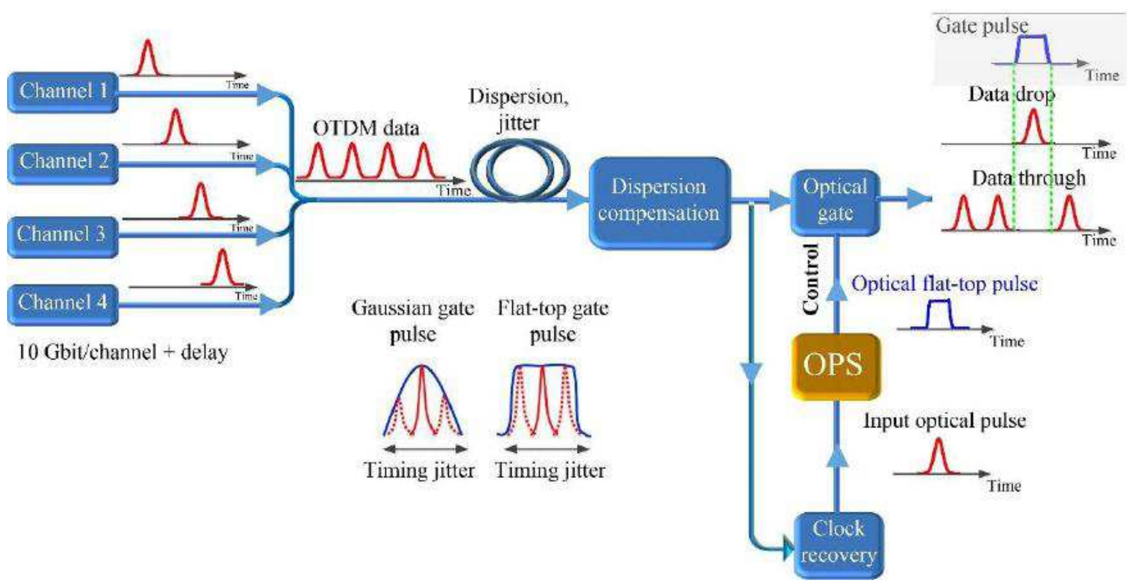

Figure 1-3 A Schematic for the use of optical flat-top pulse generated by an OPS device. This scheme is employed for demultiplexing of OTDM data by means of nonlinear switching (gating). Improved tolerance to timing jitter is expected (small inset) [37].

Another example of optical pulse shapes with practical interest are ***saw-tooth (asymmetric triangular-like) optical pulses*** [42]. These pulses are highly desired for nonlinear optical switching [43] as well as for a range of wavelength conversion applications [44, 45]. For instance, Figure 1-4 illustrates a schematic of a simple all-optical wavelength-conversion scheme based on XPM. In this scheme, a sequence of saw-tooth optical pulses and a continuous wave (CW) probe are launched together into a nonlinear medium, e.g., a highly nonlinear fiber (HNLF). The XPM will act to broaden the spectrum of the CW probe. In this way, spectral sidebands are generated on the probe signal through modulation of the phase in the nonlinear fiber. At the output of the HNLF, the sidebands on the CW probe can be extracted by spectral filtering, generating an amplitude-modulated signal from the phase modulation of the CW probe. This amplitude-modulated signal will thus form a wavelength-converted replica of the original data signal. As a very relevant example, reported in [45], 10-ps full-width at half-maximum (FWHM) saw-tooth pulses, as pump signals, are first amplified up to 20 dBm and then launched to the HNLF together with a CW probe at 1559.1 nm. The nonlinear fiber has a length of L=310 m, a dispersion of 0.31 ps/nm/km, a dispersion slope of 0.0031 ps/ nm^2 /km, a nonlinear coefficient of $\gamma = 22$/W/km, and a loss of 1.21-dB/km. Finally, two optical filters with FWHM of 0.5 nm and offset detuning of $\Delta\lambda = 1$ nm relative to the CW carrier are used to select the wavelength-converted signal.

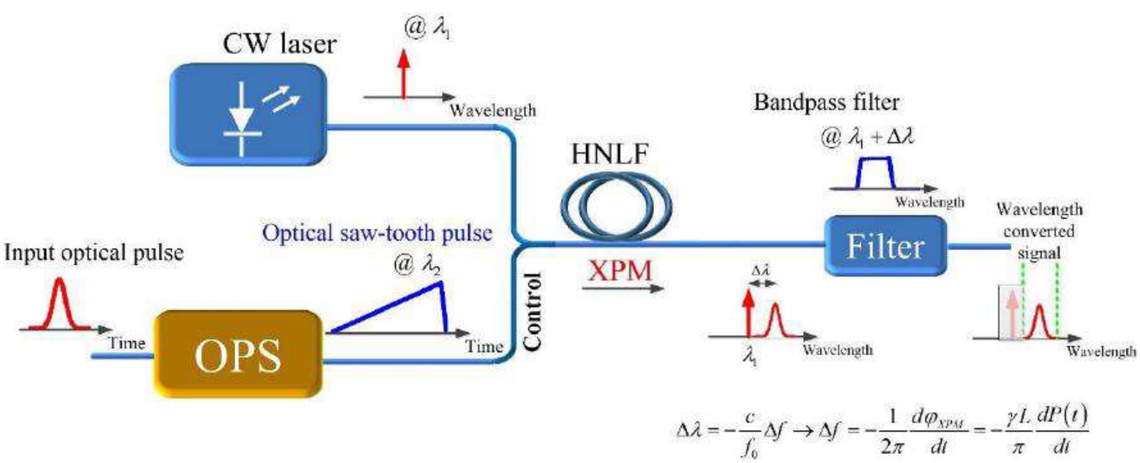

Figure 1-4 A schematic for the use of optical saw-tooth pulses, employed for an efficient all-optical wavelength-conversion scheme (c: is the speed of light in vacuum, φ_{XPM}: is the phase change induced by XPM, f_0: is central operation frequency, L: is the HNLF length, γ: is the nonlinear fiber parameter and $P(t)$: is the temporal intensity waveform of the pulse, e.g., saw-tooth) [45].

Another interesting family of pulse shapes are ***optical parabolic (quadratic intensity-like) pulses.*** In particular, femtosecond optical parabolic pulses have been previously used to achieve ultra-flat SPM – induced spectral broadening in supercontinuum generation experiments. Besides, they have found applications in extinction ratio enhancement of optical signals, retiming operations, etc [46]. For instance, Figure 1-5 illustrates a schematic for generating flat SPM-broadened spectra, so-called supercontinuum, based on seeding a HNLF with optical parabolic pulses generated using an OPS device. An example of supercontinuum generation is reported in [47] where a 10 ps (FWHM) optical parabolic pulse is fed into a 500 m long HNLF with dispersion 0.87 ps/nm/km, dispersion slope -0.0006 ps/ nm^2 /km, nonlinear coefficient ~19/W/km and total propagation loss 1-dB. Due to SPM the output pulse is a supercontinnum with spectral full width of 50 nm.

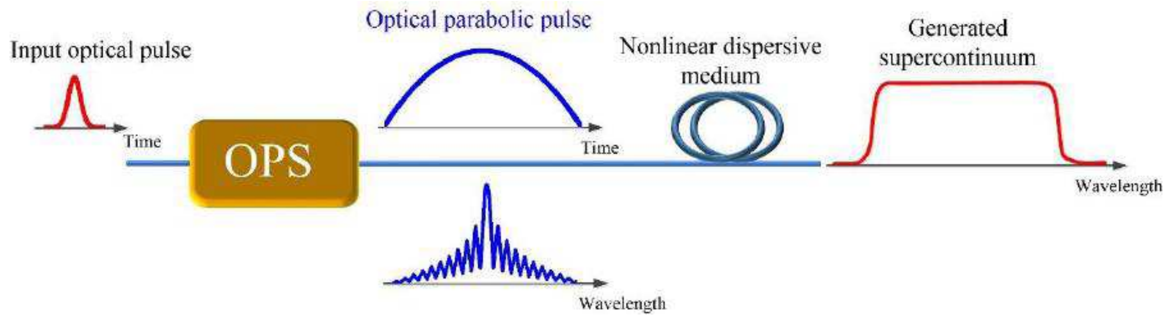

Figure 1-5 A schematic for the use of optical parabolic pulses, employed for supercontinuum generation with flat spectrum [47].

Another important example of optical waveform shapes are high-bitrate amplitude and/or phase ***optical code packets***. These optical waveforms are particularly interesting for applications requiring the generation of time-limited data streams (composed of a few consecutive optical symbols), such as for optical code-division multiple access (OCDMA) and optical label switching communications [48, 49]. In OCDMA, the assigned signals to different users, which may be overlapping both in time and frequency, share a common communication medium; multiple access is achieved by assigning different, minimally interfering code sequences to code division multiple access (CDMA) transmitters [50]. As illustrated in Figure 1-6, ultrafast amplitude and phase optical code packets generated using OPS methods can be used in a single-wavelength OCDMA application.

As an example OPS in apodized Bragg grating has been used for generation of 255-chip 320-Gchip/s quaternary phase code for a four-channel OCDMA system [51]. In a more recent work, electro-optical phase shifters on polymer waveguides have been used as decoder/encoder in an OCDMA system [52].

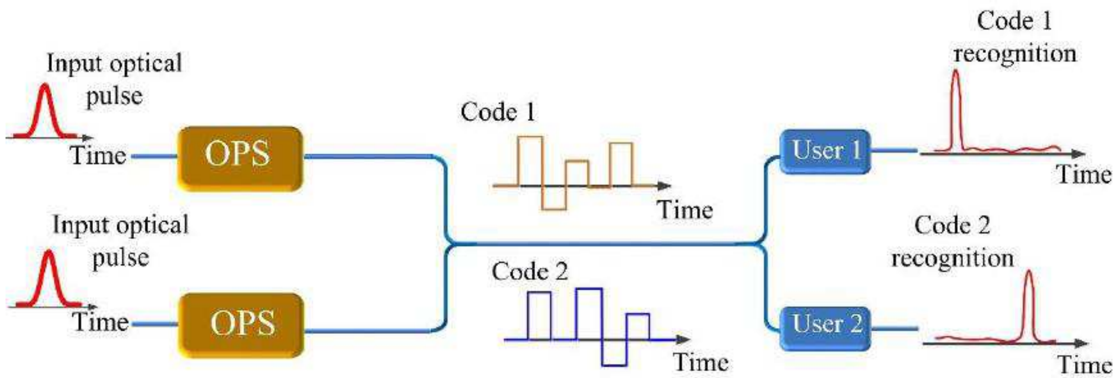

Figure 1-6 A schematic for the use of ultrafast amplitude and phase optical code packets in a single-wavelength OCDMA application using an OPS and recognition scheme.

In what follows relevant previous approaches for OPS will be reviewed.

1.3.1.1 Frequency-domain OPS

OPS based on frequency-domain (Fourier) analysis was first introduced and implemented in free-space. The implementation of ***spectral shaping in the spatial domain*** has allowed the programmable synthesis of arbitrary waveforms with resolutions better than 100 fs [30]. As illustrated in Figure 1-7 [53], this pulse shaping apparatus consists of a pair of spatial diffraction gratings, lenses, spatial (amplitude and phase) masks and it works as follows: The individual optical frequency components contained within the input incident waveform are first spatially dispersed by a diffraction grating and then, the separated frequency components are collimated on a mask or combination of masks using a lens. The masks manipulate the spectral components of the incident pulse in order to achieve the target pulse shape. After that, the light is re-focused using another diffraction grating. Note that spatially patterned amplitude and phase masks are placed midway between the two lenses at the point where the optical spectral components experience the maximal spatial separation (this configuration is known as a 4-f imaging system in free-space optics). In such a system, the second grating recombines all the frequencies into a single collimated beam, an output waveform is obtained, with a pulse shape given by the Fourier transform of the pattern transferred by the spatial masks onto the input pulse spectrum. It is worth mentioning that the amplitude/phase mask can be realized using spatial light modulators (SLMs), where the SLM allows programmable waveform generation under computer control.

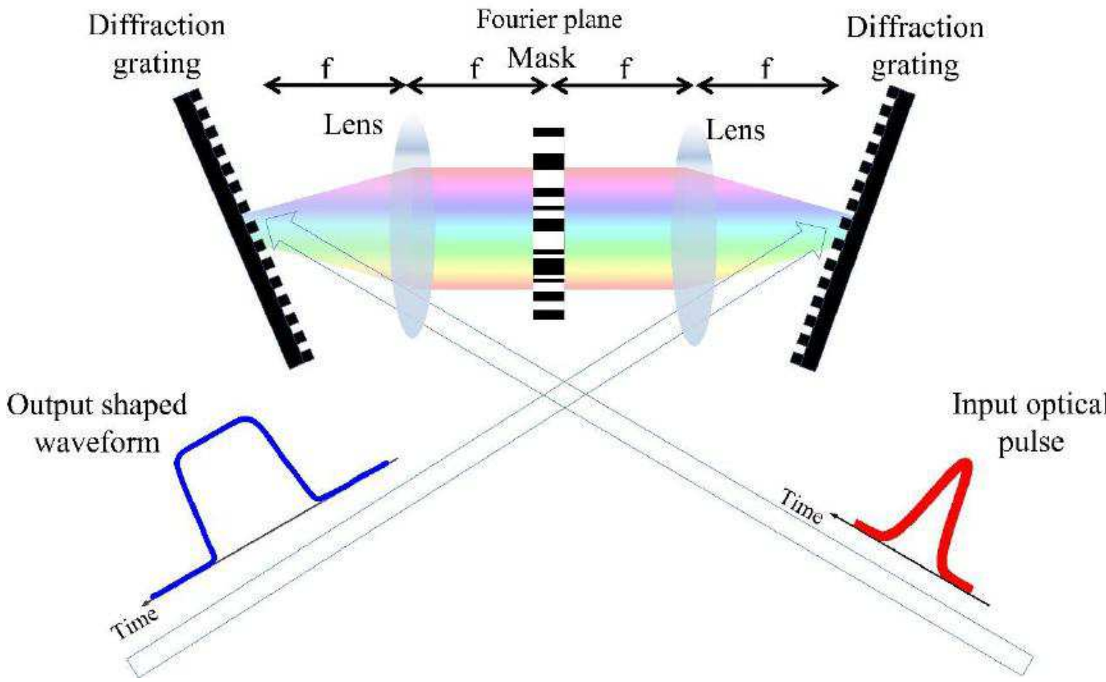

Figure 1-7 Schematic of spatial-domain pulse shaping approach for OPS. In this scheme the output waveform is determined by the Fourier transform of the pattern transferred from the spatial mask onto the input waveform spectrum [30].

The aforementioned principle has been used in the first commercially available optical wave shapers [54]. Despite the great advantages of this method, its major drawbacks are: (1) its relative complexity, which requires the use of very high-quality and expensive bulk-optics components, i.e., high-quality diffraction gratings and high-resolution spatial light modulators, (2) its limited integration capability with fiber or waveguide optics systems, inducing higher insertion losses [54], and (3) its limited frequency resolution (resolution of ~10 GHz for commercial wave shapers) [54].

To overcome the problems mentioned above, an important body of research has aimed at the implementation of spectral shaping for OPS in optical fibers and integrated waveguide platforms. These techniques include technologies based on integrated spatial arrayed waveguide gratings (AWGs) [55, 56], optical lattice filters [57], fiber/waveguide Bragg gratings [58, 59] and fiber long period gratings [60, 61].

A similar pulse shaping principle, shown in Figure 1-8, has been implemented using an ***on-chip AWG*** [62]. Light propagating in the input waveguide of an AWG will be coupled into an array of waveguides via the first star coupler. The array has been designed such that the optical path length difference between adjacent array arms is equal to an integer multiple of the central wavelength that the filter is designed for. As a consequence, the field distribution at the input aperture will be reproduced at the output aperture. Therefore, considering an input monochromatic signal, the light will be focused in the center of the image plane (provided that the input waveguide is centered in the input plane). If the input wavelength is detuned from this central wavelength, phase changes will occur in the array branches. Due to the constant path length difference between adjacent waveguides, this phase change will increase linearly from the inner to outer array waveguides, which will cause the wavefront to be tilted at the output aperture. Consequently, the focal point in the image plane will be shifted away from the center. The positioning of the output waveguides in the image plane allows for the spatial separation of the different incoming wavelengths (or frequencies). More details about AWGs are provided later on in section (1.3.2.3).

In an AWG-based OPS, first, the frequency components of an input optical pulse are spatially separated using an AWG. In particular, the temporal input optical pulse is converted into a spatial waveform by a diffractive element (e.g., AWG) and spatially dispersed into its frequency components. Then, the amplitude and/or phase of these components are manipulated with an array of modulators, usually conventional amplitude and phase modulators, or alternatively, an IQ modulator, where "I" is the "in-phase" component of the waveform, and "Q" represents the "quadrature" component. Finally, the modulated frequency components are reassembled by reversing the process in the second AWG, and a temporal output optical waveform is obtained as a convolution of the temporal input optical pulse and the impulse response of the arrayed modulation/filtering scheme [63]. Despite the great improvement in terms of compactness, AWGs still suffer from limited spectral resolution, e.g., a minimum channel spacing of 25 GHz has been realized in a SOI technology platform [64]. Note that high-resolution AWGs with channel spacing of ~ 5 GHz have been previously demonstrated using III-V materials, e.g., InP [65], requiring a considerably large foot-print of 21 mm × 22 mm. Moreover, sensitivity to fabrication errors makes it quite challenging to design and fabricate on-chip AWGs.

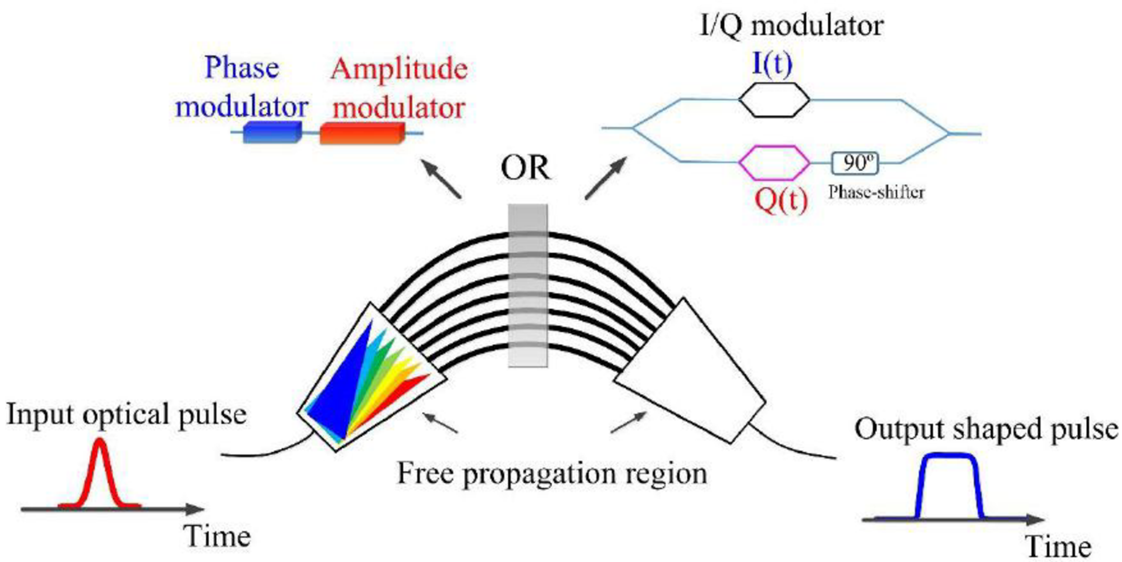

Figure 1-8 Illustration of an OPS scheme based on an integrated spatial arrayed waveguide grating (AWG) [63].

Other interesting OPS/processing devices are based upon optical ***lattice filters***. The lattice configuration has been used to manipulate poles and zeroes of a filter, in a reconfigurable fashion, in order to realize a target pulse shaping/processing functionality [57]. The schematic of a 4-stage reconfigurable lattice filter is shown in Figure 1-9.

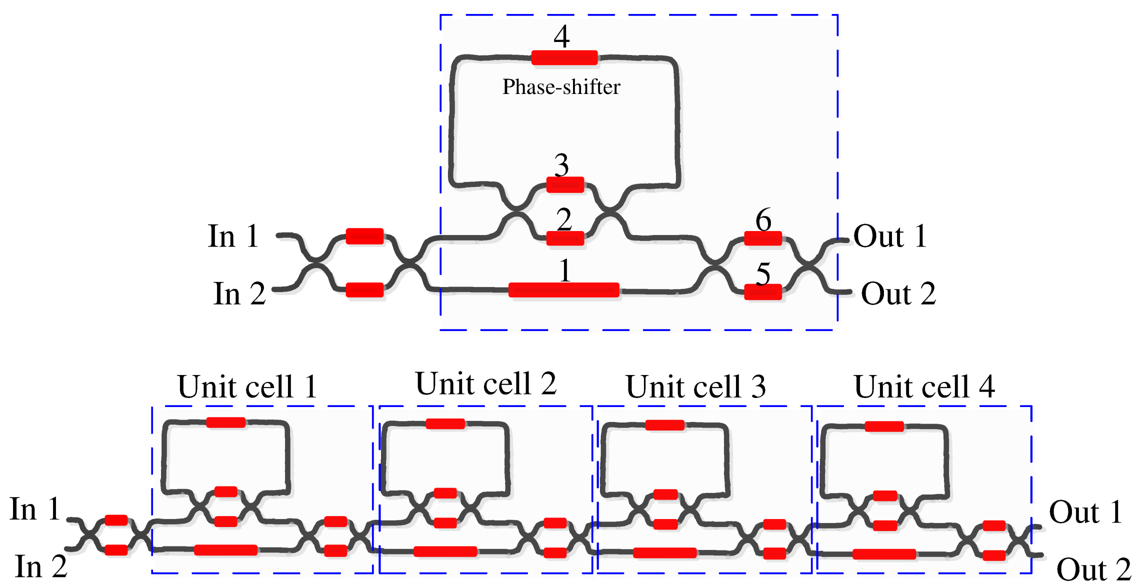

Figure 1-9 Schematic design of single unit-cell filter and four unit-cell filter. The phase-shifters have been indicated with red boxed rectangles [57].

In this scheme, each unit-cell employs a combination of a ring resonator and a MZI with tunable phase elements in both of its arms. Additionally, each unit-cell contributes a separately controllable pole and zero pair [57]. The reconfiguration of the unit-cell and four-cell silicon lattice filter is based on a recursive algorithm. This scheme brings new possibilities to radio frequency (RF) photonic processing. However, not only the device has been designed using a relatively complex spectral-domain synthesis approach, but additionally, it incorporates a phase-shifter in each ring resonator, making it difficult to scale the device for operation bandwidths above a few GHz. Recall that the bandwidth of this structure, defined by the FSR of the micro ring resonator, is inversely proportional to the ring's radius [66].

Another promising approach for OPS is based on implementing ***fiber/integrated Bragg grating structures***. A grating consists of a periodic perturbation of the refractive index along the core of an optical fiber or a waveguide (in an on-chip realization). These optical devices fall into two general categories based upon the period length of the grating: short-period or Bragg gratings (BGs), typically with sub-micron periods, and long period gratings (LPGs), with periods in the range of 100s of microns (considering operation wavelength of 1.5 µm for both cases) [12].

As illustrated in Figure 1-10, in a BG, the light from the forward-propagating mode is coupled to the counter-propagating (backward) mode due to the perturbation induced along the wave-guiding medium [67]. This coupling between two modes occurs around a very specific wavelength, defined by the Bragg phase-matching condition. Considering two counter-propagating modes with propagation constants of $\beta_1\left(=2\pi n_{eff,1}/\lambda\right)$ and $\beta_2\left(=2\pi n_{eff,2}/\lambda\right)$, the phase-matching condition is defined as [68]:

$$\beta_1-\beta_2=m\frac{2\pi}{\Lambda};\qquad m=1,2,3,... \tag{1.5}$$

where m is the Bragg-order, Λ is the nominal grating period, $n_{eff,1}$ and $n_{eff,2}$ are the effective refractive indexes of the two counter-propagating modes. Typically in first order BGs ($m=1$) the effective refractive index of two counter-propagating modes satisfy the following condition, $n_{eff,1}=-n_{eff,2}=n_{eff}$, therefore the phase matching condition can be simply represented using the following equation:

$$\lambda=2n_{eff}\Lambda \tag{1.6}$$

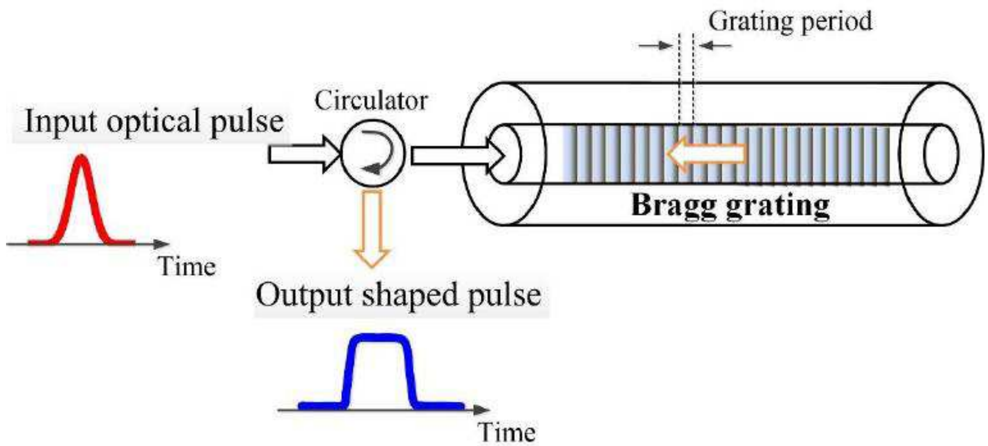

Figure 1-10 A schematic of a fiber BG working in reflection. An optical circulator is required to retrieve the reflected signal.

The refractive index variation applied on the fiber LPG induces coupling between the propagating mode in the core of the fiber and the co-propagating cladding-modes. In particular, the transmission spectrum of a fiber LPG contains a series of attenuation resonances at discrete wavelengths, each resonance corresponding to the coupling to a different cladding mode. Fiber LPGs have been used for a wide range of applications including optical sensing [69], optical filtering [70], gain flattening of optical amplifiers [71], dispersion compensation [72], etc. Note that, so far integrated waveguide LPGs have not been successfully realized for OPS applications. The schematic of a fiber LPG working in cross-coupling mode is shown in Figure 1-11.

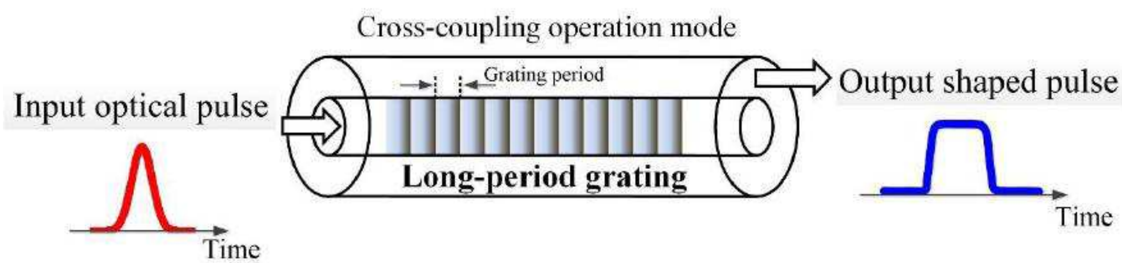

Figure 1-11 A schematic of a fiber LPG working in cross-coupling mode (coupling from the core mode to one of the cladding modes).

One of most attractive attributes of LPG and BG devices for OPS and processing applications is that they can be designed to provide a desired, arbitrary frequency response, in amplitude and in phase. With respect to this feature, these devices are today considered as one of the key components in sensing, communication and processing sub-systems [67]. Arbitrary spectral/temporal responses for OPS are mostly synthesized by BGs operating in reflection [73]. Note that the bandwidth achievable by BGs for OPS is limited by the spatial resolution with which the grating apodization profile can be realized using the available fabrication technologies (the grating apodization profile is defined as effective refractive index modulation along the device with its amplitude determined by the coupling strength and phase determined by the grating period) [58]. For instance, considering a typically feasible sub-millimetre resolution for the fiber grating apodization profiles, the temporal resolution of any target pulse shape is limited to at least several picoseconds, i.e., corresponding to a few hundreds of GHz in terms of frequency bandwidth [58].

An important drawback of the fiber grating-based OPS approach is that most BG designs need to be operated in reflection. This imposes another level of complexity and extra loss as a circulator, Y-branch or 3dB-coupler needs to be implemented in order to retrieve the signal in reflection. Additionally, it has proven difficult to add reconfigurability in these structures, e.g., through the integration of high resolution thermo/electro-optical controllers [74].

To synthesize ultrafast optical waveforms with frequency bandwidths in the THz regime, corresponding to sub-picosecond/femtosecond temporal features, LPG-based spectral shaping schemes have been previously proposed. Several drawbacks of fiber LPG-based pulse shapers include their bulkiness, sensitivity to environmental effect (this sensitivity has made LPGs interesting for optical sensing applications [70]), low power efficiency and their shortcoming in synthesization of optical pulses with temporal durations longer than ~10 ps.

Most importantly, considering the above mentioned drawbacks, both short-period (Bragg) and long-period grating devices have proven challenging to fabricate in integrated-waveguide configurations. This is particularly true if they are intended to synthesize complex waveforms, e.g., with high resolutions, below the sub-picosecond regime, over long durations, above a few picoseconds [58, 59]. One of the difficulties with the design of on-chip BGs is the complexity involved in finding the grating-strength (coupling) apodization profile that is required to implement a specific signal processing application (e.g., OPS). This is a result of non-negligible effects of waveguide dispersion, loss and dimensional variations due to fabrication uncertainties etc [75]. Consequently, to the best of author's knowledge, integrated waveguide BGs have not been previously implemented for OPS using the most general frequency-domain design approach. However, direct time-domain OPS approaches have enabled the realization of integrated waveguide BG-based optical pulse shapers [59]. This case is studied in the next section.

1.3.1.2 Time-domain OPS

Despite the advantages offered by frequency-domain OPS methods, direct time-domain pulse shaping bypasses the need for developing complex synthesis algorithms. A synthesis algorithm is a mathematical routine to design a device based on reverse engineering [76]. For instance, first the frequency-domain response of a target waveform should be calculated using Fourier transformation. Then this spectral response will be used as a target to extract the pulse shaper's specifications, e.g., amplitude/phase variations of BG apodization profile.

Alternatively, coherent synthesization and space-to-time mapping are techniques capable of re-shaping an optical pulse directly in the time-domain. Based on ***temporal coherence synthesization*** [77, 78], arbitrary optical waveforms can be generated from an input pulse (e.g. transform-limited Gaussian-like) using several optical arms/waveguides for providing delayed [78] or arbitrary-order differentiated [77] replicas of the original input pulse. These replicas, with different defined weights, are then coherently superposed to generate the target arbitrary optical waveform.

The basic implementation of coherent synthesization (coherently combining the delayed replicas of an input pulse) allows the synthesis of any desired optical waveform with time features only limited by the input pulse bandwidth. In this method, a general optimization algorithm has to be developed for designing the system specifications (number of interferometers and their relative time delays) that are required to achieve a desired OPS operation. The main drawback of this method is that in order to realize complex waveforms with high time-bandwidth products (TBPs, a measure of pulse quality defined in ***Appendix A***) [77, 78], a sufficiently large number of pulse copies are required. This significantly increases the complexity and bulkiness of these pulse shapers for generation of arbitrary optical waveforms. Besides, on-chip implementation of coherent synthesization method imposes the need for active (electro- or thermo-optics) phase tuning elements at each stage of the device.

Another category of direct time-domain pulse shaping approaches is based on the idea of ***space-to-time mapping (STM)***, first implemented for OPS based on the use of free-space components [79]. In this technique the temporal waveform is a direct scaled version (not a Fourier transform) of the pulse-shaping spatial mask. A schematic representation of the pulse-shaping components making up an STM pulse shaper is shown in Figure 1-12 [80].

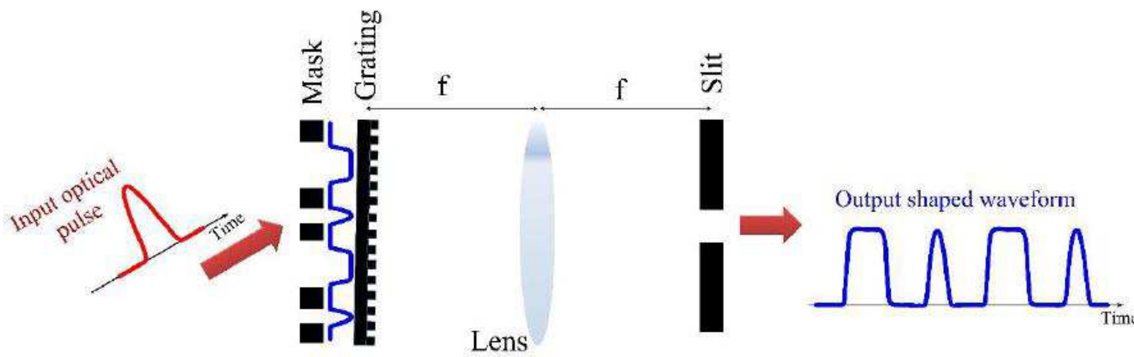

Figure 1-12 A schematic of an OPS device based on space-to-time mapping using free-space components [53].

As illustrated in Figure 1-12, in this scheme a spatially patterned mask is introduced just before a diffraction grating. A lens collects and focuses the spatially dispersed frequency components of the input beam that are diffracted from the grating. At the Fourier plane (focal plane) of the pulse shaping lens, a thin slit filters the dispersed spectrum, and generates a spatially homogeneous output beam whose temporal intensity profile is given by a scaled replica of the input spatial masking function. The scaling parameter between the spatially patterned mask and the output temporal profile can be chosen by setting the grating period and the incident angle of the input light [81]. This method provides a straight-forward solution for creating optical waveforms and data packets. However, it still suffers from relative complexity, due to the use of very high-quality and expensive bulk-optics components, and limited integration capability with fiber or waveguide optics systems [56].

Similarly, an interesting design approach for fiber/integrated waveguide gratings (BGs and LPGs) exploits the so-called first-order Born approximation, under which the devices' temporal impulse response is a direct, scaled version of the grating apodization profile [82]. This STM property greatly simplifies the grating device design for temporal pulse shaping applications [82]. It is worth noting that STM is strictly valid for weak gratings in which the relative changes of refractive index are small enough to allow the incident light to penetrate the full device length, such that the whole grating contributes equally to the reflected signal [83].

STM has been implemented in fiber and integrated waveguide BGs to synthesize arbitrary optical pulse shapes. In particular, J. Azaña and L. R. Chen have shown that using the STM method in BGs, nearly arbitrary temporal pulse shapes can be synthesized with resolutions in the picosecond regime. In this regard, the temporal resolution is directly fixed by the spatial resolution with which apodization profiles can be written in the grating [84].

In another work, L. M. Rivas et al. have used the first-order Born approximation to carry out pulse shaping using an integrated BG on-chip [59]. Particularly, the authors managed to generate 8-bit codes with resolution down to ~1 ps. As illustrated in Figure 1-13, the desired BG apodization profile has been achieved by varying the grating recess depth in a 'deeply etched' side-wall corrugated BG. In this method, the change in recess modifies the modal effective index, which in turn modulates the Bragg condition of the grating. By properly designing the local waveguide grating width and grating recess depth on a constant period BG, the Bragg wavelength and coupling coefficient can be locally controlled in order to realize a target arbitrary waveform. More details about the integrated BG design are given in ***Appendix B***.

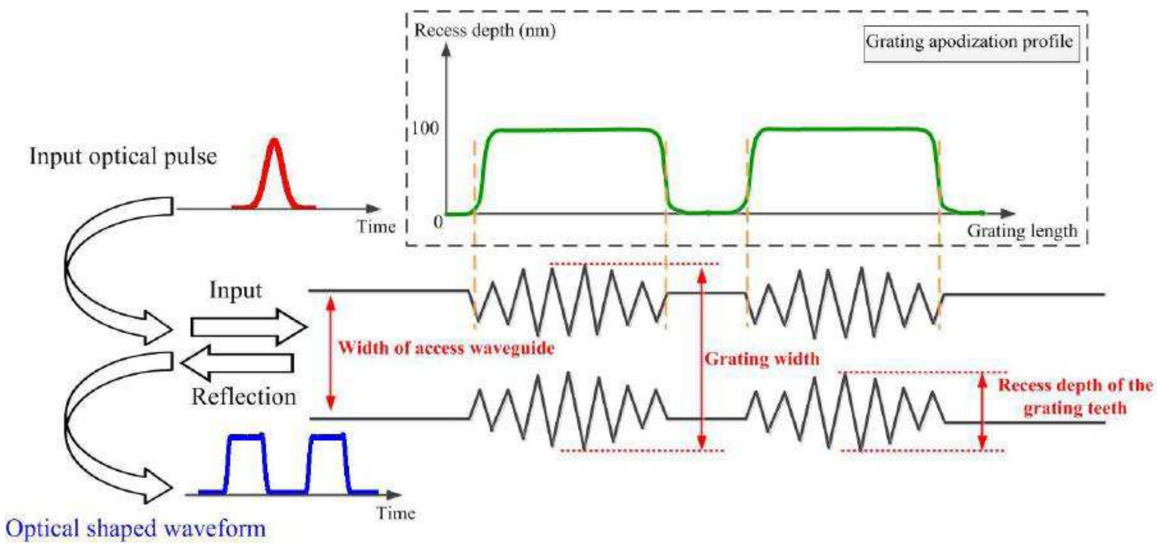

Figure 1-13 Schematic of apodized BG used for OPS on-chip.

Leveraging from the idea of STM in BGs, R. Ashrafi et al. proposed and experimentally demonstrated superluminal STM in LPG devices for arbitrary waveform generation with femtosecond time resolutions [85]. In particular, the authors have successfully synthesized sub-picosecond flat-top, saw-tooth and amplitude/ phase modulated bit sequences using this technique. Note that realization of such complex set of waveforms is very challenging using spectral-domain OPS approaches.

As illustrated in Figure 1-14**,** the scaling factor between the spatial apodization profile and the final re-shaped optical waveform in BGs and LPGs is given by $c/2n_{eff}$ and $c/\Delta N$, respectively

[86], where n_{eff} is the effective refractive index of the optical mode propagating along the core of the BG, and ΔN (in LPG) is the difference between the effective refractive index of the optical mode propagating through the core and the specific cladding mode that the light is coupled to. It is obvious that the speed of STM (defined by the above scaling factors), can be made significantly faster for LPGs, well above the speed of light in vacuum. This so-called superluminal STM enables the realization of femtosecond range optical waveforms using readily feasible fabrication resolutions [86].

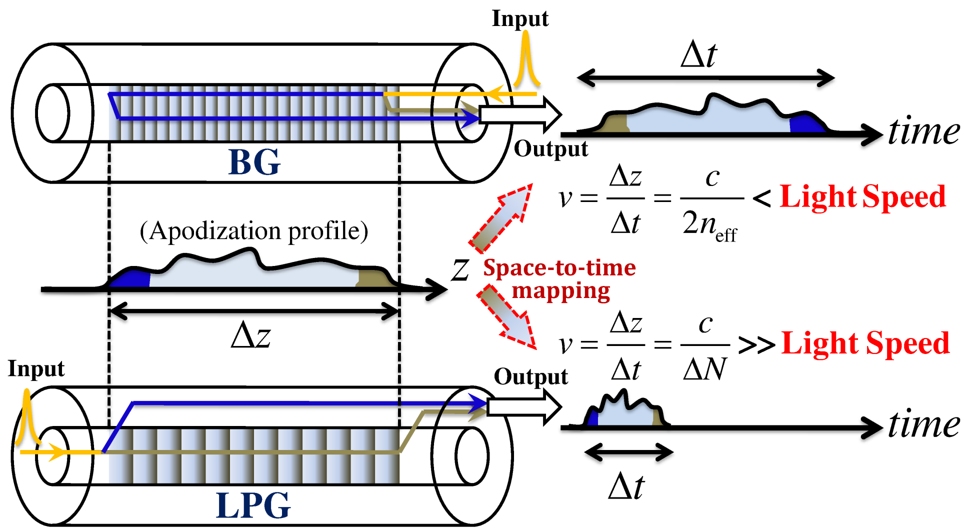

Figure 1-14 Illustration of the space-to-time mapping phenomena in fiber BG and LPG, respectively as presented in Ref. [86].

Despite the design simplicity offered by this method, as discussed above, OPS using LPGs and BGs suffers from: (i) lack of reconfigurability, (ii) difficulty of accessing the output signal (signal in reflection from BGs and signal in cladding from LPGs), and (iii) sensitivity to environmental effects and fabrications errors [86].

1.3.2 Optical signal processing/filtering

Optical filters are devices that selectively transmit light at different frequencies. Tunable band-pass/band-reject filters are highly demanded for a range of important applications in WDM telecommunications systems, all-optical signal processing, microwave photonics etc [3, 53, 87]. As illustrated in Figure 1-15, some of the defined requirements for an optical tunable filter are as follows:

- The capability of tuning the central frequency and bandwidth of the filter independently.
- Abrupt transition from pass band to rejection band of the filter.
- High extinction ratio; this parameter can be defined as the amount of suppression provided by the filter for rejection-band in comparison to pass-band.

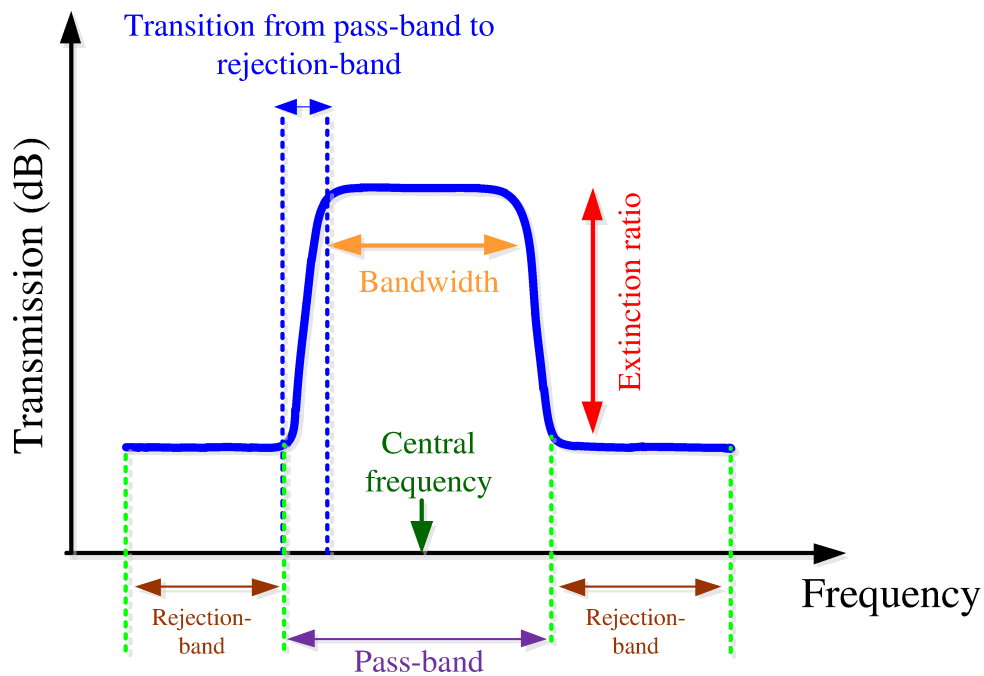

Figure 1-15 Specifications of a typical optical filter

- Non-dispersive: in many applications it is essential for the phase profile of the signal to be kept relatively unchanged after passing through the filter.
- Applicability for signals with different spectral widths: the filter's response should be applicable over a wide range of spectral widths. This limitation is mostly observed for filters with periodic spectral responses, e.g., interferomeric filters. As illustrated in Figure 1-16, the spectral periodicity of the filter's response (defined as free spectral range, FSR) imposes a limitation on the maximum spectral extent (bandwidth) of the input signal.

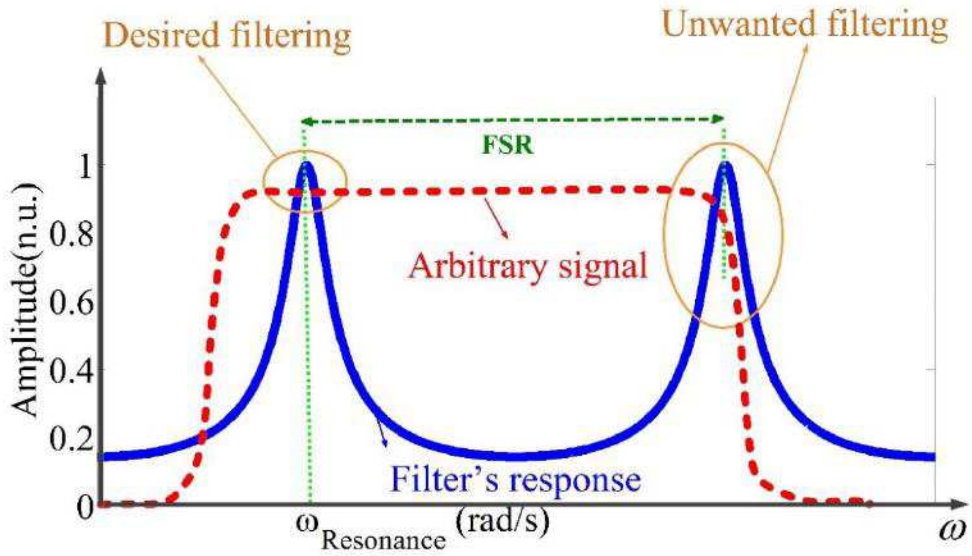

Figure 1-16 Interferometric-based filter's spectral response. The filtering process is limited to the FSR of the device, typically, determined by the relative delay in the two arms of a typical interferometer.

- Compactness: realization of the device using integrated waveguide technologies leads to significant improvement, in terms of device size, in comparison to fiber or free-space-based solutions.

Various architectures have been previously proposed to realize tunable optical filters, e.g. Fabry-Perot filters [88], interferometric filters [89], liquid crystal-based filters [90], Micro-Electro-Mechanical-Systems (MEMS)-based filters [91], acousto-optic tunable filers [92], dielectric thin-film interference based filters [93], absorption filters [94], hybrid filters [95] and grating-based filters [96]. In this sub-section, we focus on grating-based filters which are particularly interesting for telecommunication applications [67]. Wavelength selectivity of a grating is used to design filters which fall in this category. This includes filters realized based on free space-, fiber or integrated waveguide gratings.

1.3.2.1 Filters based on free-space diffraction gratings

In this scheme, the light beam to be filtered is first shined on a diffraction grating (DG). A DG is an optical component that exploits the phenomenon of diffraction of light. The light impinged on this device gets reflected back in a direction that depends on its angle of incidence, wavelength, and the grating period [12, 97]. For a given wavelength λ, the diffraction angle is defined as $\theta_B = \sin^{-1}(\lambda / 2d)$, where d is the spacing between two consecutive grating periods.

As illustrated in Figure 1-17, when a polychromatic light beam impinges on a DG, all the wavelength components are diffracted at different angles. Knowing the wavelengths, the angle of incidence and the specifications of the grating, one can calculate the angle of diffraction for each wavelength. Subsequent focusing of the diffracted wavelengths may be achieved with a lens system or with a DG in a concave form.

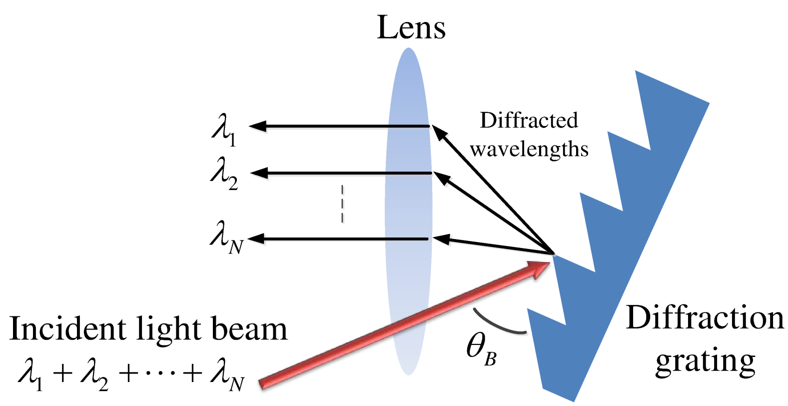

Figure 1-17 Operation of a diffraction grating for spatial separation of frequency components on an incident beam.

A possible solution for a tunable optical filtering scheme based on a DG is shown in Figure 1-18 [98]. In this configuration, a lens collimates the diffracted light from the DG. Then, the central frequency and the bandwidth of the filter can be tuned by applying a movable mirror or simply an aperture to this collimated light.

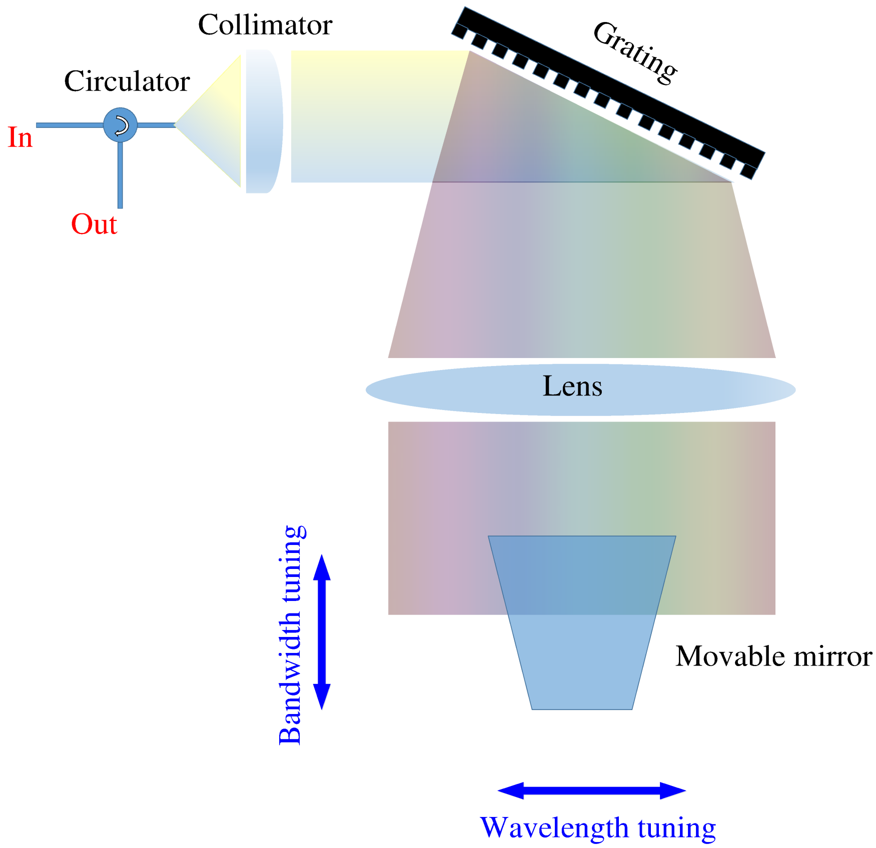

Figure 1-18 Schematic of the tunable filter based on free-space Bragg grating. Reproduced form the data sheet of OTF-350, Santec tunable filter [98].

The advantages of free-space DG-based filters are the low insertion loss, the low cross-talk that results from the low scatter level at the grating, and the potential for stable operation over a wide temperature range. The main limitations of the DG-based filters are that they are bulky and the open-optics is vulnerable to contamination and humidity. Additionally, the spectral resolution or minimum bandwidth offered by these filters is typically limited to tens of GHz [98].

A very relevant example of filters working based on diffraction in a DG is the commercially available Santec filter (model OTF-350 [98]). This device has a tunability range of ~80 nm, with a minimum bandwidth of 0.1 nm (~12 GHz). In the scheme shown in Figure 1-18, the filter's bandwidth and central frequency can be tuned independently.

1.3.2.2 Filters based on uniform and phase-shifted fiber Bragg gratings

Uniform fiber Bragg gratings (FBGs) have been used extensively as optical filters mainly because of their low insertion loss and their mature fabrication process [99]. In practice, the Bragg wavelength of FBGs, Eq. (1.6), can be shifted by applying either axial strain or temperature across the device. Inducing temperature on a FBG changes the effective refractive index of the fiber along the device (thermo-optics effect) and linearly shifts the Bragg wavelength of the grating. The theoretical tuning sensitivity of a FBG due to the thermo-optic effect is 10.7 pm/˚C [15]; consequently, a temperature change in the order of 100 ºC is required to shift the Bragg wavelength at a nanometer scale.

Mechanically-induced axial strain physically extends or compresses the grating. As the result, the grating's period, and accordingly its central wavelength, can be shifted. The excellent tolerance of silica-glass fibers to mechanical strain makes strain-tuning preferable for achieving a wide frequency tuning range in comparison to thermal-tuning. Various strain-tuning techniques have been previously demonstrated, among others, a wavelength shift as much as 45 nm has been reported by applying axial strain on a FBG in the compression mode [100]. In another work, a tunable FBG module has been realized in which the wavelength tuning was performed by lateral bending of an FBG mounted on a substrate. This module was capable of tuning the central wavelength over a 40-nm span (from 1525 to 1565 nm) [99]. Despite the wide range of tunability for the central wavelength of FBG-based filters, simultaneous tuning of the filter's operation bandwidth has proven challenging. Moreover, the minimum bandwidth of a uniform FBG-based filter is typically limited to a few GHz [67]. Additionally, optical filters working based on strain-induced tuning require piezoelectric actuators which are driven by high voltages, resulting in bulky and costly devices [67].

Alternatively, phase-shifted FBG devices operated in transmission have been designed to achieve ultra-narrow-bandwidth (<1 GHz) optical filters [101]. The phase-shift is realized by shifting the grating as much as half a period, in its center, during the fabrication process. As illustrated in Figure 1-19, the drawback of this scheme is that the spectral width of the signal to be filtered should be smaller than the overall reflection bandwidth of the grating, which is typically limited to several tens of GHz [101]. Additionally, the operation bandwidth of the filter can only be tuned over a very limited range.

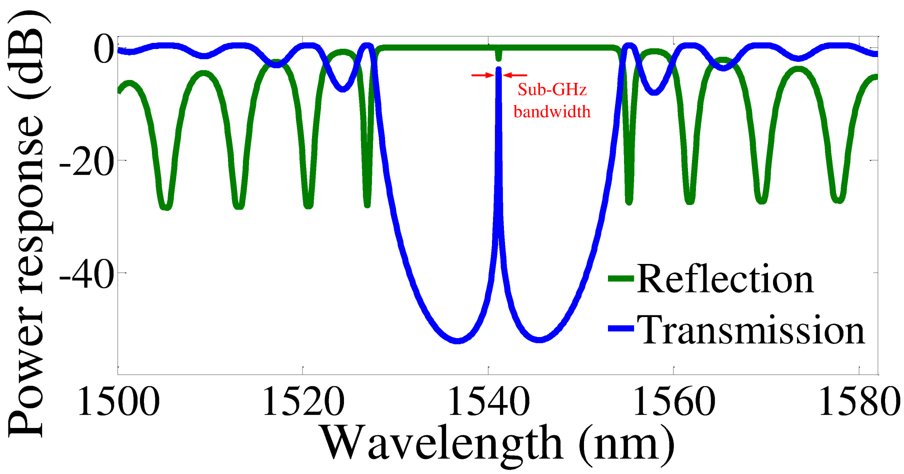

Figure 1-19 Spectral response of phase-shifted Bragg grating

1.3.2.3 Integrated waveguide grating-based filters

A similar operation principle to that of a DG has been used for on-chip filtering applications using an AWG [102]. As illustrated in

Figure 1-20, an AWG consists of two slab-waveguide star couplers, connected by a dispersive waveguide array. The star couplers are used in applications that require multiple ports (input and/or output). These couplers will distribute optical power equally from one or more input ports to two or more output ports.

AWGs have been fabricated using silica [103], InP/InGaAsP [102], silicon rib [104] and strip waveguides [105]. To the best of author's knowledge, the best performance reported so far for an AWG on SOI is a 512-channel device with 25 GHz channel spacing [104].

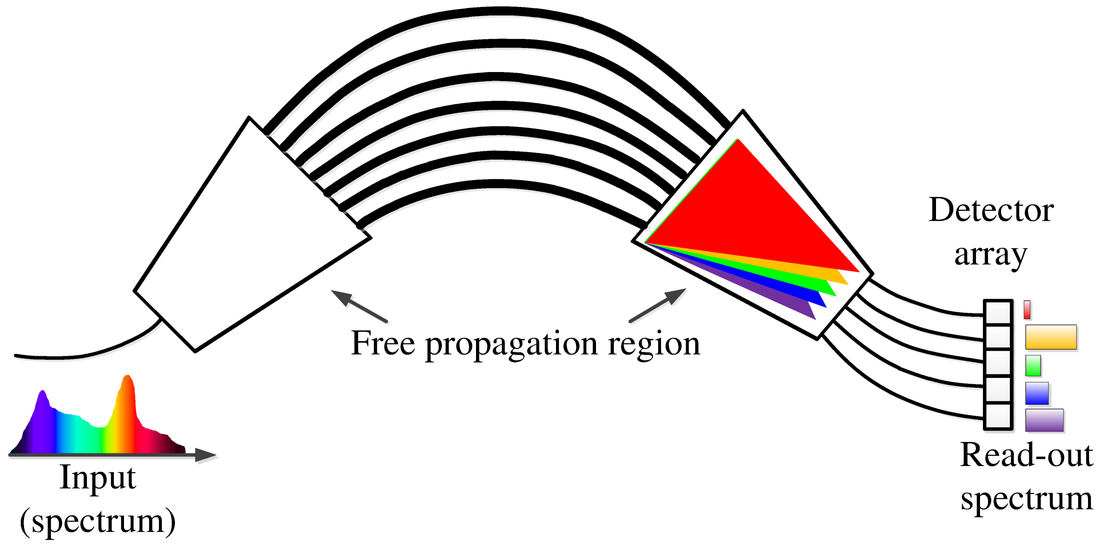

Figure 1-20 Schematic of an AWG and its operation principle.

Some of the difficulties associated with using AWGs for tunable optical filtering are as follows:

- Coupling from the slab waveguide to the waveguide array is the most significant source of loss in an AWG, because of the mismatch between the field distributions of the slab waveguide and the arrayed waveguides.
- One of the difficulties in large-scale AWGs is crosstalk deterioration caused by phase errors arising from variations in the arrayed waveguide width, thickness, material composition, and stress. Because the influence of such errors increases with the size of the waveguide array, the effect can be severe for densely spaced AWGs.
- Effective index birefringence in the arrayed waveguides may produce a polarization-dependent shift in the filter's defined central wavelength.
- The AWG's central wavelength changes with temperature. Active temperature stabilization by a heater is often used, but it requires continuous power consumption of several watts and temperature control electronics [106].
- A typical AWG has a symmetric intensity distribution across the waveguide array, and as such its chromatic dispersion is negligible. However, in a practical AWG this symmetry is disturbed by phase and amplitude errors that are randomly distributed in the arrayed waveguides. This increases chromatic dispersion. Because the errors increase with decreasing channel separation, the chromatic dispersion increases similarly.

Integrated waveguide BGs fabricated on SOI technology platform have also been implemented for tunable optical filtering applications [107]. In particular, J. St-Yves et al. have recently proposed an integrated waveguide BG-based filter that consists of a pair of cascaded contra-directional couplers (DCs), each operating as a drop filter (Contra-DCs are grating assisted add-drop filters) [96]. Analogous to waveguide BGs, the wavelength selectivity in contra-DCs is based on periodic dielectric perturbations. However, instead of back reflections in the same waveguide, the selected wavelength is dropped to another waveguide through contra-directional coupling. This allows add-drop operation without the need of a circulator.

As illustrated in Figure 1-21, the drop port of the first contra-DC is connected to the input port of the second contra-DC. Therefore, the final response at the drop port of the second contra-DC is determined by the product of the drop-port transfer functions of the two contra-DCs. Assuming the two filters are identical, the spectral response of the device is a well-defined transmission window. By changing the temperature of a single filter, the bandwidth of the finally dropped signal can be adjusted by detuning the center wavelengths of the two contra-DCs [96].

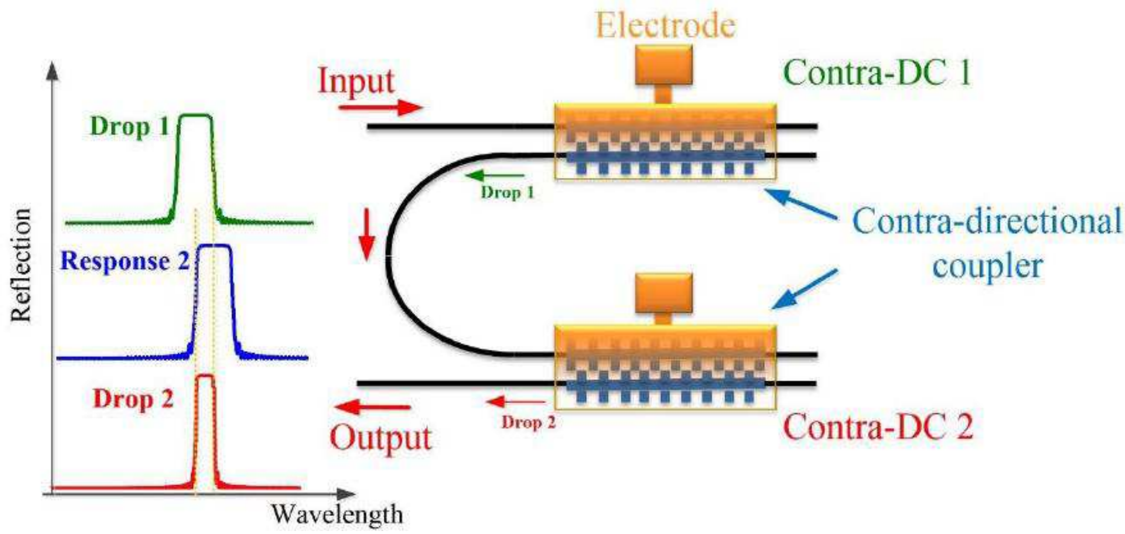

Figure 1-21 Schematic of the device. The dropped wavelength of the first contra-DC is re-filtered in an identical component. Both contra-DCs are temperature controlled with metal heaters.

Based on this scheme an integrated band-pass filter with the bandwidth continuously tuned across 670 GHz (117–788 GHz) has been experimentally demonstrated. The filter also features simultaneous bandwidth and central frequency tuning with and an unlimited FSR. Besides, an extinction ratio of up to 55 dB, low in-band ripples of less than 0.3 dB, and in-band group delay variation of less than 8 ps has been measured for this device [96].

Despite the wide range of tunability offered by this device, the phase profile of the signal to be filtered will be strongly affected by the group delay ripples of the BGs.

1.3.3 Optical signal characterization

Accurate measurement and characterization of ultrafast optical signals, with time resolutions down to the femtosecond regime, has a wide range of applications in physics, chemistry, microwave engineering and telecommunications [53, 108, 109]. Numerous optical pulse characterization techniques have been developed over the years offering different set of performance specifications. The focus of this Thesis is on techniques adapted to the problem of full characterization of the optical data signals typically found in fiber-optics telecommunication or information processing systems, namely, ultra-short light pulses or optical data streams in which information is encoded on an optical carrier from a laser source. Ideally, in fiber-optics telecommunication and information processing systems, one needs to have the ability to characterize low-intensity (with sub-milliwatt average powers), and high-speed (GHz-rate) optical signals, preferably using a fiber-optics or an integrated-waveguide measurement platform. Considering that information data signals are generally random (i.e. non repetitive), real-time measurements in a single-shot are also necessary. Finally, self-referenced techniques are of great interest as they bypass the need for a well-characterized reference pulse or local oscillator [110, 111, 62]. Moreover, the ability to measure optical time-domain phase information is becoming increasingly important in optical telecommunications. The reason is the trend towards increasing data transmission rates over fiber-optics telecommunication system by implementing complex modulation formats, e.g., phase-shift-keying [112].

In practice, conventional square-law photo-detectors can be only used to characterize the intensity of optical signals with a spectral bandwidth typically smaller than ~50 GHz. This is useful for per-channel data stream measurement in telecommunication systems based on dense wavelength-division multiplexing (DWDM) formats where the signal bandwidth is limited to 50-GHz and below. However, photo-detection provides information only on the temporal intensity profile of the signals under test. Consequently, several techniques have been developed during years to completely characterize the intensity and phase of optical data streams or ultra-short optical pulses in time and/or frequency-domains. These techniques can be categorized into two main groups, 1) nonlinear-optics based and 2) linear-optics based methods.

1.3.3.1 Nonlinear-optics based characterization techniques

Some popular optical pulse characterization methods include FROG (Frequency-Resolved Optical Gating) [108, 113], and SPIDER (Spectral Phase Interferometry for Direct Electric-Field Reconstruction) [114], and any of their multiple variants.

FROG is a spectrally resolved autocorrelation technique, first introduced in 1991 by Kane and Trebino [113]. FROG involves time-gating the pulse with itself, as in autocorrelation, but now measuring the spectrum versus the delay between the two pulses (a nonlinear medium is required to perform autocorrelation). The resulting trace of intensity versus frequency and delay is related to the pulse's spectrogram[4], a visually intuitive transform containing both time and frequency information (time-dependent spectrum). Finally, an iterative retrieval algorithm is used to characterize the temporal intensity and phase profiles of the pulse from the recorded spectrogram. It is worth noting that the temporal resolution of FROG is limited only by the response of the nonlinear medium. The schematic of a typical second harmonic generation (SHG)-FROG system is shown in Figure 1-22.

---

[4] The basic function of a spectrometer is to take in light, break it into its spectral components, digitize the signal as a function of wavelength, and read it out and display it through a computer. The first step in this process is to direct light into the spectrometer through a narrow aperture known as an entrance slit. The slit vignettes the light as it enters the spectrometer. In most spectrometers, the divergent light is then collimated by a concave mirror and directed onto a diffraction grating. The grating then disperses the spectral components of the light at slightly varying angles, which is then focused by a second concave mirror and imaged onto the detector. Alternatively, a concave holographic grating can be used to perform all three of these functions simultaneously.

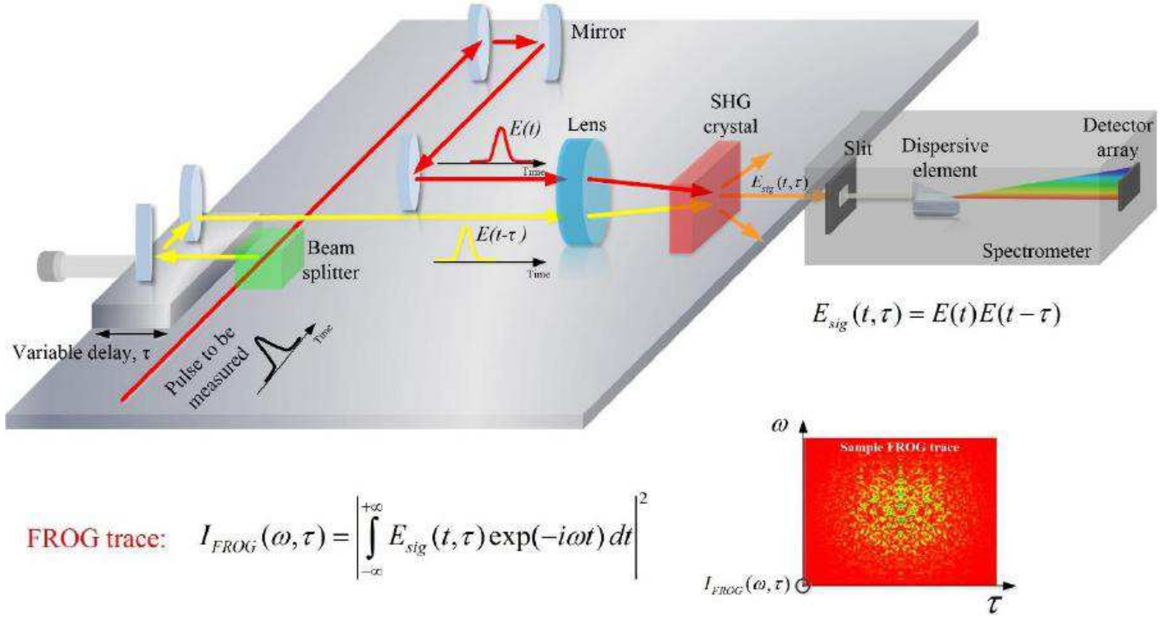

Figure 1-22 Schematic of SHG-FROG experimental setup (E(t) : envelope of complex electric field) [113].

SPIDER makes use of a spectral interferogram generated by interference of two replicas of the pulse under test [114]. The two pulses are identical with the exception that they are shifted in frequency with respect to each other. In the most conventional scheme, the replicas of the pulse to be characterized, which are separated in time by a fixed delay τ, are mixed with a frequency-chirped pulse in a $\chi^{(2)}$ nonlinear crystal. The replicas of the test pulse can be generated by a Michelson interferometer (MI). Besides, a grating compressor or dispersive element can be used to generate the needed frequency-chirped pulse from a portion of the test pulse itself (the stretched pulse must be highly chirped such that each frequency occurs at a different time). These pulses are up-converted[5] in a nonlinear medium. As the pulses in the test pair are delayed with respect to each other by τ, each is mixed with a different temporal, and hence spectral, slice of the stretched pulse. The result is a pair of replicas of the pulse under test that have been frequency shifted and are spectrally sheared by Ω. The frequency converted pulse pair is passed to a spectrometer[6] and the

[5] When two pulses, with two different carrier frequencies f_1 and f_2, are combined in a nonlinear signal-processing device, usually called a *mixer*, two new signals, one at the sum $f_1 + f_2$ of the two frequencies, and the other at the difference $f_1 - f_2$. The latter is called down-converted and the former is called up-coverted signal.

spectral interferogram is recorded with a slow detector. Because the interferogram contains spectral fringes with a period of roughly τ^{-1}, one is able to employ a robust non-iterative phase retrieval procedure to extract the phase information from the data by a series of linear transformations. The schematic of a typical SPIDER experimental setup is shown in Figure 1-23.

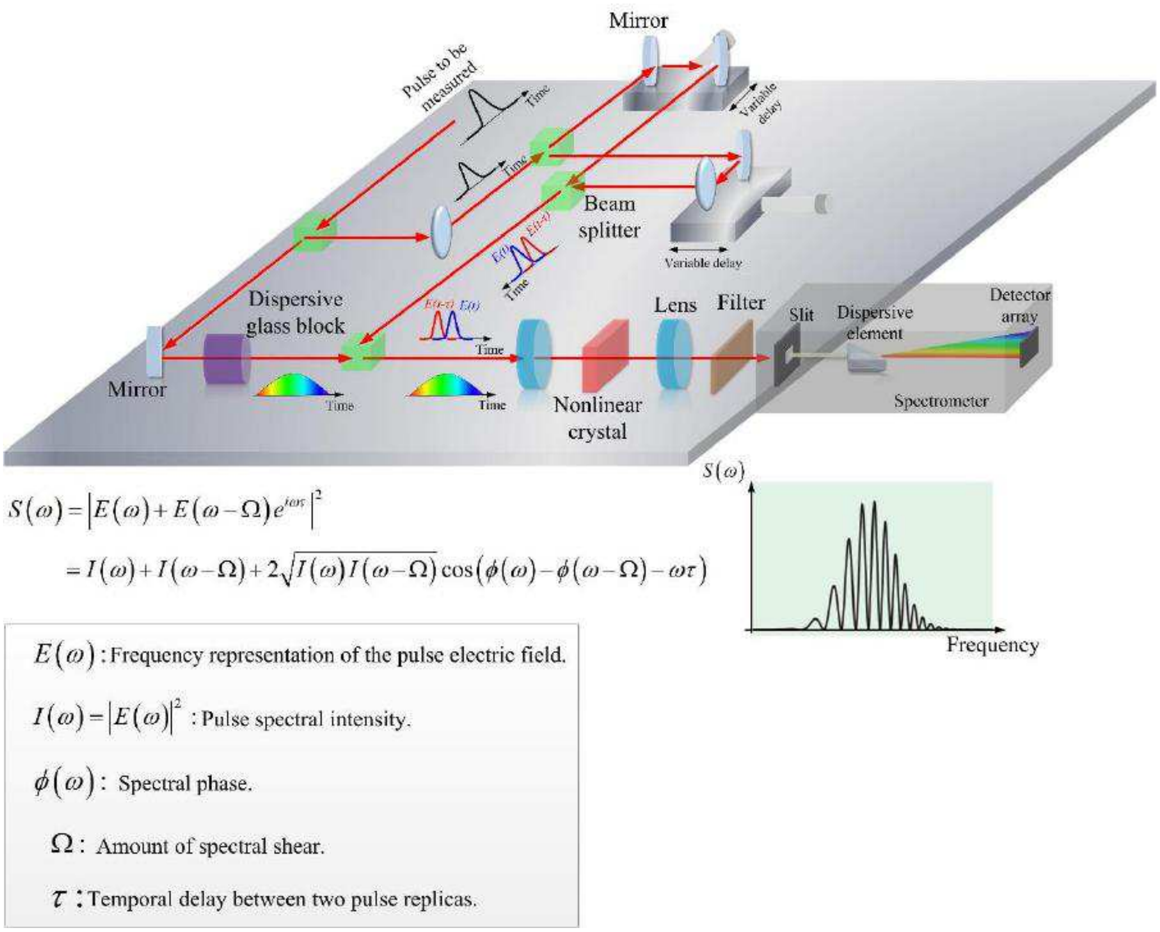

Figure 1-23 Basic schematic of SPIDER [115].

The aforementioned techniques (i.e., FROG and SPIDER) have been traditionally implemented using optical non-linearities in a variety of material or waveguide technologies. Because of the high power required in nonlinear methods they cannot easily satisfy the requirements for application in optical telecommunications [116, 117]. As a relevant example, a 45-cm long spiral waveguide made on high index doped silica glass has been used for both amplitude and phase characterization of ultrafast optical pulses with the aid of a synchronized incoherently related clock pulse [25]. The method is based on a variation of SPIDER that exploits degenerate FWM in a CMOS-compatible chip. Implementing this technique optical pulses with a frequency bandwidth of >1 THz, and up to

100 ps pulse widths, have been characterized, yielding a time–bandwidth product of >100. However, optical pulses with peak power of ~100 mW were required for successful implementation of SPIDER.

1.3.3.1 Linear-optics based characterization techniques

Significant effort has been put toward developing techniques based on linear effects. It is worth noting that as compared with more conventional nonlinear-optics techniques, linear-optics methods offer an increased sensitivity. Besides, they can be implemented in very simple and practical (e.g. fiber-based or integrated waveguide-based) platforms. Recent demonstrations include linear implementations of concepts previously proved with nonlinear processes (i.e. spectrography [118, 119] and spectral self-interferometry [120, 121]) and fundamentally new linear optics measurement schemes [122, 123, 124, 125]. A very relevant example is the implementation of SPIDER based on linear temporal phase modulation [126]. Spectral shift, required in SPIDER technique, can be obtained directly by linear temporal phase modulation. In particular, a linear temporal phase modulation $\exp(i\Omega t)$ directly induces a spectral shear on an optical pulse, provided that the temporal phase modulation is linear over the temporal duration of the pulse. In practice two copies of the pulse under test, generated using a MZI, can be spectrally sheared by a phase modulator driven by a sinusoidal radio frequency (RF) signal. The temporal phase can be linearized around one of the zero crossings of the sinusoid, which identifies the induced spectral shear. This is naturally obtained by sending two pulses separated by a delay τ in a phase modulator driven by a sinusoidal drive with a period equal to 2τ [126].

This is a highly sensitive method such that signals with average powers in the order of ~1 μW can be accurately characterized using this technique. However, the relative shear must be of the order of a few percent of the bandwidth of the signal under test which is difficult to achieve for signals with relatively large frequency bandwidths.

Coherent detection is one of the linear techniques most widely used to extract the phase information of an optical signal. In principle a coherent receiver is an interferometer-based structure combined with balanced photo-detection [127]. In this technique a local oscillator (LO) needs to be mixed with the signal under test in order to demodulate this signal. However, the mixing product is not obtained by mixing the signal and LO wave in a nonlinear crystal, but rather simply by detecting the linearly superimposed waves with a square-law photodetector. In case the LO and the carrier of optical data signals are at the same frequency the detection system is called homodyne and the resulting mixed signal is intrinsically down-converted to the baseband; in contrast, in an heterodyne detection scheme, the signal and LO have different frequencies. Consequently, the mixed signal at the photodetector is located around the so-called intermediate frequency (IF), so that an electronic LO is required to down-convert the signal to baseband. Both implementations are shown in Figure 1-24.

The advantage of heterodyne detector is that it uses only one balanced photodetector. However, the balanced photodetector should have a bandwidth at least twice the bandwidth of that of a homodyne detector [127].

Coherent detection requires the receiver to have knowledge of the carrier phase, as the received signal is demodulated by a LO that serves as an absolute phase reference. A key drawback related to this technique is that a given setup only works for a specific modulation format and at a prescribed bitrate.

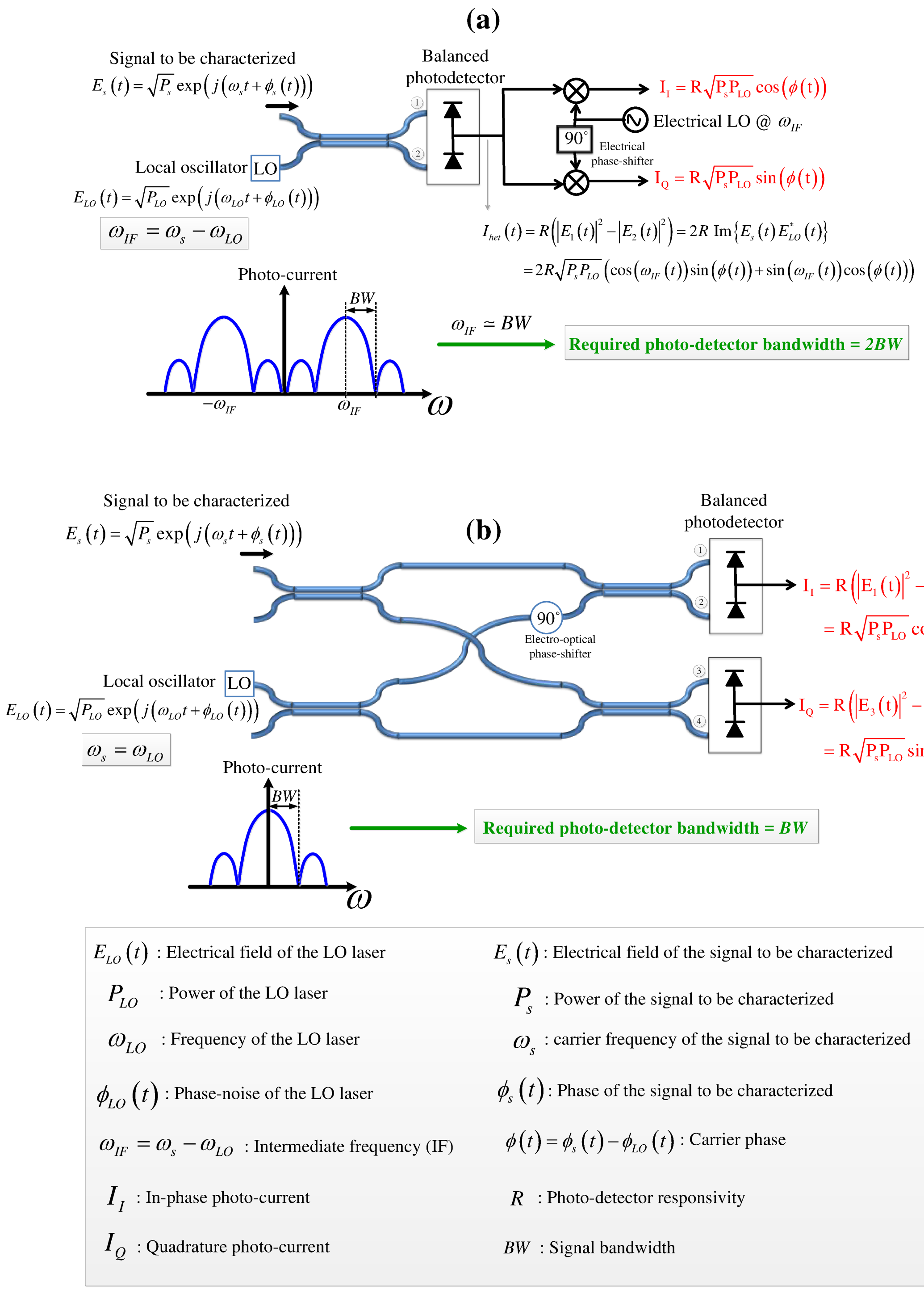

Figure 1-24 Single polarization down-convertor employing (a) heterodyne and (b) homodyne design [127].

A variety of methods have been explored in order to further extend the operation capabilities of the coherent detection technique. Among others, N. K. Fontaine et al [128], developed a new technique which combines the spectral slicing method with parallel optical homodyne detection, using a well-characterized optical frequency comb as the reference. The concept of spectral slicing is similar to bandwidth interleaving or frequency interleaving mostly used in some high-speed digitizers. In practice, spectral slicing is carried out by implementing an optical demultiplexer to select and separate different slices (frequency bandwidth) from the spectrum of the pulse to be characterized. These slices are then each combined with a single reference comb line in the receiver. Finally, all the down-converted frequency slices will be processed by a digital signal processing (DSP) unit to extract the intensity and phase profile of the signal under test. Through this method, arbitrary phase variations could be characterized with unprecedented time-bandwidth-product, both high operation bandwidth in the tens of GHz range and record time in the micro-second regime [128]. However, this method requires again a precisely synchronized optical reference. Moreover, a balanced photo-detector and one channel of a high speed digitizer were needed to characterize each slice of the spectrum. Consequently, scaling this method for characterization of THz bandwidth signals would be quite challenging.

Despite the great set of advantages offered by the coherent characterization methods, self-referenced pulse characterization techniques based on linear optics have been also developed to bypass the need for an stable, precisely synchronized LO [121, 129]. A relevant example is PROUD (Phase Reconstruction using Optical Ultrafast Differentiation), a self-referenced, linear method for phase reconstruction based on intensity measurements only [130, 131, 132, 133, 134, 135]. PROUD is particularly well adapted to the problem of signal characterization in the context of optical telecommunications. This technique can be used for full characterization of optical signals, over a very wide range of pulse time durations, from ~100 fs to well in the nanosecond regime [130, 131, 132]. Moreover single-shot and real-time measurements with power sensitivities down to the microwatt level have been demonstrated using this technique [133, 134, 135]. Besides, this method can be implemented using off-the-shelf components, resulting in very simple setups. In its most basic implementation, ***time-domain PROUD*** [130, 131, 132], the temporal phase profile of an optical signal can be recovered from two time-domain intensity measurements, namely the intensity profile of the signal under test and that of the resulting signal following photonic temporal differentiation, using a non-iterative algorithm (see Figure 1-25). The use of a non-iterative phase recovery numerical algorithm is a way to achieve single-shot and real-time signal characterization.

A photonic temporal differentiator in PROUD, also called a photonic frequency discriminator, is a linear optical filter with linear amplitude spectral response capable of providing the time derivative of the temporal complex envelope of an incoming optical signal [136, 137]. This functionality can be realized using a fiber/integrated waveguide LPG [138], a phase-shifted BG [139], or a Mach–Zehnder interferometer (MZI) [140].

Time-domain PROUD enables full characterization of a signal's temporal phase profile using conventional photo-detection followed by a numerical temporal integration.

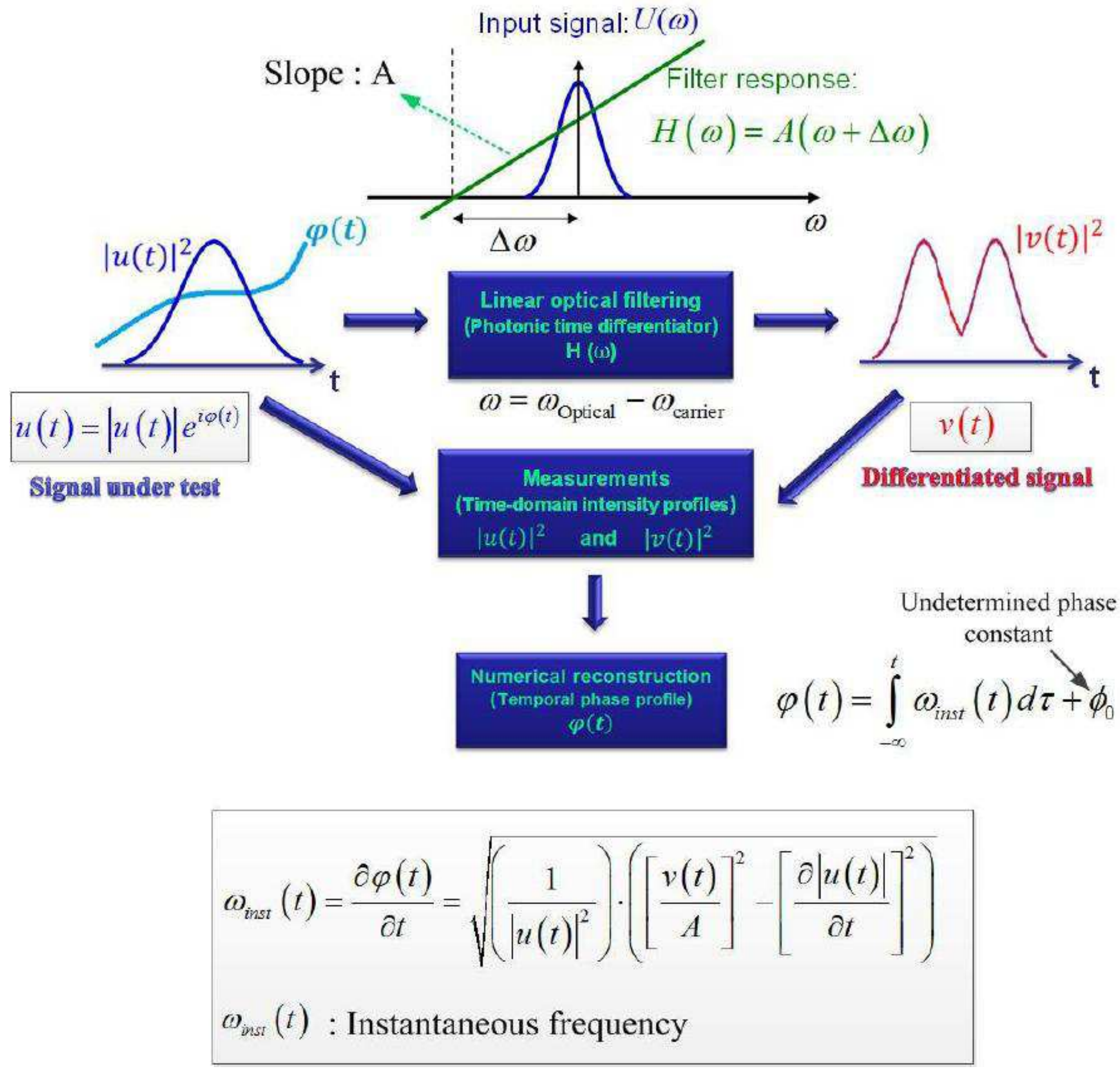

Figure 1-25 Schematic of the concept for time-domain phase reconstruction based on optical ultrafast differentiation (PROUD) [141].

In practice, the performance of time-domain PROUD is limited by the operation bandwidth (or speed) of the photodetector. However dispersion-induced time stretching incorporated into the time-domain PROUD setup extends the operation bandwidth of this method for characterization of optical pulse waveforms with durations ranging from sub- picoseconds to a few nanoseconds [132].

Briefly, a frequency-counterpart of the time-domain PROUD concept has been also proposed in order to characterize THz bandwidth pulses. This method is well suited for full characterization of optical pulse waveforms with time features in the picosecond and sub-picosecond range. Spectral PROUD can be realized by processing the signal under test with a photonic frequency differentiator, essentially temporal modulation with a linear amplitude ramp-like drive signal [131]. Note that in this Thesis we focus on time-domain PROUD.

Another time-domain implementation of PROUD is the balanced PROUD scheme. This method has been previously proposed and experimentally demonstrated to achieve simultaneous, real-time and single-shot phase characterization of WDM signals using a single processing and detection platform. In particular, in the basic time-domain PROUD the numerical procedure of differentiation is extremely sensitive to the presence of noise in the intensity waveform of the signal under test; in addition, the optical differentiation process itself is a very noisy operation since a temporal differentiator significantly amplifies the high-frequency noise present in the signals under analysis. Therefore, balanced PROUD has been considered as a solution in order to tackle this important drawback. As illustrated in Figure 1-26, balanced PROUD works based on dual-balanced optical differentiation technique, where the differentiation operation consists of two linear-amplitude optical filters, namely frequency shifted optical differentiators, which provide spectral transfer functions that depend linearly on the frequency variable in such a way that the amplitude variation slopes of the two filters are identical in magnitude but with opposite signs. In the previous demonstration of this scheme [135], the linear optical filtering that is required for temporal differentiation has been implemented using a fiber-based MZI as the dual-balanced optical differentiator. This implementation is particularly interesting because the desired balanced transfer functions are directly obtained at the two outputs of the MZI. The two linear curves forming the spectral response (transfer function) of a MZI are considered identical around any given cross-point wavelength in an ideal case. Furthermore, since the respective spectral transfer functions repeat periodically along the optical spectrum with a period defined by its FSR, the same dual-balanced differentiation process may be simultaneously applied over many wavelength channels (equally spaced in frequency by the interferometer's FSR) for WDM signal analysis and characterization.

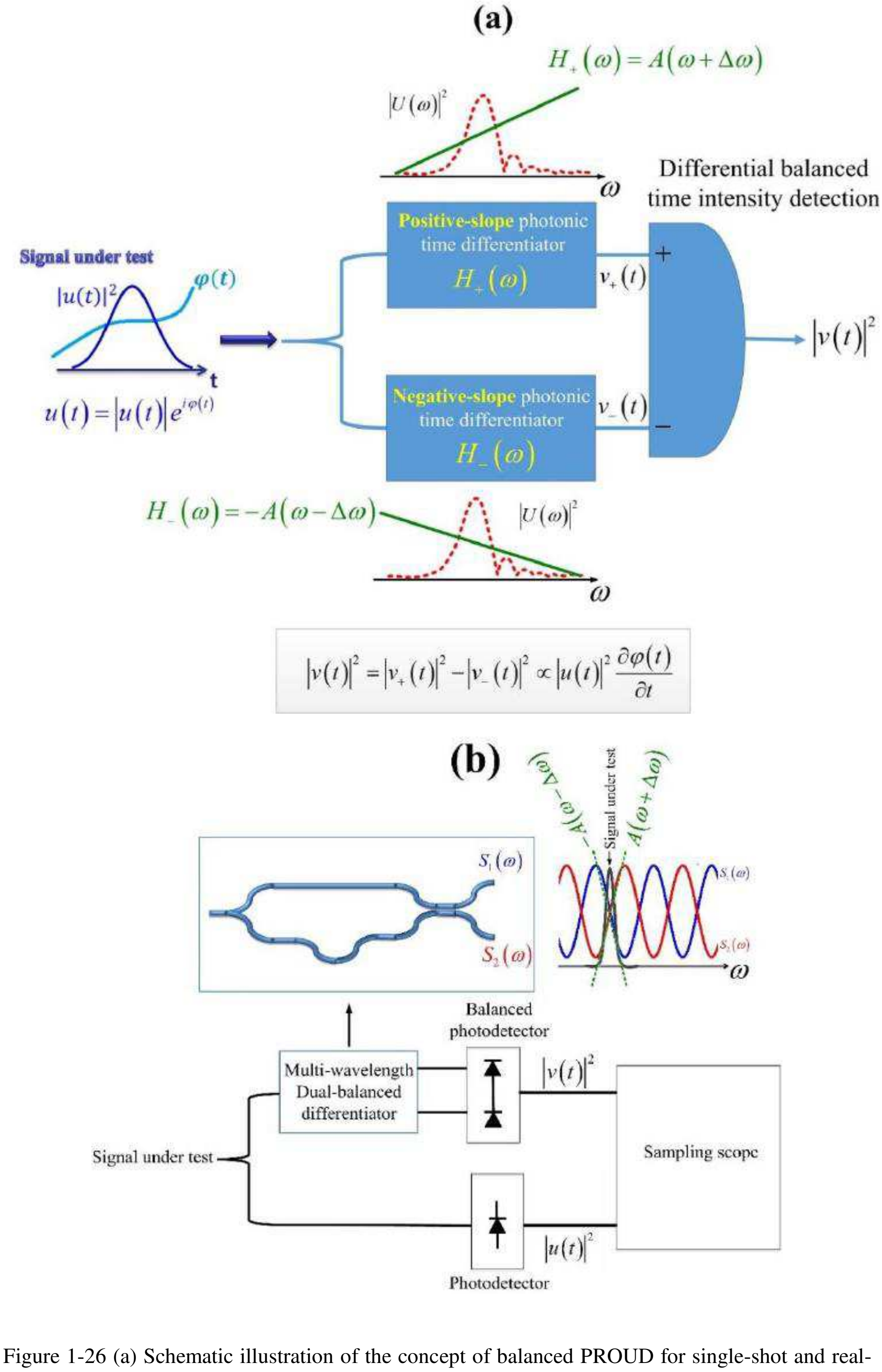

Figure 1-26 (a) Schematic illustration of the concept of balanced PROUD for single-shot and real-time optical signal characterization. (b) Principle of multi-wavelength balanced differentiation and experimental diagram for measuring the instantaneous frequencies [135].

As depicted in Figure 1-26, the two outputs of the interferometer are sent to a balanced photodetector in which the common terms cancel each other and only the desired instantaneous frequency information will remain. In other words, balancing the two output intensities followed by a subtraction operation enables a direct detection and visualization of the instantaneous frequency. One can directly obtain the desired instantaneous frequency information by simply dividing the balanced output signal by the input signal intensity. As the final step the signal phase can then be reconstructed by numerical cumulative integration of the obtained instantaneous frequency. It has been demonstrated that this scheme has the potential to provide the following crucial improvements: (i) direct detection of the signal's instantaneous frequency profile; (ii) ultra-high sensitivity to the signal's temporal phase variation; and (iii) instantaneous (non-sequential) information detection [135].

A main drawback of previously proposed time-domain balanced PROUD implementations for single-shot and real-time temporal phase recovery was the requirement of a complex scheme using two perfectly complementary linear optical filters, balanced photo-detection and a water-cooling system aimed at stabilizing the fiber interferometer [134]. As a result, single-shot and real-time phase recovery could be demonstrated only on relatively simple optical waveform variations, particularly a chirped 1-GHz sinusoid intensity-modulated signal and a 3-Gbps PRBS (pseudo-random binary sequence) phase-modulated signal, i.e., with only two phase-modulation levels (0 and π). Albeit, we anticipate an implementation of this technique in integrated waveguide technology will help to resolve these limitations

1.4 Original contributions

In what follows a brief introduction to the main outcome of my Thesis work, presented in sub-sequent chapters, is given. In particular, my contributions to tackle the problems stated in section (1.3), for on-chip optical pulse shaping, processing and measurement are briefly outlined.

1.4.1 Optical pulse shaping (OPS)

The second chapter of this PhD Thesis focuses on the development of new integrated waveguide-based solution to tackle the drawbacks of previously proposed OPS methods, namely, 1) the operation bandwidth limitation associated with the use of conventional electronics-based pulse shapers [39], 2) complexities associated with the use of bulk-optics components for OPS, e.g., bulk optics diffraction gratings, spatial light modulators etc [30], 3) the design challenges associated with the use of indirect frequency-domain pulse shaping methods [53, 30] and 4) the bandwidth limitation associated with BG-based optical pulse shapers, limited by the achievable spatial resolution of present grating fabrication technologies [59, 58].

Our relevant contributions include the following:

- Proposal and theoretical development of an OPS method based on discrete space-to-time mapping in cascaded co-directional couplers. Precise modelling of the proposed scheme has been carried out for its on-chip implementation [142, 143].

- Experimental demonstration of sub-picosecond OPS on an SOI technology platform, based on discrete space-to-time mapping. In this work, we have achieved sub-picosecond intensity-only and phase-only pulse shaping. In particular, flat-top pulses with duration ranging from 440-fs up to 3-ps, and an 8-bit 0.6-Tbit/s phase-coded pulse sequence with 4 different phase levels have been successfully generated in a compact SOI chip [144, 145].

- Additionally, we have experimentally synthesized long duration intensity-only and complex modulated signals (simultaneous phase and intensity modulated signals). In particular, flat-top pulses with durations in the range of 70 ps, and a 40-ps-long 200-Gbaud 16-quadratute amplitude modulation (QAM) data sequence have been successfully generated using our proposed scheme, proving its unique capability in synthesizing optical pulses with durations from the femtosecond range up to tens of picoseconds [146].

1.4.2 Optical signal processing/filtering

The third chapter of this Thesis focuses on the development of a new integrated waveguide-based filtering device to overcome the performance limitations of previously proposed grating-based filtering methods, enabling, 1) realization of narrow-band (sub-GHz) tunable filters, 2) the capability of tuning both filter’s bandwidth and central frequency in an independent manner [88, 90], 3) non-dispersive operation, and 4) compactness.

Our relevant contributions include the following:

- Proposal and design of a tunable, nondispersive optical filter using photonic Hilbert transformation. In this work, we have proposed and numerically demonstrated a new design concept for implementing nondispersive complementary (band-pass/band-reject) optical filters with a wide range of bandwidth and frequency tunability. The device consists of two photonic Hilbert transformers incorporated into a Michelson interferometer. By controlling the central frequency of the Hilbert transformers with respect to each other, both the central frequency and the spectral width of the rejection/pass bands of the filter are proved to be tunable. In this project bandwidth tuning from 260 MHz to 60 GHz is numerically demonstrated using two readily feasible fiber Bragg grating-based PHTs. The designed filter offers a high extinction ratio between the pass band and rejection band (>20dB in the narrow-band filtering case) with a very sharp transition with a slope of 170 dB/GHz from rejection to pass band. [147, 148, 149].
- In the quest for high-quality photonic Hilbert transformers (PHTs) to realize the proposed filter design (above), we have proposed and experimentally demonstrated PHT designs based on laterally apodized waveguide Bragg grating on SOI. In this work high-performance photonic integer and fractional-order Hilbert transformers, with processing bandwidths above 750 GHz, have been experimentally realized [150].

1.4.3 Optical signal characterization

The fourth chapter of this PhD Thesis focuses on the development of a linear-optics integrated waveguide-based scheme to overcome the limitations of previously proposed optical signal characterization methods, namely, 1) requirement of high power optical signals in nonlinear optics-based techniques [108], 2) the need for a LO in coherent detection methods [151], 3) and the need for balanced photo-detection scheme in balanced PROUD scheme to achieve single-shot and real-time operation [134].Our contribution:

- Experimental demonstration of on-chip, single-shot characterization of GHz-rate complex optical signals. In this work, temporal phase reconstruction based on optical ultrafast differentiation (basic PROUS scheme) is implemented using an integrated-waveguide MZI to demonstrate self-referenced phase characterization of GHz-rate complex modulated signals (e.g., quadrature phase shift keying and amplitude phase shift keying modulation formats), through a single-shot and real-time technique. This method is transparent to both the modulation format and bitrate, limited only by the bandwidth capabilities of the temporal intensity measurement instrumentation, while avoiding the need for a reference signal (e.g., LO) [151].

The integrated-optics devices proposed and demonstrated in this Thesis open up potential new paths for further developments of ultrafast optical telecommunication devices, all-optical computing units, all-optical information processing and measurement sub-systems on silicon chips, compatible with CMOS fabrication platform. Note that details about the waveguide design are given in ***Appendix B***.

1.5 Thesis organization

Each chapter in this Thesis is centered on a different achievement of this PhD research, see Figure 1-27. One to three journal articles have been presented in each chapter. The articles begin with a brief review and discussion on the scientific background and state-of-the-art literature of the target concept. Then, the proposed solution and design specifications are presented. Finally, in articles including experimental demonstrations, the experimental results are provided, confirming the simulation results of the designed devices.

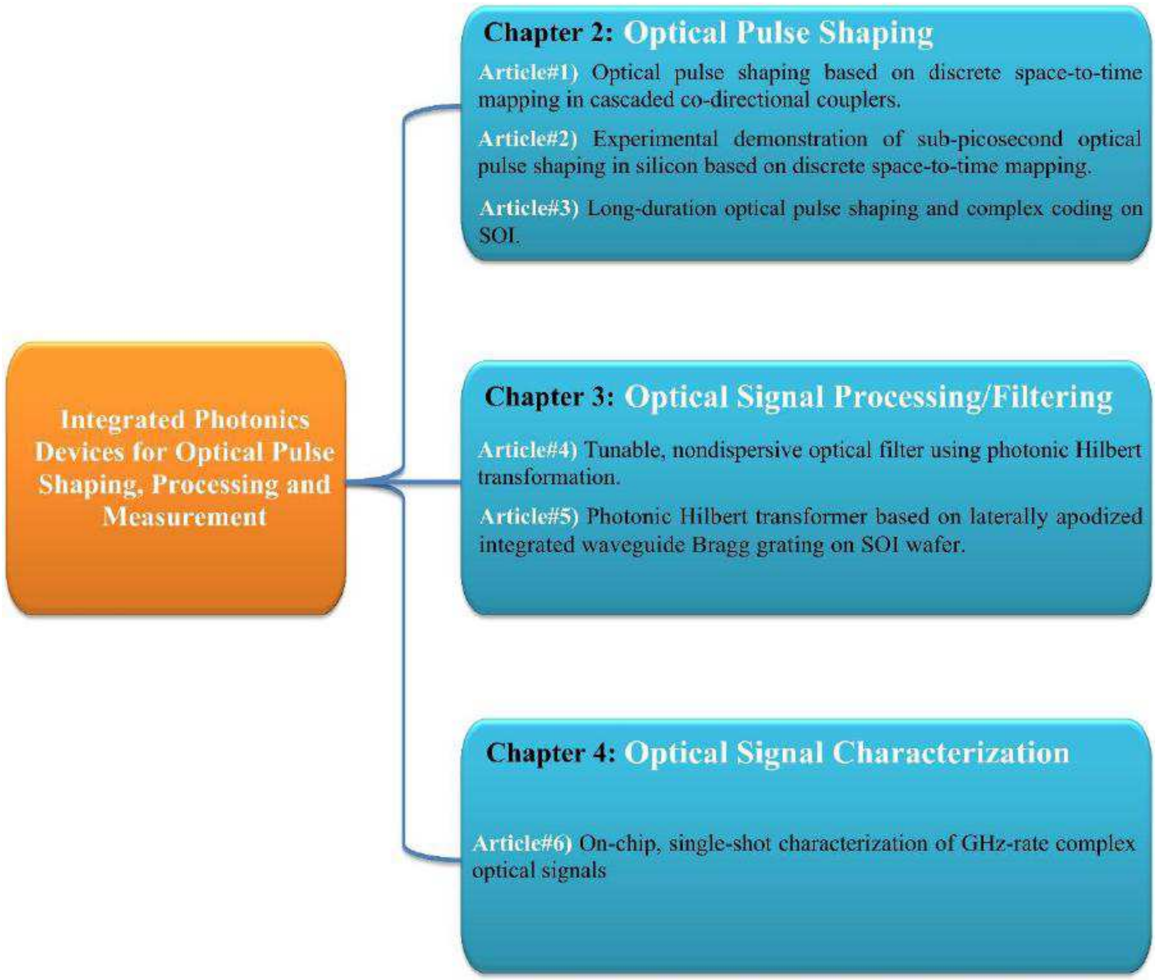

Figure 1-27 Organization of the Thesis.

In CHAPTER 2, the newly proposed direct time-domain OPS approach, namely discrete space-to-time mapping in cascaded co-directional couplers is proposed, numerically modelled and experimentally validated [142, 144, 146].

In CHAPTER 3, we address the proposal and design specifications of a bandwidth and central frequency tunable filter based on two photonic Hilbert transformers incorporated into a Michelson interferometer [149]. Additionally, we successfully design integer-order and fractional PHTs on SOI based on laterally apodized integrated Bragg gratings [152].

In CHAPTER 4, phase reconstruction based on optical ultrafast differentiation is implemented using an integrated-waveguide MZI to demonstrate self-referenced phase characterization of gigahertz-rate complex modulated signals (e.g., quadrature phase shift keying and amplitude phase shift keying modulation formats), through a single-shot and real-time technique. This method is transparent to both the modulation format and bit rate, limited only by the bandwidth capabilities of the temporal intensity measurement instrumentation [151].

Finally, CHAPTER 5 summarizes the work presented in this Thesis and proposes potential prospects for future work.

1.6 References

[1] P. J. Winzer, "Challenges and evolution of optical transport networks," in *36th European Conference on Optical Communication (ECOC 2010)*, Torino, 2010.

[2] N. S. Bergano, "Wavelength division multiplexing in long-haul transoceanic transmission systems," *Journal of Lightwave Technology,* vol. 23, no. 12, pp. 4125-4139, 2005.

[3] G. P. Agrawal, Fiber-optic communications systems, 3rd, Ed., John Wiley & sons, Inc., 2005.

[4] K. Kikuchi, "Coherent optical communications: Historical perspective and future directions," in *Optical and fiber communications reports*, M. Nakazawa, K. Kikuchi and T. Miyazaki, Eds., Springer, 2010.

[5] C. R. Doerr, "Silicon photonic integration in telecommunications," *Frontiers in Physics,* vol. 3, no. 37, pp. 1-16, 2015.

[6] R. A. Soref and B. R. Bennett, "Electro-optical effects in silicon," *IEEE Journal of Quantum Electronics,* vol. QE, no. 23, pp. 123-129, 1987.

[7] C. Tang, A. Kewell, G. Reed, A. Rickman and F. Namavar, "Development of a library of low-loss silicon-on-insulator optoelectronic devices," *IEE Proceedings Optoelectronics,* vol. 143, no. 5, pp. 312-315, 1996.

[8] P. C. Eng, S. Song and B. Ping, "State-of-the-art photodetectors for optoelectronic integration at telecommunication wavelength," *Nanophotonics,* vol. 4, no. 3, pp. 277-302, 2015.

[9] A. Liu, R. Jones, L. Liao, D. Samara-Rubio, D. Rubin, O. Cohen, R. Nicolaescu and M. Paniccia, "A high-speed silicon optical modulator based on a metal-oxide-semiconductor capacitor," *Nature,* vol. 427, pp. 615-618, 2004.

[10] B. Analui, D. Guckenberger, D. Kucharski and A. Narasimba, "A fully integrated 20Gb/s optoelectronic transceiver implemented in a standard 0.13 micron CMOS SOI technology," *IEEE Journal of Solid-State Circuits,* vol. 41, no. 12, pp. 2945-2955, 2006.

[11] 2014. [Online]. Available: http://www.wired.com/2014/07/ibm-3-billion/.

[12] M. C. Teich and B. Saleh, Fundamentals of photonics, New York: John Wiley & Sons, 1991.

[13] C. Monat, C. Grillet, M. Collins, A. Clark, J. Schroeder, C. Xiong, J. Li, L. O'Faolain, T. F. Krauss, B. J. Eggleton and D. J. Moss, "Integrated optical auto-correlator based on third-harmonic generation in a silicon photonic crystal waveguide," *Nature Communications,* vol. 5, pp. 1-20, 2014.

[14] C. Husko, T. D. Vo, B. Corcoran, J. Li, T. F. Krauss and B. J. Eggleton, "Ultracompact all-optical XOR logic gate in a slow-light silicon photonic crystal waveguide," *Optics Express,* vol. 19, no. 21, pp. 20681-20690, 2011.

[15] D. Vukovic, Y. Ding, H. Ou, L. K. Oxenløwe and C. Peucheret, "Polarization-insensitive wavelength conversion of 40 Gb/s NRZ-DPSK signals in a silicon polarization diversity circuit," *Optics Express,* vol. 22, no. 10, pp. 12467-12474, 2014.

[16] T. K. Liang and H. K. Tsang, "Role of free carriers from two-photon absorption in Raman amplification in silicon-on-insulator waveguides," *Applied Physics Letters,* vol. 84, no. 15, pp. 2745-2747, 2004.

[17] R. Claps, V. Raghunathan, D. Dimitropoulos and B. Jalali, "Influence of nonlinear absorption on Raman amplification in Silicon waveguides," *Optics Express,* vol. 12, no. 12, pp. 2774-2780, 2004.

[18] B. Jalali, "Silicon photonics: Nonlinear optics in the mid-infrared," *Nature Photonics,* vol. 4, pp. 506-508, 2010.

[19] F. Li, M. Pelusi, D.-X. Xu, R. Ma, S. Janz, B. J. Eggleton and D. J. Moss, "Silicon ring resonator based wavelength conversion via FWM at 10 Gb/s for differential phase-shift keyed signals," *Optics Express,* vol. 19, no. 23, pp. 22410-22416 , 2011.

[20] A. C. Turner, M. A. Foster, A. L. Gaeta and M. Lipson, "Ultra-low power parametric frequency conversion in a silicon microring resonator," *Optics Express,* vol. 16, no. 7, p. 4881–4887, 2008.

[21] R. Salem, M. A. Foster, A. C. Turner, D. F. Geraghty, M. Lipson and A. L. Gaeta, "All-optical regeneration on a silicon chip," *Optics Express,* vol. 15, no. 12, pp. 7802-7809, 2007.

[22] Z. Yin, J. Wu, J. Zang, D. Kong, J. Qiu, J. Shi, W. Li, S. Wei and J. Jintong Lin, "All-optical logic gate for XOR operation between 40-Gbaud QPSK tributaries in an ultra-short silicon nanowire," *IEEE Photonics Journal,* vol. 6, no. 3, pp. 1-8, 2014.

[23] S. Ayotte, S. Xu, H. Rong, O. Cohen and M. J. Paniccia, "Dispersion compensation by optical phase conjugation in silicon waveguide," *Electronics Letters,* vol. 43, no. 19, pp. 1-2, 2007.

[24] R. Salem, M. A. Foster, A. C. Turner, D. F. Geraghty, M. Lipson and A. L. Gaeta, "Optical time lens based on four-wave mixing on a silicon chip," *Optics Letters,* vol. 33, no. 10, pp. 1047-1049, 2008.

[25] A. Pasquazi, M. Peccianti, Y. Park, B. E. Little, S. T. Chu, R. Morandotti, J. Azana and D. J. Moss, "Sub-picosecond phase-sensitive optical pulse characterization on a chip," *Nature Photonics,* vol. 5, p. 618–623, 2011.

[26] A. V. Oppenheim, A. S. Willsky and S. H. Nawab, Signals and systems, 2 ed., Prentice-Hall, Inc. Upper Saddle River, NJ,, 1996.

[27] O. Wada, "Femtosecond all-optical devices for ultrafast communication and signal processing," *New Journal of Physics,* vol. 6, no. 1, pp. 183-218, 2004.

[28] J. Aracil, F. F. Callegati and V. Lopez, Enabling optical internet with advanced network technologies, J. Aracil and F. F. Callegati, Eds., Springer, 2009.

[29] J. Azaña, C. K. Madsen, K. Takiguchi and G. Cincontti, "Special issue on optical signal processing," *Journal of Lightwave Technology,* vol. 24, no. 7, pp. 2484-2767, 2006.

[30] A. M. Weiner, "Femtosecond optical pulse shaping and processing," *Progress in Quantum Electronics,* vol. 19, pp. 161-237, 1995.

[31] H. J. Song and T. Nagatsuma, "Present and future of terahertz communications," *IEEE Transactions on Terahertz Science and Technology,* vol. 1, no. 1, pp. 256-263, 2011.

[32] M. Yi, H. Kim, K. H. Jin, J. C. Ye and J. Ahn, "Terahertz substance imaging by waveform shaping," *Optics Express,* vol. 20, no. 18, pp. 20783-20789, 2012.

[33] M. C. Amann, T. Bosch, M. Lescure, R. Myllyla and M. Rioux, "Laser ranging: a critical review of usual techniques for distance measurement," *Optical Engineering,* vol. 40, no. 1, pp. 10-19, 2001.

[34] R. P. Prasankumar and A. J. Taylor, Eds., Optical techniques for solid-state materials characterization, Taylor & Francis, 2011.

[35] A. P. Zhang, S. Gao, G. Yan and Y. Bai, "Advances in optical fiber Bragg grating sensor technologies," *Photonic Sensors,* vol. 2, no. 1, pp. 1-13, 2012.

[36] D. R. Solli, J. Chou and B. Jalali, "Amplified wavelength–time transformation for real-time spectroscopy," *Nature Photonics,* vol. 2, pp. 48-51, 2008.

[37] L. Oxenlowe, R. Slavik, M. Galili, H. Mulvad, A. Clausen, Y. Park, J. Azana and P. Jeppesen, "640 Gb/s timing jitter-tolerant data processing using a long-period fiber-grating-based flat-top pulse shaper," *IEEE Journal of Selected Topics in Quantum Electronics,* vol. 14, no. 3, pp. 566-572, 2008.

[38] T. L. Paoli and J. E. Ripper, "Direct modulation of semiconductor lasers," *Proceedings of the IEEE,* vol. 58, no. 10, pp. 1457-1465, 1970.

[39] S. L. Chuang, Physics of optoelectronic devices, John Wiley & Sons Inc., 1995.

[40] 2016. [Online]. Available: http://www.tek.com/signal-generator/awg7000-arbitrary-waveform-generator.

[41] J. H. Lee, L. K. Oxenløwe, M. Ibsen, K. S. Berg, A. T. Clausen, D. J. Richardson and P. Jeppesen, "All-optical TDM data demultiplexing at 80 Gb/s with significant timing jitter tolerance using a fiber Bragg grating based rectangular pulse switching technology," *Journal of Lightwave Technology,* vol. 21, no. 11, pp. 2518-2523, 2003.

[42] B. Dai, Z. Gao, X. Wang, H. Chen, N. Kataoka and N. Wada, "Generation of versatile waveforms from CW light using a dual-drive mach-zehnder modulator and employing chromatic dispersion," *Journal of Lightwave Technology,* vol. 41, no. 1, pp. 145-151, 2013.

[43] F. Parmigiani, T. T. Ng, M. Ibsen, P. P. Petropoulos and D. J. Richardson, "Timing jitter tolerant all-optical TDM demultiplexing using a saw-tooth pulse shaper," *IEEE Photonics Technology Letters,* vol. 20, no. 23, pp. 1992-1994, 2008.

[44] F. Parmigiani, M. Ibsen, T. Ng, L. Provost, P. Petropoulos and D. Richardson, "An efficient wavelength converter exploiting a grating-based saw-tooth pulse shaper," *IEEE Photonics Technology Letters,* vol. 20, no. 17, pp. 1461-1463, 2008.

[45] F. Parmigiani, M. Ibsen, P. Petropoulos and D. Richardson, "Efficient all-optical wavelength-conversion scheme based on a saw-tooth pulse shaper," *IEEE Photonics Technology Letters,* vol. 21, no. 24, pp. 1837-1839, 2009.

[46] C. Finot, J. Dudley, B. Kibler, D. Richardson and G. Millot, "Optical parabolic pulse generation and applications," *IEEE Journal of Quantum Electronics,* vol. 45, no. 11, pp. 1482-1489, 2009.

[47] F. Parmigiani, C. Finot, K. Mukasa, M. Ibsen, M. A. F. Roelens, P. Petropoulos and D. J. Richardson, "Ultra-flat SPM-broadened spectra in a highly nonlinear fiber using parabolic pulses formed in a fiber Bragg grating," *Optics Express,* vol. 14, no. 17, pp. 7617-7622, 2006.

[48] X. Fang, D. N. Wang and S. Li, "Fiber Bragg grating for spectral phase optical code-division multiple-access encoding and decoding," *Journal of the Optical Society of America B,* vol. 20, no. 8, pp. 1603-1610, 2003.

[49] J. A. Salehi, A. M. Weiner and J. P. Heritage, "Coherent ultrashort light pulse code-division multiple access communication systems," *Journal of Lightwave Technology,* vol. 8, no. 3, pp. 478-491, 1990.

[50] Z. Jiang, D. S. Seo, S.-D. Yang, D. E. Leaird, R. V. Roussev, C. Langrock, M. M. Fejer and A. M. Weiner, "Four-user, 2.5-Gb/s, spectrally coded OCDMA system demonstration using low-power nonlinear processing," *Journal of Lightwave Technology,* vol. 23, no. 1, pp. 143-158, 2005.

[51] P. C. Teh, M. Ibsen, J. H. Lee, P. Petropoulos and D. J. Richardson, "Demonstration of a four-channel WDM/OCDMA system using 255-chip 320-Gchip/s quarternary phase coding gratings," *IEEE Photonics Technology Letters,* vol. 14, no. 2, pp. 227-229, 2002.

[52] X. Lu and R. T. Chen, "Polymeric optical code-division multiple-access (CDMA) encoder and decoder modules," *Polymers,* vol. 3, pp. 1554-1564, 2011.

[53] A. M. Weiner, Ultrafast Optics, G. Boreman, Ed., John Wiley & Sons, Inc., 2008.

[54] November 2015. [Online]. Available: https://www.finisar.com/optical-instrumentation.

[55] J. Chen, R. Broeke, Y. Du, J. Cao, N. Chubun, P. Bjeletich, F. Olsson, S. Lourdudoss, R. Welty, C. Reinhardt, P. Stephan and S. Yoo, "Monolithically integrated InP-based photonic chip development for O-CDMA systems," *IEEE Journal of Selected Topics in Quantum Electronics,* vol. 11, no. 1, pp. 66-77, 2005.

[56] D. Leaird, S. Shen, A. Weiner, A. Sugita, S. Kamei, M. Ishii and K. Okamoto, "Generation of high-repetition-rate WDM pulse trains from an arrayed-waveguide grating," *IEEE Photonics Technology Letters,* vol. 13, no. 3, pp. 221-223, 2001.

[57] B. Guan, S. S. Djordjevic, N. K. Fontaine, L. Zhou, S. Ibrahim, R. P. Scott, D. J. Geisler, Z. Ding and S. J. B. Yoo, "CMOS compatible reconfigurable silicon photonic lattice filters using cascaded unit cells for RF-photonic processing," *IEEE Journal of selected Topics in Quantum Electronics,* vol. 20, no. 4, pp. 1-10, 2014.

[58] M. H. Asghari, Ultrafast optical signal processing: devices and techniques, LAMBERT Academic Publishing, 2012.

[59] L. M. Rivas, M. J. Strain, D. Duchesne, A. Carballar, M. M. R. Sorel and J. Azaña, "Picosecond linear optical pulse shapers based on integrated waveguide Bragg gratings," *Optics Letters,* vol. 33, no. 21, pp. 2425-2427, 2008.

[60] Y. Park, M. Kulishov, R. Slavík and J. Azaña, "Picosecond and sub-picosecond flat-top pulse generation using uniform long-period fiber gratings," *Optics Express,* vol. 14, no. 26, pp. 12670-12678, 2006.

[61] M. Kulishov, D. Krcmarík and R. R. Slavík, "Design of terahertz-bandwidth arbitrary-order temporal differentiators based on long-period fiber gratings," *Optics Letters,* vol. 32, no. 20, pp. 2978-2980, 2007.

[62] N. K. Fontaine, R. P. Scott, J. P. Heritage and S. J. B. Yoo, "Near quantum-limited, single-shot coherent arbitrary optical waveform measurements," *Optics Express,* vol. 17, no. 15, pp. 12332-12344, 2009.

[63] N. K. Fontaine, D. J. Geisler, R. P. Scott, T. He, J. P. Heritage and S. J. B. Yoo, "Demonstration of high-fidelity dynamic optical arbitrary waveform generation," *Optics Express,* vol. 18, no. 22, pp. 22988-22995, 2010.

[64] S. Cheung, T. Su, K. Okamoto and S. J. B. Yoo, "Ultra-compact silicon photonics 512×512 25 GHz arrayed waveguide grating router," *IEEE Journal of Selected Topics in Quantum Electronics,* vol. 20, no. 4, pp. 1-7, 2013.

[65] W. Jiang, K. Okamoto, F. M. Soares, F. Olsson, S. Lourdudoss and S. J. B. Yoo, "5 GHz channel spacing InP-based 32-channel arrayed waveguide grating," in *Optical Fiber Communication Conference (OFC)*, San Diego, 2009.

[66] L. Chrostowski and M. Hochberg, Silicon Photonics Design Book-from Devices to Systems, Cambridge University press, 2011.

[67] R. Kashyap, Fiber Bragg gratings, London: Academic Press, 2009.

[68] T. Erdogan, "Fiber grating spectra," *Journal of Lightwave Technology,* vol. 15, no. 8, pp. 1277-1294, 1997.

[69] [Online]. Available: http://photonicssociety.org/newsletters/jun07/long_period.html.

[70] S. W. James and R. P. Tatam, "Optical fibre long-period grating sensors: characteristics and application," *Measurement Science and Technology,* vol. 14, no. 5, pp. R49-R61, 2003.

[71] A. M. Vengsarkar, J. R. Pedrazzani, J. B. Judkins, P. J. Lemaire, N. S. Bergano and C. R. Davidson, "Long period fiber-grating-based gain equalizer," *Optics Letters,* vol. 21, no. 5, pp. 336-338, 1996.

[72] S. Ghalmi, S. Ramachandran, E. Monberg, Z. Wang, M. F. Yan, F. V. Dimarcello, W. A. Reed, P. Wisk and J. Fleming, "Low loss, all-fiber high-order mode dispersion compensators for lumped or multi-span compensation," *Electronics Letters,* vol. 38, no. 24, p. 1507–1508, 2002.

[73] J. Skaar, L. Wang and T. Erdogan, "On the synthesis of fiber Bragg gratings by layer peeling," *IEEE Journal of Quantum Electronics,* vol. 37, no. 2, pp. 165-173, 2001.

[74] C. R. Raum, R. Gauthier and R. N. Tait, "Integrated heaters for the thermal tuning of Bragg grating filters on silicon-on-insulator rib waveguides," *Microwave and Optical Technology Letters,* vol. 53, no. 3, pp. 672-676, 2011.

[75] X. Wang, Y. Wang, J. Flueckiger, R. Bojko, A. Liu, A. Reid, J. Pond, N. A. F. Jaeger and L. Chrostowski, "Precise control of the coupling coefficient through destructive interference in silicon waveguide Bragg grating," *Optics Letters,* vol. 39, no. 19, pp. 5519-5522, 2014.

[76] J. Skaar, L. Wang and T. Erdogan, "On the synthesis of fiber Bragg gratings by layer peeling," *IEEE Journal of Quantum Electronics,* vol. 37, no. 2, pp. 165-173, 2001.

[77] M. H. Asghari and J. Azaña, "Proposal and analysis of a reconfigurable pulse shaping technique based on multi-arm optical differentiators," *Optics Communications,* vol. 281, no. 18, pp. 4581-4588, 2008.

[78] Y. Park, M. H. Asghari, T. J. Ahn and J. Azaña, "Transform-limited picosecond pulse shaping based on temporal coherence synthesization," *Optics Express,* vol. 15, no. 15, pp. 9584-9599, 2007.

[79] B. Colombeau, M. Vampouille and C. Froehly, "Shaping of short laser pulses by passive optical Fourier techniques," *Optics Communications,* vol. 19, no. 2, pp. 201-204, 1976.

[80] D. E. Leaird and A. M. Weiner, "Femtosecond direct space-to-time pulse shaping," *IEEE Journal of Quantum Electronics,* vol. 37, no. 4, pp. 494-504, 2001.

[81] D. E. Leaird and A. M. Weiner, "Femtosecond optical packet generation by a direct space-to-time pulse shaper," *Optics Letters,* vol. 24, no. 2, pp. 853-855, 1999.

[82] H. Kogelnik, "Filter response of nonuniform almost-periodic structures," *Bell System Technical Journal,* vol. 55, no. 1, pp. 109-126, 1976.

[83] J. Azaña and L. R. Chen, "Synthesis of temporal optical waveforms by fiber Bragg gratings: a new approach based on space-to-frequency-to-time mapping," *Journal of the Optical Society of America B,* vol. 19, no. 11, pp. 2758-2769, 2002.

[84] J. Azaña and L. R. Chen, "Synthesis of temporal optical waveforms using fiber Bragg gratings: A new approach based on space-to-frequency-to-time mapping," *Journal of the Optical Society of America B,* vol. 19, no. 11, pp. 2758-2769, 2002.

[85] R. Ashrafi, M. Li, N. Belhadj, M. Dastmalchi, S. LaRochelle and J. Azaña, "Experimental demonstration of superluminal space-to-time mapping in long period gratings," *Optics Letters,* vol. 38, no. 9, pp. 1419-1421, 2013.

[86] R. Ashrafi, M. Li, S. LaRochelle and J. Azaña, "Superluminal space-to-time mapping in grating-assisted co-directional couplers," *Optics Express,* vol. 21, no. 5, pp. 6249-6256, 2013.

[87] J. Yao, "Arbitrary waveform generation," *Nature Photonics,* vol. 4, pp. 79-80, 2010.

[88] C. F. R. Mateus, C.-H. Chang, L. Chrostowski, S. Yang, D. Sun, R. Pathak and C. J. Chang-Hasnain., "Widely tunable torsional optical filter," *IEEE Photonics Technology Letters,* vol. 14, no. 6, pp. 819-821, 2002.

[89] Y. Ding, M. Pu, L. Liu, J. Xu, C. Peucheret, X. Zhang, D. Huang and H. Ou., "Bandwidth and wavelength-tunable optical bandpass filter based on silicon microring-MZI structure," *Optics Express,* vol. 19, no. 7, pp. 6462-6470, 2011.

[90] H. J. Masterson, G. D. Sharp and K. M. Johnson., "Ferroelectric liquid-crystal tunable filter," *Optics Letters,* vol. 14, no. 22, pp. 1249-1251, 1989.

[91] D. Tripathi, j. Fei, R. Rafiei, K. Dilusha Silva, J. Antoszewski, M. Martyniuk, J. Dell and L. Faraone, "Suspended large-area MEMS-based optical filters for multispectral shortwave infrared imaging applications," *Journal of Microelectromechanical Systems,* vol. 24, no. 4, pp. 1102 - 1110, 2015.

[92] L. Bei, G. I. Dennis, H. M. Miller, T. W. Spaine and J. W. Carnahan, "Acousto-optic tunable filters: fundamentals and applications as applied to chemical analysis techniques," *Progress in Quantum Electronics,* vol. 28, no. 2, p. 67–87, 2004.

[93] L. Domash, M. Wu, N. Nemchuk and E. Ma, "Tunable and switchable multiple-cavity thin film filters," *Journal of Lightwave Technology,* vol. 22, no. 1, pp. 126-130, 2006.

[94] M. A. Kats, R. Blanchard, P. Genevet and F. Capasso, "Nanometre optical coatings based on strong interference effects in highly absorbing media," *Nature Materials,* vol. 12, p. 20–24, 2013.

[95] Y. Ningsi and R. Minasian, "A novel high-Q optical microwave processor using hybrid delay-line filters," *IEEE Transactions on Microwave Theory and Techniques,* vol. 47, no. 7, pp. 1304 - 1308, 1999.

[96] J. St-Yves, H. Bahrami, P. Jean, Larochelle, S. and W. Shi, "Widely bandwidth-tunable silicon filter with an unlimited free-spectral range," *Optics Letters,* vol. 40, no. 23, pp. 5471-5474, 2015.

[97] G. Wilson, C.-J. Chen, P. Gooding and J. E. Ford, "Spectral passband filter with independently variable center wavelength and bandwidth," *IEEE Photonics Technology Letters,* vol. 18, no. 15, pp. 1660-1662, 2006.

[98] 2015. [Online]. Available: http://www.santec.com/en/products/instruments/manualproducts/otf-350.

[99] C. S. Goh, S. Y. Set and K. Kikuchi, "Widely tunable optical filters based on fiber Bragg gratings," *IEEE Photonics Technology Letters,* vol. 14, no. 9, pp. 1306-1308, 2002.

[100] C. R. Raum, R. N. Tait and R. C. Gauthier, "Fabrication and characterization of a thermo-mechanically tunable grating-assisted suspended waveguide filter," *Proceedings SPIE,* vol. 6898, pp. 1-9, 2008.

[101] X. M. Liu, "A novel ultra-narrow transmission-band fiber Bragg grating and its application in a single-longitudinal-mode fiber laser with improved efficiency," *Optics Communications,* vol. 280, no. 1, pp. 147-152, 2007.

[102] F. Soares, N. Fontaine, R. Scott, J. Baek, X. Zhou, T. Su, S. Cheung, Y. Wang, C. Junesand, S. Lourdudoss, K. Liou, R. Hamm, W. Wang, B. Patel, L. Gruezke, W. Tsang, J. Heritage and S. Yoo, "Monolithic InP 100-channel x 10-GHz device for optical arbitrary waveform generation," *IEEE Photonics Journal,* vol. 3, no. 6, pp. 975-985, 2011.

[103] S. Kamei, M. shii, A. Kaneko, T. Shibata and M. Itoh, "NxN cyclic-frequency router with improved performance based on arrayed-waveguide grating," *Journal of Lightwave Technology,* vol. 27, no. 18, pp. 4097-4104, 2009.

[104] S. Cheung, T. Su, K. Okamoto and S. J. B. Yoo, "Ultra-compact silicon photonic 512 x 512 25 GHz arrayed waveguide grating router," *IEEE Journal of Selected Topics in Quantum Electronics,* vol. 20, no. 4, pp. 8202207-8202207, 2014.

[105] P. Cheben, J. H. Schmid, A. Delâge, A. Densmore, S. Janz, B. Lamontagne, J. Lapointe, E. Post, P. Waldron and D.-X. Xu, "A high-resolution silicon-on-insulator arrayed waveguide grating microspectrometer with sub-micrometer aperture waveguides," *Optics Express,* vol. 15, no. 5, pp. 2299-2306, 2007.

[106] K. Maru and Y. Abe, "Low-loss, flat-passband and athermal arrayed waveguide grating multi/demultiplexer," *Optics Express,* vol. 15, no. 26, pp. 18351-18356, 2007.

[107] J. Komma, C. Schwarz, G. Hofmann, D. Heinert and R. Nawrod, "Thermo-optic coefficient of silicon at 1550nm and cryogenic temperatures," *Applied Physics Letters,* vol. 101, pp. 041905-1-4, 2012.

[108] R. Trebino, frequency-resolved optical gatng: The measurement of ultrashort laser pulses, Springer Science & Business Media, 2002.

[109] C. Dorrer, "High-speed measurements for optical telecommunication systems," *IEEE Journal of Selected Topics in Quantum Electronics,* vol. 12, no. 4, pp. 843-858, 2006.

[110] L. Lepetit, G. Chériaux and M. Joffre, "Linear techniques of phase measurement by femtosecond spectral interferometry for applications in spectroscopy," *Journal of the Optical Society of America B,* vol. 12, no. 12, pp. 2467-2474, 1995.

[111] V. R. Supradeepa, D. E. Leaird and A. M. Weiner, "Single shot amplitude and phase characterization of optical arbitrary waveforms," *Optics Express,* vol. 17, no. 16, pp. 14434-14443, 2009.

[112] A. H. Gnauck and P. J. Winzer, "Optical phase-shift-keyed transmission," *Journal of Lightwave Technology,* vol. 23, no. 1, pp. 115-129, 2005.

[113] D. J. Kane and R. Trebino, "Single-shot measurement of the intensity and phase of an arbitrary ultrashort pulse by using frequency-resolved optical gating," *Optics letters,* vol. 18, no. 10, pp. 823-825, 1993.

[114] C. Laconis and l. A. Walmsley, "Spectral phase interferometry for direct electric-field reconstruction of ultrashort optical pulses," *Optics letters,* vol. 23, no. 10, pp. 792-794, 1998.

[115] M. Rhodes, M. Mukhopadhyay, J. Birge and R. Trebino, "Coherent artifact study of two-dimensional spectral shearing interferometry," *Journal of the Optical Society of America B,* vol. 32, no. 9, pp. 1881-1888, 2015.

[116] C. Dorrer and I. Kang, "Linear self-referencing techniques for short-optical-pulse characterization [Invited]," *Journal of the Optical Society of America B,* vol. 25, no. 6, pp. A1-A12, 2008.

[117] I. A. Walmsley and C. Dorrer, "Charaterization of ultrashort electromagnetic pulses," *Advances in Optics and Photonics,* vol. 1, no. 2, pp. 308-437, 2009.

[118] C. D. a. I. Kang, "Simultaneous temporal characterization of telecommunication optical pulses and modulators by use of spectrograms," *Optics Letters,* vol. 27, no. 15, pp. 1315-1317, 2002.

[119] D. Reid and J. Harvey, "Linear spectrograms using electrooptic modulators," *IEEE Photonics Technology Letters,* vol. 19, no. 8, pp. 535 - 537, 2007.

[120] C. D. a. I. Kang, "Complete temporal characterization of short optical pulses by simplified chronocyclic tomography," *Optics Letters,* vol. 28, no. 16, pp. 1481-1483, 2003.

[121] J. Bromage, C. Dorrer, I. A. Begishev, N. G. Usechak and J. D. Zuegel, "Highly sensitive, single-shot characterization for pulse widths from 0.4 to 85 ps using electro-optic shearing interferometry," *Optics Letters,* vol. 31, no. 23, pp. 3523-3525, 2006.

[122] P. Kockaert, J. Azaña, L. R. Chen and S. LaRochelle, "Full characterization of uniform ultrahigh-speed trains of optical pulses using fiber Bragg gratings and linear detectors," *IEEE Photonics Technology Letters,* vol. 16, no. 6, pp. 1540-1542, 2004.

[123] C. Dorrer, "Chromatic dispersion characterization by direct instantaneous frequency measurement," *Optics Letters,* vol. 29, no. 2, pp. 204-206, 2004.

[124] T. Ahn, Y. Park and J. Azaña, "Fast and accurate group delay ripple measurement technique for ultralong chirped fiber Bragg gratings," *Optics Letters,* vol. 32, no. 18, pp. 2674-2676, 2007.

[125] Y. Park, T. Ann and J. Azaña, "Real-time complex temporal response measurements of ultrahigh-speed optical modulators," *Optics Express,* vol. 17, no. 3, pp. 1734-1745, 2009.

[126] C. Dorrer and I. Kang, "Highly sensitive direct femtosecond pulse characterization using electro-optic spectral shearing interferometry," *Optics Letters,* vol. 28, no. 6, p. 477–479, 2003.

[127] E. Ip, A. P. T. Lau, D. J. F. Barros and J. M. Kahn, "Coherent detection in optical fiber systems," *Optics Express,* vol. 16, no. 2, pp. 753-791, 2007.

[128] N. K. Fontaine, R. P. Scott, L. Zhou, F. M. Soares and J. P. Heritage, "Real-time full-field arbitrary optical waveform measurement," *Nature Photonics,* vol. 4, no. 4, pp. 248-254, 2010.

[129] V. R. Supradeepa, C. M. Long, D. E. Leaird and A. M. Weiner, "Self-referenced characterization of optical frequency combs and arbitrary waveforms using a simple, linear, zero-delay implementation of spectral shearing interferometry," *Optics Express,* vol. 18, no. 17, pp. 18171-18179, 2010.

[130] F. Li, Y. Park and J. Azaña, "Complete temporal pulse characterization based on phase reconstruction using optical ultrafast differentiation (PROUD)," *Optics Letters,* vol. 32, no. 22, pp. 3364-3366, 2007.

[131] J. Azaña, Y. Park, T. Ahn and F. Li, "Simple and highly sensitive optical pulse-characterization method based on electro-optic spectral signal differentiation," *Optics Letters,* vol. 33, no. 5, pp. 437-439, 2008.

[132] F. Li, Y. Park and J. Azaña, "Linear characterization of optical pulses with durations ranging from the picosecond to the nanosecond regime using ultrafast photonic differentiation," *Journal of Lightwave Technology,* vol. 27, no. 21, pp. 4623-4633, 2009.

[133] F. Li, Y. Park and J. Azaña, "Single-shot real-time frequency chirp characterization of telecommunication optical signals based on balanced temporal optical differentiation," *Optics Letters,* vol. 34, no. 18, pp. 2742-2744, 2009.

[134] Y. Park, M. Scaffardi, L. Potì and J. Azaña, "Simultaneous single-shot real-time measurement of the instantaneous frequency and phase profiles of wavelength-division-multiplexed signals," *Optics Express,* vol. 18, no. 6, pp. 6220-6229, 2010.

[135] Y. Park, M. Scaffardi, A. Malacarne, L. Potì and J. Azaña, "Linear, self-referenced technique for single-shot and real-time full characterization of (sub-)picosecond optical pulses," *Optics Letters,* vol. 35, no. 15, pp. 2502-2504, 2010.

[136] J. Azaña, "Ultrafast analog all-optical signal processors based on fiber-grating devices," *IEEE Photonics Journal,* vol. 2, pp. 359-386, 2010.

[137] N. Q. Ngo, S. F. Yu, S. C. Tjin and C. H. Kam, "A new theoretical basis of higher-derivative optical differentiators," *Optics Communications,* vol. 230, pp. 115-129, 2004.

[138] R. Slavík, Y. Park, M. Kulishov, R. Morandotti and J. Azaña, "Ultrafast all-optical differentiators," *Optics Express,* vol. 14, no. 22, pp. 10699-10707, 2006.

[139] L.-M. Rivas, K. Singh, A. Carballar and J. Azaña., "Arbitrary-order ultra-broadband all-optical differentiators based on fiber Bragg gratings," *IEEE Photonic Technology Letters,* vol. 19, no. 16, pp. 1209-1211, 2007.

[140] Y. Park, T. Ahn and J. Azaña, "Stabilization of a fiber-optic two-arm interferometer for ultra-short pulse signal processing applications," *Applied Optics,* vol. 47, no. 3, pp. 417-421, 2008.

[141] J. Azaña, Y. Park and F. Li, "Linear self-referenced complex-field characterization of fast optical signals using photonic differentiation [invited]," *Optics Communications,* vol. 284, no. 15, pp. 3772-3784, 2011.

[142] H. P. Bazargani and J. Azaña, "Optical pulse shaping based on discrete space-to-time mapping in cascaded co-directional couplers," *Optics Express,* vol. 23, no. 18, pp. 5423-5426 , 2015.

[143] H. P. Bazargani, R. Ashrafi and J. Azaña, "Time-domain optical signal processing based on discrete space-to-time mapping in cascaded co-directional couplers," in *OSA Topical Meeting on Bragg Gratings, Photosensitivity and Poling in Glass Waveguides (BGPP 2014)*, Barcelona, 2014.

[144] H. P. Bazargani, M. Burla and J. Azaña, "Experimental demonstration of sub-picosecond optical pulse shaping in silicon based on discrete space-to-time mapping," *Optics Letters,* vol. 40, no. 23, pp. 5423-5426 , 2015.

[145] H. P. Bazargani, M. Burla and J. Azaña, "On-chip optical pulse shaping based on discrete space-to-time mapping in concatenated co-directional couplers," in *41st European Conference on Optical Communications (ECOC 2015)*, Valencia, 2015.

[146] H. P. Bazargani, M. Burla and J. Azaña, "Long-duration, picosecond optical pulse shaping on SOI using discrete space-to-time mapping," in *Conference on Lasers and Electro-optics (CLEO 2016)*, San Jose, CA, USA, 2016.

[147] H. P. Bazargani, M. R. Fernández-Ruiz and J. Azaña, "Bandwidth-tunable optical filters based on photonic Hilbert transformation," in *IEEE Photonics Conference (IPC 2013)*, Bellevue, 2013.

[148] H. P. Bazargani, M. R. Fernández-Ruiz and J. Azaña, "Tunable optical filter using photonic Hilbert transformation," in *OSA Topical Meeting on Signal Processing in Photonics Communications (SPPCom 2013)*, Rio Grande, 2013.

[149] H. P. Bazargani, M. R. Fernández-Ruiz and J. Azaña, "Tunable, nondispersive optical filter using photonic Hilbert transformation," *Optics Letters,* vol. 39, no. 17, pp. 5232-5235 , 2014.

[150] H. P. Bazargani, M. Burla and J. Azaña, "Photonic Hilbert transformer based on laterally apodized waveguide Bragg gratings on a SOI wafer," in *Conference on Lasers and Electro-optics (CLEO 2016)*, San Jose, CA, USA, 2016.

[151] H. P. Bazargani, J. B. Quelene, P. Dumais, A. Malacarne, M. Clerici, R. Morandotti, C. L. Callender and J. Azaña, "On-chip, single-shot characterization of GHz-rate complex optical signals," *IEEE Photonics Technology Letters,* vol. 26, no. 23, pp. 2345-2348, 2014.

[152] H. P. Bazargani and J. Azaña, "Integer and fractional-order photonic Hilbert transformer on SOI," in *OSA Topical Meeting on Integrated Photonics Research, Silicon, and Nano-Photonics (IPR 2016)*, Vanvouver, BC, 2016.

Chapter 2 On-chip optical pulse shaping (OPS)

In this chapter, we present our three journal publications which are focused on the proposal, numerical development and experimental demonstrations of optical pulse shaping using our newly proposed method, namely, discrete space-to-time mapping in cascaded co-directional couplers.

2.1 Optical pulse shaping based on discrete space-to-time mapping in cascaded co-directional couplers

Abstract: We propose and numerically validate a new design concept for on-chip optical pulse shaping based on discrete space-to-time mapping in cascaded co-directional couplers. We show that under weak-coupling conditions, the amplitude and phase of the discrete complex apodization profile of the device can be directly mapped into its temporal impulse response. In this scheme, the amplitude and phase of the apodization profile can be controlled by tuning the coupling strength and relative time delay between the couplers, respectively. The proposed concept enables direct synthesis of the target temporal waveforms over a very broad range of time-resolution, from the femtosecond to the sub-nanosecond regime, using readily feasible integrated waveguide technologies. Moreover, the device offers compactness and the potential for reconfigurability.

Published in Optics Express, vol. 23, no.18, pp. 23450-23461, 2015.

H. P. Bazargani and J. Azaña

2.1.1 Introduction

Optical pulse shaping techniques have been investigated for a wide variety of applications in high-speed communications, ultrafast information processing, waveform generation and control etc [1-3]. Presently, optical pulse shapers based on the well-established spatial-domain processing approach are commercially available, and they allow programmable synthesis of arbitrary waveforms with resolutions better than 100 fs [4,5]. However, the major drawback of this method is its relative complexity, requiring the use of very high-quality bulk-optics components, which also affects the device insertion losses in fiber-optics systems. To overcome some of these difficulties, devices based on similar pulse shaping principles have been implemented using on-chip arrayed diffraction gratings [6-8]. Despite their important advantages, particularly in terms of compactness, these devices still suffer from limited spectral resolution and sensitivity to fabrication errors. In the quest for more compact, lower loss and relatively simpler devices for optical pulse shaping/coding, all-fiber and integrated-waveguide grating structures have attracted considerable attention [9]. A particularly interesting design approach for fiber or waveguide grating exploits the so-called first-order Born approximation, under which the devices' temporal impulse response is a direct, scaled version of the grating apodization profile [9-13]. This space-to-time mapping (STM) property greatly simplifies the grating device design for temporal pulse shaping applications. However, both short-period (Bragg) and long-period grating devices have proven challenging to fabricate in integrated-waveguide configurations, particularly if they are intended to synthesize complex waveforms, e.g., with high resolutions, below the sub-picosecond regime, over long durations, above a few picoseconds [9,10]. Additionally, Bragg grating (BG) devices need to be operated in reflection and it would be also difficult to add reconfigurability in these structures, e.g., through the integration of high-resolution thermo/electro-optical controllers, due to the nanometer-scale of the grating features.

In this communication, we introduce a novel discrete co-directional coupler structure and its design approach for general time-domain optical pulse shaping. The proposed design is based on forward coupling between a main waveguide and a bus waveguide, where the coupling is controlled in a discrete fashion (point by point) through standard co-directional couplers, see scheme in Figure 2-1(a).

In particular, we show that the device can be designed so that the 'discrete' amplitude and phase 'apodization' profile along the concatenated couplers, namely coupling strength and relative time delay between couplers, can be directly mapped into the output temporal response. This approach can be interpreted as a discrete version of the STM process in waveguide gratings [9]. Similarly, the approach significantly facilitates the design of structures based on concatenated co-directional couplers for temporal pulse shaping operations, as compared with standard design approaches based on spectral-domain response synthesis, e.g., so-called lattice filters [14-18]. In particular, a lattice filter device, involving concatenated interferometer with ring resonator incorporated into its upper arm, has been recently implemented in a silicon photonics technology [18]; not only this device has been designed using a relatively more complex spectral-domain synthesis approach, but additionally, it incorporates a phase-shifter in each ring resonator, making it difficult to scale the device for operation bandwidths above a few GHz. In contrast, the devices achieved from our newly proposed design can be easily scaled for operation bandwidths into the THz range. Moreover, the resulting devices are notably simpler to fabricate than their waveguide-grating counterparts, while also enabling reconfigurability through well-established mechanisms. For instance, precise control of the temporal response amplitude or phase could be achieved by correspondingly tuning the coupling length, Figure 2-1(b), or differential delay between couplers, Figure 2-1(c), respectively.

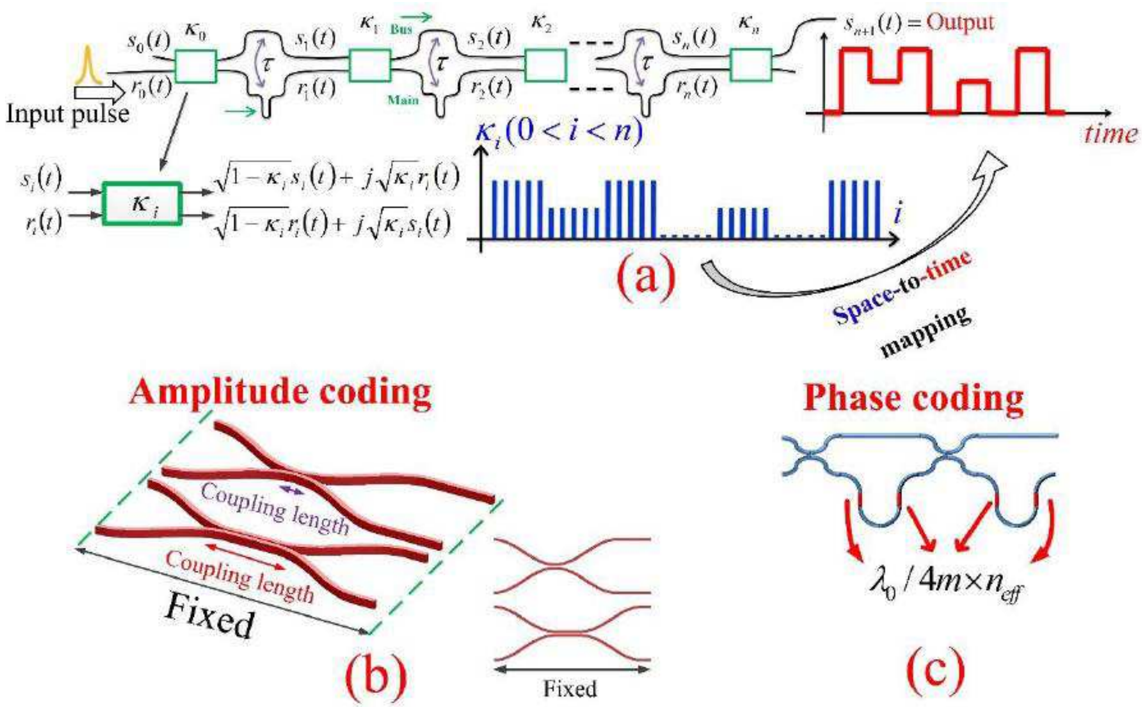

Figure 2-1 (a) Schematic of the proposed pulse-shaping device and its principle of operation (discrete STM); (b) Amplitude coding by tuning the coupling length (the overall length of the directional coupler has to be fixed in order to avoid unwanted phase change in different stages of the device); (c) Phase coding by tuning the waveguide length in the differential delay lines.

In what follows, we first introduce the concept of discrete STM through an ideal modeling of the temporal impulse response of the proposed device. The concept is subsequently validated through numerical simulations based on a transfer-matrix method (TMM), considering practical non-idealities in the device, including losses, waveguide dispersion, tolerances in the device spatial features etc. Numerical examples are shown to confirm the possibility of scaling the concept for pulse shaping over a wide range of temporal resolutions, from the femtosecond to the sub-nanosecond regime, using readily feasible, compact designs.

2.1.2 Theoretical derivation

2.1.2.1 Temporal impulse response

Let us assume $r_i(t)$ and $s_i(t)$, with $0 \le i < n$, being the time-domain complex envelopes of the signals at the input of each coupler, as shown in Figure 2-1(a). The proposed configuration consists of *n* stages, where each stage comprises a directional coupler and a delay line. These stages could be connected to each other with identical delays if a temporal impulse response with a flat phase profile is of interest. On the other hand, by changing the relative delay between different stages, it is also possible to shape the phase profile of the impulse response of the system (more details given below). In our notation, κ_i is the power coupling ratio to the cross-port of the *i*-th coupler. The central assumption in our design is that the device operates under weak-coupling conditions (i.e. strictly, $\sum_{i=0}^{n-1}\kappa_i < 0.1$). In this case, the time-domain impulse response *h*(*t*) at the output port illustrated in Figure 2-1(a) can be analytically calculated as follows (it is assumed that the coupling values, $\kappa_i s$, are real and positive):

$$\begin{cases} s_0(t)=0 \\ r_0(t)=\delta(t) \end{cases} \tag{2.1a}$$

$$\begin{cases} s_1(t)=j\sqrt{\kappa_0}\,\delta(t) \\ r_1(t)=\sqrt{1-\kappa_0}\,\delta(t-\tau)\approx\delta(t-\tau) \end{cases} \tag{2.1b}$$

$$\begin{cases} s_2(t)=j\sqrt{\kappa_0}\sqrt{1-\kappa_1}\delta(t)+j\sqrt{\kappa_1}\sqrt{1-\kappa_0}\delta(t-\tau)\simeq j\sqrt{\kappa_0}\delta(t)+j\sqrt{\kappa_1}\delta(t-\tau) \\ r_2(t)=\sqrt{1-\kappa_0}\sqrt{1-\kappa_1}\delta(t-2\tau)-\sqrt{\kappa_0}\sqrt{\kappa_1}\delta(t-\tau)\simeq\delta(t-2\tau) \end{cases} \tag{2.1c}$$

$$\begin{cases} s_n(t)\simeq j\sum_{i=0}^{n-1}\sqrt{\kappa_i}\delta(t-i\tau) \\ r_n(t)\simeq\delta(t-n\tau) \end{cases} \tag{2.1d}$$

$$h(t) = s_n(t) \simeq j\sum_{i=0}^{n-1}\sqrt{\kappa_i}\delta(t-i\tau) \tag{2.2}$$

Hence, as predicted, under the defined weak-coupling condition, the discrete-time impulse response of the device (input: main waveguide; output: bus waveguide) is a time-scaled version of the discrete coupling profile of the concatenated couplers. Notice that the nominal time-delay difference, τ, depends upon the nominal length difference, $\Delta L = \tau c / n_{eff}$, in between consecutive couplers, where n_{eff}, is the effective refractive index of the waveguide and c is the speed of light in vacuum. Additionally, to implement a π-phase-shift at a desired point of the impulse response, the length difference ΔL before the corresponding coupler should be changed to $\Delta L + \lambda_0 / 2n_{eff}$. More generally, in order to achieve phase shifts of π/m, the change in the length of the delay line should be equal to $\lambda_0 / 2mn_{eff}$, see Figure 2-1(c). Finally, we should note that on the basis of the described performance, the nominal time-delay difference τ defines the device's time resolution whereas the number of stages in the device defines the number of points (e.g., ratio between temporal duration and resolution or so-called time-bandwidth product, TBP) of the synthesized waveform.

2.1.2.2 Transfer matrix method for numerical simulations

In this paper we are specifically interested in the realization of the proposed device using silicon waveguides on a silicon-on-insulator (SOI) substrate, as this platform provides compactness and compatibility with complementary metal–oxide–semiconductor (CMOS) technology. In order to precisely model the device, waveguide dispersion, loss and also errors due to imperfections of the fabrication process have been carefully taken into account. A two-port lattice-form circuit configuration consisting of n pairs of waveguides with different path lengths and n directional couplers has been considered, in order to model the device using the TMM [17]. The first element at each stage (period) of the device is a pair of waveguides with a delay time difference of τ. The upper waveguides (sections of 'bus waveguide') are usually considered to be straight and short while the lower waveguides (different portions of the 'main-waveguide') are longer and bended to realize the delay. The transfer matrix for these unit cells can be expressed as:

$$T_{waveguide,i} = \begin{bmatrix} \exp(j\left(\frac{2\pi n_{eff}(\lambda)}{\lambda}\right)L_{u,i} + \alpha_{loss,u}L_{u,i}) & 0 \\ 0 & \exp(j\left(\frac{2\pi n_{eff}(\lambda)}{\lambda}\right)L_{1,i} + \alpha_{loss,1}L_{1,i}) \end{bmatrix} \tag{2.3}$$

where $n_{eff}(\lambda)$, is the wavelength-dependent effective refractive index of the waveguide, accounting for the waveguides' dispersions; $\alpha_{loss,u}$ and $\alpha_{loss,1}$ are the losses per unit length of the upper and lower waveguides; L_u and L_l are the lengths of the upper and lower waveguides at each stage of the device. A possible maximum error on the waveguides' lengths of $\pm 5\,\text{nm}$ due to fabrication uncertainties is considered [19], i.e., the waveguides' lengths are modeled to have each a Gaussian distribution with a mean value of L_u (and/or L_l) and a variance of 5 nm. In addition, each directional coupler is modeled using the transfer matrix:

$$T_{\text{coupler},i} = \begin{bmatrix} \sqrt{1-\kappa_i(\lambda)} & j\sqrt{\kappa_i(\lambda)} \\ j\sqrt{\kappa_i(\lambda)} & \sqrt{1-\kappa_i(\lambda)} \end{bmatrix} \tag{2.4}$$

The following equation shows the relationship between the parameters defined in section (2.1.2.1) and the TMM model:

$$\begin{bmatrix} \Im(s_{i+1}(t)) \\ \Im(r_{i+1}(t)) \end{bmatrix} = T_{\text{coupler},i} T_{\text{waveguide},i} \begin{bmatrix} \Im(s_i(t)) \\ \Im(r_i(t)) \end{bmatrix} \tag{2.5}$$

In the above notation, the operator $\Im$ holds for the Fourier transform. The overall transfer matrix of *n* concatenated stages can then be calculated as follows:

$$T = \left(\prod_{i=n-1}^{1} T_{\text{coupler},i} T_{\text{waveguide},i} \right) T_{\text{coupler},0} \tag{2.6}$$

from which one can extract the spectral transfer function and corresponding temporal impulse response of the device [17]. In particular, $\Im\left(s_n\left(t\right)\right) = T_{12} E_{in}\left(f\right)$ and $\Im\left(r_n\left(t\right)\right) = T_{22} E_{in}\left(f\right)$ in which T , is a 2×2 matrix with the following set of elements:

$$T = \begin{bmatrix} T_{11} & T_{12} \\ T_{21} & T_{22} \end{bmatrix} \tag{2.7}$$

Recall that $s_0\left(t\right) = 0$ and $\Im\left\{r_0\left(t\right)\right\} = E_{in}\left(f\right)$.

In our analysis, we consider a silicon strip waveguide with a dimension of 500 nm (width) × 220 nm (height). This waveguide is fabricated on an SOI wafer. The cladding and buried oxide layers are assumed to be made of silicon dioxide with a height of 2 μm and 3 μm, respectively.

There are three important sources of error which may affect the coupling coefficient of the directional couplers: (i) changes in coupling gap due to the lateral shift of the waveguides in the coupling region; (ii) unbalanced waveguide widths in the coupling region; and (iii) wavelength dependency of the coupling ratio due to waveguide dispersion [12]. Three-dimensional finite difference time domain (3D FDTD) numerical simulation has been used to evaluate these errors in our proposed designs.

For case (i), the coupling gap has been altered in steps of 5 nm around a typical value of 200-nm; for case (ii), we have considered two waveguides with unbalanced widths of 500 ± 4 nm at the coupling region. Finally for both cases, we have swept the coupling length (in steps of 1μm) and recorded the coupling ratio at each step, at a wavelength of 1555 nm. All directional couplers consist of 4 s-bends with the length of 4 μm and the height of 2 μm connecting the waveguides at the coupling region to cross and through ports.

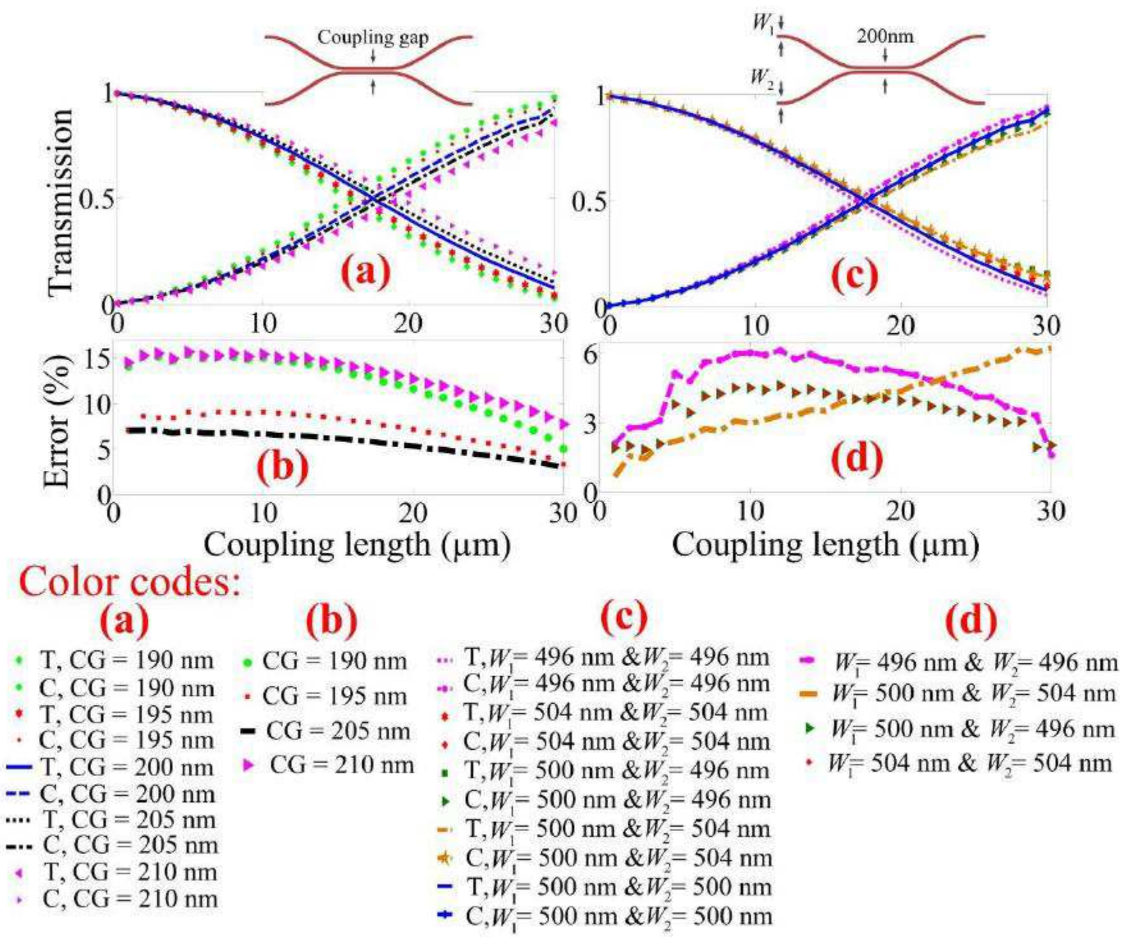

Figure 2-2 (a) Power coupling ratios in cross and through ports of the directional coupler for 500 nm wide waveguides while changing the coupling gap. (b) The percentage of error for the power coupling ratio due to the deviation of coupling gap with respect to its ideally designed value. In this case the target design is a coupling gap of 200 nm. (c) Power coupling ratios in cross and through ports of the directional coupler with a fixed coupling gap of 200 nm and unbalanced waveguide widths at the coupling region. (d) The percentage of error for the power coupling ratio due to unbalanced waveguide width with respect to the target design being a pair of balanced 500 nm wide waveguides (T: Through port, C: Cross port, CG: Coupling gap).

The results, shown in Figure 2-2, provide the relative amount of change in the coupling ratio of the coupler caused by these sources of error. According to the simulation results, we should consider a maximum of 15% and 6% variations in the coupling ratio over its nominal value due to fabrication-related fluctuations in the coupling gap or unbalanced waveguide width, respectively. Such estimates have been plugged in the TMM modeling of the couplers, Eq. (2.4), as follows: Two additive Gaussian distributions with mean values of κ_i and variances of $0.15\kappa_i$ and $0.06\kappa_i$, respectively, have been introduced into the model to account for variations in the coupling ratio. We have considered these two sources of error to be uncorrelated.

Moreover, for case (iii), 3D FDTD simulations have been carried out to study the effect of chromatic dispersion on the coupling ratio of the directional couplers. In particular κ_i has been defined to be a wavelength dependent parameter by plugging the data from the FDTD analysis into our TMM model.

2.1.3 Weak-coupling condition in cascaded co-directional couplers

The range of validity of the weak-coupling condition in the proposed device has been evaluated in deeper detail using the following strategy. We consider our output target to be a flat-top pulse, requiring the use of identical coupling ratios and delays; for a fixed number of stages, evaluations are made as the power coupling ratio at each period is increased, correspondingly increasing the peak of the device's power spectral response (PSR). We consider an upper margin for the weak-coupling condition, where half of the transmitted input power is transferred into bus-waveguide. In other words, the PSR peak from the bus-waveguide reaches 50% of the maximum PSR from the main-waveguide (for a loss-less structure, this maximum PSR value is unity).

Typical waveguide propagation loss for the bus waveguide has been considered to be 3 dB/cm [20]. Moreover, for the main-waveguide we add ($4 \cdot n \cdot LPB$) dB to this number in order to account for the extra losses in bent waveguides (*LPB* being loss per bend, from Ref. [20]). The term in parenthesis refers to the loss per bend in four (4) quarter curves, which form the delay lines. The bus- and main-waveguides have been designed to have a length difference of $2\pi R - 4R$ (= 6.85-µm for R = 3 µm, in the case under study) at each period.

For different number of couplers (i.e. n = 7, 12, …, 27) and a fixed differential delay of 6.85-µm at each stage, we target flat-top pulses with a variety of temporal durations, depending on the number of couplers. In all cases, the input waveform is a Gaussian transform-limited pulse with a full width at half maximum (FWHM) duration of 150 fs.

Assuming that $\max\left(PSR\big|_{bus-waveguide}\right) = 0.5\max\left(PSR\big|_{main-waveguide}\right)$ we then record the corresponding power coupling ratio and estimate the maximum relative deviation of the waveform with respect to the ideal one along the flat-top region. The recorded value of κ_i (i = 0,…, n-1) is the maximum power coupling ratio that one can achieve while still satisfying the prescribed upper margin of the weak-coupling condition.

The results shown in Figure 2-3, for 7 cascaded couplers confirm that the deviation in the synthesized waveform with respect to the target one is more pronounced as the coupling strength is increased; however, a higher coupling strength leads to an increased PSR peak, which translates into a higher device energy efficiency. For the flat-top case, a reasonable waveform deviation (~6% error) is still achieved for a 50% bus-waveguide PSR peak so as anticipated above, this is chosen as the condition for optimizing the trade-off between waveform deviation and device efficiency. Results from simulation concerning the 'optimal' specifications (PSR peak ~50%) for different number of couplers are presented in Table 2-1. This table confirms that the coupling coefficient must be made weaker as the number of couplers is increased in the device, i.e., as one targets the synthesis of more complex waveforms (with a higher TBP). This is in good agreement with the assumption made in Section (2.1.2) for the power coupling ratio to satisfy the weak-coupling condition ($\sum_{i=0}^{n-1}\kappa_i < 0.1$).

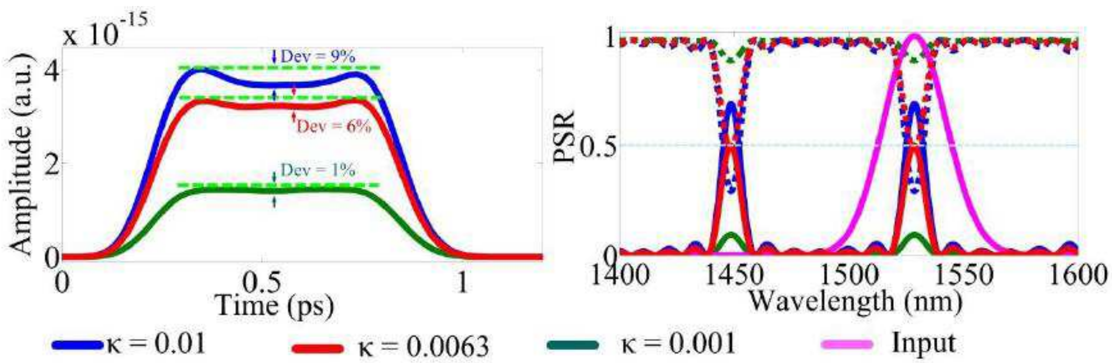

Figure 2-3 Weak coupling condition in a 7-stage device. (a) Deviation of a flat-top from its ideal case by increasing the power coupling ratio (DEV : Deviation). (b) Power spectral response (PSR) of the device at bus- and main-waveguides for different values of coupling coefficient. It is shown that, increasing the PSR peak up to 50% of its maximum value (PSR at the output of the main-waveguide), the device still offers the desired weak-coupling performance, so that the flat-top only deviates as much as ~6% with respect to the ideal case.

Table 2-1 Weak coupling condition for n couplers. MA stands for maximum relative deviation of the waveform with respect to the ideal one along the flat-top region.

(n) number of couplers	κ_i $(0 \le i < n)$	MA
7	0.0063	6%
12	0.0021	9%
17	0.0011	11%
22	0.0006	11%
27	0.0004	12%

2.1.4 Design examples for optical pulse shaping and coding

To confirm the validity of our proposed design, we have numerically simulated devices to synthesize two different waveforms, namely flat-top waveforms, and an 8-symbol optical 16-QAM signal. We target the synthesis of temporal features from the femtosecond range up to a few hundreds of picoseconds.

Our first target waveform is a ~850 fs (FWHM) flat-top pulse generated from an input ultra-short optical Gaussian pulse with a temporal duration of 150 fs (FWHM). The input optical pulse is assumed to be centered at 1529 nm. Ten couplers with identical coupling coefficients of 0.004 (corresponding to coupling gap of 200 nm and coupling length of 1 μm) are connected in series through 65.79 fs delay lines. As shown in Figure 2-4(a), the upper arms are *4R* long and the lower arms have a length of 2π*R* (*R*: bend radius for this specific example is equal to 3 μm). Adiabatic Bezier bends have been incorporated in the delay lines to reduce the bending loss [21,22]. The losses have been considered to be 3 dB/cm in the bus waveguide and 3 dB/cm + ($4 \cdot n \cdot LPB$) dB in the main waveguide. *LPB* for this specific case is ~0.01 dB/bend [20]. The overall propagation loss for the light wave travelling through the main- and bus-waveguides are ~0.48 dB and ~0.06 dB, respectively. We run the simulations for 100 times, considering discrete values of error in the coupling ratio and in the phase of each delay line due to variations in waveguide lengths, following the error statistics defined above. Figure 2-4(d) shows the overlap of the synthesized output flat-top waveform for the 100 evaluated cases, together with their mean value. A standard deviation (STD) of ~ 0.02 has been estimated for the random fluctuations of the flat-top section of the waveform around its mean value.

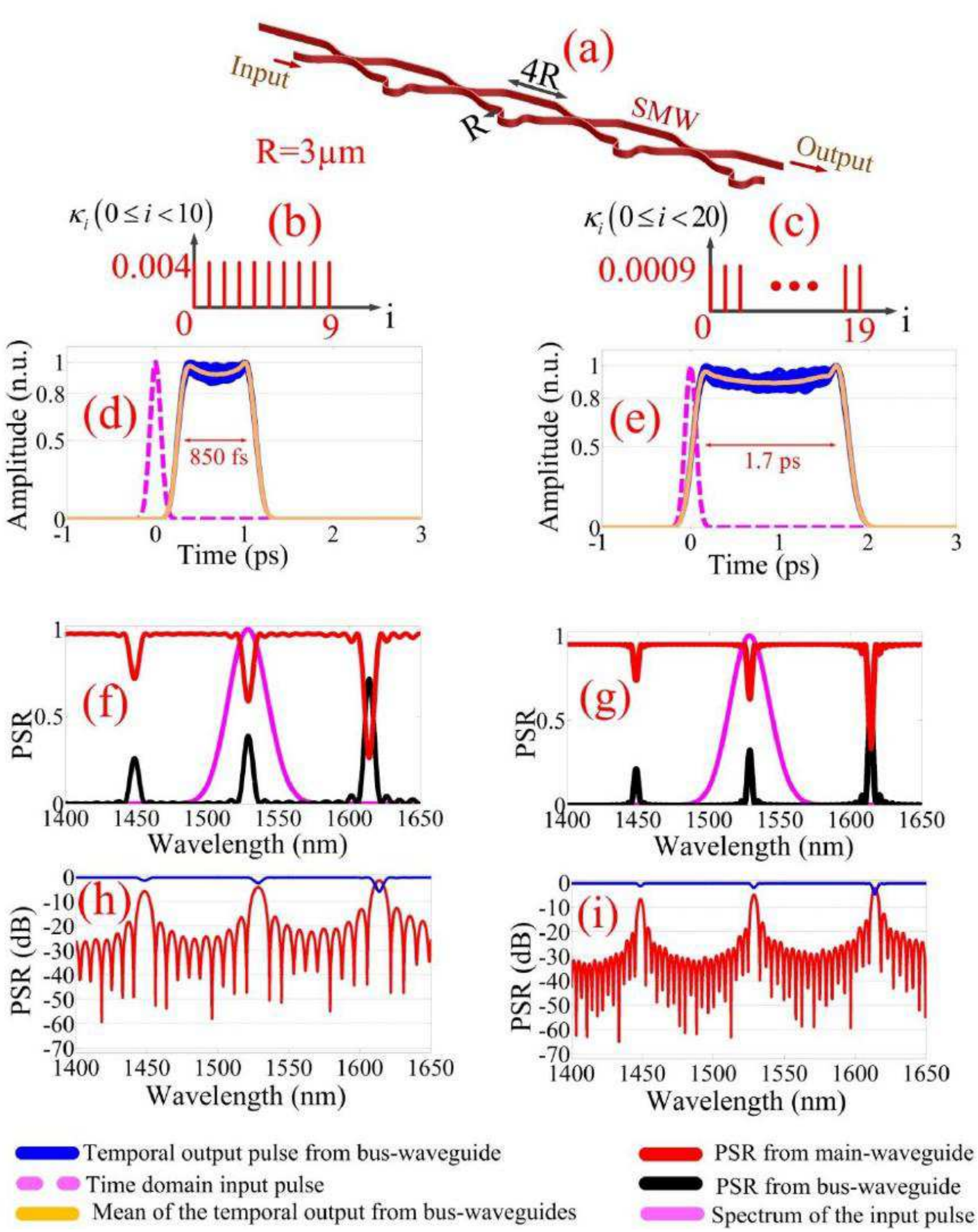

Figure 2-4 (a) Schematic of the flat-top optical pulse generator; (b-c) Profile of the coupling coefficients for the flat-top pulse shaper made of ten and twenty cascaded couplers, respectively; (d-e) Output pulses generated from the designed device for 100 times simulations with random fluctuations in the fabrication parameters, as detailed in the text; (f-g) PSRs from the main and bus-waveguides (red and black solid lines, respectively), and input pulse spectrum (pink, dashed line). (h-i) PSRs from the main and bus-waveguides in logarithmic scale (red and black solid lines, respectively). PSRs are shown only for a single simulation.

The second target waveform is a 1.7 ps (FWHM) flat-top pulse generated from an identical structure but this time cascading 20 couplers, each with a power coupling ratio of 0.0009 (corresponding to a coupling gap of 200 nm and a coupling length of zero). The expected propagation loss for the light travelling through the main- and bus-waveguides are ~0.97 dB and ~0.13 dB, respectively. The input signal is again a 150-fs (FWHM) Gaussian transform-limited pulse. Following the same numerical simulation strategy, a similar value for the STD (~ 0.02) of the generated flat top has been achieved. The obtained results are shown in Figure 2-4(e). Moreover, it is shown in Figure 2-5, that the maximum phase variation along the duration of the pulse is ~ 0.25 rad.

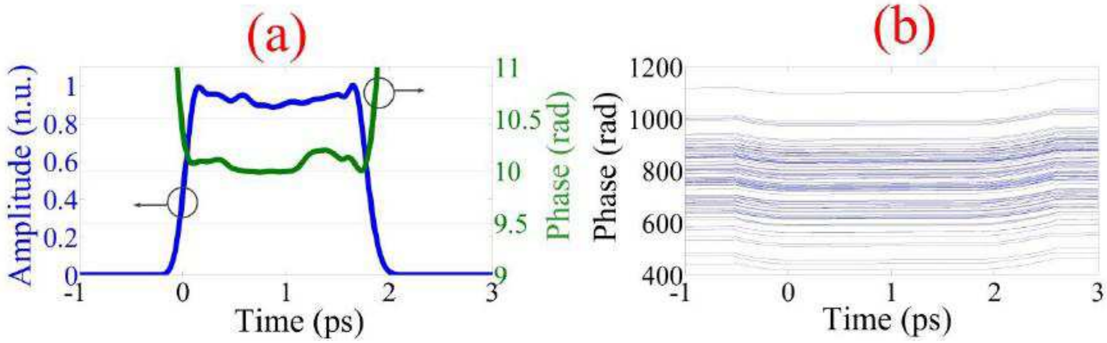

Figure 2-5 (a) Maximum phase variation of ~ 0.25 rad has been observed for the 1.7-ps, flat-top pulse synthesis design. (b) The phase profile of the flat-top pulse after repeating the simulation for 100 times.

It is worth noting that the number of sidelobes in the sync-like spectral response of the device is directly related to the TBP of the synthesized flat-top waveform (i.e., ratio of flat-top duration to the raising or decaying time of the waveform), which in turn depends on the number of concatenated couplers. Comparing Figure 2-4(h) and Figure 2-4(i), one can observe that the 2nd device provides a higher TBP. As predicted, a two-fold improvement in the TBP has been achieved for 20 cascaded couplers with respect to 10 cascaded couplers.

A third waveform synthesis case has been considered to illustrate the possibility of using the proposed method for synthesizing longer temporal shapes, in the sub-nanosecond regime. In particular, we have designed and numerically simulated a waveguide structure for generation of an 8-symbol 16-QAM signal, with a speed of 24 Gsymbol/s, from an input ultra-short optical Gaussian pulse with duration of 17 ps (FWHM). The designed amplitude and phase profiles for the target QAM coding operation, and the related constellation diagram, are shown in Figure 2-6(b-c). Twenty four couplers were used to generate an 8-bit amplitude and phase modulated code. The length of the upper arm is equal to 415 μm and the lower arm is 1,262 μm long (see Figure 2-6(a)). As anticipated, this device exhibits a far longer sampling time (differential delay of 11.78-ps and corresponding length difference of 847 μm) than for the previous flat-top pulse synthesizer designs. Consequently, the trailing copies of the input pulse will experience higher values of propagation loss. This would lead to a ramp-like response, affecting the performance of the pulse-shaping device. A solution for this problem is to use optimized designs aimed at reducing losses in the long delay lines. Multi-mode rib waveguides (MMWs) with strip widths of 3 μm, strip heights of 220-nm, slab widths of 5.1 μm, and slab heights of 90 nm have been implemented in our proposed design to reduce the propagation loss from 3 dB/cm down to less than 1 dB/cm [20]. However, SMWs are still used in the coupling region and waveguide bends, in order to ensure single-mode operation of the device. To make sure that only the fundamental mode of the MMW is excited, 100 μm-long linear tapers are used for conversion between SMWs and MMWs [13]. Using this design strategy the loss in the upper arm and the lower arm are 3 dB/cm and 1 dB/cm + ($6 \cdot n \cdot LPB$) dB, respectively. The number 6 here refers to the number of quarter Bezier curves which have been incorporated to form the delay line. The bends are 5-μm, and we consider the use of Bezier bends with ~0.008 dB/bend loss [20]. In this case, we estimate ~3 dB propagation loss for the light passing through the bus-waveguide and ~1.8 dB loss at the output of the main-waveguide. In practice, we expect higher values of loss for the main waveguide. The reason for that are the tapers that have been used in different sections of the device. If the tapers are not long enough, the mode mismatch loss between the SMW and MMW may become considerable. However, making the tapers longer will eventually reduce this source of loss to negligible values.

Four amplitude levels are achieved using directional couplers with power coupling ratios of κ, 9κ/16, κ/4 and κ/16. Considering $\kappa = 0.0016$, the coupling gaps are equal to 385 nm and coupling lengths are equal to 1 μm, 560 nm, 250 nm and 0, respectively.

Considering similar statistical variations in the fabrication parameters to those considered for the previously studied cases, the amplitude and phase profiles of the time-domain waveform at the output of the simulated device are shown in Figure 2-6(d), demonstrating again accurate generation of the target data stream.

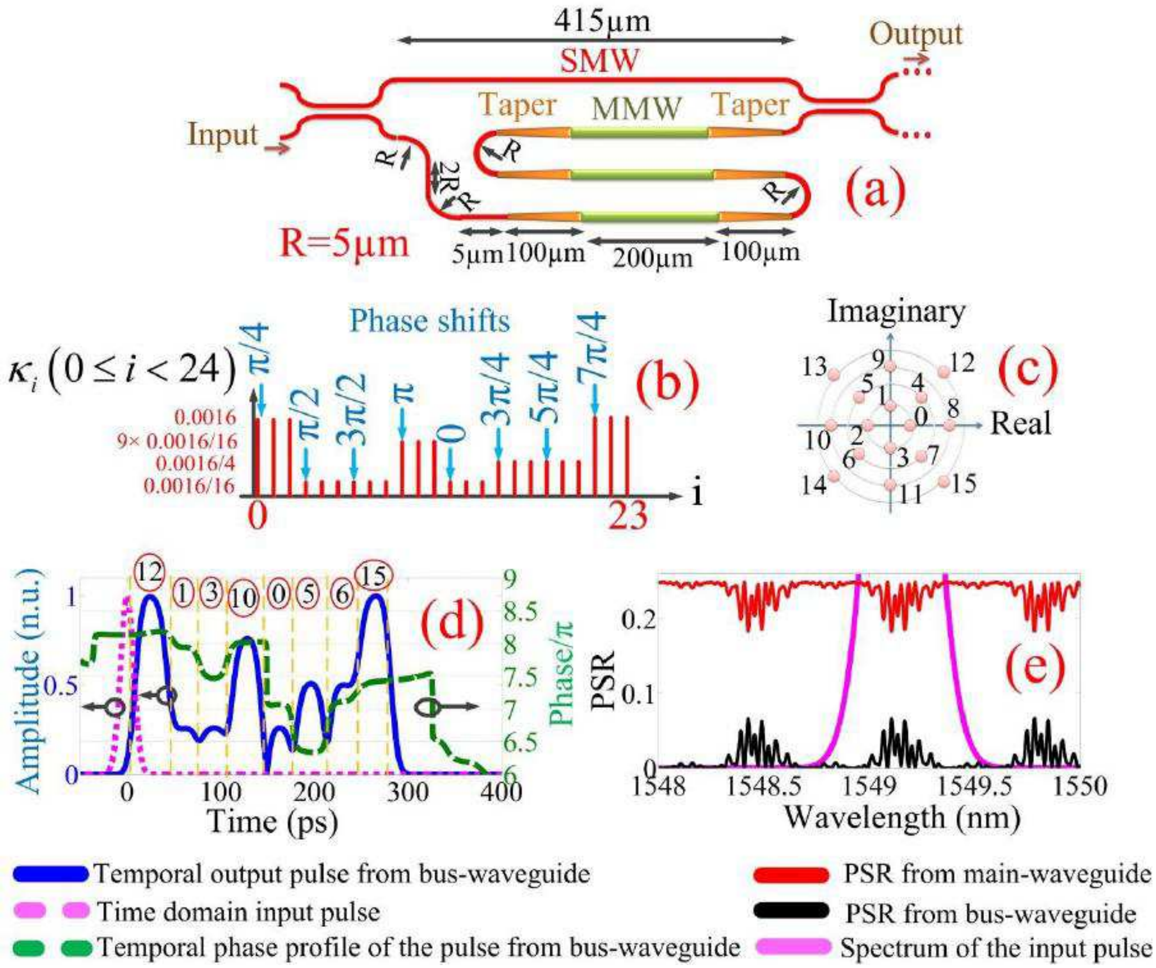

Figure 2-6 (a) Schematic of the QAM optical pulse generator; (b) Profile of the amplitude and phase of the coupling coefficients for the QAM pulse coder; (c) Constellation diagram of the 16-QAM modulated signal; (d) 24 Gsymbol/s QAM code; (e) PSRs from main and bus-waveguides.

2.1.5 Conclusions

We have proposed a new design concept for linear optical pulse shaping based on discrete space-to-time mapping in cascaded co-directional couplers. The proposed approach bypasses the problems associated with complex, indirect designs based on synthesizing the desired response in the spectral domain, by directly mapping the target time-domain impulse response along the device's spatial apodization profile (coupling-coefficient and phase-delay profile). The proposed design approach could be adapted for application over a wide range of temporal resolutions, from the sub-picosecond to the sub-nanosecond regime, and it should enable the synthesis of relatively complex (high TBP) temporal waveforms with energy efficiencies approaching 50%. The temporal resolution of the device depends on the differential path length between the bus- and main-waveguides so that adding a long phase shifter, as needed to tune the device spatial apodization profile, should be possible without affecting the fundamental device performance.

2.1.6 References

[1] P. C. Teh, M. Ibsen, J. H. Lee, P. Petropoulos, and D. J. Richardson, "Demonstration of a four-channel WDM/OCDMA system using 255-chip 320-Gchip/s quarternary phase coding gratings" *IEEE Photonics Technology Letters,* vol. 14, no. 2, pp. 227-229, 2002.

[2] F. Ferdous, H. Miao, D. E. Leaird, K. Srinivasan, J. Wang, L. Chen, L. T. Varghese, and A. M. Weiner, "Spectral line-by-line pulse shaping of on-chip microresonator frequency combs" *Nature Photonics*, vol. 5, no. 12, p.p. 770–776, 2011.

[3] Sh. Liao, Y. Ding, J. Dong, T. Yang, X. Chen, D. Gao, and X. Zhang, "Arbitrary waveform generator and differentiator employing an integrated optical pulse shaper" *Optics Express*, vol. 23, no. 9, pp. 12161-12173, 2015.

[4] J. A. Salehi, A. M. Weiner, and J. P. Heritage, "Coherent ultrashort light pulse code-division multiple access communication systems" *Journal of Lightwave Technology*, vol. 8, no. 3, pp. 478-491, 1998.

[5] A. M. Weiner, *Ultrafast optics*, (John Wiley & sons, 2011).

[6] N. K. Fontaine, D. J. Geisler, R. P. Scott, T. He, J. P. Heritage, and S. J. B. Yoo, "Demonstration of high-fidelity dynamic optical arbitrary waveform generation" *Optics Express*, vol. 18, no. 22, pp. 22988-22995, 2010.

[7] R. P. Scott, N. K. Fontaine, J. P. Heritage, and S. J. B. Yoo, "Dynamic optical arbitrary waveform generation and measurement" *Optics Express*, vol. 18, no. 18, pp. 18655-16670, 2010.

[8] B. Muralidharan, V. Balakrishnan, and A. M. Weiner, "Design of double-passed arrayed-waveguide gratings for the generation of flat-topped femtosecond pulse trains" *Journal of Lightwave Technology*, vol. 24, no. 1, pp. 586-592, 2006.

[9] L.-M. Rivas, M. J. Strain, D. Duchesne, A. Carballar, M. Sorel, R. Morandotti, and J. Azaña, "Picosecond linear optical pulse shapers based on integrated waveguide Bragg gratings" *Optics Letters*, vol. 33, no. 21, pp. 2425-2427, 2008.

[10] R. Ashrafi, M. Li, N. Belhadj, M. Dastmalchi, S. LaRochelle, and J. Azaña, "Experimental demonstration of superluminal space-to-time mapping in long period gratings" *Optics Letters*, vo. 38, no. 9, pp. 1419-1421, 2013.

[11] H. Kogelnik., "An introduction to integrated optics,"*IEEE Transactions on Microwave Theory and Techniques*, vol. 23, no. 1, pp. 2-16, 1975.

[12] H. Kogelnik, "Filter response of nonuniform almost-periodic structures" *Bell Systems Technology Journal*, vol. 55, no. 1, pp. 109-126, 1976.

[13] J. Azaña and L. R. Chen, "Synthesis of temporal optical waveforms by fiber Bragg gratings: a new approach based on space-to-frequency-to-time mapping" *Journal of the Optical Society of America B*, vol. 19, no. 11, pp. 2758-2769, 2002.

[14] J. K. Doylend, P. E. Jessop, and A. P. Knights, "Silicon photonic dynamic optical channel leveler with external feedback loop" *Optics Express***,** vol. 18, no. 13, pp. 13805-13812, 2010.

[15] K. Takiguchi, K. Okamoto, S. Suzuki and Y. Ohmori, "Planar Lightwave Circuit Optical Dispersion Equalizer" *IEEE Photonics Technology Letters*, vo. 6, no. 1, pp. 86-88, 1994.

[16] F. Khaleghi, M. Kavehrad, and C. Barnard, "Tunable Coherent Optical Transversal EDFA Gain Equalization" *Journal of Lightwave Technology*, vol. 13, no. 4, pp. 581-587, 1995.

[17] K. Jinguji and M. Kawachi, "Synthesis of Coherent Two-Port Lattice-Form Optical Delay-Line Circuit" *Journal of Lightwave Technology*, vol. 13, no. 1, pp. 73-82, 1995.

[18] B. Guan, S. S. Djordjevic, N. K. Fontaine, L. Zhou, S. Ibrahim, R. P. Scott, D. J. Geisler, Zh. Ding, and S. J. Ben Yoo, "CMOS compatible reconfigurable silicon photonic lattice filters using cascaded unit cells for RF-photonic processing" *IEEE Journal of Selected Topics in Quantum Electronics,* vol. 20, no.4, pp. 8202110-8202110, 2014.

[19] A. D. Simard, G. Beaudin, V. Aimez, Y. Painchaud, and S. LaRochelle., "Characterization and reduction of spectral distortions in Silicon-on-Insulator integrated Bragg gratings" *Optics Express*, vol. 21, no. 20, pp. 23145-23159, 2013.

[20] W. Bogaerts, and S. K. Selvaraja, "Compact single-mode silicon hybrid rib/strip waveguide with adiabatic bends" *IEEE Photonics Journal*, vol. 3, no. 3, pp. 422-432, 2011.

[21] L. Chrostowski and M. Hochberg., *Silicon Photonics Design Book-from Devices to Systems*, (Cambridge University press, 2011).

[22] H. P. Bazargani, J. Flueckiger, L. Chrostowski, and J. Azaña, "Microring resonator design with improved quality factors using quarter Bezier curves" in *Conference on Lasers and Electro-Optics: Science and Innovations,* (Optical Society of America, 2015).

2.2 Experimental demonstration of sub-picosecond optical pulse shaping in silicon based on discrete space-to-time mapping

Abstract: We experimentally demonstrate on-chip optical pulse shaping based on discrete space-to-time mapping in cascaded co-directional couplers. The demonstrated shapers validate a recent design methodology that exploits the direct relationship between the discrete complex spatial apodization profile of a structure of cascaded couplers and the time-domain impulse response of the device. In this design, the amplitude and phase of the apodization profile can be controlled through the coupling strength of each coupler and the relative time delay between the waveguides connecting consecutive couplers, respectively. This design methodology has been successfully used to demonstrate direct synthesis of high-quality flat-top and phase-coded pulse trains with resolutions down to the sub-picosecond range using passive devices in a silicon-on-insulator platform.

Published in Optics Letters, vol. 40, no. 23, pp. 5423-5426, 2015.

H. P. Bazargani, M. Burla, and J. Azaña

2.2.1 Introduction

In order to overcome the bandwidth limitation of conventional electronic arbitrary waveform and pulse generators, all-optical pulse shaping is considered a very attractive alternative for applications in high-speed communications, signal processing etc. [1]. Commercially available optical pulse shapers work based on the well-established spatial-domain processing approach. These devices allow for programmable synthesis of arbitrary waveforms with resolutions better than 100 fs [2]. However, the need for high-quality bulk-optics components makes the implementation of this method relatively complex. To overcome some of these difficulties, similar pulse shaping principles have been implemented using on-chip arrayed diffraction gratings (ADGs) [3]. On-chip ADGs offer compactness, but still suffer from limited spectral resolution. Besides, sensitivity to fabrication errors makes them quite challenging to design and fabricate. In the quest for more compact, lower loss and relatively simpler devices for optical pulse shaping, all-fiber and integrated-waveguide grating structures have attracted considerable attention [4,5]. A very interesting design strategy for fiber/waveguide grating devices uses the so-called first-order Born approximation. Under this approximation, the device's temporal impulse response is a direct, scaled version of the grating coupling-strength profile [4]. This space-to-time mapping (STM) property greatly simplifies the grating device design for temporal pulse shaping applications. However, both short-period (Bragg) and long-period grating devices have proven challenging to fabricate in integrated-waveguide configurations. Additionally, Bragg grating devices need to be operated in reflection and it would be also difficult to add reconfigurability in these structures, e.g., through the integration of high-resolution thermo/electro-optical controllers [6].

To overcome the aforementioned limitations, a new, simpler design for on-chip optical pulse shaping has been recently proposed [7]. This design is based on a structure of cascaded co-directional couplers and it exploits the fact that under relatively weak-coupling conditions, the 'discrete' amplitude and phase 'apodization' profile of the structure can be directly mapped into the output temporal response of the device, see scheme in Figure 2-7. This approach has been referred to as discrete STM. The proposed design is based on forward coupling between a main-waveguide and a bus-waveguide, where the coupling is controlled in a discrete fashion through standard co-directional couplers. In our specific structure, each of the couplers consists of four S-bends and two identical waveguides which are parallel to each other at the coupling region. In practice the vertical spacing between these waveguides (coupling gap) or their length (coupling length) could be tuned to achieve different coupling ratios, Figure 2-7(c). Additionally, the discrete phase profile can be also tuned by adjusting the relative optical path length difference between the bus- and main-waveguides connecting the upper and lower ports of consecutive couplers, respectively, Figure 2-7(b).

The devices obtained through this new design method are notably simpler to fabricate than their waveguide-grating counterparts, while potentially enabling reconfigurability through well-established mechanisms. For instance, thermo- or electro- optical effect could be implemented to design electrically-tunable variable optical attenuators, and phase-shifters to actively control the coupling strength and relative phase at each stage of the device, respectively. Moreover, we recall that this approach bypasses the problems associated with complex, indirect designs of concatenated coupler structures based on synthesizing the desired response in the spectral domain [1,2].

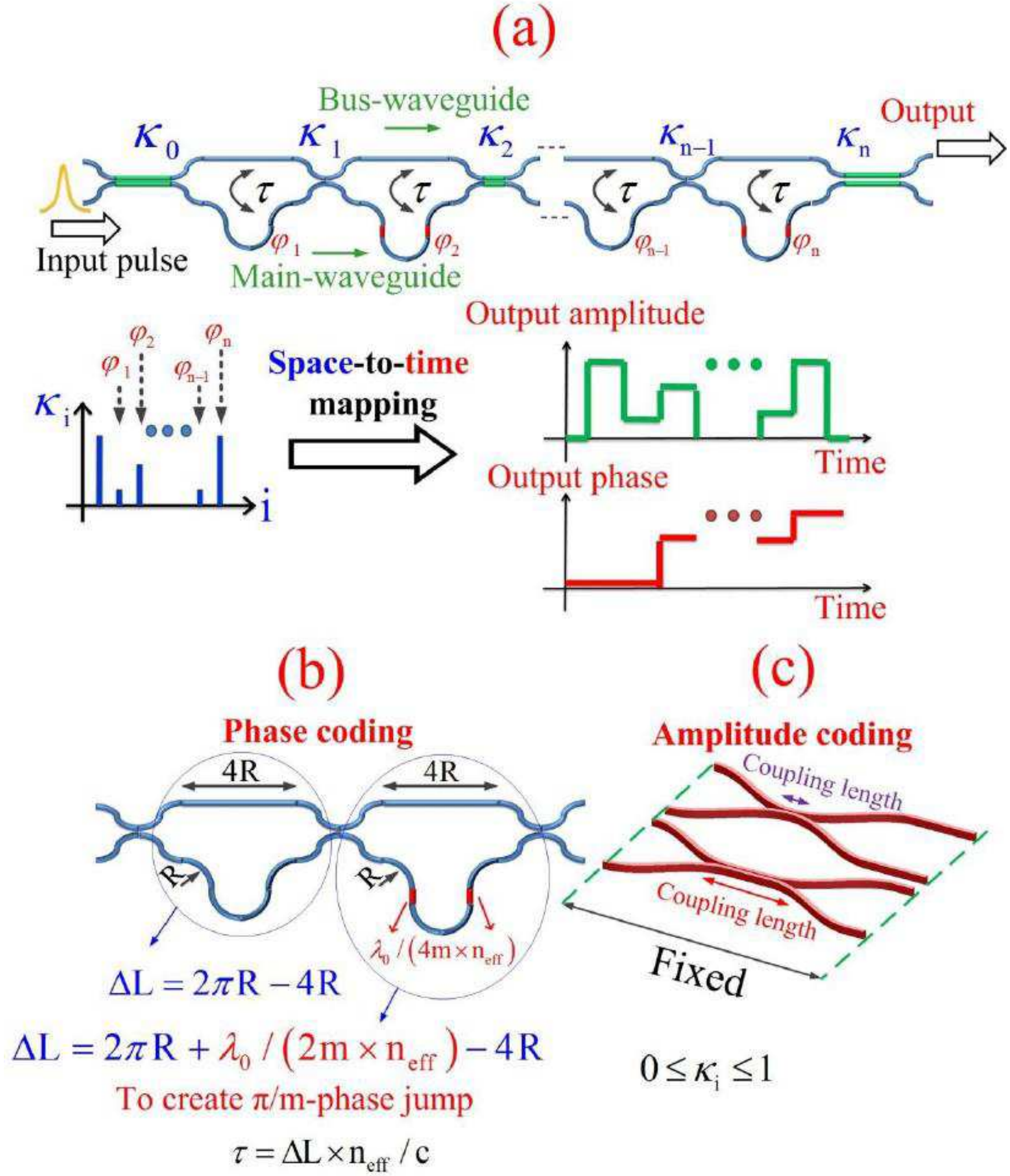

Figure 2-7 (a) Schematic of the proposed pulse-shaping device and its principle of operation (discrete STM); (b) Phase coding by tuning the waveguide length in the differential delay lines; (c) Amplitude coding by tuning the coupling length.

In this paper we experimentally demonstrate discrete STM for optical pulse shaping and coding on a silicon-on-insulator (SOI) chip platform [8], successfully achieving the synthesis of both amplitude and phase temporal shapes, e.g., flat-top pulses and phase-coded pulse trains, with resolutions ranging from the femtosecond to the picosecond regime. The fabrication of the reported devices has been carried out using single-etch, Electron-Beam Lithography at the University of Washington. In particular, we use a fully passive technology for a fairly large number of concatenated couplers (up to ~20), confirming the robustness of this newly proposed design strategy.

2.2.2 Operation principle

Briefly, the device impulse response is a scaled replica of a discrete sequence of coupling coefficients, with a sampling time τ defined by the relative length difference ΔL between the section of the bus-waveguide that connects the upper ports of consecutive couplers, and the section of the main-waveguide bridging the lower ports of the couplers at each stage. In particular, $\Delta L = \tau c / n_{\text{eff}}$, where n_{eff} is the effective refractive index of the waveguide and c is the speed of light in vacuum. To implement a π/m-phase-shift at a desired point of the impulse response, the relative length difference ΔL after the corresponding coupler should be changed to L_2 (see Figure 2-7(b)):

$$\mathrm{L}_2 = \Delta L + \lambda_0 / \left(2m \times n_{\text{eff}}\right), \tag{2.8}$$

2.2.3 Experiment

Our first experimental target waveforms are 1.25-ps and 3-ps (FWHM) flat-top pulses synthesized from an input 540-fs optical Gaussian pulse, which is directly generated from a passively mode-locked fiber laser (Pritel) with a repetition rate of 16.8 MHz. The carrier wavelength of the optical pulse is tuned at the resonance wavelength of each device, i.e. 1556 nm and 1554 nm, respectively. 10 or 20 couplers (for 1.25 ps or 3 ps pulses, respectively) with identical coupling coefficients of ~0.001 are connected in series through 11.5 μm relative-delay lines, corresponding to a sampling time of $\tau \simeq 174$ fs. Notice that the sampling time is estimated using the effective refractive index at the operation wavelength. The reported devices are made of silicon strip single-mode waveguides (SMWs), each with a dimension of 500 nm (width) × 220 nm (height), fabricated on a SOI wafer. Lumerical Mode Solutions was used to study the cross section of the SMW to extract the profile of the effective refractive index versus wavelength (see Figure 2-8).

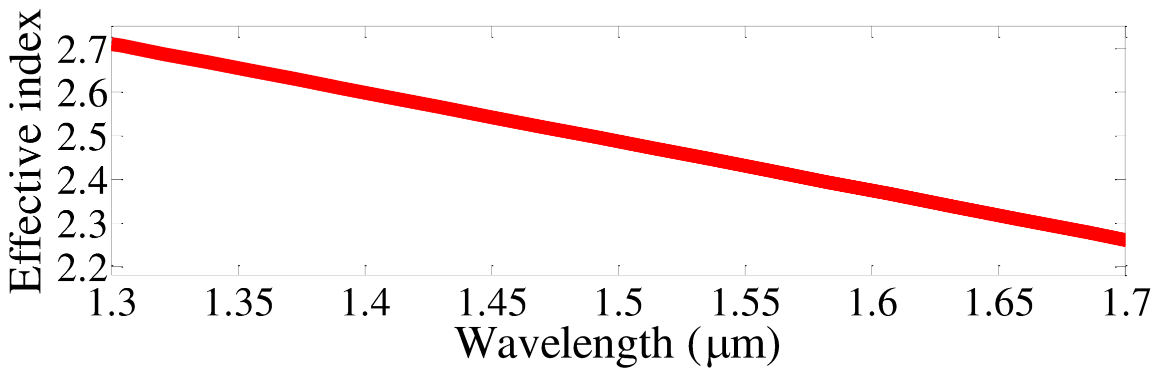

Figure 2-8 Effective refractive index at different wavelengths as numerically calculated for the used single-mode integrated waveguide.

On the other hand, the aforementioned coupling coefficient was achieved using co-directional couplers with nominal coupling gap of 200 nm and coupling length of zero. Whereas the nominal length of the parallel-identical waveguides at the coupling region is fixed to zero, still weak coupling occurs where the upper S-bends get to their closest proximity with the lower S-bends at the margins of the coupling region. The S-bends used in all our designs are 12 μm long and have a height of 6 μm.

As shown in Figure 2-7(b), the upper and lower arms in between the couplers are $4R$ and $2\pi R$ long, respectively (R: bend radius = 5 μm for this specific example giving $\Delta L = 2\pi R - 4R \simeq 11.5\mu m$). Adiabatic Bezier bends have been incorporated in the lower-arm delay lines to reduce the bending loss [9-10].

Light has been coupled to the device from the top of the chip using a fiber array. The coupling mechanism occurs between a fiber, polished with specific angle (depending on the design of the grating coupler, 28° for this case) and a grating coupler [9]. The input/output fibers have been placed in an array which should be carefully aligned to the proper grating couplers in order to optimize the optical power coupling. The spacing between the fibers in the array is fixed to be 127-μm. This has been already considered in the designed layout and the three grating couplers, i.e., input, output from bus-waveguide and output from main-waveguide, have similar spacing to match the pitch in the array.

Direct time-domain characterization of the output, synthesized waveforms has been carried out using Fourier-transform spectral interferometry (FTSI) with the input optical pulse serving as the reference [11]. The used experimental setup is shown in Figure 2-9.

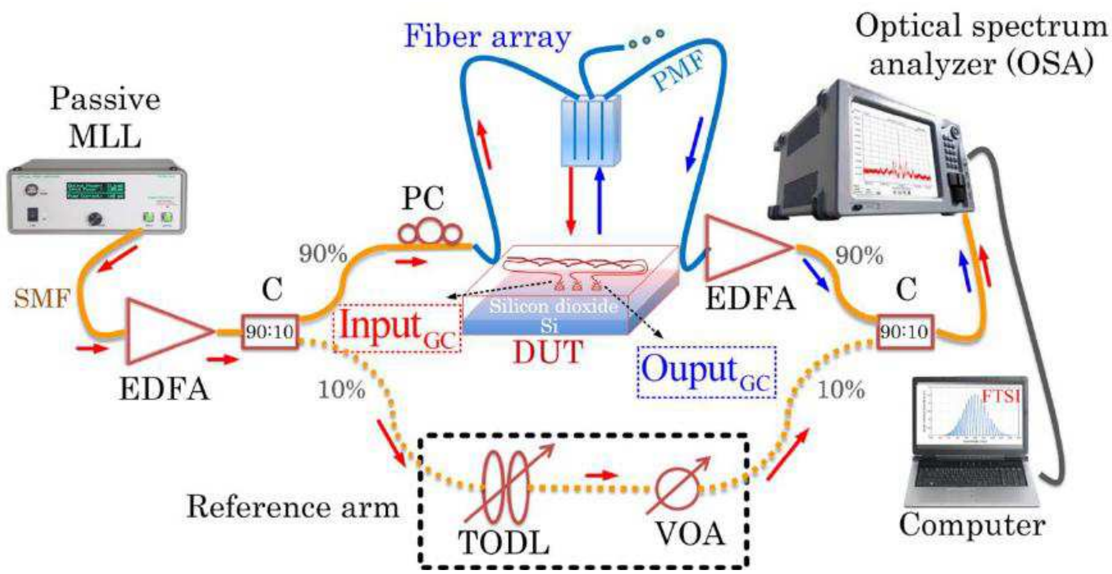

Figure 2-9 Schematic of the FTSI setup, implemented for time-domain characterization of the pulse shaper. MLL, mode locked laser; C, coupler; PC, polarization controller; SMF (orange lines), single mode fiber; PMF (blue lines), polarization maintaining fiber; GC, grating coupler.

The input Gaussian optical pulse, generated from the passive mode locked laser, enters a fiber-based interferometer, built using two 90:10 couplers, as shown in Figure 2-9. The device under test (DUT) is placed in the upper interferometer arm. The lower arm (reference arm) includes a tunable optical delay line (TODL), employed to adjust the time interval between the pulses propagating in the two arms. This interval can be accurately measured by connecting the interferometer output to a 12 ps detector (PD, New Focus 1014) and a 28 GHz oscilloscope. Two erbium-doped fiber amplifiers (EDFAs) are used to compensate for ~ 33 dB loss from the fiber-to-fiber. A variable optical attenuator (VOA) is also inserted in the reference arm to equalize the intensities of the reference and output pulses. An optical spectrum analyzer (OSA) with a minimum resolution of 10-pm has been employed to measure the spectra of the input (reference) pulse, the pulse at the output of the device and their linear interference at the interferometer output. These three spectra are then used to numerically reconstruct the complete time waveform of the processed pulse in magnitude and phase.

Additionally, in order to characterize the devices in frequency, their power spectral responses (PSRs) have been measured using an Optical Vector Analyzer (Luna Innovations) with a spectral resolution of 1.6 pm. Figure 2-10(c-f) show the experimentally measured output temporal waveforms (top plots) and PSRs (bottom plots) for the two described designs, showing a fairly good agreement with the expected results from numerical simulations. The theoretical and OVA output temporal pulses shown in Figure 2-10(c, e) are numerically calculated assuming propagation of an ideal 540-fs (FWHM) Gaussian optical pulse through a linear optical filter with the simulated and OVA-measured spectral responses of the device, results shown in Figure 2-10(d,f), respectively. Precise numerical modeling of the device has been developed using a transfer matrix method, taking into account the effect of dispersion, waveguide loss and fabrication errors [7].

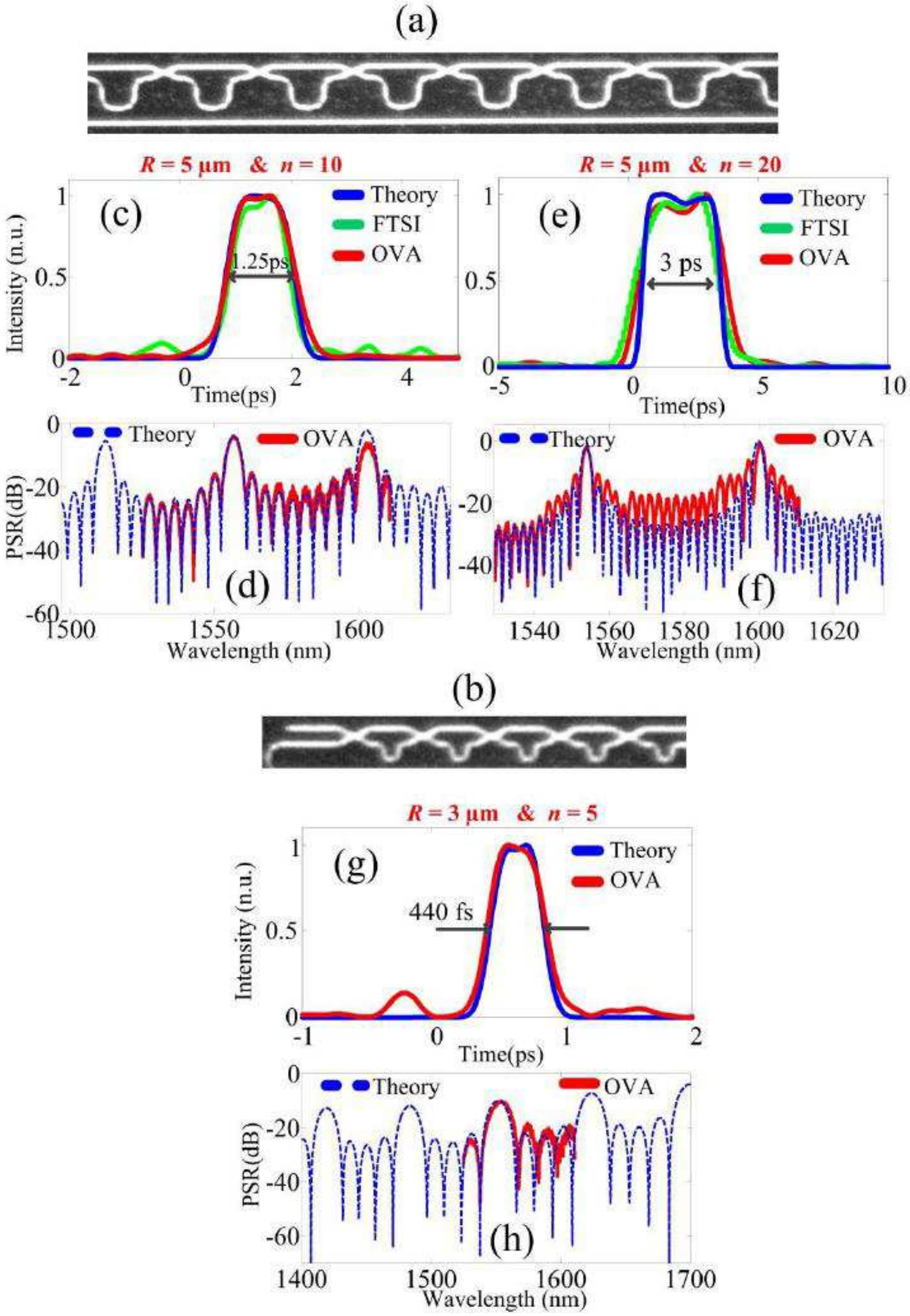

Figure 2-10 Micrographs, taken using a camera mounted on a microscope, from part of the fabricated devices with R = 5 µm and 3 µm (a and b, respectively); The simulated and measured amplitude temporal response and power spectral response (PSR) of a device consisting of n = 10 identical cascaded couplers (c and d, respectively); n = 20 identical cascaded couplers (e and f, respectively); and n = 5 identical cascaded couplers with a shorter delay difference (g and h, respectively). For the temporal waveforms, results are shown from direct FTSI measurements and by Fourier transforming the product of the assumed input Gaussian spectrum with the complex spectral responses measured by an OVA, and as obtained through numerical simulations. (OVA has a spectral measurement range from 1520nm to 1610nm).

It is important to note that the OVA-measured spectra comprise the corresponding device PSR combined with the spectral response of the grating couplers. The coupler itself shows a passband response centered at 1535 nm with a 3 dB bandwidth of approximately 40 nm. It is worth noting that in the presented results, the response of the grating-coupler structure has been subtracted from the OVA-measured spectra. The minimum value of the insertion loss (fiber-to-fiber) for the ~180-μm waveguide connecting two grating couplers to each other has been measured to be 28.7 dB at 1535 nm.

The results shown in Figure 2-10 confirm that the obtained transform-limited flat-top pulses are of very high quality, having successfully synthesized a remarkable number of spectral sidelobes, 8 and 18 sidelobes at each side of the PSR sync function for the 1.25-ps and 3-ps pulses, respectively. This is consistent with the expected waveform time-bandwidth product (TBP or ratio between full spectral width and frequency resolution of the synthesized waveform), which is directly dependent on the number of concatenated couplers.

An additional femtosecond-regime flat-top pulse synthesis experiment is reported in Figure 2-10. In this case, five identical couplers have been cascaded with a relative length difference of 6.8 μm (bend radius of 3 μm), corresponding to a time delay of $\tau \simeq 100$ fs. Due to the lack of a sufficiently short (<100-fs) optical pulse in our laboratory, results are shown in Figure 2-10(g) on the simulated temporal output pulse assuming an input Gaussian pulse of 100 fs (FWHM) for the theoretical and OVA measured frequency responses (PSRs shown in Figure 2-10(h)), confirming successful synthesis of a transform-limited 440-fs flat-top pulse.

Finally, we target the synthesis of an eight-bit phase-coded pulse sequence with a symbol rate of 0.3 Tbaud (speed of 0.6 Tb/s) from a 3.2 ps (FWHM) Gaussian-like input pulse. The target consecutive phase shifts are: $0, \pi, \pi/2, 0, 3\pi/2, \pi, 0, 3\pi/2$. In order to show the potential of our proposed method in processing pulses with longer temporal durations, we purposely target a 40-ps long waveform requiring much longer delay lines (nominal value of 588 μm) than for the flat-top cases reported above. Because of the relatively high values of loss in single-mode silicon waveguides, increasing the length of the delay lines will usually lead to a decaying (ramp-like) temporal response instead of the desired flat amplitude response at the output of the device. In order to solve this problem, multi-mode waveguides (MMWs) with strip widths of 1 μm, and strip heights of 220 nm, are implemented to reduce the scattering loss in the delay lines [8]. However, single-mode waveguides (SMWs) are still used in the coupling region and waveguide bends in order to ensure single-mode operation of the device. To excite the fundamental mode of the MMW only, 50 μm-long linear tapers are used for conversion between the SMWs and MMWs (see Figure 2-11(a-b)).

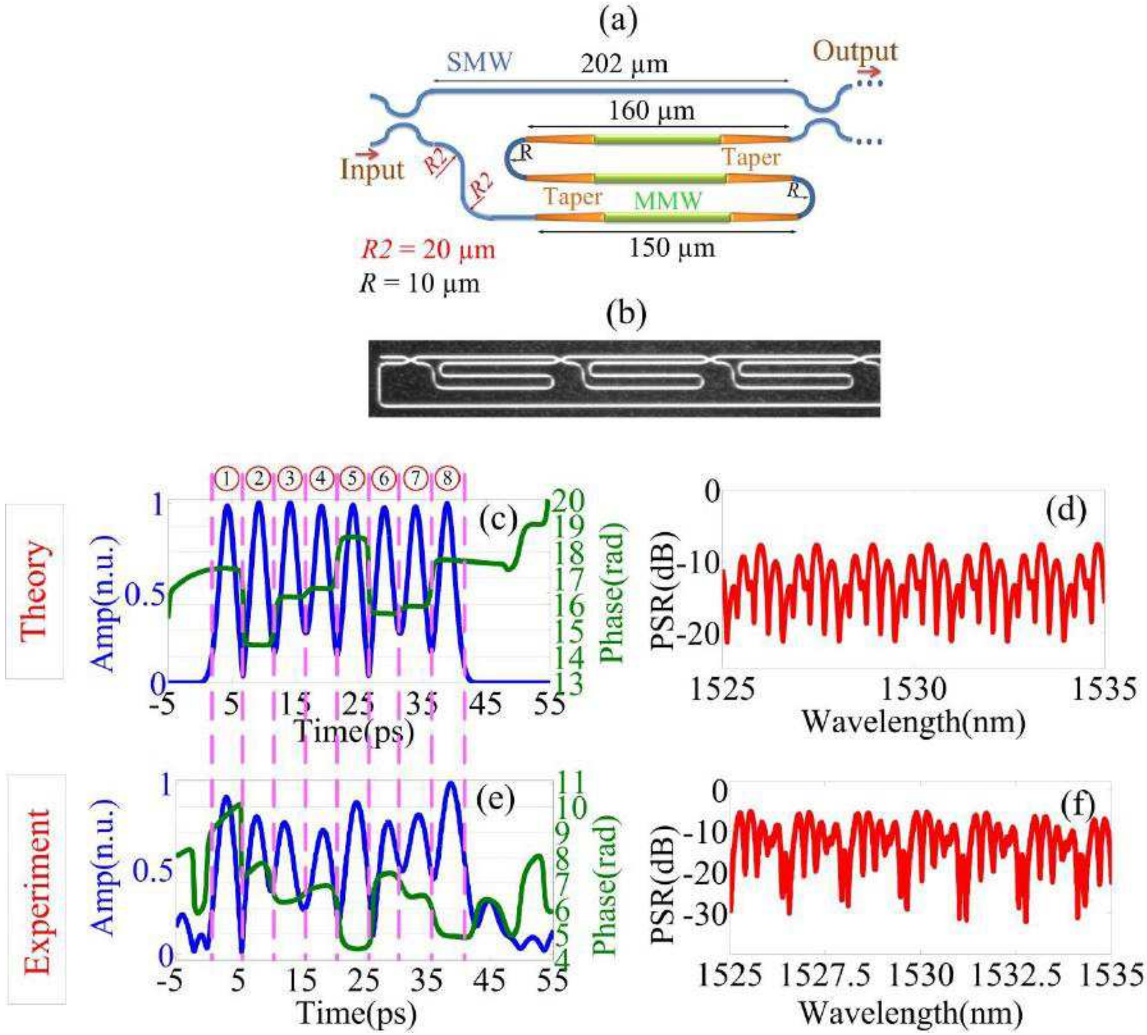

Figure 2-11 (a) Schematic of one stage of the device and (b) micrograph of a section of the fabricated device (c) The theoretically expected temporal and (d) spectral responses. (e) Experimentally measured time-domain output waveform using FTSI characterization and (f) PSR using OVA measurements.

In order to introduce the desired π/*m*-phase-shifts we use the effective refractive index estimations in Figure 2-8, to calculate the extra waveguide length required to achieve the target phase-shift (from Eq. (2.8)). Considering that the estimated effective refractive index at 1550 nm is n_{eff} = 2.426, to achieve π, π /2 and 3π/2-phase-shifts, extra lengths of 319 nm, 160 nm and 479 nm are needed, respectively. These specific numbers are beyond the minimum resolution achievable with the used fabrication process [12] though deviations in the phase shifts are anticipated considering the intrinsic variations in the device fabrication parameters (see further discussions below).

The experimental and theoretical results for the temporal (amplitude and phase) and spectral responses of the device are shown in Figure 2-11.

Moreover, precise values of phase jumps measured experimentally have been compared with the theoretical predictions in Table 1. We refer to a phase level to be ideal when the input pulse is an ideal delta dirac function. For finite-width pulses, variations from the ideal phase values are expected, as shown in the 'Theory' row from numerical simulations. Also note that a 2π phase difference over the nominal phase shift given in Table 2-2 can be observed for some of the theoretical or experimental phase jumps shown in Figure 2-11.

Table 2-2 Precise values of phase jumps for phase coded sequence.

No.	1	2	3	4	5	6	7
Ideal (rad)	3.14	1.57	0	1.57	3.14	0	1.57
Theory (rad)	2.93	1.84	0.33	1.96	2.9	0.3	1.7
Exp. (rad)	2.89	1.55	0.52	2.3	2.97	0.7	1.6

According to the results presented in Figure 2-11 and Table 2-2, a good agreement between simulations and experimental results is generally obtained. We believe that the slight mismatch between the theoretical and measured phase values (Table 2-2) is mainly due to the expected variation in the waveguide length due to fabrication imperfections. Considering a possible maximum error on the waveguides' lengths of ± 5 nm, a phase variation of ~0.3-rad is expected [7], consistently with the obtained measurements. Errors related to the used time-domain signal characterization method (i.e., FTSI) are also expected.

2.2.4 Conclusions

We recall that the demonstrated devices are fully passive so that no additional strategies have been used to tune the devices' parameters to achieve the target waveforms. Whereas this translates into the phase-shift deviations noticed above, within the constraints expected for the used fabrication process, the shown results clearly prove the reliability and robustness of the discrete STM design method for on-chip optical pulse shaping. We also note that this design approach could be adapted for application over a wide range of temporal resolutions, from the sub-picosecond to the sub-nanosecond regime, and it should enable the synthesis of relatively complex (high TBP) temporal waveforms. Moreover, the temporal resolution of the device depends on the differential path length between the bus- and main-waveguides so that adding long phase shifters, as needed to tune the device spatial apodization profile (phase and amplitude), should be possible without affecting the fundamental device performance.

2.2.5 References

[1] A. M. Weiner, *Ultrafast optics*, (John Wiley & sons, 2011).

[2] J. A. Salehi, A. M. Weiner, and J. P. Heritage, "Coherent ultrashort light pulse code-division multiple access communication systems" *Journal of Lightwave Technology*, vol. 8, no. 3, pp. 478-491, 1998.

[3] N. K. Fontaine, D. J. Geisler, R. P. Scott, T. He, J. P. Heritage, and S. J. B. Yoo, "Demonstration of high-fidelity dynamic optical arbitrary waveform generation" *Optics Express*, vol. 18, no. 22, pp. 22988-22995, 2010.

[4] L.-M. Rivas, M. J. Strain, D. Duchesne, A. Carballar, M. Sorel, R. Morandotti, and J. Azaña, "Picosecond linear optical pulse shapers based on integrated waveguide Bragg gratings" *Optics Letters*, vol. 33, no. 21, pp. 2425-2427, 2008.

[5] H. Kogelnik., "An introduction to integrated optics,"*IEEE Transactions on Microwave Theory and Techniques*, vol. 23, no. 1, pp. 2-16, 1975.

[6] Ch. R. Raum, R. Gauthier and R. N. Tait, "Integrated heaters for the thermal tuning of Bragg grating filters on silicon-on-insulator rib waveguides," *Microwave and Optical Technology Letters,* vol. 53, no.3, pp. 672-676, 2011.

[7] H. P. Bazargani, and J. Azaña, "Optical pulse shaping based on discrete space-to-time mapping in cascaded co-directional couplers,"*Optics Express*, vol. 23, no. 18, pp. 23450-23461, 2015.

[8] W. Bogaerts, and S. K. Selvaraja, “Compact single-mode silicon hybrid rib/strip waveguide with adiabatic bends” *IEEE Photonics Journal*, vol. 3, no. 3, pp. 422-432, 2011.

[9] H. P. Bazargani, J. Flueckiger, L. Chrostowski, and J. Azaña, “Microring resonator design with improved quality factors using quarter Bezier curves” in *Conference on Lasers and Electro-Optics: Science and Innovations,* (Optical Society of America, 2015).

[10] L. Lepetit, G. Chériaux, and M. Joffre, "Linear techniques of phase measurement by femtosecond spectral interferometry for applications in spectroscopy," *Journal of the Optical Society of America B*, vol. 12, no. 12, pp. 2467-2474, 1995.

[11] R. J. Bojko, J. Li, T. Baehr-Jones, M. Hochberg and Y. Aida, ”Electron beam lithography writing strategies for low loss, high confinement silicon optical waveguides*,” Journal of Vaccuum Science & Technology B*, vol. 29, no. 6, pp. 06F309, 2011.

2.3 Long duration optical pulse shaping and complex coding on SOI

Abstract: This paper evaluates novel design strategies to enhance the performance of a recently proposed waveguide-based pulse shaping method, namely discrete space-to-time mapping (D-STM), demonstrating the capability of the method to shape pulse waveforms with durations in the tens of picoseconds regime. In particular, we experimentally synthesize 70-ps high-quality flat-top pulses and a 40-ps-long 200-Gbaud 16-quadrature amplitude modulation (QAM) data sequence using D-STM in concatenated co-directional couplers. Our proposed devices have been fabricated on silicon-on-insulator (SOI) technology using ultraviolet and single-etch electron-beam (E-Beam) lithography processes. The fabricated devices are all-passive, functioning without need of post-fabrication tuning, which proves further the robust performance of the proposed scheme.

Published in IEEE Photonics Journal, vol. 8, no. 4, pp. 1-7, 2016.

H. P. Bazargani, M. Burla, Z. Chen, F. Zhang, L. Chrostowski, and J. Azaña

2.3.1 Introduction

Optical pulse shaping (OPS) and coding has been extensively explored for a variety of applications in optical signal processing and telecommunication [1-2]. Temporal waveforms with resolutions in the (sub-) picosecond range and long temporal durations, in the tens of picosecond regime and above, are particularly interesting for coding, switching and processing of long data sequences [3]. The well-established spatial-domain processing approach, based on spectral shaping, allows for programmable synthesis of arbitrary waveforms with sub-picosecond resolutions. However, this approach exhibits a limited frequency resolution, e.g., ~10 GHz for commercial wave-shapers, which places a constraint on the temporal duration of the re-shaped pulses below ~100 ps. Additionally, this method is relatively complex, bulky and costly, requiring the use of precisely aligned high-quality free-space components [3]. On-chip arrayed diffraction gratings (ADGs), working based on a similar operation principle, offer relative compactness (size of 16 mm × 11-mm) but sensitivity to fabrication errors makes their design and fabrication process challenging [4]. Moreover, their minimum spectral resolution is again severely limited, e.g., a minimum channel spacing of 25 GHz (corresponding to a maximum temporal duration below ~40 ps) has been realized in a SOI technology platform [5]. Note that high-resolution ADGs with channel spacing of ~ 5 GHz have been previously demonstrated using III-V materials, e.g. InP [6], requiring a considerably large foot-print of 21 mm × 22 mm [6].

Targeting compact and relatively simpler devices for OPS, fiber and integrated-waveguide grating structures have attracted considerable attention [7]. However, short-period (Bragg) and long-period apodized gratings have proven challenging to fabricate in integrated-waveguide configurations, particularly over long grating lengths, as required to synthesize long duration pulse shapes. Bragg grating (BG) filters have been designed on spiral-shape waveguides with bandwidths as narrow as ~12 GHz but for unconventional transverse magnetic (TM) mode operation [8].

To overcome the aforementioned limitations, we have recently proposed and experimentally demonstrated a compact on-chip OPS design based on weakly-coupled cascaded co-directional couplers, and have shown the capability of this approach to achieve sub-picosecond temporal resolutions [9,10]. Based on this design, the so-called discrete apodization profile of cascaded co-directional couplers can be directly mapped into the output temporal response of the device. The apodization profile is controlled both in amplitude and phase by tuning the coupling strength and relative time-delay between the two waveguides connecting consecutive couplers at each stage of the device, respectively. This direct mapping of apodization profile into the output temporal response is referred to as discrete space-to-time mapping (D-STM) [9]. Implementing D-STM, results in a notable simplicity in design and fabrication of pulse shapers on-chip. Previous experimental demonstrations of on-chip D-STM have achieved sub-picosecond intensity-only and phase-only OPS. In particular, flat-top pulses with duration ranging from 440 fs up to ~3 ps, and an 8-bit 0.6-Tbit/s phase-coded pulse sequence with 4 different phase levels have been successfully generated in silicon [10].

In this work, we develop design strategies to extend the operation range of the D-STM approach for synthesizing pulse waveforms with significantly longer temporal durations, in the tens-of-picoseconds regime. We also target the generation of a complex amplitude and phase coded bit-sequence to further illustrate the potential of D-STM method for advanced OPS applications. In particular, we experimentally demonstrate the re-shaping of a picosecond Gaussian optical pulse into (i) high-quality ~70-ps flat-top pulses, and (ii) a 40-ps 16-QAM bit pattern, using all-passive devices in SOI technology (with no post-fabrication tuning process involved). These set of devices have small foot-prints of 30 μm × 3 mm, and 50 μm × 5.6 mm, respectively.

2.3.2 Operation principle

Briefly, the theory of D-STM indicates that the temporal impulse response of a cascaded co-directional couplers' scheme is a scaled replica of the discrete sequence of coupling coefficients. As shown in Figure 2-12, the sampling time of the impulse response, τ , is defined by the relative length difference ΔL between the sections of the top waveguide and the bottom waveguides connecting the corresponding ports of consecutive couplers.

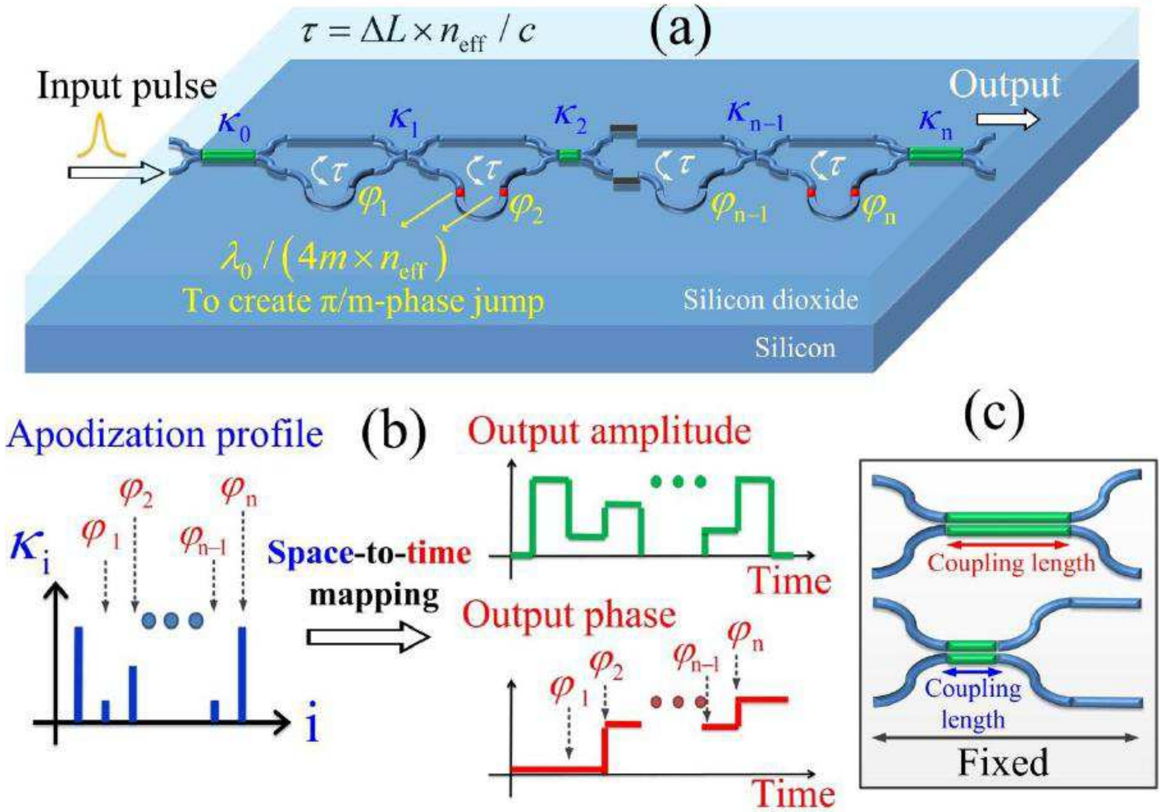

Figure 2-12 (a) Schematic representation of OPS device using D-STM; (b) The process of mapping device's apodization profile to its output amplitude and phase temporal response; (c) Amplitude shaping is done by tuning the coupling length of directional couplers.

In particular $\Delta L = \tau c / n_{eff}$, where n_{eff} is the effective refractive index of the waveguide and c is the speed of light in vacuum. Additionally, a relative π / m -phase-shift may be introduced at a desired point of the impulse response, by changing the relative length difference ΔL after the corresponding coupler to $\Delta L + \lambda_0 / \left(2m \times n_{eff}\right)$. The central assumption for D-STM to work is to satisfy the weak-coupling condition, i.e. strictly, $\sum_{i=0}^{n-1} \kappa_i < 0.1$, where κ_i is the power coupling ratio of the *i*-th coupler and *n* is the number of cascaded couplers. This condition limits the power spectral efficiency of the method to a maximum of ~50% [9]. Details about the modelling of the device using transfer-matrix method (TMM) considering different sources of error, including waveguide dimensional variations, dispersion and loss are provided in [9].

Synthesizing optical pulse shapes with long durations inevitably requires long waveguide delay-lines (e.g. in sub-mm or mm range). In a high-index contrast platform such as SOI waveguide loss and dimensional variations, causing the so-called ‘phase noise’, makes it difficult to realize such long waveguides. Moreover, simultaneous complex amplitude and phase coding so far has been possible only using active electro- or thermo-optics tuning elements [4].

The aim of this paper is not to provide a precise analysis of the phase-noise, as this topic is well-studied in many previous works, e.g. [11,12]. We rather use design strategies to mitigate the effect of waveguide thickness variations, side-wall roughness and waveguide loss on the performance of our proposed OPS technique in order to further extend its operation range. Additionally, we explore on-chip 16-QAM bit-sequence generation using the D-STM method based on an all-passive device.

As illustrated in Figure 2-13, we first use Lumerical Mode Solutions software to study the effect of waveguide width and height variations on n_{eff} of the fundamental quasi-TE mode at the wavelength of 1550 nm. The cladding and buried oxide layers are made of silicon dioxide with heights of 2 μm and 3 μm, respectively.

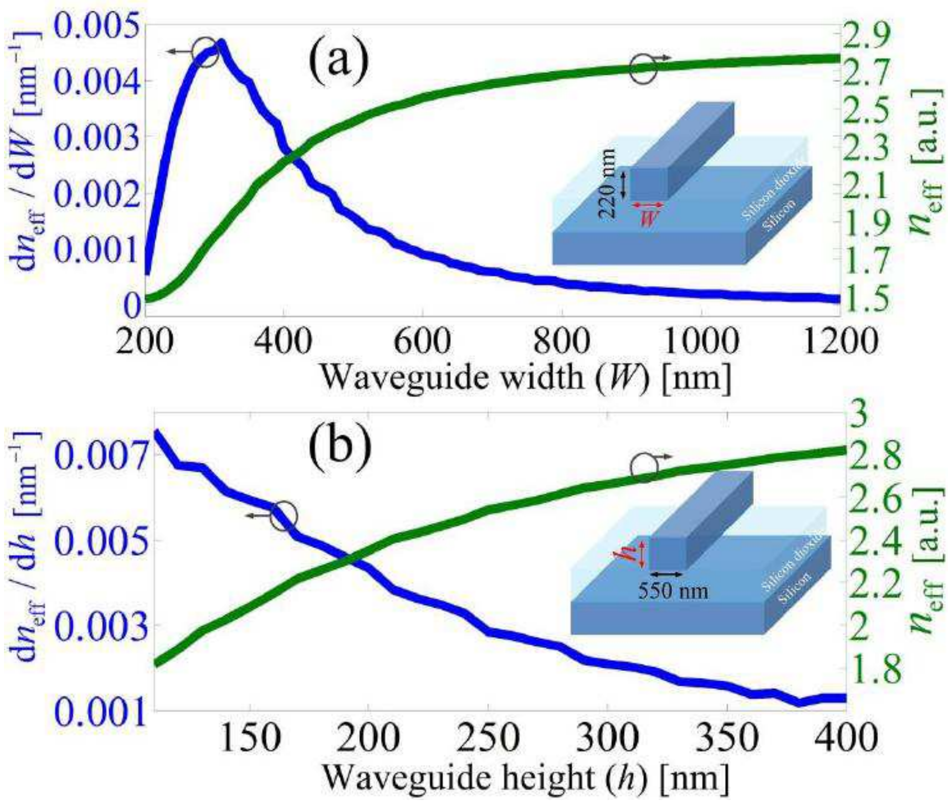

Figure 2-13 The effective refractive index of the fundamental quasi-TE mode and its sensitivity to waveguide (a) width and (b) height variations at the wavelength of 1550 nm [11].

Waveguide width variations, referred to as side-wall roughness, are introduced by lithography and etching processes. Whereas, waveguide height variations mostly caused by non-uniformities of the SOI wafer [12]. Based on the results shown in Figure 2-13(a), n_{eff} is much less sensitive to the waveguide width variations for photonic wires wider than ~1000 nm. In particular, the parameter defined to study the sensitivity ($\mathrm{d}n_{eff} / \mathrm{d}W$) is almost constant for these sets of waveguides. Consequently, using wide waveguides can be considered as a solution to mitigate the effect of phase-noise for long delay-lines [13,14]. Additionally, according to simulation results illustrated in Figure 2-13(b), the sensitivity of n_{eff} to waveguide height variations ($\mathrm{d}n_{eff} / \mathrm{d}h$) reduces for thicker waveguides. In foundry-based fabrication runs the waveguide height is predefined (e.g. standard 220 nm) and cannot be engineered by the designer. A technique to reduce the sensitivity to wafer nonuniformities is to design long delay-lines in a very compact form, e.g. using serpentine or spiral shape waveguides [11,13].

In this work, the output pulse shape is synthesized by properly combining delayed/weighted replicas of an input pulse. By increasing the length of the delay-lines, the copies of the input pulse at primary stages of the device will experience much higher values of loss. This is equivalent to time-domain convolution of the target output waveform with a ramp-like pulse shape. Consequently, design strategies are required to reduce the propagation loss in the single-mode strip waveguides. As discussed above, propagation losses in strip waveguides can be reduced by making the photonic wires wider. However, waveguides wider that 500 nm (assuming waveguide height of 220 nm) start supporting higher order modes. The presence of higher order modes is undesirable as it may lead to dispersion and unpredictable behaviour of devices that rely on interference between different optical modes [13-16]. A solution for this is to use hybrid waveguides in which a single mode waveguide (SMW) is coupled by a taper to a multimode waveguide (MMW) and vice versa. An adiabatic taper between the two waveguide regions ensures the excitation of the fundamental mode in the multimode region. Although the multimode region can support higher order modes, as long as the waveguide is straight and free of defects, the fundamental mode will propagate without exciting higher order modes. Despite the fact that defects and roughness do excite higher modes in MMW, but these modes cannot propagate in the SMW sections and therefore merely cause a loss. Implementing this technique almost thirty-fold improvement in terms of propagation loss has been reported [13-16].

2.3.4 Experiment

Our first experimental target waveforms are flat-top pulses with duration in the range of ~70 ps synthesized from 3 ps, 5 ps and 6 ps input optical Gaussian pulses, which are directly generated from a passively mode-locked fiber laser (Pritel) with a repetition rate of 16.8 MHz. The carrier wavelengths of different optical pulses are tuned at the resonance wavelength of each device. MMWs with the dimension of 1 μm (width) × 220 nm (height) are connected to SMWs with 52 μm-long linear tapers to form the hybrid sections (see Figure 2-14(a-b)). Note that SMWs are still used in the coupling region and waveguide bends in order to ensure single-mode operation of the device. Besides, Bezier bends have been used to further reduce the loss in the delay-lines [13,15]. Long delay-lines have been formed in serpentine-like shapes reducing the effect of waveguide height variations. These sets of devices were fabricated at IMEC using a CMOS-compatible process with 193 nm deep ultraviolet (UV) lithography on SOI wafer. Light has been coupled in/out of the device using a fiber array placed carefully on the top of input/output grating couplers (GCs). In particular, we have designed 3 pulse shapers with 7, 9 and 13 identical cascaded couplers. The concatenated couplers in all the devices have a coupling gap of 200 nm and zero coupling length. Based on 3D finite difference time domain (FDTD) simulation a power coupling ratio of ~0.001 has been estimated for each coupler [9]. An effective coupling larger than zero could be achieved due to the effect of the coupler bend regions.

The devices' power spectral responses (PSRs) have been measured using an Optical Vector Analyzer (OVA) with a spectral resolution of 1.6 pm; see Figure 2-14(c-e). It is important to note that the OVA-measured spectra comprise the corresponding device PSR combined with the spectral response of the GCs. Thus, in the presented results, the response of the grating-coupler structure has been subtracted from the OVA-measured spectra. The minimum value of the insertion loss (fiber-to-fiber) for the ~180-μm test waveguide connecting two grating couplers to each other has been measured to be 19 dB at 1525 nm and the amount of loss measured for the device consisting of 7 stages is equal to 6 dB. The amount of loss decreases by ~2 dB as we increase the number of cascaded couplers to 13. Direct time-domain characterization of the output, synthesized waveforms has been carried out using Fourier-transform spectral interferometry (FTSI) where the input pulse itself is used as the reference [10,17]. As shown in Figure 2-14(f-h), from left to right, nearly identical flat-top pulses are re-shaped from Gaussian waveforms with shorter temporal durations, correspondingly to the increased frequency bandwidth (and time-bandwidth product) of the devices. Finally, band-pass filtering the spectrum of the output signals, one can observe the target flat-top waveforms; see Figure 2-14(i-k).

In order to compare the quality of output pulses a figure of merit called time-bandwidth product (TBP) has been defined. TBP is the ratio between maximum to minimum signal bandwidth that can be processed with a prescribed precision. The former is determined by the pulse's minimum temporal features (resolution) and the latter, by the over-all pulse duration in time. The TBPs of the devices with 7, 9 and 13 cascaded couplers are 11.67, 14 and 23.3, respectively, showing that increasing the number of cascaded couplers, while keeping the over-all pulse duration fixed, leads to improvement in pulse quality.

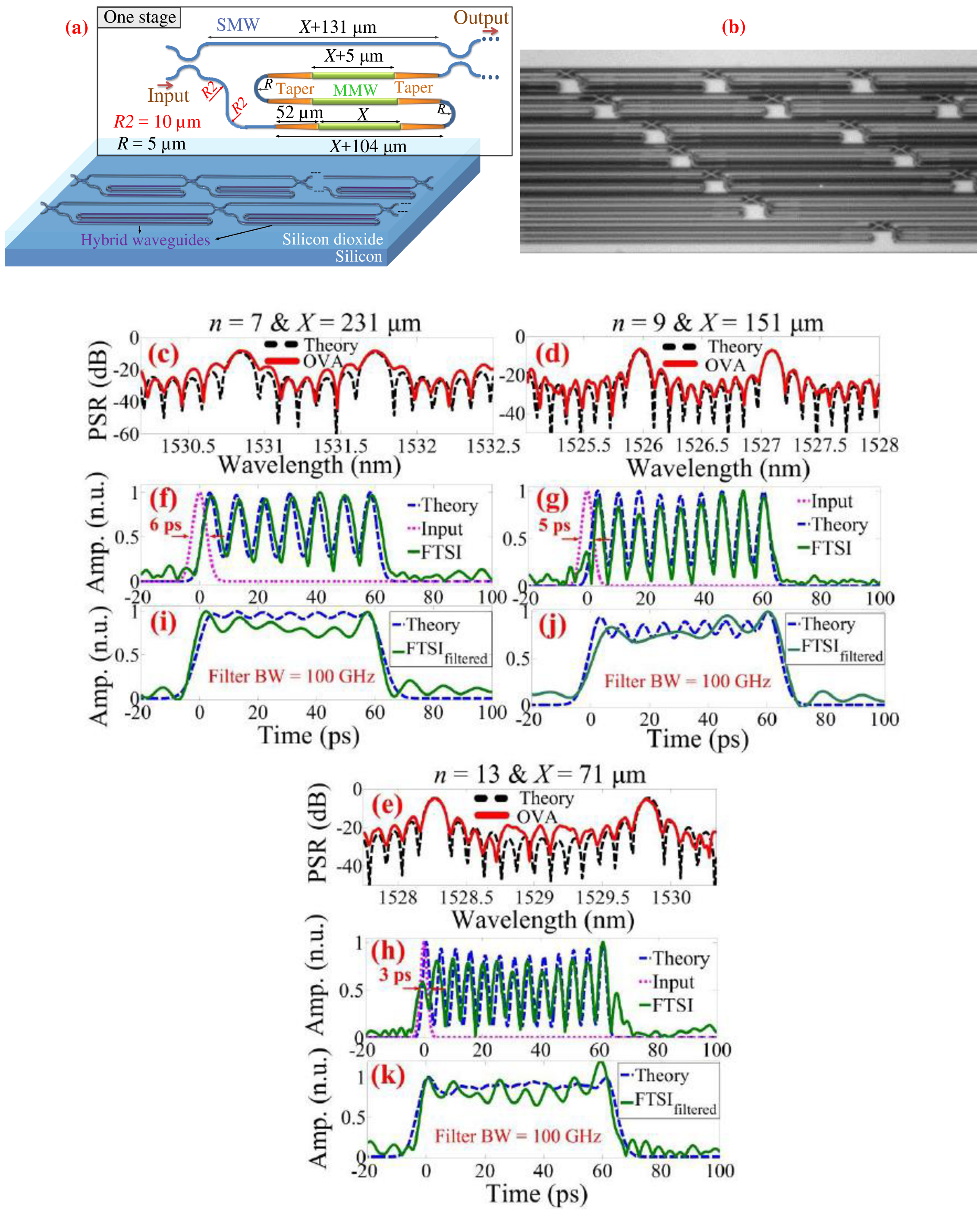

Figure 2-14 (a): Schematic of the flat-top pulse generators (X: the waveguide length and n: number of cascaded couplers); (b): Micrograph of parts of designed pulse shapers; (c-e): Simulated and measured PSRs using OVA; (f-g): Theoretically expected and experimentally measured temporal responses of the devices using an FTSI method; (i-k): Band-pass filtered temporal waveforms in order to realize the flat-top pulse shapes (the filters have a 3dB bandwidth of 100 GHz).

The second target waveform is an 8-bit amplitude and phase modulated bit sequence synthesized from an input 2.5-ps optical Gaussian pulse. 24 directional couplers are connected in series through 114-μm relative delay-lines ($\tau \simeq 1.66$ ps) to generate a 0.2-Tbaud (0.8-Tbit/s) 16-QAM complex modulated bit sequence. Each symbol in the sequence is realized using three consecutive stages (see Figure 2-15(a)). The constellation diagram of the sequence is shown in Figure 2-15(b).

The device is made of SMWs and the fabrication has been carried out using a single-etch, E-Beam Lithography at the University of Washington. The Bezier bends with a radius of 50-μm have been incorporated in all delay-lines. Directional couplers, each with a nominal coupling gap of 300 nm and coupling lengths of 6.2 μm, 4.4 μm, 1.5 μm or 0 μm, have been cascaded in series, realizing four different amplitude levels. Despite the difference in the coupling length, aimed at controlling the pulse amplitude at the corresponding time slot, the overall length of all directional couplers is fixed to ensure in-phase superposition of the different copies of the input pulse at each stage of the device, see Figure 2-12(c). Time-domain characterization has been carried out using a similar FTSI method as in the previous example. Figure 2-15(d-e) show the simulation results and experimentally measured temporal amplitude and phase profiles from the described design.

Note that, in this experiment GCs have a response which is centered at 1535 nm with a 3 dB bandwidth of ~40 nm. The minimum value of the insertion loss (fiber-to-fiber) for the ~180-μm test waveguide connecting two grating couplers to each other has been measured to be 28.7 dB at 1535 nm. After normalizing the PSR of the device with the response of the GCs, device loss has been measured to be 6.5 dB.

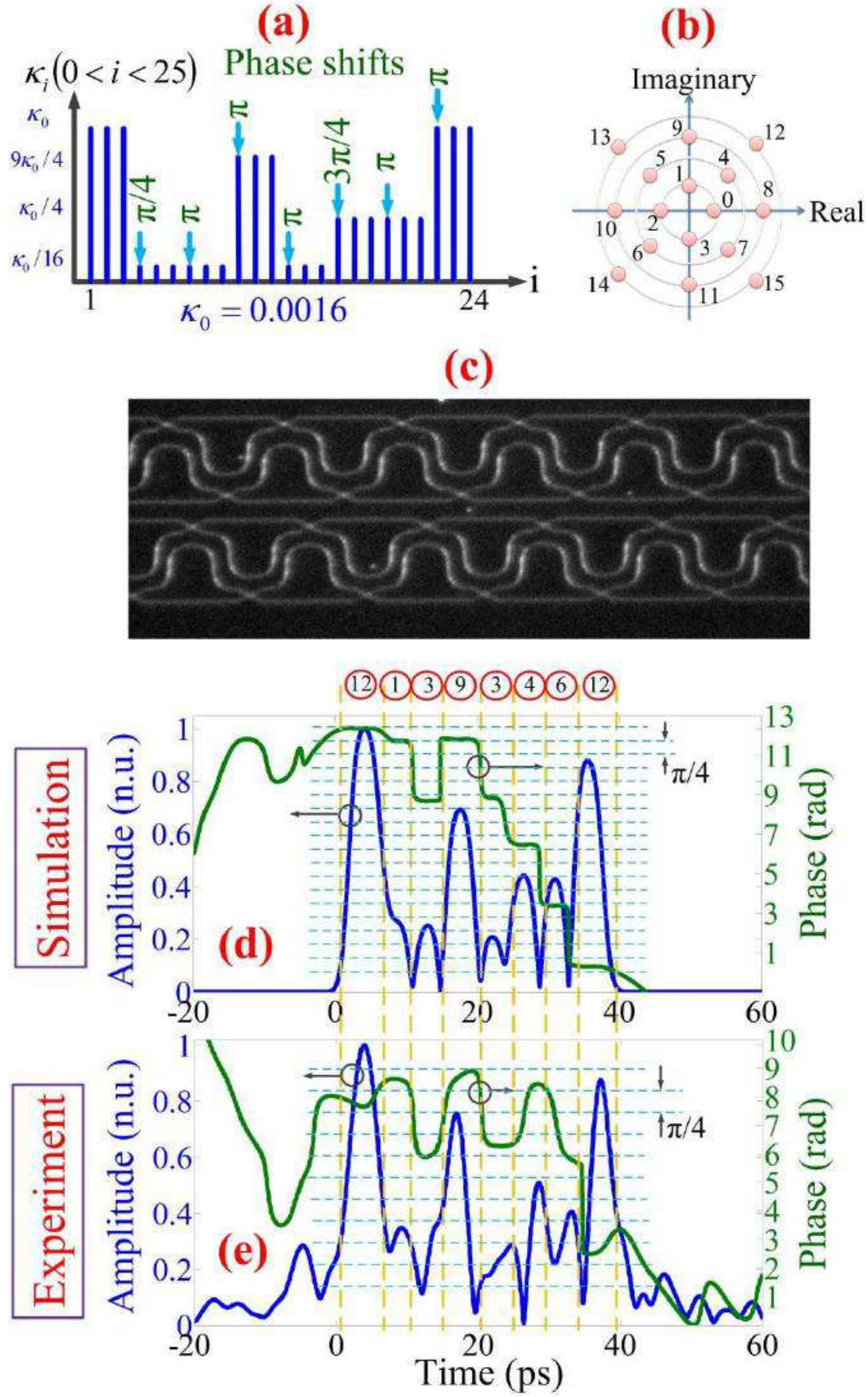

Figure 2-15 (a) Power coupling ratio at each stage of the device and introduced phase levels; (b) Constellation diagram of circular 16-QAM bit pattern; (c) Micrograph of part of the fabricated devices; (d) The theoretically expected and (e) experimentally measured temporal response of the device. The target consecutive phase shifts are: $0, \pi/4, \pi, \pi, \pi, 3\pi/4, \pi, \pi$ and the amplitude levels are 1, 1/4, 1/4, 3/4, 1/4, 2/4, 2/4, 1.

The precise values of amplitude and phase are given in Table 2-3. The amplitude/phase level is considered to be ideal when the input pulse is an ideal delta dirac function. For pulses with finite temporal durations, variations from the ideal values are expected, as shown in the "simulation" row from numerical analysis. Moreover, we attribute the slight mismatch between the simulation and measured phase/amplitude levels to the expected variation in the waveguide height and width due to fabrication imperfections, and to measurement uncertainties. Detailed simulations show that a maximum phase-error of ~0.3-rad and ~21% amplitude variations are expected for this technology platform [9], consistent with the obtained results.

Table 2-3 Comparison between the precise values of phase (in rad) and amplitude levels (theory versus experiment)

Bit no.	1	2	3	4	5	6	7	8
Ideal (Ph./Am)	0 / 1	0.63/0.25	2.93/0.23	3.05/0.69	2.84/0.2	2.29/0.44	3/0.42	3.09/0.87
Theory(Ph./Am)	0 /1	0.63/0.25	2.93/0.23	3.05/0.69	2.84/0.2	2.29/0.44	3/0.42	3.09/0.87
Exp. (Ph./Am)	0 / 1	0.9/0.34	2.73/0.34	2.99/0.76	2.62/0.24	2.16/0.5	2.67/0.4	3.39/0.87

2.3.5 Conclusions

In this work we have experimentally demonstrated on-chip OPS with durations in tens-of-picosecond regime. These sets of results are complementary to our previously presented work in sub-picosecond OPS proving the capability of D-STM approach for synthesizing pulse shapes over a wide range of temporal durations using very compact device sets.

2.3.5 References

[1] P. C. Teh, M. Ibsen, J. H. Lee, P. Petropoulos, and D. J. Richardson, "Demonstration of a four-channel WDM/OCDMA system using 255-chip 320-Gchip/s quarternary phase coding gratings" *IEEE Photonics Technology Letters,* vol. 14, no. 2, pp. 227-229, 2002.

[2] J. Azaña, L. K. Oxenløwe, E. Palushani, R. Slavik, M. Galili, H. Hans chriatian, H. Hu, A. Clausen, and P. Jeppesen, "In-fiber subpicosecond pulse shaping for nonlinear optical telecommunication data processing at 640 Gbit/s," *Interntional Journal of Optics*, vol. 12, pp. 1-16, 2011.

[3] A. M. Weiner, *Ultrafast optics*, John Wiley &Sons, 2011.

[4] N. K. Fontaine, D. J. Geisler, R. P. Scott, T. He, J. P. Heritage, and S. J. B. Yoo, "Demonstration of high-fidelity dynamic optical arbitrary waveform generation," *Optics Express,* vol. 18, no. 22, pp. 22988-22995, 2010.

[5] S. Cheung, T. Su, K. Okamoto, and S. J. B. Yoo, "Ultra-compact silicon photonics 512×512 25 GHz arrayed waveguide grating router," *IEEE Journal of Selected Topics in Quantum Electron*ics, vol. 20, no. 4, pp. 1-7, 2013.

[6] W. Jiang, K. Okamoto, F. M. Soares, F. Olsson, S. Lourdudoss, and S. J. B. Yoo, "5 GHz channel spacing InP-based 32-channel arrayed waveguide grating," *Optical Fiber Communication Conference* (*OFC*)*,* San Diego, CA, 2009.

[7] L.-M. Rivas, M. J. Strain, D. Duchesne, A. Carballar, M. Sorel, R. Morandotti, and J. Azaña, "Picosecond linear optical pulse shapers based on integrated waveguide Bragg gratings,"*Optics Letters,* vol. 33, no. 21, pp. 2425-2427, 2008.

[8] Z. Chen, J. Flueckiger, X. Wang, F. Zhang, H. Yun, Z. Lu, M. Caverley, Y. Wang, N. A. F. Jaeger, and L. Chrostowski, "Spiral Bragg grating waveguides for TM mode silicon photonics," *Optics Express,* vol. 23, no. 19, pp. 25295-25307, 2015.

[9] H. P. Bazargani, and J. Azaña, "Optical pulse shaping based on discrete space-to-time mapping in cascaded co-directional couplers," *Optics Express,* vol. 23, no. 18, pp. 23450-23461, 2015.

[10] H. P. Bazargani, M. Burla, and J. Azaña, "Experimental demonstration of sub-picosecond optical pulse shaping in silicon based on discrete space-to-time mapping," *Optics Letters,* vol. 40, no. 23, pp. 5423-5426, 2015.

[11] A. D. Simard, G. Beaudin, V. Aimez, Y. Painchaud, and S. LaRochelle, "Characterization and reduction of spectral distortions in Silicon-on-Insulator integrated Bragg gratings," *Optics Express,* vol. 21, no. 20, pp. 23145-23159, 2013.

[12] S. K. Selvaraja, W. Bogaerts, P. Dumon, D. V. Thourhout, R. Baets, "Subnanometer linewidth uniformity in silicon nanophotonic waveguide devices using CMOS fabrication

technology," *IEEE Journal of Selected Topics in Quantum Electron*ics, vol. 16, no. 1, pp. 316-324, 2010.

[13] M. A. Guillén-Torres, K. Murray, H. Yun, M. Caverley, E. Cretu, L. Chrostowski, and N. A. F. Jaeger, "Effects of backscattering in high-Q, large–area silicon-on-insulator ring resonators," *Optics Letters,* vol. 41, no. 7, pp. 1538-1541, 2016.

[14] H. Lee, T. Chen, J. Li, O. Painter, and K. J. Vahala, "Ultra-low-loss optical delay line on a silicon chip," *Nature Communications* **3**, no. 867, pp. 1-7, 2012.

[15] H. P. Bazargani, J. Flueckiger, L. Chrostowski, and J. Azaña, "Microring resonator design with improved quality factors using quarter Bezier curves," *Conference on Lasers and Electrooptics* (*CLEO*)*,* San Jose, CA, 2015.

[16] W. Bogaerts, and S. K. Selvaraja, "Compact single-mode silicon hybrid rib/strip waveguide with adiabatic bends," *IEEE Photonics Journal*, vol. 3, no. 3, pp. 422-432, 2011.

[17] L. Lepetit, G. Chériaux, and M. Joffre, "Linear techniques of phase measurement by femtosecond spectral interferometry for applications in spectroscopy," *Journal of the Optical Society of America B,* vol. 12, no. 12, pp. 2467-2474, 1995.

Chapter 3 On-chip optical signal processing (filtering)

In this chapter, we present our two journal publications with the focus on optical signal processing, in particular filtering. In the first paper we show that two photonic Hilbert transformers (PHTs) incorporated into a Michelson interferometer can provide tunable, nondispersive band reject/band pass filtering operation. As the first demonstration, the design has been carried out based on using apodized fiber/silica planar waveguide Bragg gratings. In the quest for high-quality PHTs to realize the proposed filter design on SOI, we have proposed and experimentally demonstrated PHT designs based on laterally apodized waveguide Bragg grating on silicon-on-insulator (SOI). In particular, high-performance photonic integer and fractional-order Hilbert transformers, with processing bandwidths above 750 GHz, have been experimentally realized

3.1 Tunable, non-dispersive optical filter using photonic Hilbert transformation

Abstract: We propose and numerically demonstrate a new design concept for implementing non-dispersive complementary (band-pass/band-reject) optical filters with a wide range of bandwidth tunability. The device consists of two photonic Hilbert transformers (PHTs) incorporated into a Michelson interferometer (MI). By controlling the central frequency of PHTs with respect to each other, both the central frequency and the spectral width of the rejection/pass bands of the filter are proved to be tunable. Bandwidth tuning from 260 MHz to 60 GHz is numerically demonstrated using two readily feasible fiber Bragg grating-based PHTs. The designed filter offers a high extinction ratio between the pass band and rejection band (>20dB in the narrow-band filtering case) with a very sharp transition with a slope of 170 dB/GHz from rejection to pass band.

Published in Optics Letters, vol. 39, no. 17, pp. 5232-5235, 2014.

H. P. Bazargani, M. R. Fernández-Ruiz and J. Azaña

3.1.1 Introduction

Tunable band-pass/band-reject filters are highly demanded for a range of important applications in wavelength-division-multiplexing (WDM) telecommunications systems and all-optical signal processing. Various architectures have been previously proposed to construct tunable optical filters, including waveguide grating routers [1], and all-pass ring resonators in a Mach-zehnder interferometer (MZI) configuration [2]. However, the response of these types of filters is intrinsically periodic in the frequency domain and the pass-band spectral width cannot be generally tuned over a wide range. Uniform-period Bragg gratings (BGs) have been also used for narrow-band optical filtering. However, the bandwidth of these filters is not tunable and the minimum spectral width achievable, considering standard fabrication limitations, is in the range of at least a few gigahertz [3]. Alternatively, phase-shifted fiber Bragg grating (FBG) devices operated in transmission have been designed to achieve ultra-narrow-bandwidth (< 1GHz) optical filters of specific interest for a variety of signal-processing applications [4], in the context of microwave photonics. However, in these schemes, the spectral width of the signal to be filtered should be smaller than the overall reflection bandwidth of the grating, which is typically limited to several tens of GHz [4]. Segawa et al. proposed a wavelength-tunable filter structure using cascaded MZI with apodized sampled gratings [5]. The filter exhibits a wavelength tuning range of 16 nm, and an extinction ratio of 20 dB. However, the 3 dB transmission bandwidth of this filter could not be tuned and was fixed to be 32 GHz.

In our proposed structure, two photonic Hilbert transformers (PHTs) are incorporated into the two arms of a symmetric Michelson interferometer (MI), implementing a widely tunable, non-dispersive band-pass/band-reject optical filter. Various methods have been demonstrated to implement PHTs, e.g., phase-shifted apodized FBGs [6,7], and integrated apodized BGs [8,9]. Both the bandwidth and the central frequency of our proposed filter design can be tuned by simply modifying the Bragg frequency of one of the gratings with respect to the other, using widely available axial strain or temperature tuning methods [10]. In this paper, a design using readily feasible FBG – based PHTs is numerically simulated, demonstrating the filter's capability for bandwidth tuning from 260 MHz to 60 GHz. The designed filter offers a high extinction ratio (>20 dB for the narrow-band filtering case) with a very sharp transition from rejection to pass band.

3.1.2 Operation principle

A PHT or spectral phase-shifter is essentially an all-pass linear optical filter providing a single phase shift at the filter's central frequency [6,11]. The spectral response of a PHT is $H_{PHT}(f) \propto -j \cdot \mathrm{sgn}(f - f_0)$, where sgn is the Signum function, f is the frequency variable and f_0 is the central frequency of the filter. This defined ideal PHT response is non-causal and thus, physically unrealizable. According to the Paley-Wiener theorem [12], the frequency response of a practical PHT must be band-limited with the required phase alternation occurring in a smooth fashion. The amplitude and phase spectral and temporal responses of an ideal (dashed line) and practical (solid line) PHT are shown in Figure 3-1.

The operation bandwidth of the PHT, BW_{op} is defined as the spectral width of the pass band of the filter where the amplitude reaches half of its maximum value (3 dB bandwidth). Inside the spectral width of the PHT, the phase should have a transition from $\pi/2+\varphi_0$ (low frequency side) to $-\pi/2+\varphi_0$ (high frequency side), in which φ_0 is simply a constant reference phase. The transition between the two levels of phase occurs smoothly along a transition bandwidth of BW_{tr}. Moreover, Figure 3-1(b) shows that the bandwidth specifications BW_{op} and BW_{tr} of the PHT are inversely related to the zero-to-zero width of the side lobes and the total duration of the device's temporal impulse response, respectively [6].

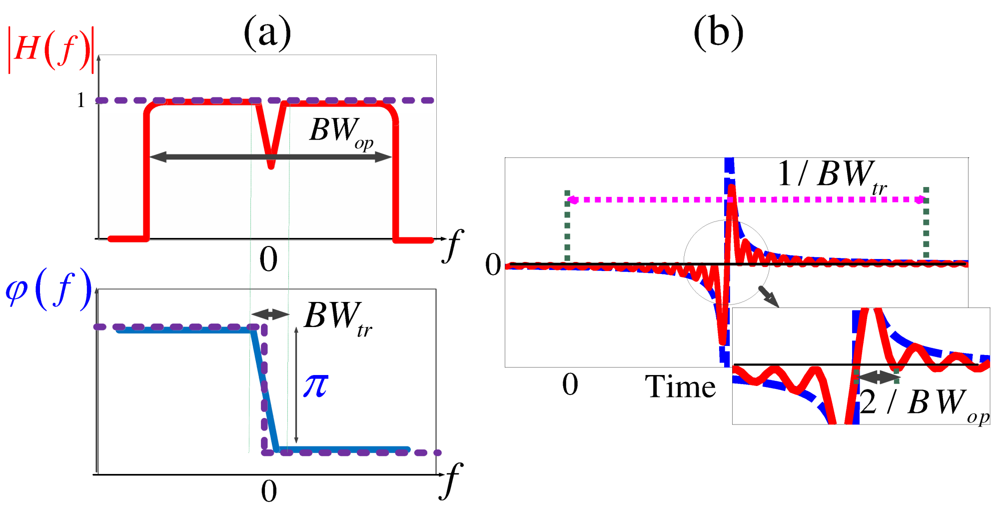

Figure 3-1 (a): Amplitude and phase response of an ideal (dashed-line), and practical (solid-line) PHT. (b): the envelope of the temporal impulse response of an ideal (dashed-line), and a physically realizable PHT (solid-line).

The complementary optical filter concept presented in this paper is schematically shown in Figure 3-2. Two PHTs are incorporated within two arms of a symmetric MI (power coupling coefficient of the coupler is equal to 0.5). The power responses at the two output ports of a MI are related to the squared sine or cosine of $\Delta\varphi/2$, where $\Delta\varphi = \varphi_{H_1} - \varphi_{H_2}$ is the difference between the phase profiles in two arms of MI (φ_{H_1} and φ_{H_2} are the spectral phase profiles of PHTs 1 and 2, respectively). As illustrated in Figure 3-2(b) (cases for minimum and maximum achievable filter's bandwidths), $\Delta\varphi$ is nearly π over a spectral band determined by the frequency shift between the two PHTs and approaches 0 well outside this band. Thus, the proposed structure provides the response of a band-pass filter (BPF) or band-rejection filter (BRF), respectively at the two outputs of the MI. The bandwidth of the BPF/BRF can be easily tuned by shifting the central frequency of any of the PHTs with respect to the other one. Thus, considering the spectral response of practical PHTs (Figure 3-1), the bandwidth of the designed optical filter can be tuned from a minimum value of $\sim 2BW_{tr}$ up to a maximum value of $\sim BW_{op}/2$, see illustrations in Figure 3-2(b). Moreover, the BPF/BRF central operation frequency can also be tuned through proper control of the central frequency of the two PHTs, i.e., by shifting the central frequency of the two PHTs the same amount, while keeping the same relative frequency shift between them.

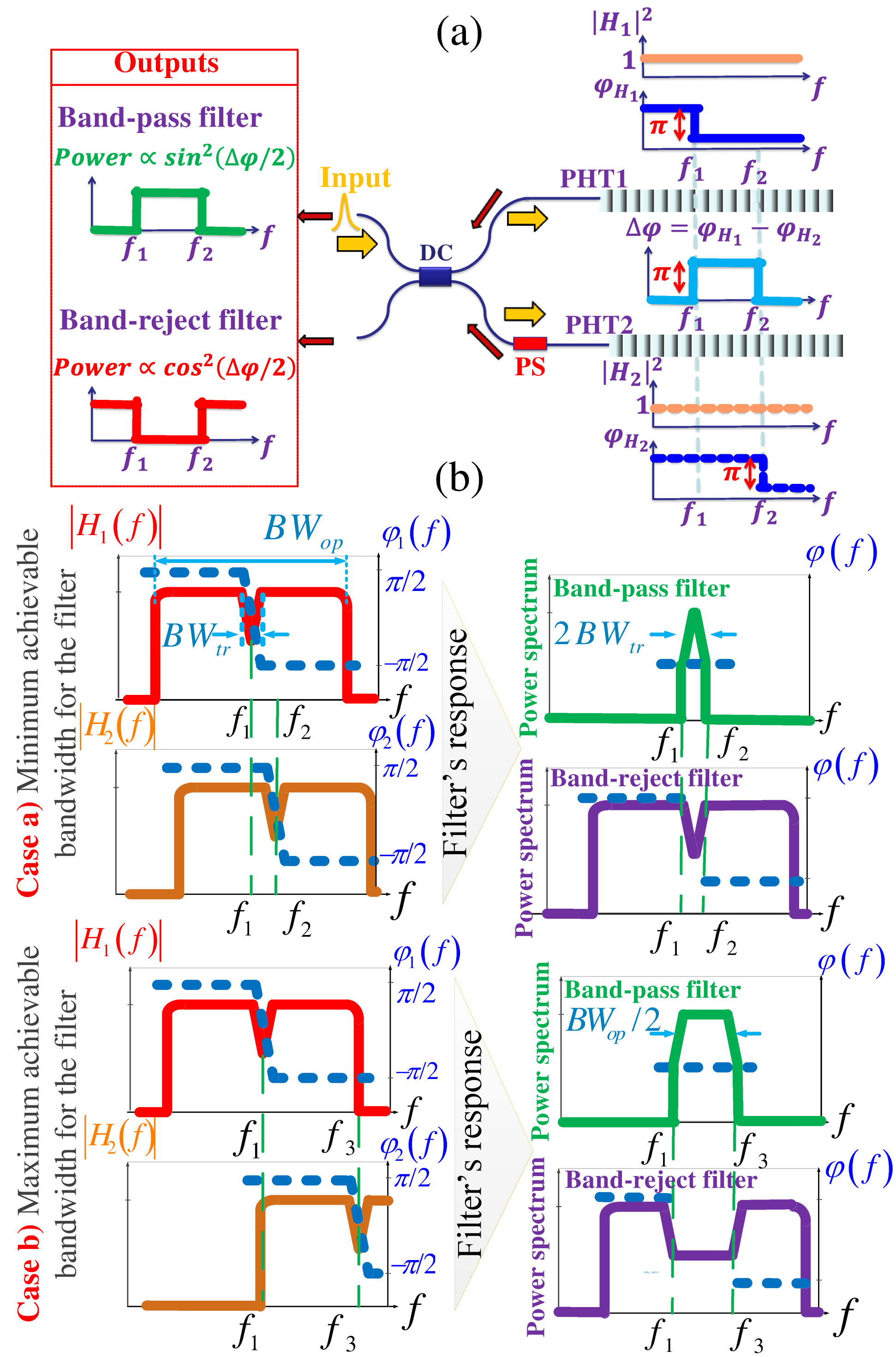

Figure 3-2 (a): Configuration of the proposed optical filter structure. (b): Realization of BPF/BRF at the two output ports of MI. DC: directional coupler, and PS: phase shifter.

It is worth mentioning that the relative phase between the two arms of the MI should be fixed to zero or multiples of 2π, to guarantee the proper functionality of the filter, as described above. This could be done using a phase-modulator driven with a direct current (dc) voltage or a thermo-optic phase shifter (PS in Figure 3-2(a)). An additional interesting feature of the device is that by inducing π/2-phase shift between the two arms of the MI, one could easily switch the port in which band-reject and/or band-pass filters could be realized.

To demonstrate the feasibility and operating range of the proposed scheme, we have numerically modeled a tunable filter based on the use of FBG-based PHTs. Two identical gratings have been designed, and their central wavelength is assumed to be controlled by means of strain/temperature.

To design the PHTs, the required apodization profiles are obtained by means of an inverse scattering algorithm based on Coupled-Mode Theory (CMT) combined with the transfer matrix method (TMM) [13]. The target specifications are those of the FBG–PHTs experimentally demonstrated in Ref. [7], considering $f_0 =$ 193 THz, a 3 dB operation bandwidth BW_{op} = 120 GHz and a maximum reflectivity of 99%. The resulting FBGs have a length of 14.5 cm, and a constant period of 534.89 nm. The refractive index modulation has a maximum value of 8×10^{-4}, and several oscillations are required in the grating apodization profile as shown in Figure 3-3(a). Those oscillations impose the need for three phase jumps, whose positions are marked in red in Figure 3-3(a). In the region of the 14.5 cm-long grating which is not shown in Figure 3-3, the refractive index modulation decays smoothly down to a minimum value of 2×10^{-6}. It is important to consider the whole grating length, since it determines the BW_{tr} of the PHT, as described above (Figure 3-1).

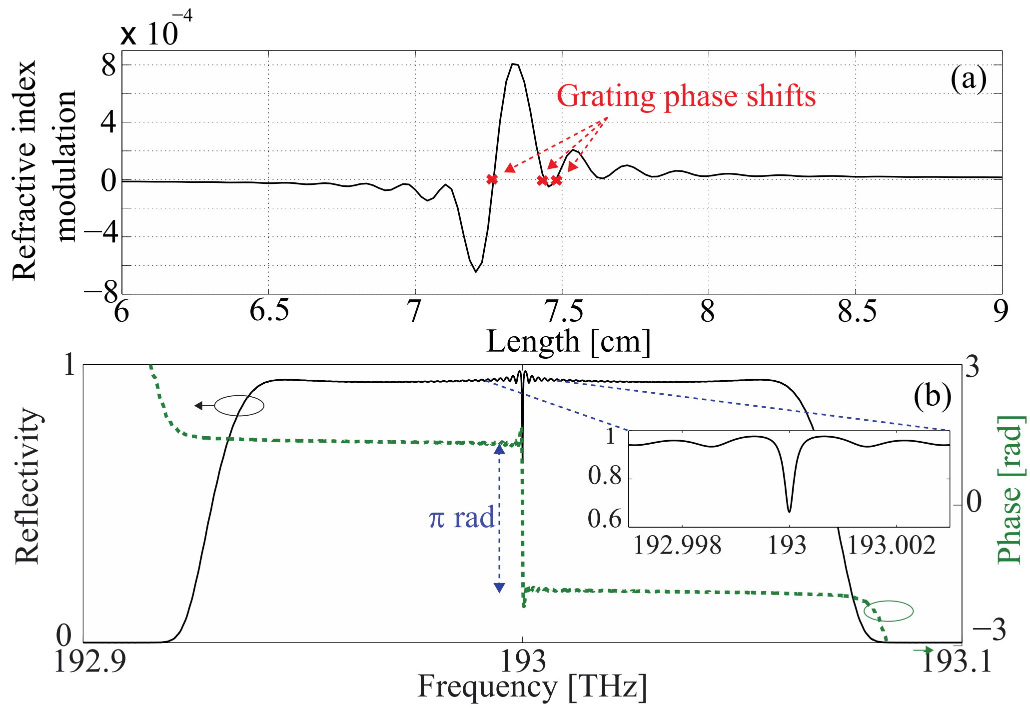

Figure 3-3 (a) Apodization profile of the designed gratings. The red crosses indicate the π-phase shifts in the profile (b) Reflectivity and phase spectral response of the gratings.

3.1.3 Numerical modelling

After obtaining the gratings' apodization and period profiles from the CMT-based synthesis tool, we have modeled deviations in the grating profiles as induced by practical limitations of the fabrication process. In particular, deviations in the amplitude and phase of the refractive index modulation have been modeled by zero-average, stationary Gaussian variables whose standard deviations have been set to 1% of the maximum amplitude refractive index change and to 0.05% of the nominal period along the grating length, respectively. Then, an analysis of the resulting profiles is carried out by means of a CMT + TMM tool. The obtained reflectivity and the phase spectral response are shown in Figure 3-3(b). With the employed grating parameters, BW_{tr} is approximately 125 MHz. Considering that the resulting grating apodization profile is approximately a scaled version of the device's temporal impulse response in Figure 3-1(b), a narrower BW_{tr} can be obtained by increasing the length of the BG-based PHTs. On the other hand, a higher resolution in writing the apodization profile would enable creating a shorter zero-to-zero width of the side lobes of the refractive index modulation, which in turn would translate into a broader BW_{op}.

With current technology the spatial resolution for writing the apodization profile in fiber is limited to approximately 100 μm and the total grating length could be in the range of tens of centimeters [6]. Experimental FBG-based PHTs providing a BW_{tr} of 100 MHz and BW_{op} of 150 GHz have been previously reported [7], in line with the specifications considered in our simulations. Moreover, the resolution with which one can tune the central frequency of PHTs with a piezoelectric device is estimated to be approximately 215 MHz, which corresponds to an incremental axial strain of ~30 nm [14]. Besides, considering the gratings at the room temperature (~25ºC) the same amount of frequency shift in grating's response could be achieved by 0.16ºC thermal increase [10].

Now, we present numerical simulation results for a narrow (few hundreds of MHz range) BPF and BRF and a broad (tens of GHz range) BPF and BRF, achieved using the FBGs designed above. Assuming that one of the gratings is kept with the fixed period as defined above while the other FBG is axially stretched, the spectral 3 dB bandwidth of the filter could be tuned from 260 MHz (20 dB bandwidth of 560 MHz) to more than 60 GHz. This tuning could be practically achieved by axially stretching the fibers from ~30nm to ~45 μm (increasing the corresponding grating period by approximately 0.17 nm). In case of using thermal tuning the temperature should be tuned from ~0.194ºC up to ~44.883ºC (variation from room temperature). The numerically simulated spectral response of the filters at the two output ports of the MI are shown in Figure 3-4(a-c).

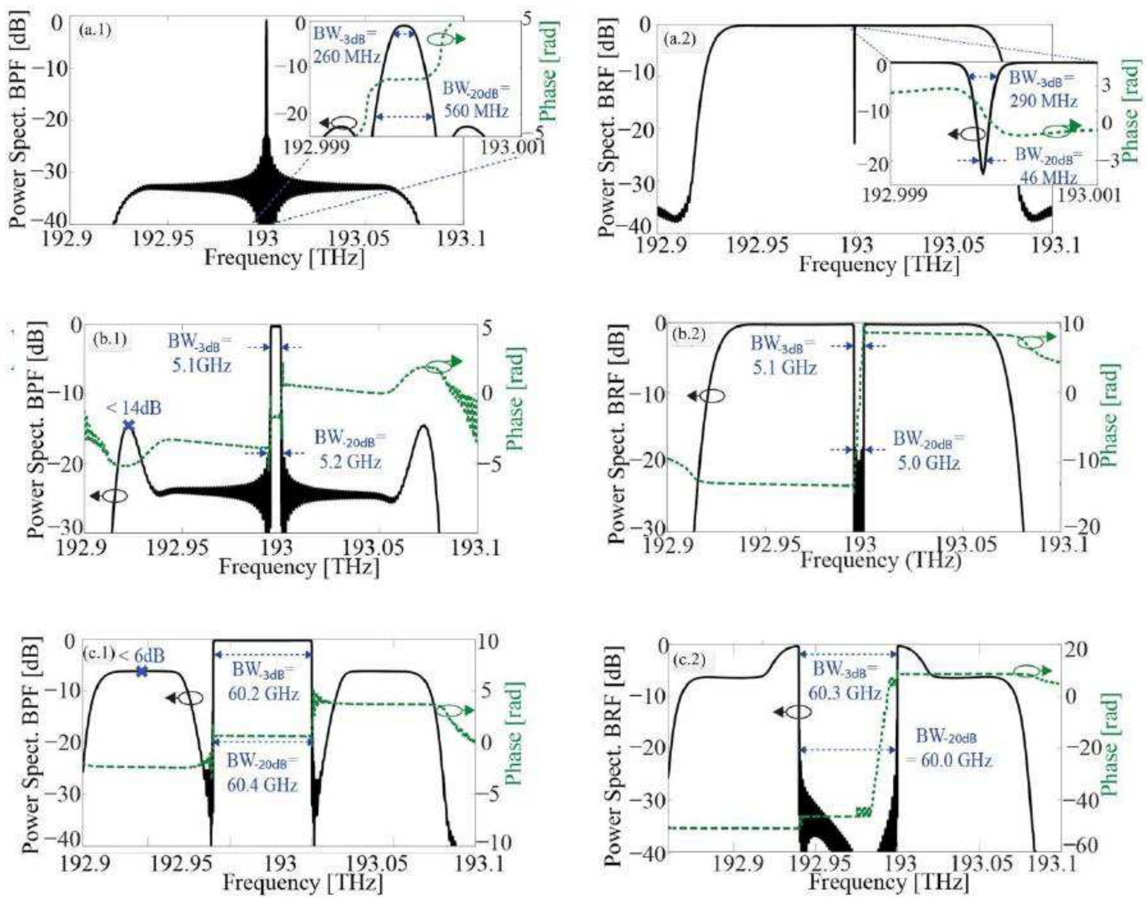

Figure 3-4 The spectral response of the optical filter with (a) minimum 3dB bandwidth of 260 MHz; ((a.1) BPF; and (a.2) BRF); (b) 5.1 GHz ((b.1) BPF and (b.2) BRF), and (c) 60.2 GHz ((c.1) BPF and (c.2) BRF).

The numerical simulations emulate the setup shown in Figure 3-2. In order to obtain the spectral response of the filter, we consider a Dirac delta function entering at the input port, i.e. a uniform spectrum, and we show the obtained output spectral response. The FBGs in both arms of the MI have the parameters presented in Figure 3-3. To account for potential differences between the two PHTs due to deviations during the fabrication process, we have carried out two different analysis from the synthesized gratings, in such a way that the two considered PHTs have suffered from different random variations in the nominal apodization and period profiles. Numerically, we stretch one grating, inducing the variation in the central frequency of this grating with respect to the other. Also note that in our simulations, we assume that the signals propagating through the two MI arms undergo identical phase delays; as mentioned above, to satisfy this assumption in practice, a phase shifter needs to be incorporated in one of the MI arms. Simulations have been also conducted to account for deviations in the power coupling coefficient of the optical coupler and potential differences between the two PHTs, as described below. The results shown in Figure 3-4 confirm that the filter is non-dispersive. The spectral phase profile is nearly constant (after eliminating the linear term associated to a constant average delay) with a peak-to-peak phase ripple in the filter's pass-band < 0.06 rad.

The BPF device provides a fairly high value of extinction ratio (ER) when set to operate as a narrow-band filter, exceeding ~20dB for the minimum bandwidth case (~260MHz). Nonetheless, the presented results also show that the ER of the BPF deteriorates as the operation bandwidth of the filter is increased. This degradation is mainly associated with the fact that each FBG exhibits a limited reflection bandwidth, in such a way that an unbalance in the reflected power from the two gratings is induced towards the edges of the grating's reflection bandwidth as the central frequency of one grating is shifted with respect to the other one. Obviously, this effect is more pronounced as this frequency shifting is increased, i.e., for filters set to provide a broader spectral bandwidth. The ER of the BPF is reduced to ~6dB for the maximum filter's bandwidth case (~60GHz). An intermediate case, offering an operation bandwidth of ~5GHz, is also investigated in our simulations, Figure 3-4(c-d), showing an ER for BPF of ~14dB.

Finally, we have investigated the impact of unbalanced losses in the two arms of the interferometer. This unbalance could be caused by the difference in peak reflectivity of the fabricated gratings or the difference between the powers coupled into the two arms of the MI (coupling ratio $\neq 0.5$). Numerical simulations (not reported here) show that the bandwidth and the steepness of the filters remain unaffected. However, a potential power unbalance degrades the insertion loss (IL) of the BRF and ER of the BPF, as detailed by the simulation data provided in Table 3-1.

Table 3-1 IL and ER for the BPF and BRF, considering different power at two arms of the interferometer.

	Band reject filter		Band pass filter	
Power ratio	IL	ER	IL	ER
50:50	0.6 dB	30 dB	0.6 dB	30 dB
45:55	0.65 dB	30 dB	0.6 dB	20 dB
40:60	0.75 dB	30 dB	0.6 dB	15 dB
35:65	1 dB	30 dB	0.6 dB	11 dB
30:70	1.3 dB	30 dB	0.6 dB	9 dB

Whereas the filtering device simulated here was limited to provide a maximum operation bandwidth in the tens of GHz range, the potential implementation of the device in an integrated platform could allow scaling the operation bandwidths into the terahertz range. Recently, a terahertz bandwidth PHT has been experimentally demonstrated in an integrated silica-on-silicon platform [8,9], where direct UV grating writing (DGW) technique has been used to overcome the spatial resolution limitation of FBGs. Using this technique it is possible to engineer the grating's structure (apodization profile) at the sub-10 microns level. Therefore, tunable optical filters based on this newly presented PHT technology could be implemented using our proposed design with a potential bandwidth tuning capability from hundreds of megahertz up to a few terahertz. It should be also possible to integrate micro-heaters on this kind of gratings to achieve tunability on the filters' central frequency and bandwidth.

3.1.4 Conclusions

We have proposed a new architecture for implementation of widely tunable, non-dispersive, sharp-edge optical band-pass and band-rejection filters using a fiber-optic or integrated-waveguide scheme based on two PHTs incorporated into an MI. Bandwidth tuning from 260 MHz to >60 GHz has been numerically demonstrated using readily feasible FBG-based PHT devices.

3.1.5 References

[1] K. Takad, M. Abe, T. Shibata, and K. Okamoto, "1-GHz-Spaced 16-Channel arrayed-Waveguide grating for a wavelength reference standard in DWDM network systems," *Journal of Lightwave Technology*, vol. 20, no. 5, pp. 850-853, 2002.

[2] C. K. Madsen, "Efficient architectures for exactly realizing optical filters with optimum bandpass designs," *IEEE Photonics Technology Letters*, vol. 10, no. 8, pp. 1136-1138, 1998.

[3] F. Zeng, and J. Yao, "All-optical microwave filters using uniform fiber Bragg grating with identical reflectivities"*Journal of Lightwave Technology*, vol. 23, no. 3, pp. 1410-1417, 2005.

[4] X. M Liu, "A novel ultra-narrow transmission-band fiber Bragg grating and its application in a single-longitudinal-mode fiber laser with improved efficiency," *Optics Communications*, vol. 280, no.1, pp. 147-152, 2007.

[5] T. Segawa, S. Matsuo, Y. Ohiso, T. Ishii, Y. Shibata, and H. Suzuki, "Fast tunable optical filter using cascaded Mach–Zehnder interferometers with apodized sampled gratings," *Journal of Lightwave Technology,* vol. 17, no. 1, pp. 139-141, 2005.

[6] M. H. Asghari and J. Azaña, "All-optical Hilbert transformer based on a single phase-shifted fiber Bragg grating: design and analysis," *Optics Letters*, vol. 34, no. 3, pp. 334-336, 2009.

[7] M. Li and J. Yao, "All-fiber temporal photonic fractional Hilbert transformer based on a directly designed fiber Bragg grating," *Optics Letters*, vol. 35, no. 2, pp. 223-225, 2010.

[8] Ch. Sima, J. C. Gates, C. Holmes, P. L. Mennea, M. N. Zervas, and P. G. R. Smith, "Terahertz bandwidth photonic Hilbert transformers based on synthesized planar Bragg grating fabrication," *Optics Letters*, vol. 38, no. 17, pp. 3448-3451, 2013.

[9] Ch. Sima, J. C. Gates, H. L. Rogers, P. L. Mennea, C. Holmes, M. N. Zervas, and P. G. R. Smith, "Phase controlled integrated interferometric single-sideband filter based on planar Bragg gratings implementing photonic Hilbert transform," *Optics Letters,* vol. 38, no. 5, pp. 727-729, 2013.

[10] S. Kim, K. Lee, J. H. Lee, Je-M. Jeong, and S. B. Lee, "Temperature insensitive fiber Bragg grating-based bending sensor using radio-freqeuncy-modulated reflective semiconductor optical amplifier," *Japanese Journal of Applied Physics*, vol. 48, no. 6R, pp. 1-5, 2009.

[11] H. Emami, N. Sarkhosh, L. A. Bui, and A. Mitchell, "Wideband RF photonic in-phase and quadrature phase generation," *Optics Letters,* vol. 33, no. 2, pp. 98-100, 2008.

[12] S. L. Hahn, A. D. Poularikas, *The Transforms and Applications Handbook* (Academic 2000).

[13] T. Erdogan, "Fiber grating spectra," *Journal of Lightwave Technology*, vol. 15, no. 8, pp. 1277-1294, 1997.

[14] Newport, "Picomotor actuator," http://search.newport.com/?x2=sku&q2=8302.

3.2 Photonic Hilbert transformers based on laterally apodized integrated waveguide Bragg gratings on SOI wafer

Abstract: We experimentally demonstrate high-performance integer and fractional-order photonic Hilbert transformers (HTs) based on laterally apodized Bragg gratings in a silicon-on-insulator technology platform. The sub-millimeter-long gratings have been fabricated using single-etch electron beam lithography, and the resulting HT devices offer operation bandwidths approaching the THz range, with time-bandwidth products between 10 to 20.

Accepted for publication in Optics Letters, vol. 41, no. 21 , 2016.

H. P. Bazargani, M. Burla, L. Chrostowski and J. Azaña

3.2.1 Introduction

Hilbert transformation is a fundamental signal processing operation with wide range of applications in microwave engineering, radar system, image processing, telecommunications and filtering [1,2]. A photonic Hilbert transformer (HT) can exhibit a considerably higher processing speed than its electronic counterpart [3]. Among the proposed techniques for realization of HTs, integrated waveguide approaches offer compactness and repeatable performance. Moreover, HTs fabricated using complementary metal-oxide-semiconductor (CMOS) technology, offer important, additional advantages, such as the possibility of integration with electronic processing units and their potential for mass production at a lower cost. The first realization of an on-chip HT was based on an all-pass optical filter configuration using micro-ring resonator [4]. Despite having the advantage of small foot-print, the device operation bandwidth was limited to few GHz. This fundamental restriction was due to the fact that thermo-optics tuning elements, essential for the operation of the device, limit micro ring's size and consequently its operation bandwidth. In another work, an apodized Bragg grating (BG) on silica-on-silicon platform has been used to design a THz-bandwidth HT [5]. This approach suffers from an intrinsic limitation on the maximum effective index modulation that can be achieved through the employed ultraviolet (UV) writing method, which imposes the need for long gratings (~1 cm) to achieve the desired performance. Most recently, M. Burla et al. have demonstrated the first fractional-order HT on a silicon-on-insulator (SOI) platform, based on uniform, phase-shifted waveguide BGs [6]. Although this design avoids the need for a complex grating apodization profile, this previous work has shown that the device performance, e.g., evaluated through the time-bandwidth product (TBP) of the device's temporal/spectral response (ratio between maximum operation bandwidth and minimum signal bandwidth that can be processed with a prescribed precision), strongly depends on the HT order and it quickly deteriorates for an integer-order HT (fractional order = 1). In this latest case (integer-order HT), the design proposed in Ref. [6] provides a low TPB, approaching the minimum possible, so that only very simple time optical waveforms, e.g., transform-limited Gaussian-like pulses, could be processed with this previous design. Recall that in principle, integer-order Hilbert transformation is the most interesting functionality from a practical application viewpoint. A main conclusion of the work in Ref. [6] is that highly-performing integer-order HTs would still require the use of a relatively complex grating apodization profile, including the need to control the refractive index modulation over a large dynamic range. However, realization of such a grating apodization profile has proved challenging through direct control of the physical corrugation depth applied along a strip waveguide [7] or slab of a ridge waveguide [8]. Generally, the BG designs would be strongly affected by fabrication imperfections, such as lithography smoothing effects and waveguide thickness variations. Additionally, the latter design imposes the need for two steps of etching and lithography. Finally, the effects mentioned above lead to a limited effective index modulation dynamic range and consequently low TPB for the device.

3.2.2 Operation principle

In this work, we design and demonstrate the first high-performance (high TBP) integrated photonic fractional and integer order HTs fabricated through a standard single-etch electron-beam (Ebeam) lithography process. The fabricated devices are based on sub-millimeter long, laterally apodized waveguide BGs on SOI platform. This design uses two individual superposed gratings [7,9] (see Figure 3-5). This approach offers increased tolerance to fabrication errors, so that it allows the control of grating apodization with very high precision over a large dynamic range, enabling for instance the realization of an integer HT with a processing bandwidth as large as ~750 GHz and a TBP above 20. In particular, assuming a fabrication resolution of $\Re = 5\text{ nm}$, the effective refractive index modulation of a grating implemented using the laterally apodized BG design approach [9] can be controlled with a resolution at least one order of magnitude higher than for the case of a conventional BG design, where we recall that the index modulation is controlled through direct variation of the grating physical corrugations [8]; this estimate is obtained considering that the minimum effective index modulation of a conventional BG can be still reduced by a factor of $\sim \cos\left(\pi\Delta L / \Lambda\right)$, where $\Delta L = 0.5\Lambda - \Re$ in this equation calculates the maximum amount of lateral shift between two gratings that can be practically achieved within the fabrication resolution constraints.

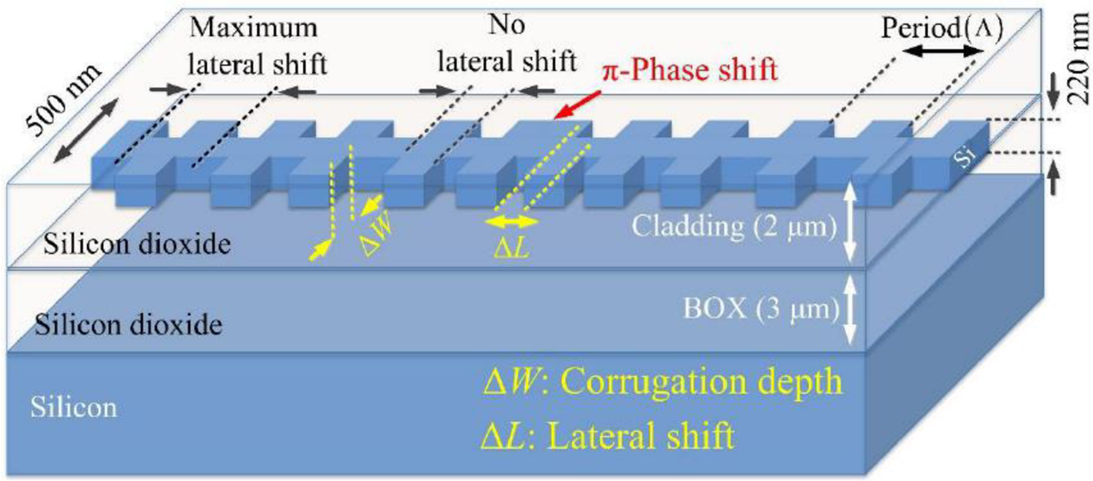

Figure 3-5 Schematic of a laterally-apodized waveguide BG.

A HT is essentially an all-pass linear optical filter providing a single phase shift of value $P\pi$ at the filter's central frequency [3]. For $P=1$, the transformation is called integer, and otherwise fractional-order HT [3]. However, the spectral response of a practical HT is band-limited with the required phase transition occurring in a smooth fashion, over a finite spectral region. Figure 3-6(a), shows the amplitude and phase spectral responses of an ideal (dashed line) and practical (solid line) HT.

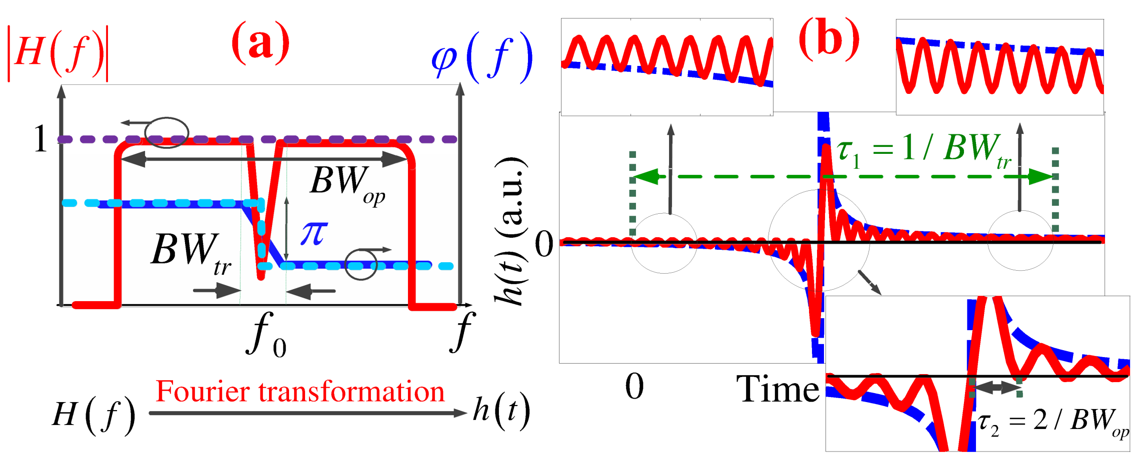

Figure 3-6 (a) Amplitude and phase spectral response of an ideal (dashed-line), and practical (solid-line) HT of integer order. (b) Envelope of the temporal impulse response of an ideal (dashed-line), and physically realizable HT (solid-line).

As illustrated in Figure 3-6(b), the bandwidth specifications BW_{op} (operation bandwidth), and BW_{tr} (transition bandwidth), of the HT are inversely proportional to the zero-to-zero width of the main lobes and the total duration of the device temporal impulse response, respectively [3]. A main figure of merit of a HT is the TBP of its linear temporal/spectral response, defined as the ratio between the operation and transition frequency bandwidths, $TBP = BW_{op} / BW_{tr}$ [3]. A critical challenge in the design of on-chip BGs is the complexity involved in finding the grating-strength (coupling) apodization profile that is required to implement a specific linear temporal/spectral response, e.g., as desired for realization of a signal processing functionality (a HT). This is a result of the non-negligible effects of waveguide dispersion, loss and dimensional variations due to fabrication uncertainties etc [9]. First-order Born approximation is considered as a very powerful solution for the design of weak-coupling gratings. Under this approximation, the index-modulation apodization profile that is required to achieve a target linear response is simply a version of the desired device temporal impulse response, suitably mapped along the device length [8]. The grating index-modulation apodization profile that is required to realize an integer-order HT, scaled version of the device temporal impulse response envelope shown in Figure 3-6(b), is mathematically defined as [10]:

$$\Delta n(z) \propto \frac{\sin^2\left(\pi n_{av} \Delta f \left(z - z_c\right) / c\right)}{z - z_c}, \tag{3.1}$$

where n_{av} is the average refractive index of quasi-transverse electric (TE) mode, c is the speed of light in vacuum, z_c is the center of the grating, and $\Delta f = c / n_{av} \Delta z$ is the operation bandwidth of the device, with Δz being the zero-to-zero width of the main grating-apodization lobes. Consequently, the device bandwidth can be engineered by controlling Δz. On the other hand, a narrower transition bandwidth, leading to higher TBP, requires increasing the total grating length. According to Eq. (3.1) and as per the illustration shown in Figure 3-6(b), the effective refractive index modulation (Δn) should become weaker (still not zero) toward both ends of the grating, thus requiring a relatively large dynamic range for the grating index-modulation variation. Such specification has proved challenging to achieve using previously reported integrated BG-based HT designs [6]. Generally, realization of weak-index BGs is extremely difficult through direct small physical corrugations (ΔW) along the side walls of an optical waveguide, considering practical limitations in the resolution with which one can control the grating corrugations [7,8]. As illustrated in Figure 3-5, our design utilizes two superposed gratings with a fixed side-wall corrugation depth, where the target apodization profile is mapped into lateral shifts (ΔL) between the corresponding periods of these two gratings. This design approach allows high-precision control of the grating index-modulation profile from 0 –achieved for maximum misalignment between the superposed gratings of half a period, $\Lambda / 2$ –to the maximum achievable Δn for a particular ΔW, which is achieved when there is no misalignment between the superposed gratings (assuming a duty-cycle of 50% for grating periods). In contrast to the side-wall corrugated BG, in a laterally apodized BG, Bragg wavelength will remain unchanged for different values of ΔL [9].

In our design, the grating corrugations have been defined on the side-walls of a single-mode silicon strip waveguide with a dimension of 500 nm × 220 nm (width × height) fabricated on a SOI wafer. The cladding and buried oxide layers are made of silicon dioxide with heights of 2 μm and 3 μm, respectively. As the first step, Lumerical Mode Solutions has been used to extract the effective refractive index of the waveguides. Then, transfer matrix method (TMM) has been implemented to model the BG device. Assuming a fixed corrugation depth, the target grating apodization has been transferred to the lateral shift between the relevant periods of the device according to the following equation [9]:

$$\Delta n = n_0 \cos\left(\pi \Delta L / \Lambda\right) \tag{3.2}$$

where n_0 is the effective-index modulation for the BG device with no misalignment ($\Delta L = 0$). The grating period (Λ) is considered to be 318 nm, with a duty-cycle of 50%, to achieve operation around a telecommunication wavelength (~1555 nm). The misalignment (ΔL) is varied from 0 to 159 nm ($\Lambda / 2$).

As an example, we report here the numerical analysis of an integer (order $P = 1$) HT with $\Delta f = 750$ GHz using a waveguide BG with 1,000 periods. Figure 3-7 shows a set of results where the goal was to study the effect of corrugation depth on the device performance. The BG with $\Delta W = 1$ nm provides very nearly the design operation bandwidth of 750 GHz (~6 nm), an indication that this corrugation depth still closely satisfies the weak-coupling condition. On the other hand, the simulation results in Figure 3-7 also show that the device still performs well as an integer HT as the corrugation depth is increased but with a reduced operation bandwidth (in the range of ~260 GHz for a corrugation depth of $\Delta W = 2\,\text{nm}$). Moreover, different fractional order HTs can be realized as the coupling strength is further increased, e.g., $P = 1.84$ for $\Delta W = 10$ nm, without introducing any additional change in the shape of the grating apodization profile; see Figure 3-7(f). Note that larger values of ΔW result in an increased reflection bandwidth of the BG. However, as the corrugation depth is increased, the operation bandwidth of the device, where the phase profile matches the expected phase profile of a fractional-order HT, shrinks to only a fraction of the overall reflection bandwidth. In particular, the effect of waveguide corrugation depth on the 3-dB bandwidth of the device and fractional order of HT have been studied in Figure 3-7(e).

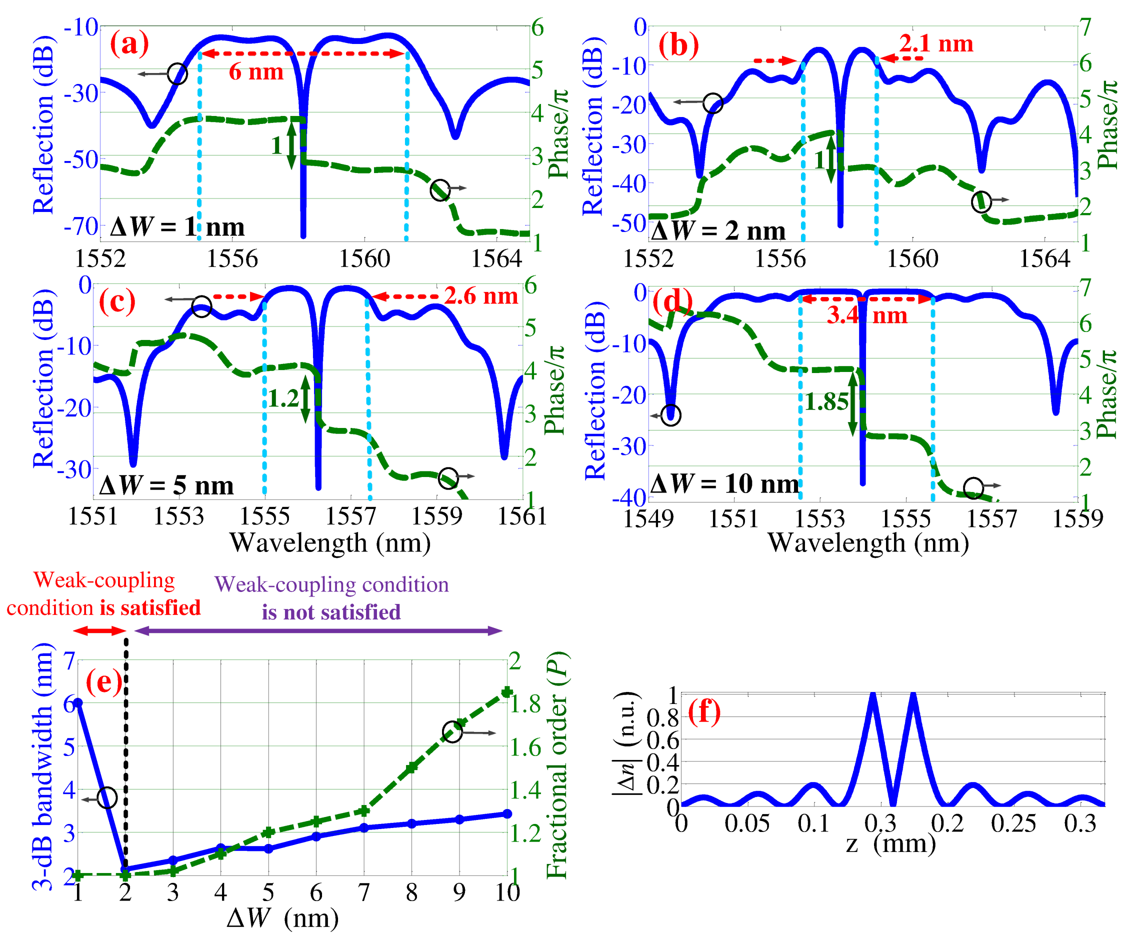

Figure 3-7 (a-d) Simulated amplitude and phase spectral responses of apodized HTs with different corrugation depths (1 nm, 2nm, 5 nm and 10 nm). (e) 3-dB bandwidth and fractional order for different corrugation depths. (f) Effective refractive index modulation profile.

3.2.3 Experiment

The proposed design methodology has been experimentally validated to realize integer and fractional order HTs operating at typical optical telecommunication wavelengths. The first examples are integer-order HTs, designed using laterally apodized BGs with 500 and 1000 periods, respectively, and a similar corrugation depth of 5 nm. Results for smaller corrugation depths were not satisfactory due to the impact of fabrication errors. Figure 3-8 shows the schematic and scanning electron microscope (SEM) image of a sample device.

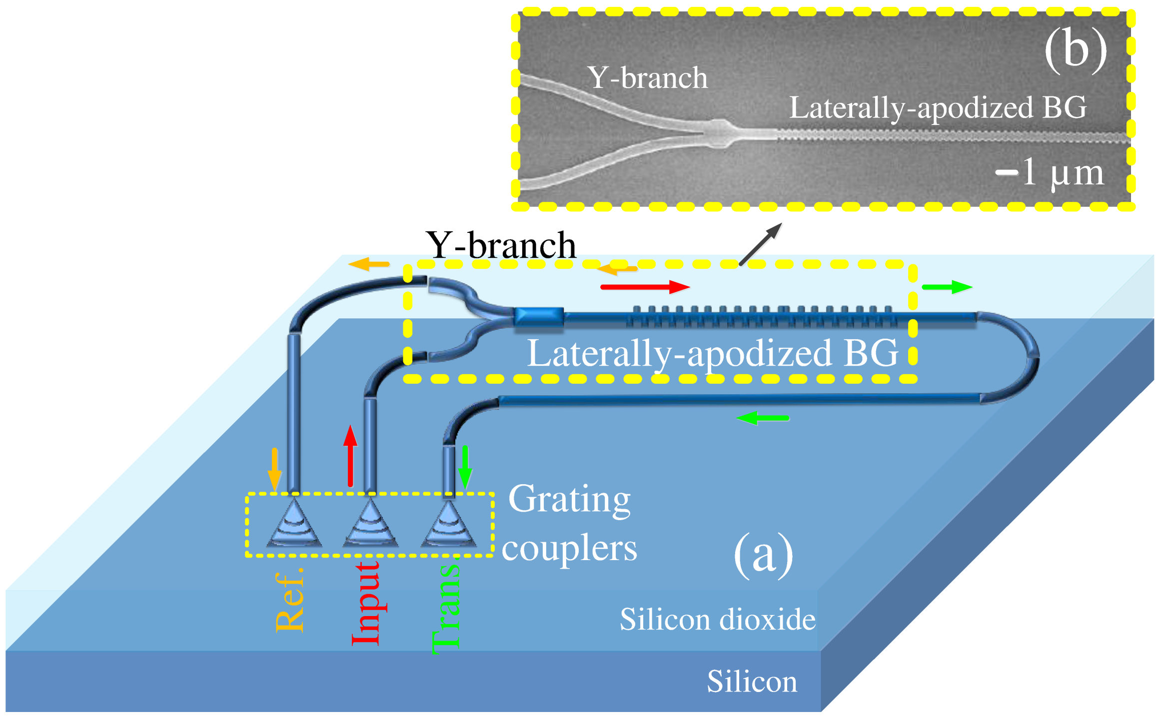

Figure 3-8 (a) Schematic of the realized device. (b) SEM image of a sample device. The grating couplers are designed to support TE mode.

The spectral amplitude and phase responses of the device are measured using an optical vector analyzer (OVA, Luna Innovations) with a spectral resolution of 1.6 pm; simulation and experimental results are shown in Figure 3-9(a-b, d-e). Note that time windowing of temporal impulse response has been carried out in order to isolate the BG response from strong reflective events, i.e. the reflection from input fiber cleave, the back-scattering from the surface grating couplers and silicon waveguides [11,12].

In general there is a discrepancy between the waveguide-corrugation depths assumed in simulation with respect to those designed for the experimentally fabricated device. This could be mainly attributed to variations (reductions) in the corrugation depth of the fabricated gratings induced by significant side-wall smoothing effects due to lithography and etching processes [11]. Consequently, throughout the entire design process the effective refractive index modulation has been reduced by ~41% to match the experimental results [8].

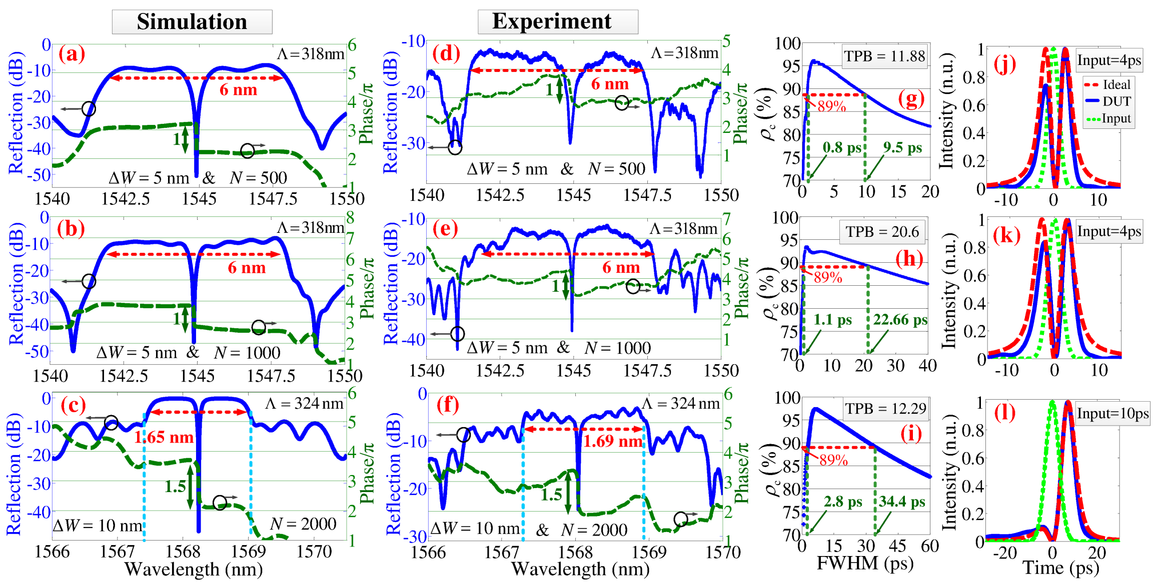

Figure 3-9 (a-c) simulated and (d-f) measured amplitude and phase spectral responses, (g-i) the cross-correlation coefficients and (j-l) comparison between the temporal responses of ideal HTs with the response from the DUTs to different Gaussian pulses, for the integer and fractional HTs.

In order to provide an estimate of the device TBP, we numerically simulated the time-domain response of a linear optical filter with the OVA-measured spectral transfer function (spectral amplitude and phase) to an ideal Gaussian optical pulse, and calculated the cross-correlation coefficient (ρ_c) versus the FWHM time pulse width [6]. ρ_c provides a precise estimate of the similarity between the two time domain complex fields, 1) from an ideal HT, and 2) from the device under the test (DUT) [6].

The TBP of each evaluated device is estimated as the ratio of the longest input pulse time-width to the shortest pulse time-width that provides a minimum prescribed cross-correlation coefficient (89% in the evaluations reported here). According to Figure 3-9(g-h), doubling the number of grating period results in approximately two-fold improvement in the device's TBP, from nearly 12 to above 20. Figure 3-9(j-k) show examples of the temporal response of the measured DUT to a 4-

ps full width at half maximum (FWHM) sample Gaussian pulse, compared with the ideal HT response.

The second experimentally tested example is a fractional-order HT with $P = 1.5$, designed using a similar grating structure but with 2000 periods of 324 nm, and a larger corrugation depth of 10-nm. Again, the device amplitude and phase spectral responses have been measured using the OVA; simulation and experimental results are shown in Figure 3-9(c,f). The measured operation bandwidth is ~212 GHz and similar calculations on the device time-domain response, Figure 3-9(i), provide an estimated TBP slightly above 12. Finally, the temporal response of the measured DUT to a 10-ps FWHM Gaussian pulse is compared with the ideal HT response in Figure 3-9(l).

3.2.4 Conclusions

On the basis of the reported results, we conclude that the laterally-apodized waveguide BG design approach offers significant improvements in terms of effective-index dynamic range, which in turn enables realization of signal processing functionalities requiring complex grating apodization profiles, e.g, such as the high-performance (high TBP) HT devices demonstrated here on a SOI platform. We anticipate such an approach should prove useful for implementation of other complex optical filtering and signal-processing functionalities, beyond the capabilities of conventional waveguide BG designs.

3.2.5 References

[1] H. P. Bazargani, M. R. Fernandez-Ruiz, and J. Azaña, "Tunable, nondispersive optical filter using photonic Hilbert transformation," *Optics letters*, vol. 39, no. 17, pp. 5232-5235, 2014.

[2] S. L. Hahn, *Transforms and Applications Handbook*, A. D. Polarikas, ed., 2nd ed. CRC, 2000.

[3] M. H. Asghari, and J. Azaña, "All-optical Hilbert transformer based on a single phase-shifted fiber Bragg grating: design and analysis," *Optics letters*, vol. 34, no. 3. pp. 334-336, 2009.

[4] L. Zhuang, M.R. Khan, W. Beeker, A. Leinse, R. Heideman, and Ch. Roeloffzen, “Novel microwave photonic fractional Hilbert transformer using a ring resonator-based optical all-pass filter,” *Optics Express*, vol. 20, no. 24, pp. 26499-26510, 2012.

[5] Ch. Sima, J.C. Gates, C. Holmes, P. L. Mennea, M. N. Zevras, and P. G. R. Smith, “Terahertz bandwidth photonic Hilbert transformers based on synthesized planar Bragg grating fabrication,” *Optics letters*, vol. 38, no. 17, pp. 3448-3451, 2013.

[6] M. Burla, M. Li, L. R. Cortes, X. Wang, M. R. Fernandez-Ruiz, L. Chrostowski, and J. Azaña, “Terahertz-bandwidth photonic fractional Hilbert transformer based on a phase-shifted waveguide Bragg grating on silicon,” *Optics letters*, vol. 39, no. 21, pp. 6241-6244, 2014.

[7] A. D. Simard, M. J. Strain, L. Meriggi, M. Sorel, and S. LaRochelle, “Bandpass integrated Bragg gratings in silicon-on-insulator with well-controlled amplitude and phase responses,” *Optics letters*, vol. 40, no. 5, pp. 736-739, 2015.

[8] M. Verbist, W. Bogaerts, and D. V. Thourhout, “Design of weak1-D Bragg grating filters in SOI waveguides using volume holography techniques,” *Journal of Lightwave Technology,* vol. 32, no. 10, pp. 1915-1920, 2014.

[9] X. Wang, Y. Wang, J. Flueckiger, R. Bojko, A. Liu, A. Reid, J. Pond, N. A. F. Jaeger, and L. Chrostowski, “Precise control of the coupling coefficient through destructive interference in silicon waveguide Bragg grating,” *Optics letters*, vol. 39, no. 19, pp. 5519-5522, 2014.

[10] H. Kogelnik, “Filter response of uniform almost-periodic structures,” *Bell System Technical Journal*, vol. 55, no. 1, pp. 109-126, 1976.

[11] J. Pond, X. Wang, J. Flueckiger, A. Reid, J. Niegemann, A. Liu, L. Chrostowski, “Design and optimization of photolithography friendly photonic components,” *Proceedings SPIE,* vol. 9751, pp. 1-6, 2016.

[12] N. Ayotte, A. D. Simard, and S. LaRochelle, “Long integrated Bragg grating for SOI wafer metrology,” *IEEE Photonics Technology Letters,* vol. 27, no. 7, pp. 755-758, 2015.

Chapter 4 On-chip optical signal characterization

In this chapter, we propose and experimentally demonstrate, an integrated-waveguide implementation of the single-detection time domain PROUD (Phase Reconstruction using Optical Ultrafast Differentiation) scheme using a high index contrast (4%) silica-on-silicon Mach-Zehnder interferometer (MZI) as the ultrafast optical differentiator. PROUD has been implemented for single-shot and real-time characterization of GHz-rate communications signals and is shown to be transparent to the modulation format.

4.1 On-chip, single-shot characterization of GHz-rate complex optical signals

Abstract: Phase reconstruction based on optical ultrafast differentiation (PROUD) is implemented using an integrated-waveguide Mach-Zehnder Interferometer to demonstrate self-referenced phase characterization of GHz-rate complex modulated signals (e.g., quadrature phase shift keying, and amplitude phase shift keying modulation formats), through a single-shot and real-time technique. This method is transparent to both modulation format and bit rate, limited only by the bandwidth capabilities of the temporal intensity measurement instrumentation.

Published in IEEE Photonics Technology Letters, vol. 26, no. 3, pp. 2345-2348, 2014.

H. P. Bazargani, J.-B. Quélène, P. Dumais, A. Malacarne, M. Clerici, R. Morandotti, C. L. Callender and J. Azaña

4.1.1 Introduction

Accurate measurement and full (amplitude and phase) characterization of high-speed optical signals is an essential task in high-speed communication fiber-optics links, optical signal processing and optical regeneration, particularly as complex modulation formats are increasingly introduced. Some popular optical pulse characterization methods include frequency resolved optical gating (FROG) [1] and spectral phase interferometry for direct electric-field reconstruction (SPIDER) [2], and any of their multiple variants.These techniques have been traditionally implemented by use of optical non-linearities in a variety of material and/or waveguide technologies. Over the years, these methods have been adapted to operate on a broader range of pulse time durations, frequency bandwidths and energies. Nevertheless, in fiber-optics telecommunication and information processing systems, we need to have the ability to characterize low-intensity (with sub-milliwatt average powers), and high-speed (GHz-rate) optical signals, preferably using a fiber-optics or an integrated-waveguide measurement platform [3]. Considering that information data signals are generally random (i.e. non repetitive), real-time measurements in a single shot are also necessary. However, the aforementioned methods cannot easily satisfy this stringent set of requirements. On the other hand, linear interferometric methods have proved greatly successful for full characterization of optical telecommunication signals [4]. However, these methods usually need a precisely synchronized optical reference (local oscillator), significantly increasing the complexity and cost of the measurement setup [4]. To overcome these difficulties, self-referenced optical signal measurement methods are attracting an increased interest [5]. A relevant example is PROUD (Phase Reconstruction using Ultrafast Optical Differentiation), a self-referenced, linear method based on time-domain intensity measurements at the input and output of an ultrafast photonic differentiator [6]. This technique offers high sensitivity and it relies on a simple non-iterative phase recovery numerical algorithm, thus being well suited for real-time operations. Previous implementations of PROUD are based on fiber-optics [7]. As a result, these implementations suffer from system instabilities, which ultimately affect the measurement performance. For instance, for single-shot and real-time measurements, previous PROUD implementations required the use of a complex scheme using two perfectly complementary linear optical filters, balanced photo-detection and a water-cooling system aimed at stabilizing the fiber interferometer [8]. As a result, single-shot and real-time phase recovery could be demonstrated only on relatively simple optical waveform variations, particularly a chirped 1-GHz sinusoid intensity-modulated signal and a 3-Gbps PRBS (pseudo-random binary sequence) phase-modulated signal, i.e., with only two phase-modulation levels (0 and π).

In this communication, we report an integrated-waveguide implementation of the single-detection PROUD scheme using a high index contrast (4%) silica-on-silicon Mach-Zehnder Interferometer (MZI) as the ultrafast optical differentiator. This allows us to achieve real-time and single-shot phase characterization of GHz-rate complex signals under different (arbitrary) complex modulation formats and bit rates using a greatly simplified setup (single filtering stage and single photodetection) and without needing a reference oscillator. In particular, the integrated-waveguide scheme demonstrated here is successfully proved for full characterization of GHz-rate signals exhibiting quadrature phase shift keying (QPSK) and amplitude phase shift keying (APSK) modulation formats. To demonstrate the transparency of the proposed method to modulation format and bit rate, different symbol/bit rates have been purposely used for the two experiments reported here on QPSK (1Gbaud) and APSK (0.7Gbaud) modulated signals. Besides, no temperature stabilization mechanism has been used in the performed experiment.

4.1.2 Operation principle

Let us assume that the temporal complex envelope of the signal under test is $u(t)=|u(t)|\exp\{j\varphi(t)\}$. To implement PROUD, we need a linear optical filter providing a spectral transfer function $H(\omega)\propto jA\omega$ (linear spectral amplitude response [6,7]). This filter is an optical first-order time differentiator, where A is the differentiator's amplitude coefficient and ω is the base-band frequency ($\omega=\omega_{opt}-\omega_0$, in which ω_{opt} is the optical frequency variable and ω_0 is the filter's resonance frequency at which the transmission is ideally zero). In PROUD, the carrier frequency of the signal under test should be spectrally shifted with respect to the differentiator's null frequency by a quantity $\Delta\omega$. In this case, $V(\omega)=-jA(\omega-\Delta\omega)U(\omega)$, where $U(\omega)$ and $V(\omega)$ are the Fourier transforms of the temporal complex envelopes of the waveform at the filter's input (signal under test, $u(t)$) and the waveform at the filter's output, $v(t)$, respectively. It has been previously demonstrated that the input waveform's chirp (instantaneous frequency) can be obtained from measurements of the time-domain intensity profiles of the input ($|u(t)|^2$) and output ($|v(t)|^2$) waveforms using the following equation [6],

$$\frac{\partial \varphi(t)}{\partial t} = \sqrt{\frac{\left[\left(\frac{|v(t)|}{A}\right)^2 - \left(\frac{\partial |u(t)|}{\partial t}\right)^2\right]}{|u(t)|^2}} - \Delta\omega \tag{4.1}$$

where we recall that $\varphi(t)$ is the temporal phase profile of the input signal under test and $\partial\varphi(t)/\partial t$ is its instantaneous frequency. If the frequency-shift Δω is sufficiently large so that it satisfies $\Delta\omega > \partial\varphi(t)/\partial t$, along the entire time duration of the signal under test, then the term $\Delta\omega + \partial\varphi(t)/\partial t$ in Eq. (4.1) is always positive and the input signal's phase can be then unambiguously reconstructed by numerical cumulative integration of the obtained instantaneous frequency [8]. The aforementioned condition is satisfied when the entire (full-width) spectrum of the signal under test is located only on one side of any of the MZI destructive resonance frequencies. Additionally, the MZI transfer function should exhibit a linear amplitude variation over the entire spectral width of the signal under test. Some of the spectral regions over which the signal under test should fit are illustrated in Figure 4-1(a) – measured spectral transmission response of the MZI: Dotted-green shaded or solid-orange shaded regions in Figure 4-1(a) give positive and negative values of *A* (in Eq. (4.1)), respectively. It is worth noting that, the parameter $\Delta\omega$ can be measured directly from the spectral transfer function of the implemented filter (e.g. MZI).

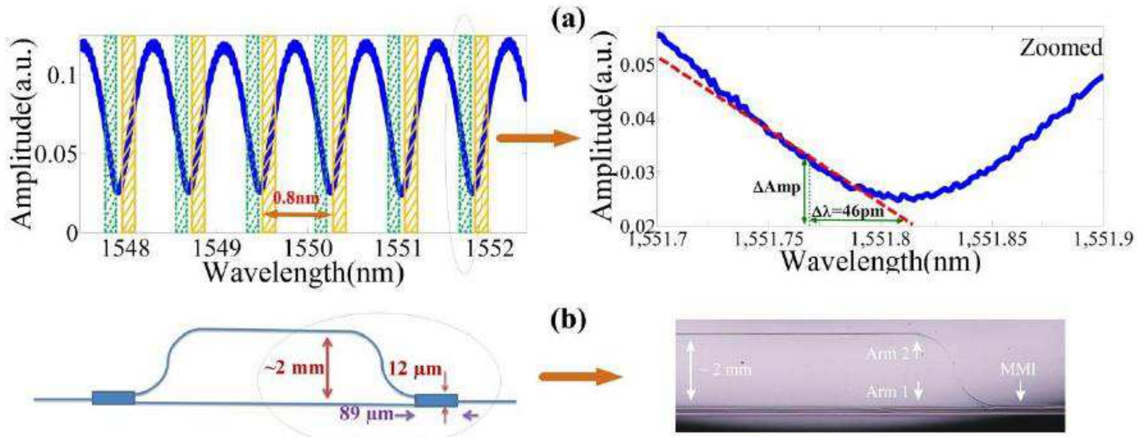

Figure 4-1 (a) The amplitude of the transfer function of the MZI. The shaded areas are the regions in which the signal under test could be located. The green-dotted regions give positive values of A(in Eq. (4.1)), and the orange-dashed areas will lead to negative values of A. In experiments, the accurate value of this parameter is derived from the slope of the function $V(\omega)/U(\omega)$, in which $U(\omega)$ and $V(\omega)$ are the Fourier transforms of the temporal complex envelopes of the waveforms at the filter's input (signal under test, $u(t)$) and the waveform at the filter's output, $v(t)$ (See Figure 4-2(b)) (b) Circuit model and micrograph of part of the fabricated MZI.

However, the slope of the filter's amplitude spectral response at its linear part can be estimated more precisely through a measurement of the transfer function $V(\omega)/U(\omega)$ (see Figure 4-2(b)). The difference between, comes from the fact that the signal under test will experience different amount of attenuation at reference arm with respect to the signal which passes through the filter. For a correct phase reconstruction operation, we have estimated that the bandwidth of the signal under analysis has to be about 25% of the MZI's free spectral range (FSR), approximately corresponding to the linear-amplitude spectral region of the MZI spectral transfer function. Recall that the full spectrum of the signal under the test should be located at either side of any of the destructive interference wavelengths of the MZI transfer function. Each of these sides will cover 50% of the device's FSR. Considering the fact that the MZI's spectral transfer function can be approximated by a linear-amplitude spectral response only through approximately half of each of these spectral regions, we derived the mentioned rule of thumb: the signal spectral bandwidth should not exceed about one fourth (or 25%) of the MZI's FSR.

4.1.3 Experiment

In this work a one by one (1×1) integrated MZI is employed to act as the differentiator filter. The measured transmission spectrum of the fabricated MZI, its circuit model and micrograph are shown in Figure 4-1(a-b). The light is coupled into the two arms of the MZI through a multimode interference (MMI) coupler. The device is based on high index contrast (4%) silica-on-silicon waveguides of 2×2 μm^2 cross-section fabricated using a combination of plasma-enhanced chemical vapour deposition, photolithography and dry etching processes [9]. The FSR of the MZI is measured to be 100 GHz (0.8 nm). Figure 4-2(a) shows the schematic of the experimental setup used in our new implementation of PROUD. The CW laser source operates at a central wavelength of 1551.77 nm. By choosing this as the carrier wavelength of the signal and by ensuring that the spectral width of the modulated signal is narrower than ~25 GHz, proper operation of the method is guaranteed (See Figure 4-2(b)).

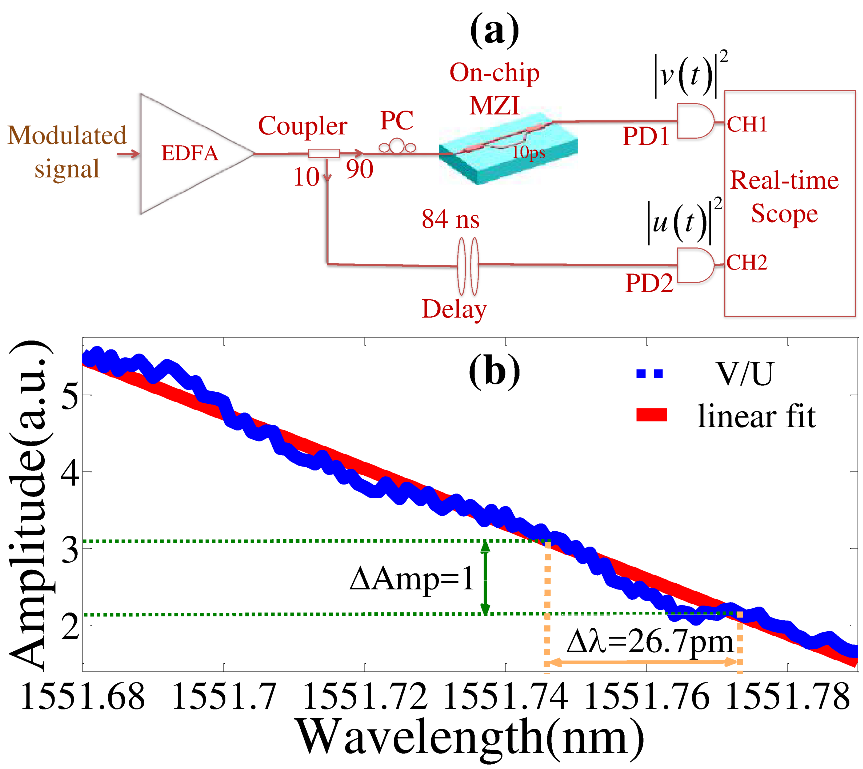

Figure 4-2 (a)The experimental setup (PC is polarization controller, EDFA is Erbium-doped fiber amplifier, PD is photo-detector), (b) $V(\omega)/U(\omega)$ and the fitted line to calculate $|A| = |\Delta Amp/\Delta\lambda| = 37.46\ nm^{-1} = 0.0477\ GHz^{-1}$.

In the first reported experiment, an electronic arbitrary waveform generator (AWG) with a sample rate up to 24 GS/s and analog bandwidth of 9.6 GHz, connected to a phase modulator was used to modulate the phase of the CW laser with four different levels (0, $\pi / 2$, π, and $3\pi / 2$), temporal duration of 82 ps and period of 1 ns, thus creating the 1 Gbaud (2 Gb/s) QPSK signal under test. In particular, we defined a sequence of twenty different phase jumps at the input of the setup, emulating a telecommunication QPSK signal. The input driving electric signal from AWG was amplified using a 12 GB/s RF amplifier and acquired using the 8-GHz real-time oscilloscope. The RF power is adjusted so that the π-phase shift could be obtained at $V\pi = 6$ V (nominal value of the used EO modulator).The full spectral width of the signal under test was measured to be ~0.13 nm (~16 GHz), clearly satisfying the above defined constraints. An Erbium-doped fiber amplifier (EDFA) was used in order to compensate for the losses caused by the fiber/waveguide/fiber coupling to the integrated waveguide. In order to measure the linear variation of the MZI transfer function with an improved accuracy, we swept the wavelength of a CW laser with a resolution of 1 pm around the linear part of the transfer function measuring the ratio of the differentiated signal spectrum over the reference signal spectrum for all the wavelengths (dotted blue curve in Figure 4-2(b)). Subsequently, we used a linear fitting to calculate A (solid red line in Figure 4-2(b)).

The slope of the fitted line was $A=0.0477\ GHz^{-1}$ and the difference between the central wavelength of the CW signal (1551.77 nm) and the null wavelength at MZI's transfer function was $\Delta\lambda \approx 46\ pm$, for which the conversion from wavelength to angular frequency leads to $\Delta\omega \approx 36.08\ GHz$. The time-domain intensity profiles of both the signal under test $|u(t)|^2$ and the signal after differentiation $|v(t)|^2$ were measured using two high-speed photo-detectors, each with a 3-dB bandwidth of 45 GHz, connected to two different channels of an 8-GHz real-time oscilloscope. 84-ns delay was used to synchronize the differentiated and reference signals (the delay depends on the length of the device and optical path length between the coupler and the photo-detector). No averaging was used in these measurements so that to prove the single-shot capabilities of our measurement setup. Using these measurements, the QPSK phase profile was successfully reconstructed in real-time following the above described methodology. The corresponding results are shown in Figure 4-3.

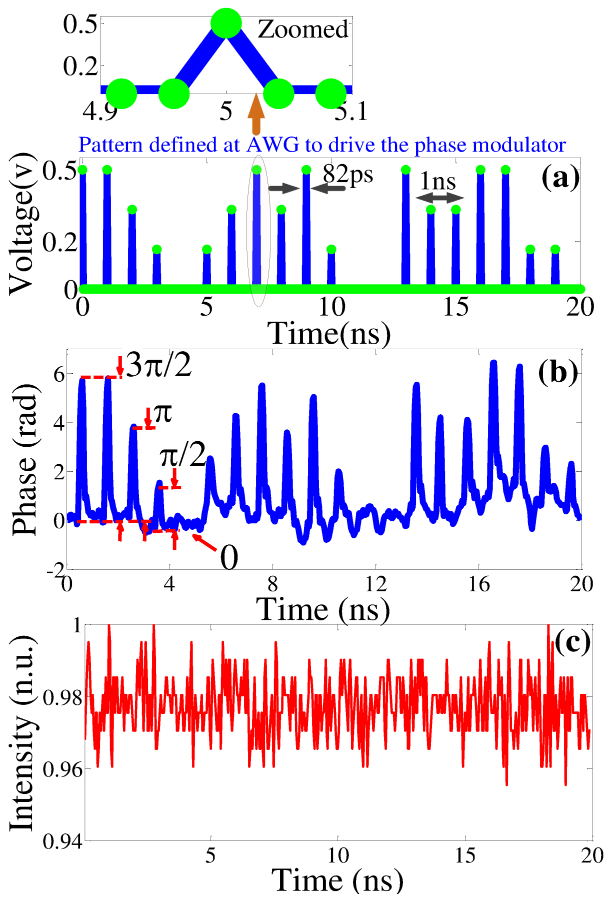

Figure 4-3 (a) The phase profile defined at AWG that has been used to drive the phase modulator. The zoomed region shows that a single sample point from the AWG defines each symbol along the data sequence. (b) The reconstructed phase and (c) intensity profiles of the QPSK modulated signal.

In a second experiment, characterization of an APSK modulated signal was targeted. In this case, an intensity modulator cascaded with a phase modulator was used to generate a customized 0.7 Gbaud (2.8 Gb/s) signal (with 82 ps temporal duration of each sample and a period of 1.4 ns). The parameters A, $\Delta\omega$ and the central wavelength of the CW laser were kept the same as for the previous experiment. Two different channels of the AWG were now used in order to define the different desired profiles for the intensity and phase variations of the signal, namely with four different phase levels and four different intensity levels. A precise delay of 41.47 ns was used between intensity and phase modulators to force the two sequences to overlap in time and create the desired intensity plus phase modulated signal. This delay depends on the length of the fiber and polarization controller which have been used to connect two modulators in series. Notice that the APSK signal which is used in this experiment represents 13 points in the constellation diagram as we have considered zero intensity as one level for modulating the light intensity.

Again, single-shot and real-time recovery of the signal's phase profile was successfully achieved from the measured input and differentiated temporal intensity patterns using the same strategy and setup as that described above for the QPSK signal experiment (results in Figure 4-4).

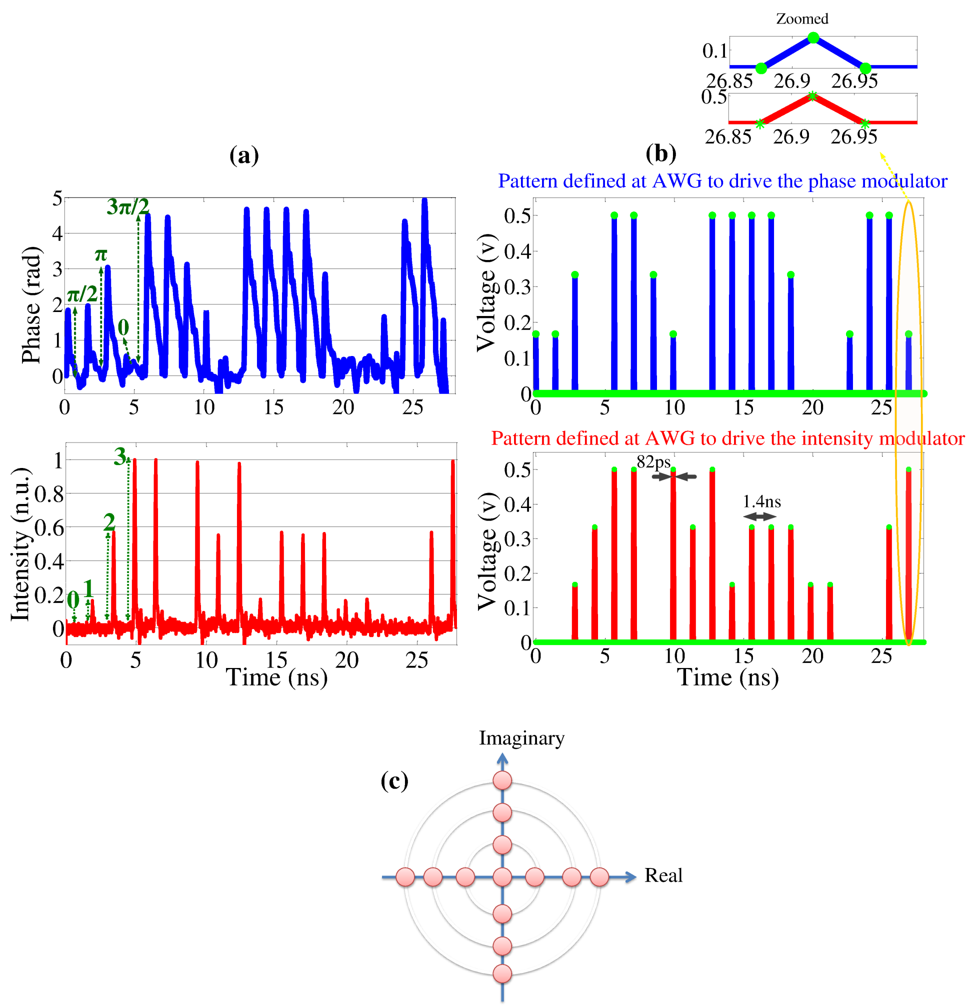

Figure 4-4 (a) The reconstructed phase and intensity profiles of the APSK modulated signal.(b) The profiles that were defined at the AWG to drive the phase modulator (top, right) and intensity modulator (bottom, right). The zoomed region shows that only one symbol at AWG defines a bit, and (c) The constellation diagram of the APSK modulated signal.

To have an estimate about the sensitivity of this method, we examined the achieved sequence for fifteen iterations (corresponding to 300 bits) with different levels of power at the input of the chip. An error parameter was defined as the ratio of incorrect bits over the total number of bits under study (300). The measurements show an error parameter of approximately zero for input signal powers exceeding ~17 milliwatts .This amount of power may seem like to be high for conventional telecommunication data receivers. However, the insertion loss of the integrated MZI is measured to be -18 dB. To be noticed that this loss could be reduced to less than -4 dB with proper fiber pigtailing. In light of this possible improvement in the setup, the characterization method could have error-free operation for power level as low as 650 microwatts. It should be noted that no temperature controlling system was used during the experiment; this improvement was enabled by the considerably higher stability of the inteferometric structure implemented in an integrated-waveguide, as compared with previously reported fiber-optics interferometers.

4.1.4 Conclusions

A simple integrated-waveguide implementation of PROUD has been demonstrated for full (amplitude and phase) characterization of GHz-rate, complex modulated optical data streams in a single-shot and in real-time, without using a reference local oscillator. The characterization setup includes a single filter and a single conventional photodetector. The reported results clearly evidence that the method is entirely transparent to the modulation format as well as to the symbol rate of the signal, as long as the data spectrum fits in the linear region of the differentiation filter. Moreover, the needed tunable reference delay line and two photo-detectors could be integrated along with the MZI [10-11]. In this way, the proposed method could be used to create a fully integrated module capable of real-time, single-shot characterization of GHz-rate data signals with potentially improved compactness, stability and sensitivity.

4.1.5 References

[1] D.J. Kane and R. Trebino, “Single-shot measurement of the intensity and phase of an arbitrary ultrashort pulse by using frequency-resolved optical gating,” *Opics Letters*, vol. 18, no. 10, pp. 823-825, 1993.

[2] C. Iaconis and I.A. Walmsley, “Spectral phase interferometry for direct electric-field reconstruction of ultrashort optical pulses,” *Opics Letters*, vol.23, no. 10, pp. 792-794, 1998.

[3] C. Dorrer, “High-speed measurements for optical telecommunication systems,” *IEEE Journal of Selected Topics in Quantum Electronics,* vol. 12, no. 4, pp. 843-858, 2006.

[4] N.K. Fontaine, R.P. Scott, L. Zhou, F. M. Soares, J.P. Heritage and S.J. B. Yoo, "Real-time full-field arbitrary optical waveform measurement," *Nature Photonics*, vol. 4, pp. 248-254, 2010.

[5] V. Loriot, G. Gitzinger, and N. Forget, "Self-referenced characterization of femtosecond laser pulses by chirp scan," *Opt. Express,* vol. 21, no. 21, pp. 24879-24893, 2013.

[6] F. Li, Y. Park, and J. Azaña**,** "Complete temporal pulse characterization based on phase reconstruction using optical ultrafast differentiation (PROUD)," *Opics Letters*, vol. 32, no. 22, pp. 3364-3366, 2007.

[7] J. Azaña, Y. Park and F. Li, "Linear self-referenced complex-field characterization of fast optical signals using photonic differentiation," *Optics Commununications,* vol. 284, no. 15, pp. 3772-3784, 2011.

[8] Y. Park, M. Scaffardi, L. Potì, and J. Azaña**,** "Simultaneous single-shot real-time measurement of the instantaneous frequency and phase profiles of wavelength-division-multiplexed signals," *Optics Express,* vol. 18, no. 6, pp. 6220-6229, 2010.

[9] C. L. Callender, P. Dumais, C. Blanchetiere, S. Jacob, C. Ledderhof , C. W. Smelser, K. Yadav, and J. Albert, "Compact silica-on-silicon planar lightwave circuits for high speed optical signal processing," *Proceeding SPIE*, vol. 8357, pp. 82570.1-83570.10, 2012.

[10] H. Lee, T. Chen, J. Li, O. Painter, and K. J. Vahala, "Ultra-low-loss optical delay line on a silicon chip," *Naure Communications*, vol. 3, no. 867, pp. 1-7, 2012.

[11] Y. Zhang, Sh. Yang, Y. Yang, M. Gould, N. Ophir, A. E. Lim, G. Lo, Pe. Magill, K. Bergman, T. Baehr-Jones, and M. Hochberg, "A high-responsivity photodetector absent metal-germanium direct contact," *Optics Express*, vol. 22, no. 9, pp. 11367-11375, 2014.

Chapter 5 Conclusions and perspectives

We conclude all the work that has been reported in this Thesis and provide information on possible future works for each of the explored research lines.

5.1 Summary

In this Thesis, we have developed integrated-optics devices and techniques for arbitrary optical pulse shaping (OPS), optical signal processing and optical signal characterization. In particular, we have targeted OPS devices with operation bandwidths ranging from a few GHz well into THz range. In order to fulfill this task, a novel theory has been proposed and accordingly, we have designed and experimentally demonstrated GHz and THz-bandwidth integrated waveguide-based arbitrary optical pulse shapers [1-3]. In another work, we have developed two important basic building-blocks for on-chip optical signal processing, namely tunable band-pass/band-reject filtering and real-time photonic Hilbert transformation, using Bragg gratings [4-6]. Finally, we have demonstrated on-chip real-time, single-shot GHz-rate optical telecommunication signal characterization based on a linear, self-referenced method called PROUD (Phase Reconstruction using Optical Ultrafast Differentiation) [7].

In CHAPTER 2, we have proposed and experimentally demonstrated a novel design approach enabling OPS with operation bandwidth ranging from a few GHz up to a few THz. The proposed design is based on forward coupling between a so-called “main-waveguide” and a “bus-waveguide”, where the coupling is controlled in a discrete fashion (point by point) through standard co-directional couplers. In particular, our proposed scheme consists of cascaded co-directional couplers connected to each other in series using un-balanced optical waveguides. We have shown that the device can be designed so that the ‘discrete’ amplitude and phase ‘apodization’ profile along the concatenated couplers, namely coupling strength and relative time delay between the optical waveguide connecting consecutive couplers, can be directly mapped into the output temporal response. This approach can be interpreted as a discrete version of the space-to-time mapping (STM) process extensively studies in waveguide/fiber gratings [8]. Similarly, this approach significantly facilitates the design of structures based on concatenated co-directional couplers for temporal pulse shaping operations, as compared with standard design approaches based on spectral-domain response synthesis, e.g., so-called lattice filters [9,10].

The devices achieved from our newly proposed design can be easily scaled for operation bandwidths into the THz range. Moreover, the resulting devices are notably simpler to fabricate than their waveguide-grating counterparts, while also potentially enabling reconfigurability through well-established mechanisms. For instance, precise control of the temporal response amplitude or phase could be achieved by correspondingly tuning the coupling length or differential delay between couplers, respectively. Therefore, the proposed method opens up a promising new avenue to overcome the fundamental time-resolution limitations of present in-fiber and on-chip OPS and processing devices, which are generally limited by the spatial resolution of available fabrication technologies.

As the next step in CHAPTER 2, we have numerically and experimentally demonstrated straightforward applications of the discrete STM phenomenon for synthesizing customized complex optical waveforms using all-passive integrated waveguides designs. Relevant contributions of our work include the following:

- Proposal and theoretical development of an OPS method based on discrete STM in cascaded co-directional couplers. Precise modelling of the proposed scheme has been carried out for its on-chip implementation [1].

- Experimental demonstration of sub-picosecond OPS on an SOI technology platform, based on discrete space-to-time mapping. In this work, we have achieved sub-picosecond intensity-only and phase-only pulse shaping. In particular, flat-top pulses with duration ranging from 440-fs up to 3-ps, and an 8-bit 0.6-Tbit/s phase-coded pulse sequence with 4 different phase levels have been successfully generated in a compact SOI chip [2].

- Additionally, we have experimentally synthesized long duration intensity-only and complex modulated signals (simultaneous phase and intensity modulated signals). In particular, flat-top pulses with durations in the range of 70 ps, and a 40-ps-long 200-Gbaud 16-quadratute amplitude modulation (QAM) data sequence have been successfully generated using our proposed scheme, proving its unique capability in synthesizing optical pulses with durations from a few femtoseconds up to tens of picoseconds [3].

Our numerical simulations and experimental implementations of this scheme have confirmed that customized complex optical temporal waveforms, with sub-picosecond resolutions, can be easily generated and/or processed using all-passive integrated waveguide based devices.

In CHAPTER 3, we have proposed a tunable, nondispersive optical filter design using photonic Hilbert transformation (PHT). In this project, we have proposed and numerically demonstrated a new design concept for realizing nondispersive complementary (band-pass/band-reject) optical filters with a wide range of bandwidth tunability. The device consists of two PHTs incorporated into a Michelson interferometer (MI). By controlling the central frequency of PHTs with respect to each other, both the central frequency and the spectral width of the rejection/pass bands of the filter are proved to be tunable [4]. The proposed design is specifically interesting for tunable narrow band filtering. In this project bandwidth tuning from 260 MHz to 60 GHz is numerically demonstrated using two readily feasible fiber Bragg grating-based PHTs. The designed filter offers a high extinction ratio between the pass band and rejection band (>20dB in the narrow-band filtering case) with a very sharp transition with a slope of 170 dB/GHz from rejection to pass band [4].

In the quest for high-quality PHTs to realize the proposed filter design (explained above), we have proposed and experimentally demonstrated PHT designs based on laterally apodized waveguide Bragg gratings (BGs) on silicon-on-insulator (SOI). In particular, in this work high-performance photonic integer Hilbert transformer with processing bandwidths above 750 GHz has been experimentally realized using laterally apodized Bragg gratings on SOI wafers. We have demonstrated a notably increased tolerance to fabrication errors offered by this technology in comparison to conventional apodized BG designs, e.g., direct control of the depth of physical corrugations on a straight integrated waveguide [5,6]. In principle a high dynamic range in refractive index modulation is required in order to realize a high quality PHT (high time-bandwidth product). Such specification is of particular importance for realization of our proposed narrow-band filtering scheme.

Finally in CHAPTER 4, we have demonstrated on-chip characterization of GHz-rate complex optical signals. In this work, phase reconstruction based on optical ultrafast differentiation is implemented using an integrated-waveguide Mach–Zehnder interferometer to demonstrate self-referenced phase characterization of GHz-rate complex modulated signals (e.g., 1-Gbaud quadrature phase shift keying (QPSK) and 0.7-Gbaud amplitude phase shift keying modulation (APSK) modulated signals), through a single-shot and real-time technique. This method is transparent to both modulation format and bit rate, limited only by the bandwidth capabilities of the temporal intensity measurement instrumentation [7]. Moreover, the characterization setup includes only a single filter and a single conventional photodetector.

5.2 Future research

Although many of the first-time demonstrations shown in this Thesis are useful in proving the corresponding principle of operation, the optimization of these devices and demonstration of their applications in photonic-based optical waveform generation, processing and characterization schemes will require intensive research.

In CHAPTER 2, we have explored the idea of discrete STM and successfully realized different pulse shapes using passive devices. However, reconfigurable OPS can be considered as a very interesting research line to further develop this idea. In particular, we could consider replacing directional couplers with thermo- or electro-optically tunable variable optical attenuators and incorporating phase-shifters in the delay-lines to enable the capability of programming the synthesis of arbitrary pulse shapes with temporal durations determined by the amount of delay at each stage of the device and the input pulse width.

In CHAPTER 3, we have proposed a tunable filtering scheme based on two PHTs incorporated into a MI. We have also managed to design high quality integer-order PHTs on SOI. The final step for this project would be to incorporate the BG-based PHTs into a MI and add thermo- or electro-optics tuning elemnts on each of them in order to realize the proposed tunable filter scheme. In particular, considering our designed PHTs we could target a tunable filter with bandwidth tenability ranging from ~50 GHz to ~325 GHz.

In CHAPTER 4, we have demonstrated on-chip single-shot and real-time signal characterization by using an integrated MZI as the optical differentiator. However, the needed tunable reference delay line and two photo-detectors could be integrated along with the MZI. In this way, the proposed method could be used to create a fully integrated module capable of real-time, single-shot characterization of GHz-rate data signals with potentially improved compactness, stability and sensitivity. Additionally, we have studied this method for only 20-bit sequence. A great improvement would be to repeat the experiment with a pseudo random binary sequence (PRBS) sequence. Moreover, after pig-tailing the chip (in order to reduce the insertion fiber-to-chip and chip-to-fiber loss), a comprehensive bit error rate will help further develop the potential of this technique for optical signal characterization.

Finally, the author believes that the extension of innovative research lines proposed in this Thesis for on-chip OPS, signal processing and signal characterization will greatly contribute to the realization of all-optical signal processing units on-chip.

5.3 References

[1] H. P. Bazargani and J. Azaña, "Optical pulse shaping based on discrete space-to-time mapping in cascaded co-directional couplers," *Optics Express,* vol. 23, no. 18, pp. 5423-5426 , 2015.

[2] H. P. Bazargani, M. Burla and J. Azaña, "Experimental demonstration of sub-picosecond optical pulse shaping in silicon based on discrete space-to-time mapping," *Optics Letters,* vol. 40, no. 23, pp. 5423-5426 , 2015.

[3] H. P. Bazargani, M. Burla, Z. Chen, F. Zhang, L. Chrostowski and J. Azaña, "Long-duration optical pulse shaping and complex coding on SOI," *IEEE Photonics Journal,* vol. 8, no. 4, pp. 1-7 , 2016.

[4] H. P. Bazargani, M. R. Fernández-Ruiz and J. Azaña, "Tunable, nondispersive optical filter using photonic Hilbert transformation," *Optics Letters,* vol. 39, no. 17, pp. 5232-5235 , 2014.

[5] H. P. Bazargani, M. Burla and J. Azaña, "Photonic Hilbert transformer based on laterally apodized waveguide Bragg gratings on a SOI wafer," in *Conference on Lasers and Electro-optics (CLEO 2016)*, San Jose, CA, USA, 2016.

[6] H. P. Bazargani and J. Azaña, "Integer and fractional-order photonic Hilbert transformer on SOI," in *OSA Topical Meeting on Integrated Photonics Research, Silicon, and Nano-Photonics (IPR 2016)*, Vanvouver, BC, 2016.

[7] H. P. Bazargani, J. B. Quelene, P. Dumais, A. Malacarne, M. Clerici, R. Morandotti, C. L. Callender and J. Azaña, "On-Chip, Single-Shot Characterization of GHz-Rate Complex Optical Signals," *IEEE Photonics Technology Letters,* vol. 26, no. 23, pp. 2345-2348, 2014.

[8] L. M. Rivas, M. J. Strain, D. Duchesne, A. Carballar, M. M. R. Sorel and J. Azaña, "Picosecond linear optical pulse shapers based on integrated waveguide Bragg gratings," *Optics Letters,* vol. 33, no. 21, pp. 2425-2427, 2008

[9] T. Takiguchi, K. Okamoto, S. Suzuki and Y. Ohmori, "Planar Lightwave Circuit Optical Dispersion Equalizer," *IEEE Photonics Technology Letters*, vol. 6, no. 1, pp. 86-88, 1994.

[10] F. Khaleghi, M. Kavehrad and C. Barnard, "Tunable Coherent Optical Transversal EDFA Gain Equalization," *Journal of Lightwave Technology*, vol. 13, no. 4, pp. 581-587, 1995.

Appendix A

Time bandwidth product

As illustrated in **Figure A.1**, the time–bandwidth product (TPB) of a pulse is the product of its temporal duration and spectral width (in frequency domain). In ultrafast laser physics, it is common to specify the full width at half-maximum (FWHM) in both time and frequency domain. The minimum possible TBP is obtained for bandwidth-limited pulses or the so called 'transform-limited' pulses. For example, it is ≈ 0.315 for bandwidth-limited sech-shaped pulses and ≈ 0.44 for Gaussian-shaped pulses. This means that for a given spectral width, there is a lower limit for the pulse duration. This limitation is essentially a property of the Fourier transform.

The TBP is often used for indicating how close a pulse is to the transform limit, i.e., how close the pulse duration is to the limit which is set by its spectral width. This is an aspect of "pulse quality"; bandwidth-limited pulses have the minimum possible TBP, whereas chirped pulses have larger values.

In this thesis we have used the concept of TBP to study the pulse/filter quality. Higher numbers for TBP indicates higher quality for a target pulse shape or filtering operation and can be used as a figure of merit for applications like OPS.

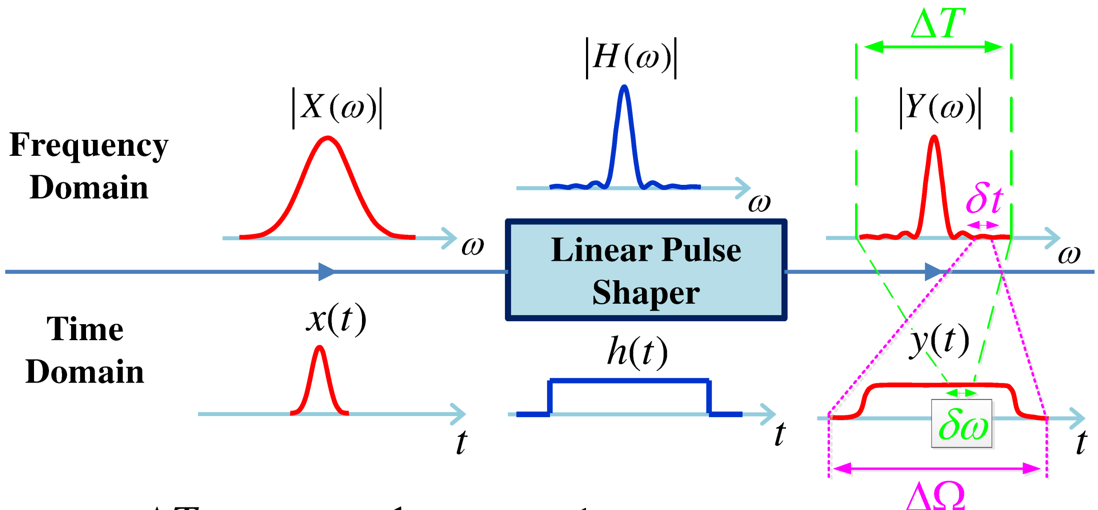

$$\mathrm{TBP} = \frac{\Delta T}{\delta t}, \quad \Delta T = \frac{1}{\delta\omega}, \quad \delta t = \frac{1}{\Delta\Omega}$$

Figure A.1 Schematic illustration of time-bandwidth product (TBP) considering a linear pulse shaper as an LTI system.

Appendix B

B.1 Transfer matrix method (TMM)

Precise modelling of different devices, studied in this Thesis, has been carried out using transfer matrix method (TMM) in combination with two-dimensional and three-dimensional electromagnetic simulations tools, i.e., Lumerical Mode Solution and Lumerical Finite Difference Time Domain (FDTD), respectively. In what follows we first study the TMM for a thin film and multilayered structure [1]. We then provide details about the specific devices that have been designed throughout this Thesis.

B.1.1 2×2 Matrix formulation for a thin film

We first start with a structure described by Figure B.1.

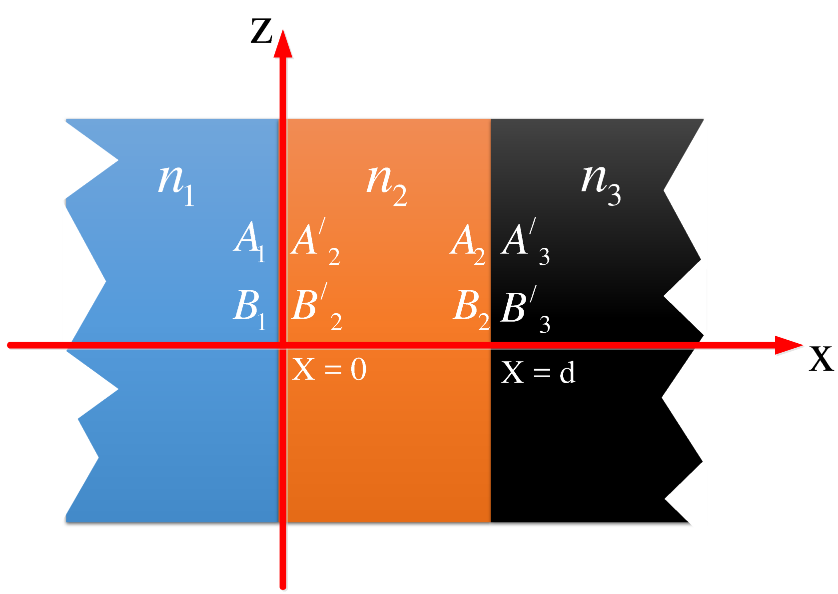

Figure B.1 A thin layer of dielectric medium (the first and last layers in the stack are assumed to be extended to infinity in x-direction).

$$n(x)=\begin{cases} n_1, & x<0, \\ n_2, & 0<x<d, \\ n_3, & d<x, \end{cases} \tag{B.1}$$

where n_1 , n_2 and n_3 are the refractive indices and *d* is the thickness of the film. Considering the whole medium to be homogeneous in the z direction (i.e., $\partial n/\partial z=0$), the electric field that satisfies Maxwell's equations has the form,

$$E=E(x)e^{i(\omega t-\beta z)}, \tag{B.2}$$

where β is the z component of the wave vector and ω is the angular frequency. In (B.2), we assume that the electromagnetic wave is propagating in the xz plane, and we further assume that the electric field is either an s wave (with E$\|$y) or p wave (with H$\|$y).

The electric field $E(x)$ consists of a right-travelling wave and a left-travelling wave and can be written as:

$$E(x)=Re^{-ik_x x}+Le^{ik_x x}\equiv A(x)+B(x), \tag{B.3}$$

where $\pm k_x$ are the x components of the wave vector and *R* and *L* are constants in each homogeneous layer. Let $A(x)$ represent the amplitude of the right-travelling wave and $B(x)$ be that of the left-travelling one. To illustrate the matrix method, we define

$$\begin{aligned} A_1&=A(0^-), \\ B_1&=B(0^-), \\ A'_2&=A(0^-), \\ B'_2&=B(0^+), \\ A_2&=A(d^-), \\ B_2&=B(d^-), \end{aligned} \tag{B.4}$$

$$A'_3 = A\left(d^+\right),$$

$$B'_3 = B\left(d^+\right),$$

where 0^- represents the left side of the interface, $x = 0,$ and 0^+ represents the right side of the same interface. Similarly, d^- and d^+ are defined for the interface at $x = d.$ Note that $E\left(x\right)$ for the s wave is a continuous function of $x.$ However, as a result of the decomposition of Eq. (B.3), $A\left(x\right)$ and $B\left(x\right)$ are no longer continuous at the interfaces. If we represent the two amplitudes of $E\left(x\right)$ as column vectors, the column vectors shown in Figure B.1 are related by:

$$\begin{pmatrix} A_1 \\ B_1 \end{pmatrix} = D_1^{-1} D_2 \begin{pmatrix} A_2' \\ B_2' \end{pmatrix} \equiv D_{12} \begin{pmatrix} A_2' \\ B_2' \end{pmatrix} \tag{B.5}$$

$$\begin{pmatrix} A_2' \\ B_2' \end{pmatrix} = P_2 \begin{pmatrix} A_2 \\ B_2 \end{pmatrix} \equiv \begin{pmatrix} \exp(\mathrm{i}\varphi_2) & 0 \\ 0 & \exp(-\mathrm{i}\varphi_2) \end{pmatrix} \begin{pmatrix} A_2 \\ B_2 \end{pmatrix} \tag{B.6}$$

$$\begin{pmatrix} A_2 \\ B_2 \end{pmatrix} = D_2^{-1} D_3 \begin{pmatrix} A_3' \\ B_3' \end{pmatrix} \equiv D_{23} \begin{pmatrix} A_3' \\ B_3' \end{pmatrix} \tag{B.7}$$

where D_1, D_2 and D_3 are the dynamical matrices given by:

$$D_\alpha = \begin{cases} \begin{pmatrix} 1 & 1 \\ n_\alpha \cos\theta_\alpha & -n_\alpha \cos\theta_\alpha \end{pmatrix} & \text{for s wave} \\ \begin{pmatrix} \cos\theta_\alpha & \cos\theta_\alpha \\ n_\alpha & -n_\alpha \end{pmatrix} & \text{for p wave} \end{cases} \tag{B.8}$$

where $\alpha = 1, 2, 3$ and θ_α is the ray angle in each layer and is related to β and $k_{\alpha x}$ by:

$$\beta = n_\alpha \frac{\omega}{c} \sin\left(\theta_\alpha\right), \tag{B.9}$$

$$k_{\alpha x} = n_\alpha \frac{\omega}{c} \cos\theta_\alpha \tag{B.10}$$

P_2 is the so-called propagation matrix, which accounts for propagation through the bulk of the layer, and φ_2 is given by:

$$\varphi_2 = k_{2x}d \tag{B.11}$$

The matrices D_{12} and D_{23} may be regarded as transmission matrices that link the amplitudes of the waves on the two sides of the interfaces and are given by:

$$D_{12} = \begin{pmatrix} \frac{1}{2}\left(1+\frac{k_{2x}}{k_{1x}}\right) & \frac{1}{2}\left(1-\frac{k_{2x}}{k_{1x}}\right) \\ \frac{1}{2}\left(1-\frac{k_{2x}}{k_{1x}}\right) & \frac{1}{2}\left(1+\frac{k_{2x}}{k_{1x}}\right) \end{pmatrix} \quad \text{for s wave} \tag{B.12}$$

and

$$D_{12} = \begin{pmatrix} \frac{1}{2}\left(1+\frac{n_2^2 k_{2x}}{n_1^2 k_{1x}}\right) & \frac{1}{2}\left(1-\frac{n_2^2 k_{2x}}{n_1^2 k_{1x}}\right) \\ \frac{1}{2}\left(1-\frac{n_2^2 k_{2x}}{n_1^2 k_{1x}}\right) & \frac{1}{2}\left(1+\frac{n_2^2 k_{2x}}{n_1^2 k_{1x}}\right) \end{pmatrix} \quad \text{for p wave} \tag{B.13}$$

The expressions for D_{23} are similar to those of D_{12}, except that the subscript indices need to be replaced with 2 and 3. Equations (B.12-13) can be written formally as:

$$D_{12} = \frac{1}{t_{12}}\begin{pmatrix} 1 & r_{12} \\ r_{12} & 1 \end{pmatrix} \tag{B.14}$$

where t_{12} and r_{12} are the Fresnel transmission and reflection coefficients [1], respectively, and are given by:

$$r_{12} = \begin{cases} \dfrac{k_{1x} - k_{2x}}{k_{1x} + k_{2x}} & \text{for s wave} \\ \dfrac{n_1^2 k_{1x} - n_2^2 k_{2x}}{n_1^2 k_{1x} + n_2^2 k_{2x}} & \text{for p wave} \end{cases} \tag{B.15}$$

and

$$r_{12} = \begin{cases} \dfrac{2k_{1x}}{k_{1x}+k_{2x}} & \text{for s wave} \\ \dfrac{2n_1^2 k_{1x}}{n_1^2 k_{1x}+n_2^2 k_{2x}} & \text{for p wave} \end{cases} \quad \text{(B.16)}$$

respectively.

From Eqs. (B.5-7), the amplitudes A_1, B_1 and A_3', B_3' are related by:

$$\begin{pmatrix} A_1 \\ B_1 \end{pmatrix} = D_1^{-1} D_2 P_2 D_2^{-1} D_3 \begin{pmatrix} A_3' \\ B_3' \end{pmatrix} \quad \text{(B.17)}$$

Note that, the column vectors representing the plane-wave amplitude in each layer are related by a product of 2×2 matrices in sequence. Each side of an interface is represented by a dynamical matrix, and the bulk of each layer is represented by a propagation matrix. Such a recipe can be extended to the case of multiplayer structures.

B.1.2 2×2 Matrix formulation for a multilayer system

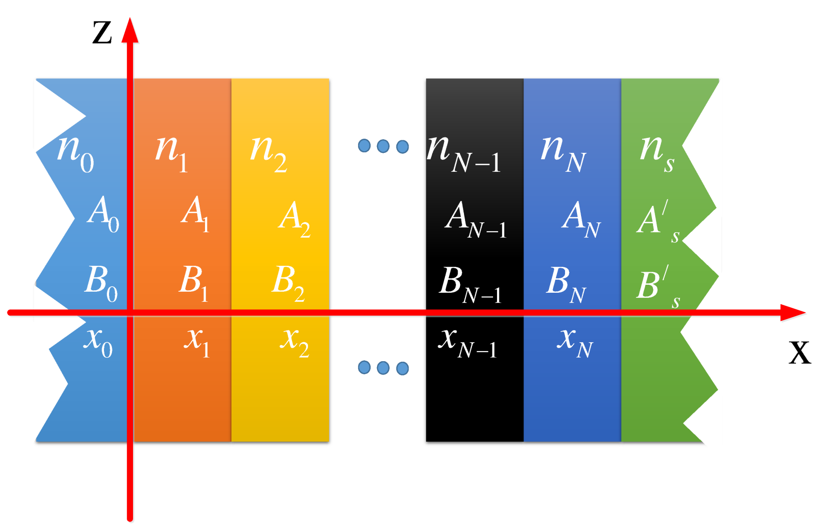

Figure B.2 A multilayer dielectric medium (the first and last layers in the stack are assumed to be extended to infinity in x-direction).

Referring to Figure B.2, we now consider the case of multilayer structures. The dielectric is described by:

$$n(x) = \begin{cases} n_0 & x < x_0 \\ n & x_0 < x < x_1 \\ \vdots & \vdots \\ n_N & x_{N-1} < x < x_N \\ n_s & x_N < x \end{cases} \tag{B.18}$$

where n_l is the refractive index of the lth layer, x_l is the position of the interface between the lth layer and the (l+1)th layer, n_s is the substrate index of refraction, and n_0 is that of the incident medium.

The layer thickness d_l are related to the x_l's by:

$$\begin{aligned} d_1 &= x_1 - x_0 \\ d_2 &= x_2 - x_1 \\ &\vdots \\ d_N &= x_N - x_{N-1} \end{aligned} \tag{B.19}$$

The electric field of a general plane-wave solution of the wave equation can still be written as:

$$E = E(x)e^{i(\omega t - \beta z)}, \tag{B.20}$$

where the electric filed distribution $E(x)$ can be written as

$$E(x) = \begin{cases} A_0 e^{-ik_{0x}(x-x_0)} + B_0 e^{ik_{0x}(x-x_0)} & x < x_0 \\ A_l e^{-ik_{lx}(x-x_l)} + B_l e^{ik_{lx}(x-x_l)} & x_{l-1} < x < x_l \\ A_s^{/} e^{-ik_{0x}(x-x_0)} + B_s^{/} e^{ik_{0x}(x-x_0)} & x_N < x \end{cases} \tag{B.21}$$

where k_{lx} is the x component of the wave vectors

$$k_{lx} = \left[\left(n_l \frac{\omega}{c}\right)^2 - \beta^2\right]^{1/2}, \qquad l = 0,1,\dots,N,s \tag{B.22}$$

and is related to the ray angle θ_l by

$$k_{lx} = n_l \frac{\omega}{c} \cos\theta_l \tag{B.23}$$

According to Eqs. (B.21) and (B.3), A_l and B_l represent the amplitude of plane waves at interface $x = x_l$. Thus, using the same argument as in previous section (B.1.1) we can write

$$\begin{pmatrix} A_0 \\ B_0 \end{pmatrix} = D_0^{-1} D_1 \begin{pmatrix} A_1 \\ B_1 \end{pmatrix} \tag{B.24}$$

$$\begin{pmatrix} A_l \\ B_l \end{pmatrix} = P_l D_l^{-1} D_{l+1} \begin{pmatrix} A_{l+1} \\ B_{l+1} \end{pmatrix}, \qquad l = 1,2,\dots,\mathrm{N},$$

where $N+1$ represents s, $A_{N+1} = A_s^{/}, B_{N+1} = B_s^{/}$ and the matrices can be written as:

$$D_l = \begin{pmatrix} 1 & 1 \\ n_l \cos\theta_l & -n_l \cos\theta_l \end{pmatrix} \qquad \text{for s wave} \tag{B.25}$$

and

$$D_l = \begin{pmatrix} \cos\theta_l & \cos\theta_l \\ n_l & -n_l \end{pmatrix} \qquad \text{for p wave} \tag{B.26}$$

respectively, and

$$P_l = \begin{pmatrix} \exp(i\varphi_l) & 0 \\ 0 & \exp(-i\varphi_l) \end{pmatrix}, \tag{B.27}$$

with

$$\varphi_l = k_{lx} d_l \tag{B.28}$$

The relation between A_0, B_0 and $A_s^{/}$, $B_s^{/}$ can thus be written as

$$\begin{pmatrix} A_0 \\ B_0 \end{pmatrix} = \begin{pmatrix} M_{11} & M_{12} \\ M_{21} & M_{22} \end{pmatrix} \begin{pmatrix} A_s^{/} \\ B_s^{/} \end{pmatrix} \tag{B.29}$$

with the matrix given by

$$\begin{pmatrix} M_{11} & M_{12} \\ M_{21} & M_{22} \end{pmatrix} = D_0^{-1} \left[\prod_{l=1}^{N} D_l P_l D_l^{-1} \right] D_s \tag{B.30}$$

Here, we recall that N is the number of layers, A_0 and B_0 are the amplitudes of the plane waves in medium 0 at $x = x_0$, and $A_s^{/}$, $B_s^{/}$ are the amplitudes of the plane waves in medium s at $x = x_N$.

B.1.3 Transmittance and reflectance

Using 2×2 matrix method, we now discuss the reflectance and transmittance of monochromatic plane waves through a multilayer dielectric structure. If the light is incident from medium 0, the reflection and transmission coefficients are defined as:

$$r = \left(\frac{B_0}{A_0} \right)_{B_s = 0} \tag{B.31}$$

and

$$t = \left(\frac{A_s}{A_0} \right)_{B_s = 0}, \tag{B.32}$$

respectively. Here we drop the prime ($^{/}$) and define $A_s = A_s^{/}$, $B_s = B_s^{/}$.

Using the matrix equation (B.29) we obtain:

$$r = \frac{M_{21}}{M_{11}} \tag{B.33}$$

and

$$t = \frac{1}{M_{11}} \tag{B.34}$$

Reflectance is given by:

$$R = |r|^2 = \left|\frac{M_{21}}{M_{11}}\right|^2 \tag{B.35}$$

provided medium 0 is lossless.

If the bounding media $(0, s)$ are both pure dielectric with real n_s and n_0, transmittance T is given by:

$$T = \frac{n_s \cos\theta_s}{n_0 \cos\theta_0} |t|^2 = \frac{n_s \cos\theta_s}{n_0 \cos\theta_0} \left|\frac{1}{M_{11}}\right|^2 \tag{B.36}$$

provided both the incident wave and the transmitted wave have real propagation vectors (i.e., real θ_0 and θ_s).

B.2 Integrated waveguide design

Different set of devices studied throughout this Thesis consist of standard single-mode or multi-mode waveguide sections on silicon-on-insulator (SOI) wafer. As illustrated in Figure B.3, designed waveguides are 220 nm high (predefined by fabrication foundries) with their widths ranging from 500 nm (single-mode operation) up to 1 µm (multi-mode operation), depending on the application. The cladding and buried oxide (BOX) layers are made of silicon dioxide with a height of 2 µm and 3 µm, respectively.

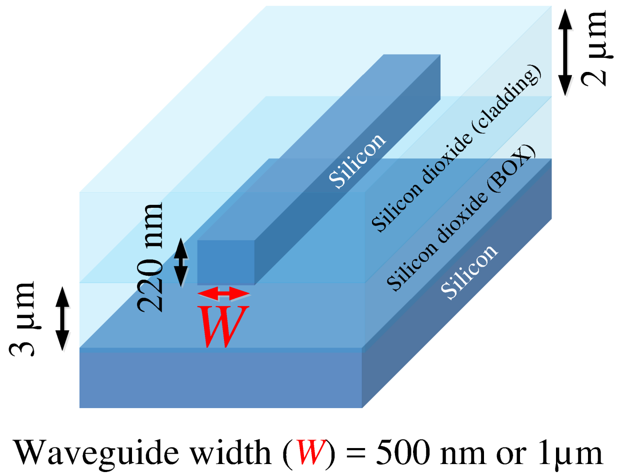

Figure B.3 Schematic of the silicon strip waveguide on SOI.

Precise modelling of different devices, studied in this Thesis, has been carried out using transfer matrix method (TMM) in combination with two-dimensional and three-dimensional simulations tools, i.e., Lumerical Mode Solution and Lumerical Finite Difference Time Domain (FDTD), respectively. As an example the propagation constant for light passing through a waveguide section can be defined as

$$\beta = \frac{2\pi n_{eff}(\lambda)}{\lambda} - j\frac{\alpha}{2} \tag{B.37}$$

where $n_{eff}(\lambda)$, is the wavelength-dependent effective refractive index of the waveguide, accounting for the waveguide's dispersions and α is the loss per unit length of the waveguide. In contrast to optical fibers, the amount of dispersion in a silicon strip waveguide is significant. Consequently, for the sake of precision, the effective refractive index profile need to be carefully calculated at different wavelengths. Then, the relevant vector ($n_{eff}(\lambda)$) should be plugged into the transfer matrix model of the waveguide. As illustrated in Figure B.4, Lumerical Mode Solutions has been used in order to study the cross-section of the waveguide and extract $n_{eff}(\lambda)$.

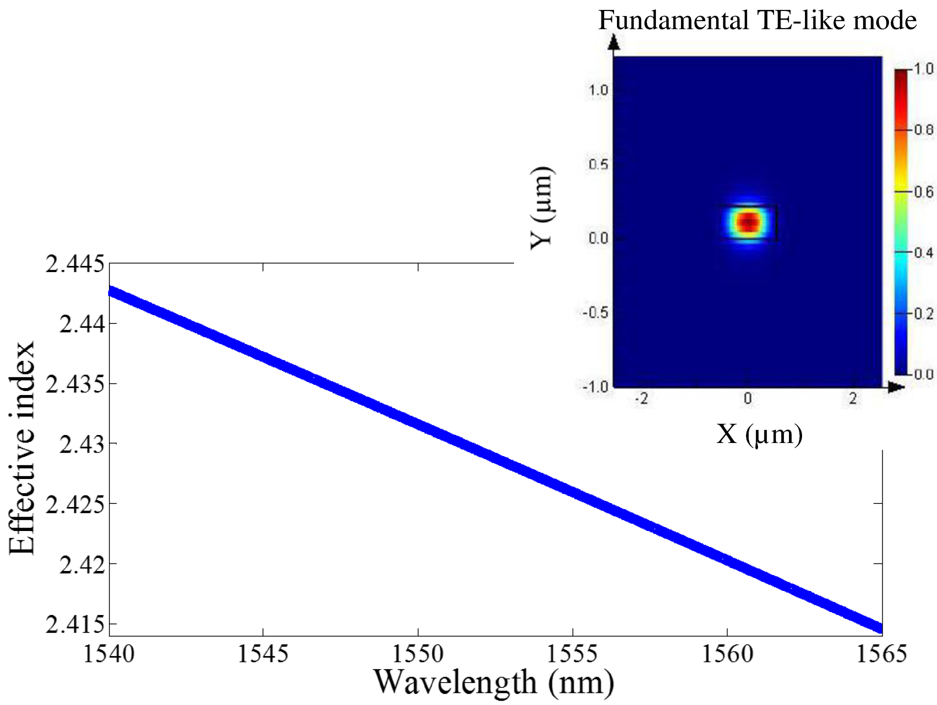

Figure B.4 The effective refractive index profile of fundamental quasi-transverse electric (quasi-TE) mode for 500 nm × 220 nm (width × height) waveguide. The inset shows the quasi-TE mode profile at the cross-section of the waveguide.

Finally, plugging Eq. (B.37) into Eq. (B.30) a device consisting of different waveguide sections can be precisely modelled.

B.3 Integrated Bragg grating design

An integrated Bragg grating can be also regarded as a multi-layer structure for which the above model can be applied. The precise modelling of an apodized Bragg grating can be done using three dimensional (3D) FDTD method. However, simulating an integrated Bragg grating using 3D simulation tools is computationally expensive. The reason for that is the nanometer range resolution required along the grating's length (in the order of hundreds of microns to several millimeters) to achieve meaningful results out of the simulation tool.

A simple solution for this problem is to use the TMM method as explained above. However, dispersion and waveguide loss are two important parameters which have not been taken into account in the developed model [2]. As illustrated in Figure B.5**,** a similar method as what is explained in section (B.2) is used for precise modelling of Bragg gratings on SOI.

Finally, the transmission and reflection responses can be obtained from Eqs. (33-34).

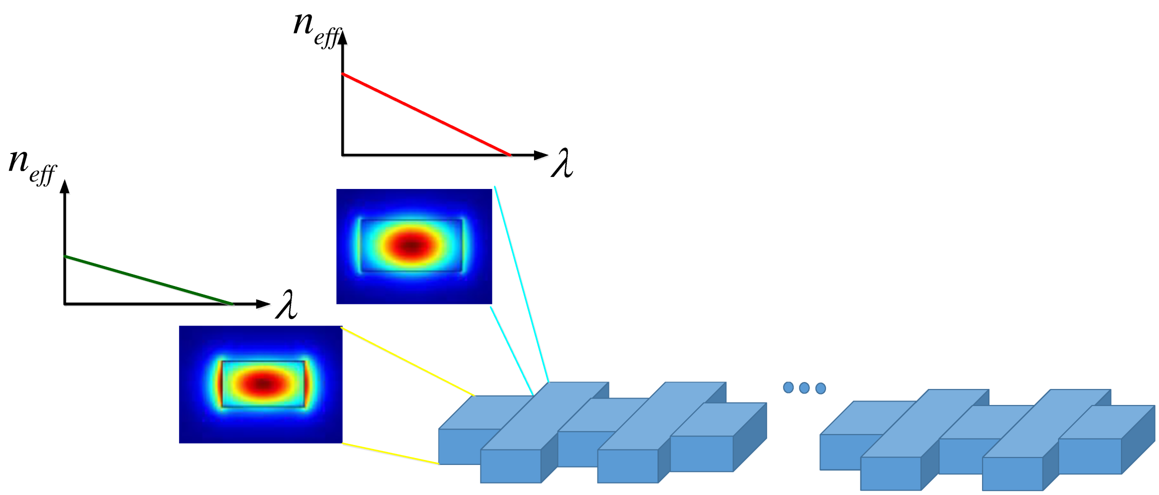

Figure B.5 The process for precisely simulating an integrated Bragg grating, considering dispersion and waveguide losses.

B.4 References

[1] P. Yeh, Optical waves in layered medias, *Wiley*, 2005.

[2] L. Chrostowski and M. Hochberg, Silicon Photonics Design Book-from Devices to Systems, *Cambridge University press*, 2011.

Appendix C

C.1 Associated publications

C.1.1 Journal publications

[1] **H. P. Bazargani**, M. Burla, L. Chrostowski, and J. Azaña, “Photonic Hilbert transformers based on laterally apodized integrated waveguide Bragg gratings on SOI wafer,” *Accpeted for publication in Optics Letters, vol. 41, no. 21, 2016.*

[2] **H. P. Bazargani**, M. Burla, Z. Chen, J. Zhang, L. Chrostowski and J. Azaña, “Long-duration optical pulse shaping and complex coding in SOI using discrete space-to-time mapping,” *IEEE Photonics Journal*, vol. 8, no. 4, pp. 1-7, 2016.

[3] **H. P. Bazargani**, M. Burla, J. Azaña, “Experimental demonstration of sub-picosecond optical pulse shaping in silicon based on discrete space-to-time mapping,” *Optics Letters*, vol. 40, no. 23, pp. 5423-5426, 2015.

[4] **H. P. Bazargani**, J. Azaña, “Optical pulse shaping based on discrete space-to-time mapping in cascaded co-directional couplers,” *Optics Express*, vol. 23, no. 18, pp. 23450-23461, 2015.

[5] **H. P. Bazargani**, M. R. Fernández-Ruiz, J. Azaña, "Tunable, nondispersive optical filter using photonic Hilbert transformation," *Optics Letters*, vol. 39, no. 17, pp. 5232-5235, 2014.

[6] **H. P. Bazargani**, J-B. Quélène, P. Dumais, A. Malacarne, M. Clerici, R. Morandotti, C. L. Callender, J. Azaña, “On-chip, single-shot characterization of GHz-rate complex optical signals,” *IEEE Photonics Technology Letters*, vol. 26, no. 23, pp. 2345-2348, 2014.

C.1.2 International conference papers

[1] **H. P. Bazargani** and J. Azaña, “Realization of arbitrary complex apodization profiles using integrated Bragg grating on SOI,” *Conference on Lasers and Electro-optics Focus Meeting 42nd European Conference on Optical Communications* (*ECOC 2016*), September 18-22, 2016, Dusseldorf, Germany (**Accepted**).

[2] **H. P. Bazargani** and J. Azaña, "Integer and fractional-order photonic Hilbert transformer on SOI," *OSA Topical Meeting on Integrated Photonics Research, Silicon, and Nano-Photonics* (*IPR 2016*), July 18-20, 2016, Vancouver, BC, Canada. Paper IW2A.2**.**

[3] **H. P. Bazargani** and J. Azaña, "On-chip optical pulse shaping using cascaded co-directional couplers," *Progress In Electromagnetics Research Symposium (PIERS 2016),* August 8-11, 2016, Shanghai, China. (**Invited**).

[4] **H. P. Bazargani,** M. Burla and J. Azaña, "Long-duration, picosecond optical pulse shaping on SOI using discrete space-to-time mapping," *Conference on Lasers and Electro-optics (CLEO 2016),* June 5-10, 2016, San Jose, CA, USA. Paper SM3E.3.

[5] **H. P. Bazargani,** M. Burla and J. Azaña, "Photonic Hilbert transformer based on laterally apodized waveguide Bragg gratings on a SOI wafer," *Conference on Lasers and Electro-optics (CLEO 2016),* June 5-10, 2016, San Jose, CA, USA. Paper SM3E.4.

[6] **H. P. Bazargani**, M. Burla, J. Azaña, "On-chip optical pulse shaping based on discrete space-to-time mapping in concatenated co-directional couplers,"*41st European Conference on Optical Communications* (*ECOC 2015*), September 27 – October 1, 2015, Valencia, Spain. Paper p2.7.

[7] **H. P. Bazargani**, R. Ashrafi, J. Azaña, "Time-domain optical signal processing based on discrete space-to-time mapping in cascaded co-directional couplers," *OSA Topical Meeting on* B*ragg Gratings, Photosensitivity and Poling in Glass Waveguides* (*BGPP 2014*), July 27-31, 2014, Barcelona, Spain. Paper BW4D.4.

[8] **H. P. Bazargani**, M. R. Fernández-Ruiz, J. Azaña, "Bandwidth-tunable optical filters based on photonic Hilbert transformation," *IEEE Photonics Conference* (*IPC 2013*), September 8–12, 2013, Bellevue, WA, USA, Paper ThG1.2.

[9] **H. P. Bazargani**, J.-B. Quélène, P. Dumais, A. Malacarne, M. Clerici, R. Morandotti, C. L. Callender, J. Azaña, "On-chip single-shot and real-time self-referenced phase characterization of GHz-rate telecommunication signals," *Conference on Lasers and Electro-optics (CLEO 2013),* June 9-14, 2013, San Jose, CA, USA. Paper CM1G.3.

[10] **H. P. Bazargani**, M. R. Fernández-Ruiz, J. Azaña, "Tunable optical filter using photonic Hilbert transformation," *OSA Topical Meeting on Signal Processing in Photonics Communications* (*SPPCom 2013*), June 14-17, 2013, Rio Grande, PR, USA. Paper SpM4D.6.

[11] **H. P. Bazargani**, J.-B. Quélène, P. Dumais, A. Malacarne, C. Callender, J. Azaña, "Single-shot and real-time self-referenced phase characterization of GHz-rate QPSK signals," *OSA Topical Meeting on Signal Processing in Photonics Communications* (*SPPCom 2012*), June 17-21, 2012, Colorado Springs, CO, USA. Paper SpTu4A.3.

C.2 Other publications not directly related to the Thesis

C.2.1 Journal publications

[1] M. Li, P. Dumais, R. Ashrafi, **H. P. Bazargani**, J-B. Quélène, C. Callender, and J. Azaña "Ultrashort flat-top pulse generation using on-chip CMOS-compatible Mach-Zehnder Interferometers," *IEEE Photonics Technology Letters,* vol. 24, no. 16, pp. 1387-1389, 2012.

C.2.2 International conference papers

[1] **H. P. Bazargani,** J. Flueckiger, L. Chrostowski, J. Azaña, "Microring resonator design with improved quality factors using quarter Bezier curves," *Conference on Lasers and Electro-optics (CLEO 2015),* May 10-15, 2015, San Jose, CA, USA. Paper JTu5A.

[2] M. Burla, **H. P. Bazargani**, J. St-Yves, W. Shi, L. Chrostowski, J. Azaña, "Widely tunable microwave photonics notch filter based on a waveguide Bragg grating on silicon," *IEEE Photonics Conference* (*IPC 2014*), October 12 – 16, 2014, San Diego, CA, USA. Paper TuC.15.

[3] M. Burla, **H. P. Bazargani**, J. St-Yves, W. Shi, L. Chrostowski, J. Azaña, "Frequency agile microwave photonics notch filter based on a waveguide Bragg grating on silicon," *International Topical Meeting on Microwave Photonics* (*MWP 2014*), October 20-23, 2014, Sapporo, Japan. Paper WD-4.

[4] M. Li, P. Dumais, R. Ashrafi, **H. P. Bazargani**, J.B. Quélène, C. Callender, J. Azaña, "Ultrashort flat-top pulse generation using an integrated Mach-Zehnder interferometers," *IEEE Photonics Conference* (*IPC 2012*), September 23 – 27, 2012, Burlingame, California, USA. Paper ThQ-4.